Eulerian-Lagrangian definition of coarse bed-load transport

Theory and verification with low-cost inertial measurement units

By

GEORGIOS MANIATIS

School of Geographical and Earth Sciences
UNIVERSITY OF GLASGOW

A dissertation submitted to the University of Glasgow in accordance with the requirements of the degree of DOCTOR OF PHILOSOPHY in the College of Science and Engineering.

AUGUST 2016

Word count: 46210

Statement of Originality

I certify that the thesis presented here for examination for a PhD degree of the University of Glasgow is solely my own work other than where I have clearly indicated that it is the work of others (in which case the extent of any work carried out jointly by me and any other person is clearly identified in it).

I declare that the thesis does not include work forming part of a thesis presented successfully for another degree.

I declare that this thesis has been produced in accordance with the University of Glasgow's Code of Good Practice in Research.

Georgios Maniatis 22/08/2016

Abstract

Fluvial sediment transport is controlled by hydraulics, sediment properties and arrangement, and flow history across a range of time scales. This physical complexity has led to ambiguous definition of the reference frame (Lagrangian or Eulerian) in which sediment transport is analysed. A general Eulerian-Lagrangian approach accounts for inertial characteristics of particles in a Lagrangian (particle fixed) frame, and for the hydrodynamics in an independent Eulerian frame. The necessary Eulerian-Lagrangian transformations are simplified under the assumption of an ideal Inertial Measurement Unit (IMU), rigidly attached at the centre of the mass of a sediment particle. Real, commercially available IMU sensors can provide high frequency data on accelerations and angular velocities (hence forces and energy) experienced by grains during entrainment and motion, if adequately customized. IMUs are subjected to significant error accumulation but they can be used for statistical parametrisation of an Eulerian-Lagrangian model, for coarse sediment particles and over the temporal scale of individual entrainment events. In this thesis an Eulerian-Lagrangian model is introduced and evaluated experimentally. Absolute inertial accelerations were recorded at a 4 Hz frequency from a spherical instrumented particle (111 mm diameter and 2383 kg/m^3 density) in a series of entrainment threshold experiments on a fixed idealised bed. The grain-top inertial acceleration entrainment threshold was approximated at 44 and 51 mg for slopes 0.026 and 0.037 respectively. The saddle inertial acceleration entrainment threshold was at 32 and 25 mg for slopes 0.044 and 0.057 respectively. For the evaluation of the complete Eulerian-Lagrangian model two prototype sensors are presented: an idealised (spherical) with a diameter of 90 mm and an ellipsoidal with axes 100, 70 and 30 mm. Both are instrumented with a complete IMU, capable of sampling 3D inertial accelerations and 3D angular velocities at 50 Hz. After signal analysis, the results can be used to parametrize sediment movement but they do not contain positional information. The two sensors (spherical and ellipsoidal) were tested in a series of entrainment experiments, similar to the evaluation of the 111 mm prototype, for a slope of 0.02. The spherical sensor entrained at discharges of 24.8 ± 1.8 l/s while the same threshold for the ellipsoidal sensor was 45.2 ± 2.2 l/s. Kinetic energy calculations were used to quantify the particle-bed energy exchange under fluvial (discharge at 30 l/s) and non-fluvial conditions. All the experiments suggest that the effect of the inertial characteristics of coarse sediments on their motion is comparable to the effect hydrodynamic forces. The coupling of IMU sensors with advanced telemetric systems can lead to the tracking of Lagrangian particle trajectories, at a frequency and accuracy that will permit the testing of diffusion/dispersion models across the range of particle diameters.

ACKNOWLEDGEMENTS

Professor Trevor Hoey contributed significantly in the material presented in this thesis as my first supervisor. He devoted a lot of time discussing my ideas and shared openly his valuable experience and insight. I also thank him for making my development as independent scientist a priority for this project.

I am also thankful to the team of my co-supervisors. Professor Joseph Sventek, Dr. Rebecca Hodge and Dr. Tim Drysdale supported me greatly and refined my work. Dr. Manousos Valyrakis also offered me his time and support in many occasions, as well as, access to the flume laboratory of the School of Engineering (University of Glasgow) .

One of the most valuable experiences during this project was my research visit to the University of British Columbia. I want to specially thank Professor Marwan Hassan for his supervision and his generosity.

Other people also helped in various ways. Each contribution was very important and I am very grateful to all of them.

Professor Daniel Haydon helped me to begin with this project and trusted me with his reference. Ewan Russell contributed to the design and production of the 3D printing cases. Shawn Chartrand, Rick Ketler, David Reid and Matteo Saletti helped me to set up and run the experiments in UBC. Richard Warwick was the person in Kinneir Duffort that helped me manage the construction of the CAM aluminium cases. Thanos Alexakis helped me with the callibration of the sensors during the latest stages of this project.

Katerina Georgiou is the partner, friend and motivator that helped me finish this work. She also helped me with the graphics of this thesis.

Finally, I want to acknowledge my parents, Stavros and Tota, and my two mentors, Professor Dimitrios Patelis and Professor Vasilis Gekas. Without them I would be a very different person.

Στην Κατερίνα

TABLE OF CONTENTS

List of Tables

List of Figures

Figure **Page**

Nomeclature

Statistics

PDF	=	Probability Density Function
KDE	=	Kernel Density Estimates
OVL	=	Overlapping coefficient
P_E	=	probability of Entrainment
V_f	=	random fluctuation of vector V
F_{V_f}	=	cumulative distribution of V_f
f_{V_f}	=	Probability density function of F_{V_f}
y_t	=	Observation vector (Kalman Filter Definition)
θ_t	=	Unobserved vector (Kalman Filter Definition)
V, Ω	=	Observation and Evolution (process) covariances (Kalman Filter Definition)
p_i	=	Probabilities
Y_i	=	Binary variable (Logistic Regression)
X_i	=	Vector of predictors (Logistic Regression)
β	=	Vector of regression coefficients (Logistic Regression)

Rigid Body Kinematics

d_p	=	Particle diameter
R	=	Particle radius
m	=	Mass
V	=	Magnitude of vector
g	=	Acceleration due to gravity (1g)
$\|CA\|$	=	Absolute acceleration after gravity compensation
F_D	=	Drag force exerted by the flow on the particle
W	=	Submerged weight of the particle
ΣT_L	=	Sum of support forces the center of the mass of the pebble
F_L	=	Lift force of the flow
ΣT_R	=	Sum of friction forces applied on the surface of a pebble
I_{cm}	=	Moment of inertia (uniform for a sphere)
V_{norm}	=	Norm of linear velocities
Ω_{norm}	=	Norm of angular velocities
q_s, q_x, a_y, a_z	=	Quaternion components
Bu	=	Buoyancy force
G	=	Gravity force
F_M	=	Added mass force
I_{axis}	=	Moment of inertia along each axis
$KE_{bf,total}$	=	Total kinetic energy calculated in the body frame
$KE_{bf,trans}$	=	Translational kinetic energy
$V_{E,z}$, $V_{E,y}$, $V_{E,x}$	=	Vector axes in Eulerian frame
$V_{b,z}$, $V_{b,y}$, $V_{b,x}$	=	Vector axes in Body frame

Hydrodynamics

d	=	Flow depth measured from the level of the bed
ρ_p/ρ_F	=	Ratio of an experimental particle density to fluid density
P/d_p	=	Ratio of the particle protrusion P to particle diameter D
S_b	=	Bed slope
U_b	=	Bulk mean velocity derived from the fraction Q/A
Q	=	Flow rate
A	=	Cross sectional area of the flow
R_b	=	Bulk Reynolds number derived from the fraction $U_b d/\nu$
ν	=	Fluid kinematic viscosity
F	=	Froude number
B/d	=	Aspect ratio
B	=	Flume width
d/d_p	=	Flow submergence
u_*	=	Shear velocity
R_*	=	Friction Reynolds number
R_p	=	Particle Reynolds number
τ_*	=	Shields number
τ_p	=	Particle time scale (relaxation time of a particle)
τ_f	=	Fluid time scale (characteristic time of the fluid-flow)
ρ_p	=	Particle density
μ_p	=	Fluid dynamic viscosity

CHAPTER 1

INTRODUCTION

Many contemporary sensing applications entail the remote, continuous, unattended and *in-situ* monitoring of natural processes. Such applications are possible due to recent developments in the fields of Micro Electro-Mechanical Sensors (MEMS) and Wireless Sensor Networks (WSN) and can pose technologically challenging demands, which were not *a priori* incorporated in the design/optimization criteria for either of these two fields [*Hart and Martinez*, 2006; *Corke et al.*, 2010; *Oliveira and Rodrigues*, 2011].

Harsh and very variable natural environments such as the ocean [*Benelli et al.*, 2012], volcanoes [*Werner-Allen et al.*, 2006], glaciers [*Martinez et al.*, 2009] and rivers (on Earth and other planets [*Pedersen et al.*, 2003]) are particularly challenging. Complex processes take place, the understanding of which is based on the quality of the sensed data.

Along with the practical considerations, it is crucial to understand how the sensor itself affects the process of data-acquisition, hence the quality of the derived data and the general theoretical context in which such data are analysed. For highly dynamic environments the electro-mechanical components of the sensor must be capable to capture the full range and the natural frequency of the target instance. In parallel, the physical properties (e.g shape, weight, density) of the sensor are especially important in the case of inertial sensors that are deployed for monitoring movement (such accelerometers and gyroscopes) because the sensors inevitably become part of the process.

1.1 Problem statement - Motivation

This thesis focuses on sensors that measure aspects of grain movement in rivers. Advances in sediment transport theory have been delayed by the absence of suitable technology to test theoretical predictions (e.g. *Nikora et al.* [2002]; *Diplas et al.* [2008]; *Ganti et al.* [2010]) across the range of sediment sizes. The lack of continuous data with accurate positional and timing references precludes reliable mathematical and statistical descriptions of the system, therefore restricting the use of these predictions [*McEwan et al.*, 2001].

The scope of this work is to evaluate the deployment of commercially available Inertial MEMS for the sensing of sediment dynamics in natural fluvial settings. Starting from practical and technical considerations (such us the construction of robust and representative enclosures), it is shown how this particular technology can be used *in-situ*. Specific concerns about the coherency of the derived data leads to a search for a consistent mathematical framework that can contextualise the inertial measurements in the existing descriptions of fluvial sediment transport.

1.2 Thesis Structure

Much of the material in this thesis is included in journal papers that either published, accepted or in preparation. This observation is especially relevant to the Chapters 3 to 7. It is also necessary to mention that the papers are extensive, hence any necessary technical information is explained and summarised in the Appendices.

Chapter 2 is a concise literature review of the technologies used today for the monitoring of coarse bed-load transport in fluvial settings. This presentation is restricted to the technologically advanced techniques that are relevant to the problem under consideration. In the same chapter the problem of high-frequency monitoring of sediment grain dynamics *in-situ* is formally introduced.

Chapter 3 contains the formalisation of a procedure to construct purpose specific sensor enclosures, in the context of monitoring individual sediment grains. The technique is tested for a number of available inertial sensors and two sensor assemblies are presented, which are used in subsequent fluvial transport laboratory experiments. Material in this chapter is published in the *Journal of Sensor and Actuator Networks* [*Maniatis et al.* [2013], Appendix G] and has been updated here.

Chapter 4 presents the theoretical connection between the technology (Inertial Micro Sensors) and the mathematics of fluvial sediment transport. The transformation of the dynamics measured in the frame of an individual grain (Lagrangian) to the frame of water flow generated dynamics (Eulerian) and *vice versa* is analysed. This chapter also defines the title of this thesis. Material from this chapter is submitted to the *Journal of Hydraulic Engineering* as part of the published paper *Maniatis et al.* [2016a].

Chapter 5 presents the results from incipient motion fluvial experiments that took place in the flume laboratory of the Department of Geography of the University of British Columbia. It concerns the testing of a simplification of the model presented in Chapter 4. Part of this chapter is included in the same *Journal of Hydraulic Engineering* manuscript as Chapter 4 [*Maniatis et al.*, 2016a].

Chapter 6 contains the experimental verification of the complete Eulerian-Lagrangian model defined in Chapter 4. The focus is on the limitations of the technology and how it it can be used to extract coherent data, relevant to single particle dynamics. Parts of Chapter 4 and 6 are in preparation for submission as a pair of papers (theory and application) to the *Journal of Geophysical Research: Earth Surface*.

I am not the only author of the corresponding published, accepted or in preparation journal papers. Professor Trevor Hoey, is the first supervision of this project and he contributed significantly in the final form of all the manuscripts. Professor Joseph Sventek was the second supervisor of this PhD for the first year, and he contributed to the submission of *Maniatis et al.* [2013]. Dr Tim Drysdale, Dr. Rebecca Hodge are the co-supervisors of this project and revised the manuscripts of *Maniatis et al.* [2016a] and the in-preparation *Journal of Geophysical Research* submissions. Dr. Manousos Valyrakis, provided a critical insight from the point of Hydraulic Engineering to the same manuscripts. Finally Professor Marwan Hassan supervised the fluvial experiments of *Maniatis et al.* [2016a] and revised the manuscript.

For all the above manuscripts, I performed the literature review, conceived and formalised the techniques, conceived and performed the fluvial experiments, performed the analysis and developed the theoretical/mathematical derivations. Finally, I was the author of the initial versions and revised the material for inclusion in this thesis.

1.3 Definition of the terms Eulerian and Lagrangian

The two terms are extensively used in this work, and a formal definition is necessary before the specific introduction of Chapter 2.

According to the classical definition, the Lagrangian specification describes the way an observer will follow individual fluid parcels in space and time. A *pathline* defines the subsequent Lagrangian positions through time. Usually the centre of the mass of the parcel is used to parametrise time independent vector fields. If x_0 is the initial Lagrangian position then

$$U(x_0, t) \tag{1.1}$$

is the flow velocity giving the position of the x_0 parcel at time t. For sediment transport a grain defines a Lagrangian parcel (e.g. *Bialik* [2015]).

An Eulerian specification of a flow field, defines the observation of the fluid motion at a specify location past which the fluid passes through as a function of time. As a result, the flow velocity in

a Eulerian representation is given by

$$u(x,t) \tag{1.2}$$

which gives a function of velocity at the specific observers location. x_0 and x are the Lagrangian and the Eulerian coordinates of the flow. Specific discussion about how the two frames are used in sediment transport is included in Chapter 4.

Here a clarification is necessary, since the terms Eulerian and Lagrangian are not used consistently across all the disciplines. A difference in coordinate systems between the Eulerian an the Lagrangian domains is not a general requirement for their definition (x_0 and x can be expressed in the same coordinate system). For example, in the literature of fluid dynamics the two domains are rarely separated in terms of coordinates. However, in the literature of navigation, and especially Inertial Navigation (Chapter 4), the convention of two coordinate frames is used because the Lagrangian domain is rotating in relation to the (usually) static Eulerian domain. In this thesis the convention of two coordinate systems, a Lagrangian and an Eulerian, is used as rotation is included in mathematical definitions and a large part of the analysis for the acquired measurements is based on Inertial Navigation theory and equations.

CHAPTER 2

PREVIOUS RELEVANT WORK

There is no better indication for the complexity of bed-load transport processes than the lack of a bed-load transport equation that is reliable enough to support prediction, after 140 years of on-going research and practice (the first bed-load equation was introduced by Du Boys in 1893 [*McEwan et al.*, 2001]).

The importance of effective bed-load monitoring is magnified by the influence of sediment processes on the morphology of river [*Reid*, 2009], estuary and coastal landforms [*Bailard*, 1981], on bedrock river incision [*Chatanantavet*, 2007] and hence landscape evolution [*Whipple and Tucker*, 2002], and on in-stream ecosystems [*Allan*, 2004]. Mass transport of discrete particles is a key geomorphic transport process across environments (e.g. aeolian [*Anderson*, 1990]). This thesis is concerned with bedload transport in coarse-grained rivers, but the principles introduced are applicable to a range of other environments where mass transport of individual grains occurs.

The techniques used for monitoring sediment fluxes vary from tracers [*Hassan and Roy*, 2016] and sediment traps [*Bunte et al.*, 2004] to morphological estimations [*Hovius et al.*, 1997]. The basic conceptual and mathematical difference between the diffent methods, is the difference between the Eulerian and the Langrangian descriptions of the natural process [*McEwan et al.*, 2001; *Habersack*, 2003]. All the applications implement either the Eulerian or the Lagrangian concept but the results are in essence case specific [*Hassan and Roy*, 2016; *Hassan and Ergenzinger*, 2003; *Habersack et al.*, 2010]. The difficulty of balancing between the spatial and temporal variability of the natural system [*Syvitski et al.*, 2000] and the accuracy needed to describe the stability of the bed [*Carling*, 1987], leads to what is often a binary choice between either cross-sectional measurements (Eulerian concept, e.g. *Bunte et al.* [2003]) or measurements of individual particles/tracers (Lagrangian concept, e.g. *Hassan and Roy* [2016]).

In parallel, while cross-sectional sediment measurements are used to identify bulk bed-load

characteristics (e.g. discharge), tracers are used to identify the position of particles for long time periods and infer different modes of sediment transport. This Lagrangian framework was compatible with the mathematisation introduced by *Einstein H. A.* [1937] and the characterisation of transport modes in a Markovian series of entrainments, translations and depositions [*Hodge et al.*, 2011a]. Cross-sectional measurements have mostly been associated with Shield's model [*Shields*, 1936] and the definition of a hydrodynamically determined average bed-shear stress.

Several aspects of the differences between Eulerian and Lagrangian models as well as the fundamentals of H.A Einstein's Lagrangian framework are discussed in detail in Chapters 4, 5 and 6. This chapter addresses the advanced sensing techniques that are used in order to a) identify individual sediment tracer positions in a fluvial setting which is a purely Lagrangian problem; and, b) approximate the range of forces that occurs during sediment transport, which takes place using both Eulerian and Lagrangian approaches.

2.0.1 Focus of this Chapter

First uses of tracers were painted or naturally distinctive stones [*Wilcock*, 1997]; although low recovery rates, these studies provided useful insights into entrainment and dispersion of sediment grains. In the recent *Tools of Fluvial Geomorphology* [*Hassan and Roy*, 2016] summarise in detail the techniques that are used for coarse particle tracking in fluvial environments. In this chapter, the emphasis is on those contemporary approaches and methods that assist in the development and understanding of sensors and which can enhance the design criteria. Consequently, the term "advanced techniques" refers to tracing or measuring techniques that implement some type of electromechanical equipment.

In addition, I summarise the results from impact-force measurements from field applications and add the latest advances in the development of smart pebbles (with reference to fluvial geomorphology), which have only been validated under laboratory conditions. The smart pebbles are the only laboratory related equipment reviewed, as my interest is the development of a sensing system that can be used in the field. Advanced computer vision techniques [*Papanicolaou et al.*, 1999; *Niño and García*, 1998; *Furbish et al.*, 2012a; *Heyman and Ancey*, 2014] are not relevant to field deployments at the moment.

Finally, the review does not include the applications that refer to the sensing of bulk bed-load quantities. Today many researchers are working on the use of evaluating geophones [*Rickenmann et al.*, 2012; *Tsakiris et al.*, 2014] or seismometers [*Krein et al.*, 2016] to estimate bed-load discharges and other characteristics. Again the review is restricted to the applications that provide direct information regarding the dynamics of sediment transport either indirectly in the from of individual grain positions or explicitly in the form of forces (accelerations).

2.1 Passive and Active Lagrangian Position Tracking

Specially instrumented natural and/or artificial tracers have been applied to several fluvial environments (mainly estuaries and rivers), in an effort to measure characteristics of the movement of individual bed particles. Besides the many application-specific differences (usually subjected to the scale of the monitoring area) the technical characteristic that divides the literature is the use of either active or passive tracers.

The main difference between active [*McNamara et al.*, 2008] and passive [*Nichols*, 2004a] tracers is the demand for on board power supply. A passive tracer will disturb an electro-magnetic field because of it is natural characteristics. This field is generated by a detector which is either fixed (so the tracer passes through or above it) or hand-held and works in a very similar way to a metal detector. Two different types of passive tags have been used: magnetic and Passive Integrated Transponders (PIT) which is a radio-tracking technique.

In contrast, active transponders permit the continuous monitoring of the position of a moving particles. An active transponder emits signals constantly that declare its position and in fluvial environments only Radio-Tracking techniques have been used (e.g. *Ergenzinger et al.* [1991]; *Schmidt and Ergenzinger* [1992]; *Busskamp and Hasholt* [1996]; *Liedermann et al.* [2010, 2013]).

2.1.0.1 Passive Applications

The sampling techniques used in all the passive applications are relatively similar. The preparation of tracers, involves the installation of magnetic or PIT tag (transducer) into an artificial or natural pebble [1]. The second stage is the emplacement of the pebble into the river with an accurate determination of the initial position, and the third stage, after a distinct event such as a flood or a tide or a certain time period, is the localisation and recovery of the tagged particles using detection equipment (static or mobile detectors).

Magnetic Tracking: Naturally or artificially magnetised tracers have been used to measure bed-load transport. The first pioneering works where the ones of *Froehlich* [1982] and *Ergenzinger and Conrady* [1982]. Magnetic tracking techniques (automatic or not) have been used for the past three decades (e.g. *Hassan et al.* [1991, 1992]; *Schmidt and Ergenzinger* [1992]; *Warburton and Demir* [2000] and more). An extensive reference list and analysis on the technique is provided in *Hassan and Roy* [2016]. The measurements from the magnetic systems include travel distances, virtual velocities, depth or burial, 3D dispersion, flow competence, sources and destinations and the volume of the moving sediments. In terms of disadvantages, the magnetic systems are susceptible to background noise. The latter reduces recovery rates in ways which may not be random and can bias results. A significant observation is that the deployment must be long so that the tracer population gets time to mimic the bed grains population [*Ferguson et al.*, 2002].

[1] with the exception of natural magnetic pebbles [*Ergenzinger and Conrady*, 1982]

A recent example of a magnetic tracking system is the Bed-load Magnetic Detector (BMD) system [*Tunnicliffe et al.*, 2000]. The system consists of an array of sensors housed in an aluminium beam. The main improvement is the confinement the magnetic field of the system so that, technically, is not influenced by magnetic distortions outside the monitoring area. It is also empirically parametrised by *Hassan et al.* [2009], connecting sensor signal variables with the characteristics of passing objects. However, *Hassan et al.* [2009] observed large differences in the signal response to the same particle passing over the edge or the centre of the sensor array. This is potentially a major limitation for the identification of individual tracers.

Radio Frequency Identification and PIT tagging: The first application of the PIT technique in a fluvial environment was reported by *Nichols* [2004a]. Since then a number of publications have reported results for river catchments [*Schneider et al.*, 2010; *Lamarre et al.*, 2005; *Lamarre and Roy*, 2008; *Liébault et al.*, 2012; *Phillips et al.*, 2013; *Bradley and Tucker*, 2012] and from the application of the same technique into estuarine environments [*Allan et al.*, 2006; *Allan and Hart*, 2007; *Benelli et al.*, 2012]. Again *Hassan and Roy* [2016] analyse the technique in detail and provide an extensive reference list.

The information provided by such systems is the same as that from magnetic systems (travel distances, virtual velocities, depth or burial etc.). The disadvantages of PIT tagging are very similar to the disadvantages of the magnetic tracking, with the addition of the labour inventiveness of the RFID technique and, perhaps more importantly, the fact that it is currently limited to sizes > 40 mm.

On the plus side, the RFID equipment is standardised. Except for *Benelli et al.* [2012] who used a custom system and *Schneider et al.* [2010] who used a different detection antenna (but the same reader), the system used for the majority of studies is the *TEXAS Instruments Series 2000 Low Frequency Micro RFID* [*T.I*, 2001], which uses a Low Frequency (134.2 kHz) wireless automatic identification system. This system consists of a reader-control unit, an antenna and transponder(s) and it comes with full support in terms of deployment details. The Oregon RFID kit (the most recent instrumentation used in *Phillips et al.* [2013]) operates in the same end-user friendly philosophy. In parallel, there is a tendency to reduce the size of the PITs. In the early studies, 32 mm transponders were used, but most contemporary studies [*Schneider et al.*, 2010; *Liébault et al.*, 2012; *Bradley and Tucker*, 2012] report results from 23 mm PITs.

2.1.0.2 Active Applications

Active techniques are included in *Hassan and Roy* [2016], as well as most of the references mentioned in this subsection. However, I increase the level of detail (especially in the technical and the interpretation related information) since these techniques are the only ones designed to address the problem of high-frequency positioning of individual pebbles during flooding events. Understanding the technical limitations and the technical shifting to a purely Lagrangian context was critical for the subsequent developments in this thesis.

In 1989, two independent groups reported very similar systems that implemented the application of active radio tracers in fluvial environments. The first team worked on the River Lainbach, Germany [*Ergenzinger et al.*, 1989] and the second team was American [*Chacho et al.*, 1989].

The German system consisted of four basic components: the cobble-transmitters, the receiver, which was connected to detection antennas, and the data logger. The cobble-transmitters were natural cobbles, which were drilled to accommodate a transmitter, an antenna and a mercury switch (for adequate signal changes according to the rotation of the pebble, see Figure 14.4 in *Hassan and Roy* [2016]). The lifetime expectancy of the system was approximately 3 months.

Preliminary results [*Ergenzinger et al.*, 1989] reported the proof of the concept and maximum accumulative travel paths. Later publications [*Ergenzinger et al.*, 1991; *Schmidt and Ergenzinger*, 1992; *Busskamp and Hasholt*, 1996] discuss the results in the context of Einstein's [*Einstein H. A.*, 1937] stochastic analysis and evaluate the potential of the method for the quantification of individual step lengths and the duration of rest periods. Distributions fitted to the step length are heavy tailed (exponential and gamma), which confirms Einstein's theory, but the step lengths are significantly larger than his assumption of 100 grain diameters [*McEwan et al.*, 2001]. Other important comments concern the initial placing of the tracers (since they are considered to be embedded in a natural position) after the first movement and the discretisation of Einstein's stochastic model, with the particles moving in a series of transport steps and non-moving intervals [*Schmidt and Ergenzinger*, 1992]. Both of these comments have been considered in later studies [*McEwan et al.*, 2001; *Habersack*, 2003; *Hassan and Ergenzinger*, 2003; *Ergenzinger and De Jong*, 2003; *Nikora et al.*, 2002].

Ergenzinger and De Jong [2003] comment that the results are positive for shallow rivers of low salinity (making the system unsuitable for estuarine environments). They further suggest that the signals can be located from vehicles and that there are several surveying techniques (grouping many cobbles into defined similar frequencies, switching on and of the system according to the occurrence of events) that can lead to an accurate determination of the bed-load discharge.

The third group of applications of active radio-tracers initially employed the German system and conducted experiments into two alpine catchments in Austria [*Habersack*, 2001; *Habersack et al.*, 2001; *Habersack*, 1998]. They report low recovery rates and inadequate data acquisition for quantification of mean step lengths (also reported in *McEwan et al.* [2001]). The first report for these experiments was unpublished.

In 1998 and 1999, experiments were conducted in the Waimakariri River, New Zealand. The system used was a improvement of the German system [*McEwan et al.*, 2001; *Habersack et al.*, 2001]. Sixteen active traces were deployed and the system had a detection range of 100 m. After the event, the exact location of the tracers was performed with a handheld antenna. Both natural and artificial pebbles were instrumented with swinging quartz, which emitted a signal of 150 MHz at impulse intervals, between 450 and 600 ms. *Habersack* [2003] comments that this technique is expensive and thus complementary in a way to other tracing techniques, since the actual position of the particles (at a catchment scale) was very difficult to determine and the number of tracers was limited.

Lenzi [2004] reports on the deployment of 40 radio transmitting tracers similar to those described in *Schmidt and Ergenzinger* [1992] in the small stream of Rio Cordon. Very few details are reported on the deployment of the radio tracers as they were used complementary to marked tracers. The type of results are very similar to the reports from Wimakariri River in New Zealand. The study compares the effects of extreme and ordinary events on the mobilisation of different sediment classes.

The most recent application of the current version of the German system is reported for a large survey at the Austrian part of Danube [*Liedermann et al.*, 2010, 2013]. The monitoring approach was different, since the tracers were observed either weekly or after a flow event. Consequently, the information gathered concerns successive rest periods and positioning after the individual movement (which is very similar to the passive techniques). The technological innovation of this project is the development of active radio tracers, which could be detectable at over 200 m horizontal distances under mean flow conditions and over 50 m at bankfull discharge conditions. The longitudinal (or lateral) accuracy of the technique is between 10 and 15 m. These new transmitters were installed into artificial tracers (whose construction was based on natural prototypes) and the whole development of the tracers was done by LOTEK-wireless^{TM}. The overall system is capable of detecting the position of 40 artificial tracers, while only 3 to 7% of the tracers are not accurately detected, resulting into a 93% recovery rate.

The American system [*Chacho et al.* [1989]; Chacho et al.,*1994, 1996, cross-reference from McEwan et al.* [2001]; *Habersack et al.* [2010]] was very similar to the German system in principle, as well as in technical capabilities [*McEwan et al.*, 2001]. The basic difference was the size of the transmitter (18 x 72 mm), which had an operational lifetime of 10 months. Moreover, this system implemented a motion sensor, which indicated the motion period (and the rest period) for each particle [*Hassan and Ergenzinger*, 2003]. The operational radio-frequency was the same (150 MHz). Experiments using this system were conducted, between 1988 and 1992, into three sites in Alaska (Toklat River, Phelan Creek and Lignite Creek) and the acquired data concerned the proof of the active-radio tracing concept and the quantification of step lengths of individual cobbles. A tendency, towards step-lengths, shorter than 100 grain diameters was observed [*McEwan et al.*, 2001].

Active tracers instrumented with motion sensors: One important site where active transducers have been deployed for particle tracking, is the Reynolds Creek Experimental Watershed in Ohio. *McNamara and Borden* [2004] describe the deployment of 5 pebble radio-transmitters in a system very similar to the German in terms of the radio telemetry. The innovation was the deployment of on-board motion sensors that triggered the system only for periods of motion. They managed to measure accumulative travel distances of individual particles by counting the number of motion and rest periods during separate stream flow events. By using discharge data for the events, it was possible to identify the times and the flow rates at initial and final motion, which leads to counting the number of motion and rest periods in between those times. Importantly, no data were extracted for the magnitude of the acceleration these pebbles experience, hence the estimation of forces at incipient motion is approximated approximated using Shields equation. The most useful result from the analysis is the differences in mobility between increasing and decreasing discharges. In a second deployment, *McNamara et al.* [2008] reported a low recovery rate (26%) for the smart tracers due to technical problems and the extreme mobilisation of sediments during the monitoring period.

The latest active transmission of radio signals from tracers took place in Trinity River leading to the publication of *May and Pryor* [2014]. The radio-transmitters were cylinders of 81 x 23 mm, weighting approximately 0.040 kg and had a battery life of approximately 2 years. Impressively, the tracking distance reached the 800 m before the radio pulse begun to deteriorate. The pulse rate of the 'active' signal (the signal during transport) was 667 ms.

Not transmitting active tracers: The active sensors deployed by *Olinde and Johnson* [2015] do not fall into any of the above categories. The closest characterisation is active only because of the on-board power supply. Seventy-three coarse concrete particles were instrumented with RFID (hence passive in terms of telemetry) discs and motion sensors (*HOBO Pendant G data loggers*) for the derivation of acceleration data ($\pm$3 g measurement range, 10 min interval). The results show a positive correlation between motion statistics (probabilities of transport, individual step lengths, cumulative displacement lengths) and the increase of flow discharge. Interestingly, the report does not include any acceleration values indicating that the sensing of sediment motion was restricted to the identification of motion and rest periods, which is similar to *McNamara and Borden* [2004] and *May and Pryor* [2014].

Finally, the last application of active sensors that is difficult to classify is the intelligent pebble of *Sear et al.* [2002]. No motion sensor is implemented and the mobile tracers are loggers of magnetic signals. The signals are produced by an assembly of buried cable antennas which produce a known magnetic field. Although this not mentioned in the reports for this system, the technique is defined as magnetic-inductive tracking and it has been recently used for the tracking of underground wild animals with success [*Markham et al.*, 2012].

The basic advantages of this technique are the low on-board power demand (since the pebble uses its battery for information storage only) and satisfactory positional accuracy. The main

disadvantages reported were that the prototypes were restricted into monitoring relatively coarse particles (72 mm b-axis) and the implmentation cost could make the technology infeasible. In terms of the evaluation of the extracted data, comprehensive measurements are possible only when the pebble is still. Hence, the position is practically monitored at every rest period, a problem that is common amongst the passive techniques [*Lamarre and Roy*, 2008; *Bradley and Tucker*, 2012]. The acquired data were used to calibrate the existing tidal models for the beach with good spatial but poor temporal results. Notably none of these restrictions is reported for the more recent magneto-inductive system presented in *Markham et al.* [2012].

2.2 Measurements of Lagrangian Inertial Kinematics

The common ground between all the above applications is the focus on the position of the individual particles. For a fully Lagrangian description it is necessary to determine the time distribution and the intensity of the causal factors of individual grain movements. As a result, a tracer that can perform this kind of measurements during the transport process is needed.

With contemporary technology these dynamic measurements can be performed from the inertial frame of the particles, and this is the contemporary definition of the smart pebble: a mobile, self-powered, multi-sensor able to measure the surrounding instances. In the context of sediment transport the focus is on the surrounding hydrodynamic forces and the contemporary relevant sensors are the accelerometers (sensors that measure the imposed forces) and (more recently) the gyroscopes (sensors that measure the angular velocities of the fixed inertial frame). These definitions are adequate for the overview in this chapter and are discussed in the subsequent analysis of Chapters 4, 5 and 6.

2.2.1 Preliminary attempts

There are two reported applications that attempted to measure the hydrodynamic forces applied on individual particles.

The first is the *COSSY* (Cobble Satellite System) system [*Ergenzinger and Jupner*, 1992]. This system is a variation of the *PETSY* system developed by the same team [*Ergenzinger et al.*, 1989], which was expanded by the implementation of five pressure sensors and an accelerometer. The pressure sensors were differential and they measured the pressure difference between the top and the bottom of the cobble from 4 points on the flow cross-section. The fifth sensor measured absolute pressure and the accelerometer was used for better determination of the initiation of motion. In principle, this approach is static, since the experiment was designed to measure the forces acting on the grain before entrainment.

The second attempt to detect and evaluate the impact and friction forces acting on single particles was the project of *SPY-COBBLE* [*Šolc et al.*, 2012]. The device was capable of measuring global acceleration (due to movement), but it can also measure the impact of friction indirectly

(via acoustic emission). In addition, it operates as a data-logger, since there is no real-time data acquisition (during the measurement the device is stand-alone). The stored digital values are extracted when the device is removed from the system and plugged into a PC, via a built-in connector.

The biggest restriction of this device is storage capacity. The data is by default sampled by a frequency of 2665 samples per second, which permits measurement for 130 s until the memory is full. In terms of energy consumption, the device is acceptably efficient, since all the parts have standard power needs (120 mA in total during operation), which is well below the capacity provided by standard 9 V batteries. Without the restriction of memory storage, the device could measure for more than 4 hours consequently.

2.2.2 State of the art

Smart Sediment Particle *Akeila et al.* [2010]: This device was designed as a autonomous Inertial Navigation System (INS) with the ambition to track its own 3-dimensional trajectory when placed in a riverbed. It deploys two dual axis accelerometers (ADXL202) and three yaw rate gyroscopes (ADXRS150) to measure 3D acceleration and rotation rate about each axis. The sensors were interfaced initially around a Microchip PIC microprocessor for reading the measurements. This was later replaced by a *Silicon Labs C8051F931* chip mainly to reduce energy consumption. The data are stored into an external flash memory and can be retrieved after logging.

This work demonstrated the concept of deploying low cost commercial off-the-shelf sensors for an autonomous tracking device. The critical achievements of this project are the development of an inductive power transfer wireless recharge system for this device and the proposition of a mathematical framework for post event analysis of the data in order to resolve the trajectory of the pebble.

Further testing has helped to calibrate corresponding error models in order to control error propagation during the tracking of the trajectory. However, the validation of calculated trajectories showed significant inaccuracies, especially at the moments close to entrainment [*Akeila et al.*, 2010]. This result outlines the limits of inertial navigation (the technique to infer positions from acceleration values) when available off-the-shelf components are used.

Also the error compensation is restricted by the measurement range of the sensor (± 2 g) since it is assumed that "the peak amplitude matches the full-scale range of the ADC component" [*Akeila et al., 2010, pp. 5*]. This assumption enhances the overall performance of the system if the full range of the analog signal (the range of imposed accelerations in this cases) is captured. In a real river system the acceleration range scales in the magnitude of ± 100 g (see Section 2.3). Finally, although the team performed a flume evaluation of the sensor, the application is not contextualised in sediment transport theory. Although accurate positional tracking is not possible with this system, the team reported plans to this prototype with the concept of a *Gyro-Free INS*

[*Akeila et al.*, 2008]. The team has also turned its interest to hydraulic environments where there is no demand for high accuracy [*Kularatna et al.*, 2010].

The eco-pebble, *Frank* [2014]; *Frank et al.* [2015]: This application is focused on coastal environments, but the approach (measuring acceleration towards the measurement of actual forces applied on individual grains) is a general Lagrangian approach. The team has used a programmable platform called Eco [*Park and Chou*, 2006], which has been developed since 2006. The first smart pebble they tested was equipped with a sensor weighing 0.6 g and measuring 13 x 11 x 2 mm (including the microcontroller), which was instrumented with a tri-axial accelerometer, a temperature sensor, an infrared sensor and an antenna. Initially, they tested several enclosures (to simulate the physical properties of quartz) and performed a number of sensitivity (for acceleration measurements) and signal transmission efficiency (through air) tests on shaking tables. The results showed that these devices can accurately resolve accelerations in an optimum range between ±0.06 g (noise threshold) and ±3 g (max device measuring range). These results where produced by post-correlating, the observed displacement with the measurements derived. Moreover, dry wireless transmission was acceptable for all the enclosures. In *Frank et al.* [2015] the sensor is used a a tilt/orientation measurement device, correlated with flow generated oscillations and cross-compared with PIV measurements with good statistical agreement.

The Smartstone system, *Gronz et al.* [2016]: This is the newest smart pebble. The team evaluate the BMX055 Bosh probe for use in the context of sediment movement, with an emphasis to the wireless data transmission (which reaches the 1.5 m under water). They also performed a series of flume experiments for initial motion The acceleration range of this sensor is ±4 g. The pebble is also equipped with a micro-compass and a gyroscope which are fused with the accelerometer towards the calculation of absolute orientation. The orientation from the sensor measurement was compared with orientation derived from high-speed cameras and the reported absolute mean deviation reaches the order of 63%.

2.3 Impact from static piezoelectric accelerometers

From the review above, it is clear that:

- field particle sensing data to date has measured grain positions, and there are not data on forces (accelerations),
- lab experiments have shown that it is feasible to measure forces.

Crucially, there is no available data for direct Lagrangian impact estimation (data that represent the actual acceleration experienced by the individual particles) from real systems. For an estimation of the magnitude of impact, it is only possible to use data that are derived by a completely different approach and comprise an indirect impact estimation. Here the word impact is used exactly with the meaning of Newtonian force, hence only the applications that use accelerometers are considered. This clarification is important since the term *impact* has also been used for conditioned acoustic signals (geophones or hydrophones, e.g. *Barrière et al.* [2015]).

Instead of monitoring individual particles, these applications concern the deployment of logging impact sensors, fixed flush with the channel bed, which measure the impact of moving sediment clasts (an Eulerian approach). Practically, in the field, the impact sensors record either the number of impacts or the maximum acceleration produced by impacting bed load particles during a predetermined sampling interval.

There are four reports from the application of this technique, the first three quantify the impact of moving sediment using the number of impacting particles [*Rickenmann and McArdell*, 2007; *Richardson et al.*, 2003; *Reid et al.*, 2007] and only the fourth [*Vatne et al.*, 2008] reports results for acceleration.

Richardson et al. [2003] report the development of a new instrument that can (potentially) be used for the detection of the acceleration of a steel plate fixed to a rock riverbed, when it is struck by a clast. The acceleration sensor was placed within the data logger and used the same power supply, but since the device was not accurately calibrated, it was not possible to define the threshold of detection (hence the minimum size of the particles that do cause a detectable impact). Consequently, the magnitude of the recorded acceleration is not representative and the results concern the correlation of the number of impacts (counts) to the discharge (or the modelled/estimated shear stress). However, it is stated that particles as small as few mm can be detected. This sensor was limited to record up to 3 impacts (or counts) per second, which accounts for a maximum 1800 counts in a 10 minute interval. The main effect of this limitation is that the response of the sensor is not linear to a transport rate increase, since the likelihood of two impacts occurring less than one third of a second apart increases with transport rate.

The two later studies [*Rickenmann and McArdell*, 2007; *Reid et al.*, 2007] that applied this method and presented similar results (number of impacts) faced the same limitations. Both overcame the problem by calibrating the sensor and fixing (setting) the threshold of detection.

For example *Reid et al.* [2007], used the *Tinytag Plus GPR1201* which were set to detect only grains greater than 20 mm in diameter at 5 minute intervals.

The common important result from these three studies is is the identification of hysteresis of bedload transport with transport persisting at lower shear stresses than those required to initiate. This is a general observation from many researchers, but this methodology contributes greatly by allowing the development of robust semi-empirical relationships regardless of the different approaches estimating critical shear stress. Moreover, these equations can be extracted from the full range of flows that occur in a given catchment [*Reid et al.*, 2007].

Vatne et al. [2008] present data of raw acceleration which are more relevant to the framework of this project. They used a set of *Gemini Tinytag Data loggers* (TGP-061) of dimensions 34 x 68 x 73 mm and weighing 140 g, to measure the maximum acceleration caused by impacting particles in a given sampling interval (initially 1 minute and then 5 minutes).

The reading range of this sensor is $0 - 100$ g with an accuracy of 0.4 g. The smallest particle that could be detected was 10 mm (intermediate axis). Even with this indirect estimation though, their results suggest that transported particles can generate an impact (hence experience an acceleration) of an order of 100 g which is by far higher than the reading range of the motion sensors deployed in any of the Lagrangian applications. Moreover these impacts occur relatively frequently, especially when the discharge rises. However, it is also crucial to address the fact that these maximum accelerations could mask lower impacts, since the information of the number of impacts is missing from the work of *Vatne et al.* [2008].

To sum up, the static sensors have the potential to generate magnitude estimates of the accelerations and forces exerted by grains during transport, but the following limitations must be considered:

- The detection of the thresholds of sediment motion and cessation is very difficult. Calibration is needed to account for the specific characteristics of the sediments (types, size, shapes etc.) at the site.
- Relative intensities of transport through time are not known.
- The lack of information on the grain-size distribution of the bed load limits accuracy, especially for short observation periods with relatively small bed-load volume.
- Any large impact probably masks a number of smaller impacts.

2.4 Critical conclusions

The overview of the literature reveals several critical issues concerning the application of RFID tracer techniques in fluvial environments. Although the initial motivation for the application of these techniques was the evaluation of the assumptions of Einstein's stochastic conceptualisation, in practice reliable data for very few parameters related to the motion of individual particle movement have been acquired. These parameters are mostly relevant to the position between events (accumulative step lengths, time of rest periods etc.).

However, the Lagrangian description of bed-load transport demands information for all the three stages of movement (entrainment, translation and deposition). The stochastic nature of the related concepts creates the need for quantification of the impacts of the forces acting on the individual particles in order to determine the causal factors that drive the process.

Passive applications (PIT tags) were developed for use in a wide range of research and commercial fields, and consequently were available for rapid uptake and refinement for sediment transport studies. The availability of equipment and support made the application in the field almost as easy as the rest of the tracing techniques.

Active radio tracer applications have not undergone such extensive development. Historically the intended use was to determine characteristics of individual grain movements during a given event, which proved to be a much more difficult task than initially considered. The above lead to the first critical conclusion:

At at field scale we have relatively accurate determination of grain position (from either passive or active tracers) before and after an event, but no information on the within-event process. Even the deployment of accelerometers [May and Pryor, 2014; Olinde and Johnson, 2015] is targeted towards the detection of incipient motion without representative or easily interpreted magnitudes for acceleration.

At a laboratory scale, Mikos's $SPY-COBBLE$ system [*Šolc et al.*, 2012] showed how physical properties can be translated into data that represent the hydrodynamic forces acting on individual particles. Poor data storage and processing facilities of the system makes the it currently inapplicable in natural environments and incapable of providing positional information. The eco-pebble team had the potential to overcome these limitations but they are currently used as tilt sensors [*Frank*, 2014; *Frank et al.*, 2015]. The Smart-Particle localisation method proposed in *Akeila et al.* [2010] and the orientation method proposed in *Gronz et al.* [2016] are each subject to a number of theoretical and practical constraints, which are further discussed in Chapter 5.

In a more fundamental level, the restriction for all the inertial sensors developed in the context of sediment tracing is the reading range of their acceleration sensors. This is much smaller that the magnitude suggested by the works with static piezoelectric sensors questioning the feasibility of the developed prototypes under real circumstances. In summary, the second critical conclusion is the following:

At a laboratory scale we have measurements of the grain-acceleration, hence the of forces applied on individual grains, but it is not possible to track the individual trajectories accurately dew to theoretical and practical constrains. In parallel, the current acceleration measurement range of these sensors is incompatible with the scheme of forces developed during natural sediment transport (Figure 2.1).

Finally, there are two theoretical concerns that arise from the literature review.

The first is the need to cross-compare Eulerian with Lagrangian measurements. Although these terms are used extensively in the context of sediment transport, there is no clear framework to transpose the sediment dynamics from an Eulerian to a Lagrangian frame and *vice versa*. In this thesis I am going to show that the main reason for this inadequacy was the lack of sensors that can simplify the mathematical framework.

The second concerns the coherence of the data derived from individual pebbles when inertial information is recorded (MEMS accelerometers, gyroscopes etc.). It was noted above that the magnitude of forces is important, although the physical characteristics of the sensor assembly (e.g. shape, density) can alter the measurements significantly since they can alter the inertial frame. In other words, the sensor itself becomes part of the measurement and this is the problem that is discussed in the following chapter: the development of a sensor that can approximate the behaviour of a natural pebble.

Table 2.1: Summary of smart pebbles

	Šolc et al. [2012]	*Akeila et al.* [2010]	*Frank* [2014]	*Gronz et al.* [2016]
Name	SPY-Cobble	Smart-Pebble	Eco-pebble	SmartStone
Acceleration range	2000 g	±2 g	±3 g	±4 g
Other sensors	No	Gyroscope	Gyroscope	Gyroscope and Micro-compass
Type of experiments	Abrasion mill	Entrainment experiment	Entrainment experiment (oscillatory flows)	Entrainment experiment (episodic)
Type of results	Impact	Impact and Angular velocities	Orientation	Orientation

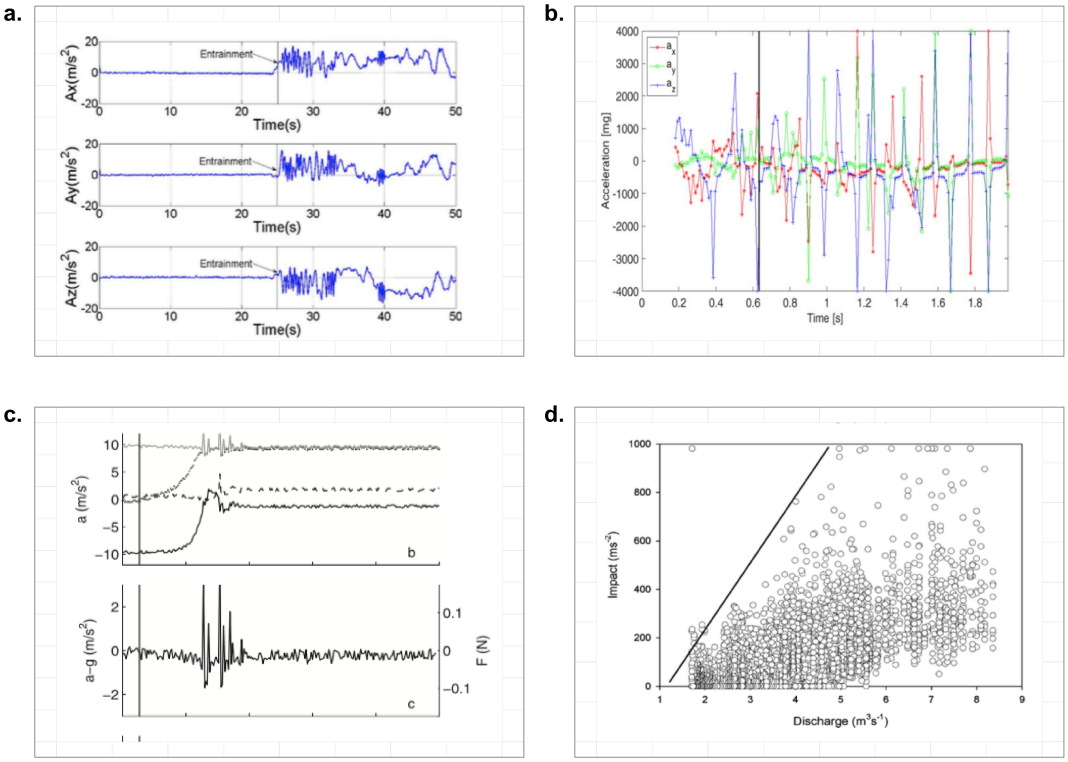

Figure 2.1: **Acceleration ranges.** In the laboratory deployments of smart pebbles (a. *Akeila et al.* [2010], b. *Gronz et al.* [2016] and c. *Frank* [2014]), the recorded accelerations range between 0 and ±4 g. This range is not compatible with the impact values recorded form the static piezoelectric sensors in *Vatne et al.* [2008] (d). In practice there is a deviation of an order of magnitude between the capabilities of the newest smart-pebbles and the mean acceleration that occurs during sediment transport (approximately 40 g) even when the restrictions described in Section 2.3 are taken into account.

CHAPTER 3

SENSOR DEVELOPMENT

Parts of this chapter are a re-print from the published paper: Maniatis, G., T. Hoey, and J. Sventek (2013), Sensor enclosures: example application and implications for data coherence, Journal of Sensor and Actuator Networks, 2(4), 761. 132, Appendix G

Hereafter, the term "smart pebble" refers to pebbles equipped with Mechanical-Electrical Micro Sensors (MEMS) that measure instantaneous dynamics (acceleration, angular velocity, orientation etc.). The enclosures of previous smart pebbles (Section 2.2 of the previous Chapter) were always highly idealised and a discussion regarding the physical characteristic of the sensor assemblies is absent from the relevant literature until the paper of *Gronz et al.* [2016].

Gronz et al. [2016] investigated the effects of the physical properties of the sensor enclosure by installing probe-sensor into three different natural stones of different sizes and materials and formally reported their natural properties. All the previous researchers were working with spherical artificial enclosures.

The error accumulation in *Gronz et al.* [2016] suggests that the inertial frame of the sensor (here, the stone that is installed into in this case) can exert greater control on the derived dynamical data than it is assumed. Also, the physical characteristics of the inertial frame are highly idealised in the theory that defines this type of sensors as explained in the Chapters 4 and 6.

The influence of particle shape on sediment entrainment and motion has been investigated previously [*Demir*, 2000; *Ergenzinger and Jupner*, 1992; *Krumbein*, 1941; *Carling et al.*, 1992; *Gomez*, 1994]. Theoretical analyses, however, have assumed idealised spherical grains (e.g *Wiberg and Smith* [1989]); this simplification makes the solution of the force-balance equations feasible, and the consequent results have been found to have widespread applicability (e.g. *Papanicolaou et al.* [2002]; *Diplas et al.* [2008]; *Hodge et al.* [2011b]).

As well as grain shape, the density of the sensor assembly must either replicate or be corrected to account for the density of natural material [*Cheetham*, 1979]. The deployment of sensors such as accelerometers is useful only if the sensor behaves as a rigid body of uniform density (something that can be assumed for individual natural grains). The overall density, and distribution of mass within the sensor,

must match those of natural materials without affecting the operation of the smart pebble.

The material properties of the case (such as the roughness of the surface, the hardness or the plasticity) also affect the quality of the data. Experience from previous field studies shows that the design criteria include several environmental factors, such as chemical weathering of the case or its trapping by trees or debris that affect greatly the long-term deployment of the sensor.

These factors cannot be addressed if the system optimization is based exclusively on electronics-computing related criteria. Given the natural variability of sediments, the above form a series of requirements for accurate design and/or control of the physical characteristics of the enclosures of the sensors that are going to operate in a natural fluvial environment. This requirement extends the common design criteria for underwater enclosures such as durability, waterproofness and robustness.

In this chapter I present the results from the development of two new mobile prototype sensors, designed for acquiring data representative of the instantaneous forces experienced by individual pebbles in a river or similar natural environment. The general framework can potentially address the key challenge of constructing an artificial enclosure that has similar physical properties with a natural stone. I discuss how the combination of available 3D modelling tools and fast prototyping technology (3D-printing and Computer Aided Manufacturing, CAM) speeds up the development process and has the potential to enhance the coherence of the sensed data. The design techniques also enable calculations of the distribution of mass in natural particles, such that the centre of mass of the particles can be located accurately, which is important when sensors are to be inserted into natural, or naturally shaped, particles.

3.0.1 A note on underwater sensor-housings

The majority of the existing underwater-sensing equipment has been developed for oceanographic applications often associated with sub-sea infrastructures [*Heidemann et al.*, 2012], where there is a general requirement for robustness and long-lasting water-proof performance under very high pressures and harsh conditions. Environmental applications deployed static sensing units until very recently [*Hart and Martinez*, 2006] and underwater sensor-mobility is investigated either in a context of robotics and vehicle navigation [*Fiorelli et al.*, 2006] or for depth adjustments towards the optimization of underwater acoustic networking techniques [*Detweiler et al.*, 2010].

In rivers the common sensing equipment used is also static (pressure sensors, chemical sensors etc) and the casing requirements are relevant to oceanographic applications [*Hanrahan et al.*, 2004]. However, there is no requirement durability under high pressures and both salt weathering and bio-fouling are less important. The common sensor housing practice is mounting of the sensors on a steady frame which is protected by a durable cover made of PVC or metal.

Although the enclosures have never been addressed as a separate research challenge for underwater sensing systems [*Akyildiz and Vuran*, 2010], research has been performed for increasing the life time of the case against specific erosion processes such as bio-fouling [*Delauney et al.*, 2010]. However, the contemporary casing design criteria do not restrict or specifically define properties such as the size, the shape or the density of the enclosures as long as durability is secured.

3.1 Prototyping Sensor enlocures: 3D-Printing

3.1.1 Case design procedure

Initially, it is critical to ensure that the elctromechanical components of the sensor will not be excessively stressed and will remain dry during operation. The second critical requirement is to keep the sensor immobile and permanently oriented in relation to the final frame of the case. Achieving this integrity would be difficult if the whole design matched a natural shape. Hence a two part design is implemented: a) an internal case for the sensor that has internal structure to fit the sensor, hold it in place and keep it operational; and, b) an outer case which fits rigidly around the first and defines the overall shape of the sensor.

Many new sensors come with an enclosure that does not leave the electronics exposed and it can also be water-tight (e.g. *Yost Labs* [2016]). The first part of the design (the internal case) becomes relevant when high-level of customisation is needed for the electronics, which is highly likely for a purpose specific application. Furthermore, the design criteria of the commercial sensors do not account for the necessary rigidness of the whole assembly. This is a very important requirement for high energy environments as demonstrated in Section 3.3.2.

3.1.2 Design and construction of internal case

This phase begins with a 3D representation (a 3D model) of the actual sensor platform around which the inner casing is to be constructed. Figure 3.1 shows the 3D models of two commercial platforms that were tested for this application: the AdvanticSys CM4000 mote platform [*AdvanticSys*, 2013a] with the C01000 sensor platform [*AdvanticSys*, 2013b] attached, and the SOWNET G-node mote platform with the G-Colta sensor board attached [*Sownet Technologies*, 2013]. The G-Colta sensor board is equipped with the ADXL-345 3-axial accelerometer with a maximum measurement range of ±16 g produced by Analog Devices [*Analogue Devices*, 2013].

The software used to produce the designs was Solid-Works^{TM} provided by Dassault Systèmes [*Système*, 2016]. Although the sensor platforms can have relatively complicated 3D structures, it is possible to input the geometrical metrics at a 1:1 scale without significant error. However, a 3D scanner can be used to input an initial point-cloud sketch which can then be manipulated through the software and corrected using manual measurements. The design can then be input into a 3D printer, producing a plastic 3D copy of the sensor's structure. Figure 3.1 shows the digital and the actual copies for the two sensor platforms.

Given the 3D model of the sensor platform as a base, it is possible to modify regular 3D shapes to incorporate the structure of the mote with great accuracy. The tools provided by the software enable production of regular shapes (like ellipses and cubes) so they have an inertial form shaped as the exact negative of the sensor platform's 3D structure while keeping the overall shape unaffected. This exact fit of a void within the regular shape to the sensor platform guarantees that the sensor platform will be immobile within the inner casing, and consistently oriented relative to the outer casing. This enables the platform to be calibrated appropriately. Examples of the designs and the constructed internal enclosures are shown in Figure 3.2 for the two sensor platforms.

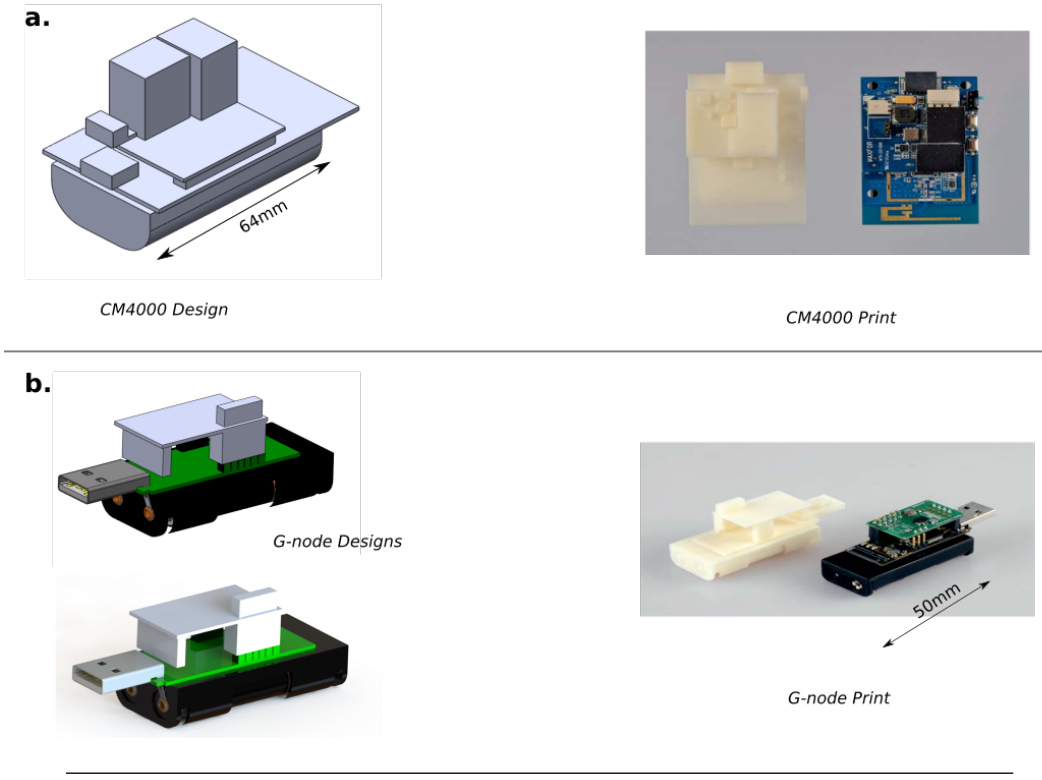

Figure 3.1: **3D models of tested sensors.** a. Digital design (left) and 3D-printing right of the CM4000 sensor mote with the compatible attached sensor board (right). The 3D design of the sensor is the base for the design of the case making the fit exact. b. Design and 3D-printing of the G-node with the compatible G-Colta sensor board.

3.1.3 Outer case

The initial stage in the process of development of this type of purpose-specific sensors is the testing of commercial, off-the-shelf platforms to assess the level of customization needed to fulfil the requirements of the application. The casing developed for this calibration/evaluation procedure must be idealized and regular in order to permit comparisons. As a result, the methodology was initially developed for idealized enclosures of regular shape and subsequently extended for the construction of cases with more realistic and natural shapes.

3.1.3.1 Cases of regular shape

The inner case is used as a base around which to construct an outer case that has a desirable shape. As previously, the software tools enable enclosure of the inner case with high precision.

The outer case must also have the internal support required to ensure overall durability (ensure that the plastic will not crack under a sudden stress) and can be used to enhance the water-proofing of the entire system. Durability is achieved by designing strong internal support structures and waterproofing by sculpturing structures like O-rings which can be filled with insulating materials (e.g silicon or rubber). The internal structure can be also used to control the density of the whole assembly. To achieve this, an

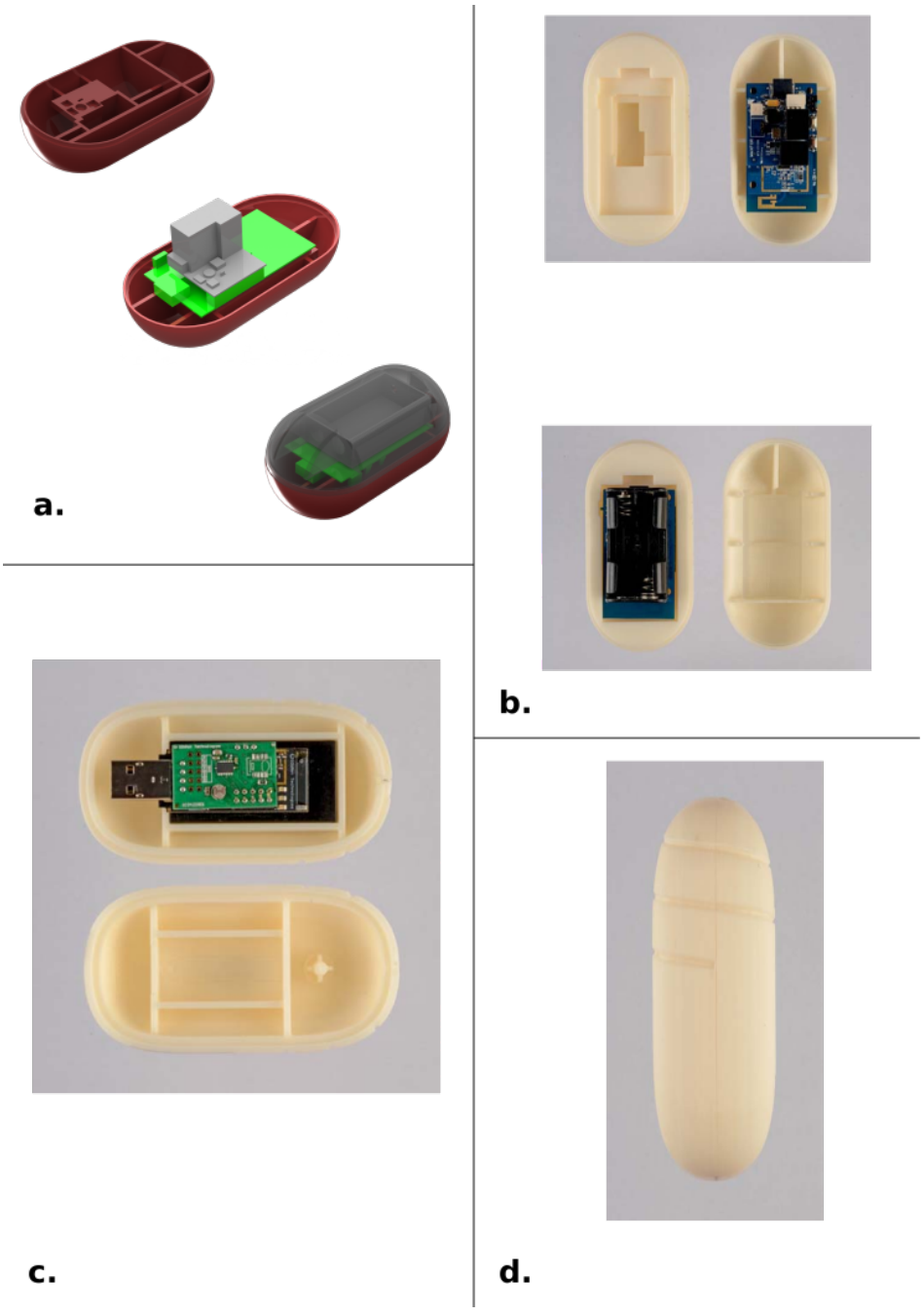

Figure 3.2: **The development of internal case:** a. The sensor is accommodated rigidly by the internal structure of the case matching the structure of the sensor, shown here for the CM4000 sensor-mote. b,c. The final 3D-printed case fits the sensor accurately keeping the overall assembly compact and minimizing the movement of the sensor (examples for CM4000 (b) and G-node (c)). d. Modifications can be made to accommodate special features, such as the modified antenna of the G-node which can be secured within the spiral sculptured into the external surface of the case constructed for the G-node (d)

outer case was constructed with support structures and void spaces that can be filled with materials of known density that enable control over total mass and density (Figure 3.3a).

A challenge is to enable easy access to the sensor when required without risking the case coming open during operation. This requirement is fulfilled by building locking structures into the joins that keep the case firm and rigid when it is closed but enable it to be opened by moving it in a specific way (Figure 3.3c).

3.1.3.2 Cases of non-regular shape

The ultimate goal is the construction of an outer case to simulate the movement of natural pebbles of variable shape (so that the sensor data is as representative as possible). Here the major concern is to copy effectively the shape of a natural pebble and use it as prototype for the overall case. For this purpose, the internal case is placed in a modified outer enclosure to generate a more natural shape. There is no single representative shape for any rock type or sedimentary environment [*Benn and Ballantyne*, 1993], but modern scanning technology allows replication of any shape.

Two very different natural stones are modelled to illustrate the procedure. The first is a compact blade-shaped stone with medium sphericity (Pebble A in Figure 3.4), and the second is a compact platy stone with low sphericity (Pebble B in Figure 3.4) [*Benn and Ballantyne*, 1993]. 3D models of these two cases where generated by a 3D-laser scanner (Roland^{TM} 600 DS [*Roland*, 2013]).

Simpler shapes such as Pebble A could be represented using simpler input methods such as those used for the prototypes of the sensors, but this approach is inadequate for capturing the complexity of the pebbles such as Pebble B. The design for the second case is exclusively based on the 3D-scan, as this is the most accurate and fastest procedure. A basic advantage of this design process is that it is possible to integrate almost directly the internal structure designed for the spherical case (which secures durability and control of the density), by following simple scaling and integration tools provided by the software.

The above method is very versatile in terms of scaling, since it is possible to construct cases that are based on stones much larger or much smaller than the actual sensor. Accurate scaling can enhance the representativeness of the derived data, because when a representative pebble shape is determined for a specific site it can be scaled to fit the sensor, no matter how diverse is the sample of stones upon which this decision was based [1]. For example in Figure 3.4, the 3D-representation of Pebble A printed at 1:1 scale for demonstration (Figure 3.4B), and the constructed case based on this pebble (Figure 3.4B and C) were designed using the same input. Figure 3.4 also shows a scaled representation for Pebble B .

[1]The procedure for deciding the representative shape of the grains for a specific site involves sampling and performing a number of statistical calculations that result in a number of characteristic shapes for the site

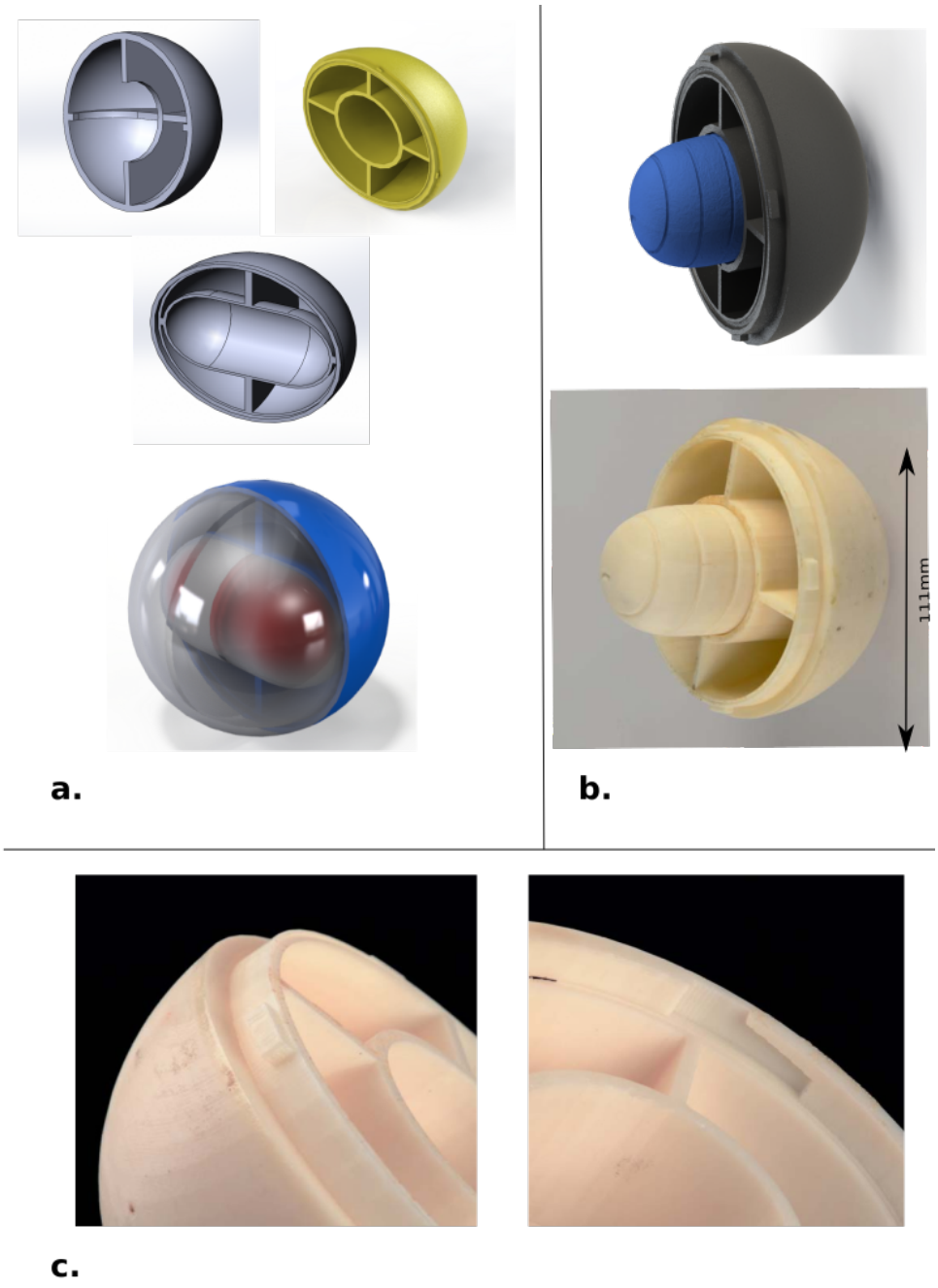

Figure 3.3: **Spherical outercase.** a. Designs for the internal structure of the outer case. The case can be designed to enhance durability (support structures), water-proof performance (O-rings) and density control (voids). b. Incorporation of the internal case for the G-node (design and photograph). c. Demonstration of the locking system to make the overall assembly rigid but not impossible to open.

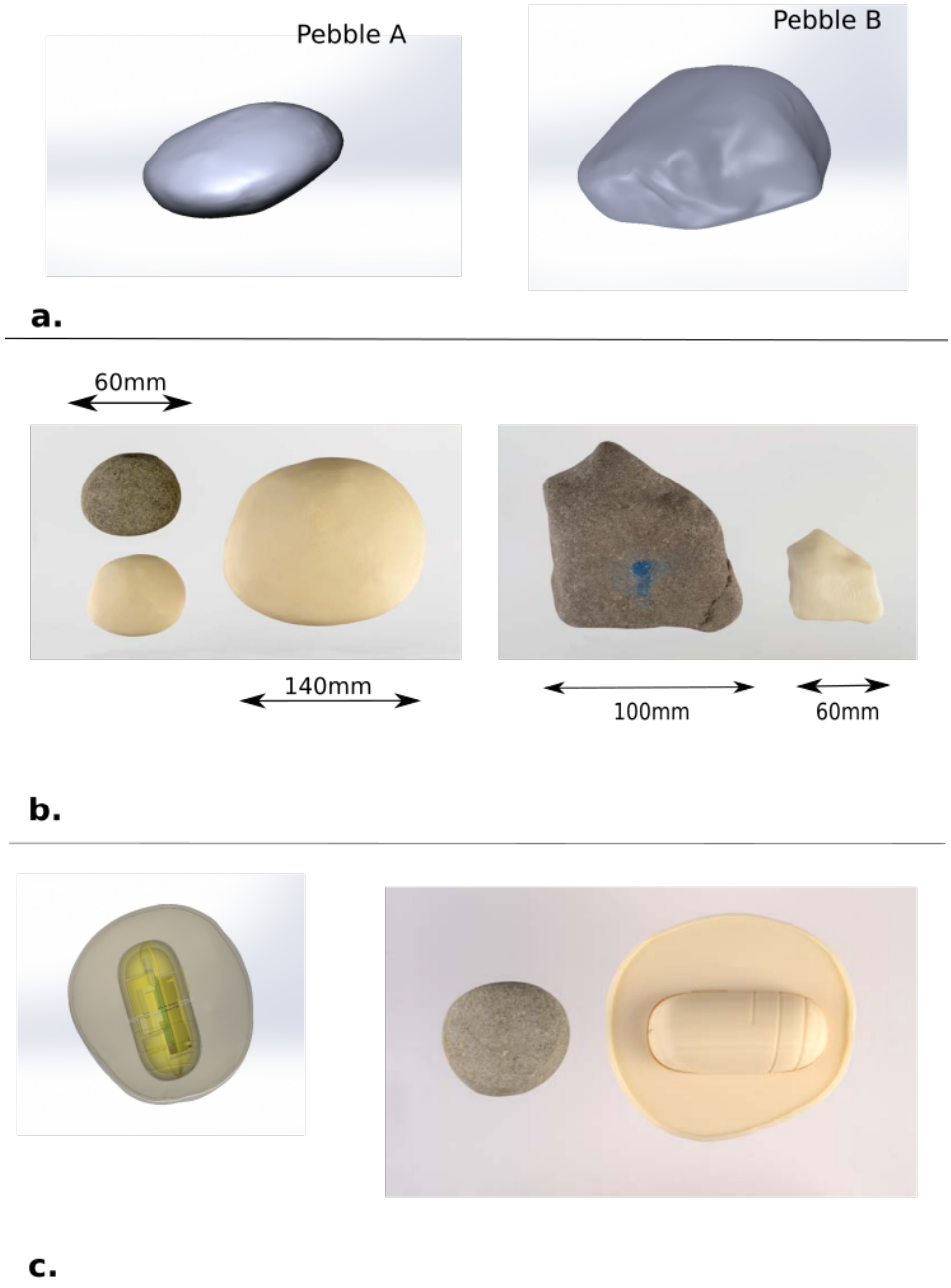

Figure 3.4: **Scaled copies of natural stones and representative example case.** a. 3D designs of natural stones after processing the data from the 3D scanner. Note differences in angularity and sphericity (Pebble A is blade-shaped with medium sphericity; Pebble B is a compact and platy with low sphericity). b. Scaled 3D printings of Pebble A (left) and Pebble B (right). c. Outer case based on Pebble A. The internal structure incorporates the internal case for the G-node. This outer case has a simple internal structure, but more complicated internal designs such used for the spherical cases can be incorporated (Figure 3.3).

3.1.4 Technical and Development considerations

For 3D-printing a HP Designjet^{TM} 3D printer [*Hp*, 2013] was used with the standard, compatible with the printer, ABS (density 900 kg/m^3 - 1530 kg/m^3: median 1070 kg/m^3) plastic. The quality of the printer is crucial for the time of development (3D-printing proved to be the most time consuming part of the whole procedure), as well as for the quality of the final product. This becomes more apparent during the latter stages of the development where the actual enclosures are produced. As an indication, the printing time for the replicates of the sensors (Figure 3.1) (a length of 64 mm for the CM4000 for example) is close to 4 hours, while the 3D-printing of the outer enclosures varies from 8 to 20 hours, depending upon the thickness, the internal supports and the complexity of the shapes being reproduced.

The time required to produce the 3D designs is highly variable and depends up on the experience of the modeller and familiarity with the software. A modeller relatively familiar with the toolbox of Digital Design and commonly used 3D-Modelling/CAD software, can be expected to create a first prototype for a given sensor in less than a week, especially if the outer case is based on a natural pebble or an enclosure that can be scanned.

It is important that fast prototyping and 3D-printing are possible for other materials besides the ABS plastic that is used for this application [*Lipson and Kurman*, 2013]. Moreover, the same design process can be followed to create casts for the creation of cases constructed with different materials (e.g carbon-fibre, or metals) that can address the requirements for several applications. The inputs and the initial designs in this case would be manipulated following exactly the same procedure. The only differences would be at the final stage where the designs used as input from the 3D printer must be modified to represent the exact negatives of the desired enclosure (a process very similar to the one followed in order to enclose accurately the sensors in the internal case).

To conclude for this technique, 3D-printing can be excellent as a demonstration tool and as a rapid prototyping technique if advanced materials are used. Also it is a developing technique which means that it will improve in terms of precision, robustness and speed in the coming years. In this project I used an ABS 3D-printed case for the laboratory experiments that are presented in Chapter 5. All the features incorporated in the design process were useful as they provided a very accurate definition of the physics of the sensor and full control over the physical characteristics such as density. The important consideration for using ABS enclosures under water is water-tightness. Because the ABS is porous the external case was varnished with yacht varnish, which is a good solution for a control environment such as the lab, but not for *in-situ* conditions.

3.2 From 3D-printing to CAM modelling

For an enclosure that can survive and operate in the natural environment, industrial rigidness and waterproof standards are necessary (higher than IP65 in Ingress Protection Rating for DIN 40050-9). This was achieved in cooperation with Kinneir Dufort^{TM}, a leading company in sensor construction based in Bristol, UK. They were provided with detailed 3D designs and they used their CAM machinery to construct two sensor enclosures. They also offered critical advice for securing the water-tightness of the enclosures (O-ring desing).

3.2.1 The latest prototype sensor

The sensor is the TSS-DL-HH-S sensor from Yost Labs^{TM} [*YEI*, 2014] equipped with a 3D gyroscope ($\pm 2000°/s$ sensitivity) and an 3D accelerometer with a maximum range of ± 400 g. As I discussed in Chapter 2, the accelerometer range is one of the main restricting factors for the use of IMU technology in natural environments and only recently have accelerometers of range greater than ± 200 g been commercially available. The nominal sampling frequency of the sensor is 50 Hz which permits consequent logging for approximately 3 hours. The factory maximum sampling frequency is 250 Hz.

One 3D-digital model of the sensor was used as a basis to construct one spherical and one pebble-shaped enclosure (Figure 3.5). The 3D-CAD models were given to the technicians of Kinneir Duffort who progressed to the CAM construction of two corresponding solid aluminium enclosures. A pressure O-ring was used to seal the enclosures and make them suitable for long term use in fluvial settings. The two sensors were deployed in the laboratory experiments described in Chapter 5.

3.3 Initial testing under random oscillations

3.3.1 1D-raw acceleration signal

The evaluation of the overall assembly (for both the spherical and the elliptical enclosures), has been performed using a shaking table which produces random one-directional vibration. The displacement of the table is controlled with a screw-based mechanism. Extensive analysis of the acceleration signals is performed in Chapters 4, 5 and 6. Here, the response of the TSS-DL-HH-S accelerometer to random oscillatory displacements with a maximum of 25 mm before any data-processing is demonstrated. The direction of the vibration is parallel to the horizontal level and the x-axis of the sensor assembly (which is parallel with the TSS-DL-HH-S x-axis from the construction phase, Figure 3.6). This particular setting is revisited in Chapter 6 where a calibration of the processing filter is performed for the calculation of displacements from the accelerometer signals.

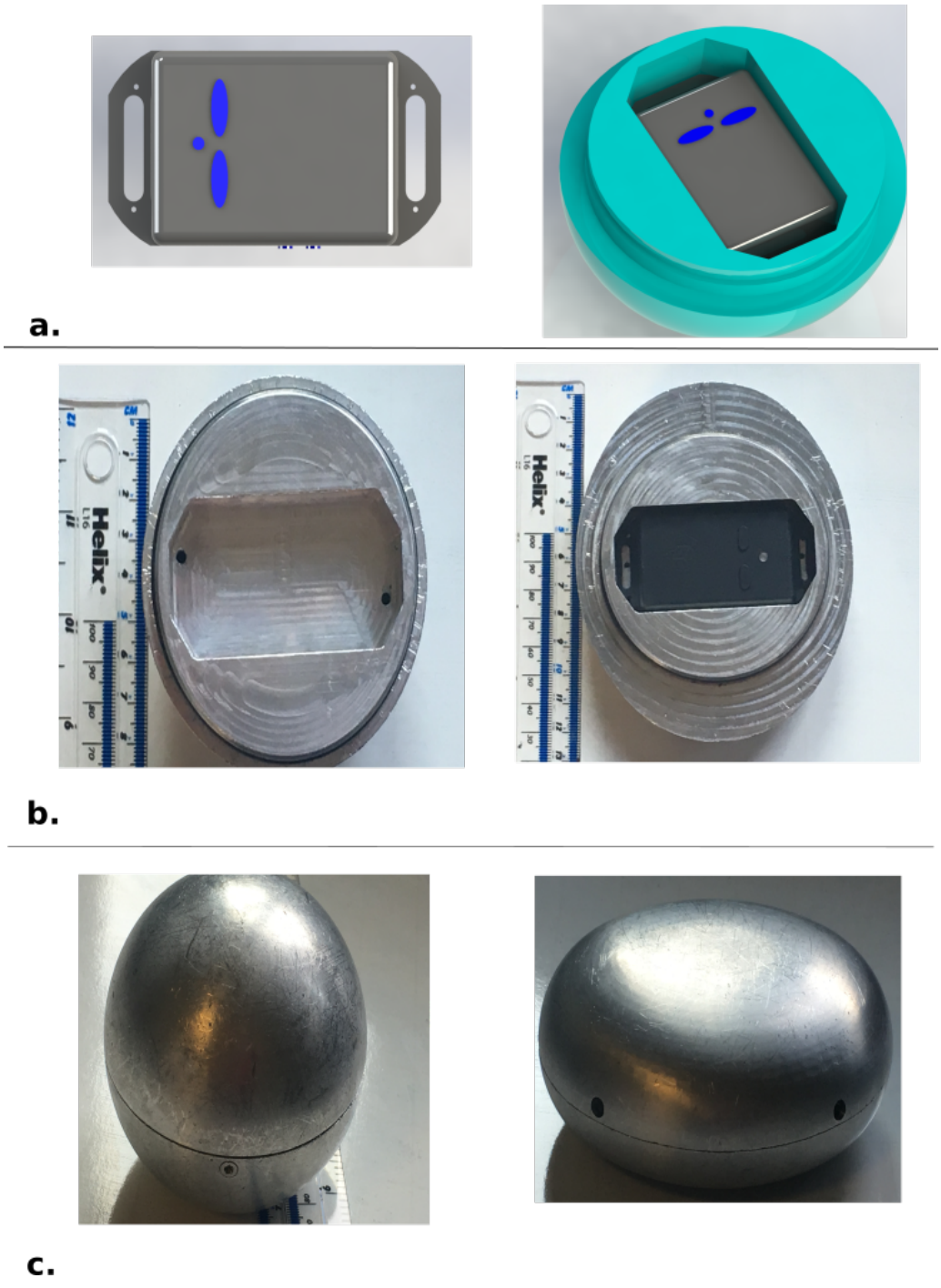

Figure 3.5: **The latest prototype sensor** a. Photorealistic 3D-renderings of the TSS-DL-HH-S sensor (left) and the sensor enclosed (right); b and c. The aluminium cases after the construction. Spherical enclosure is on the left and ellipsoidal one on the right.

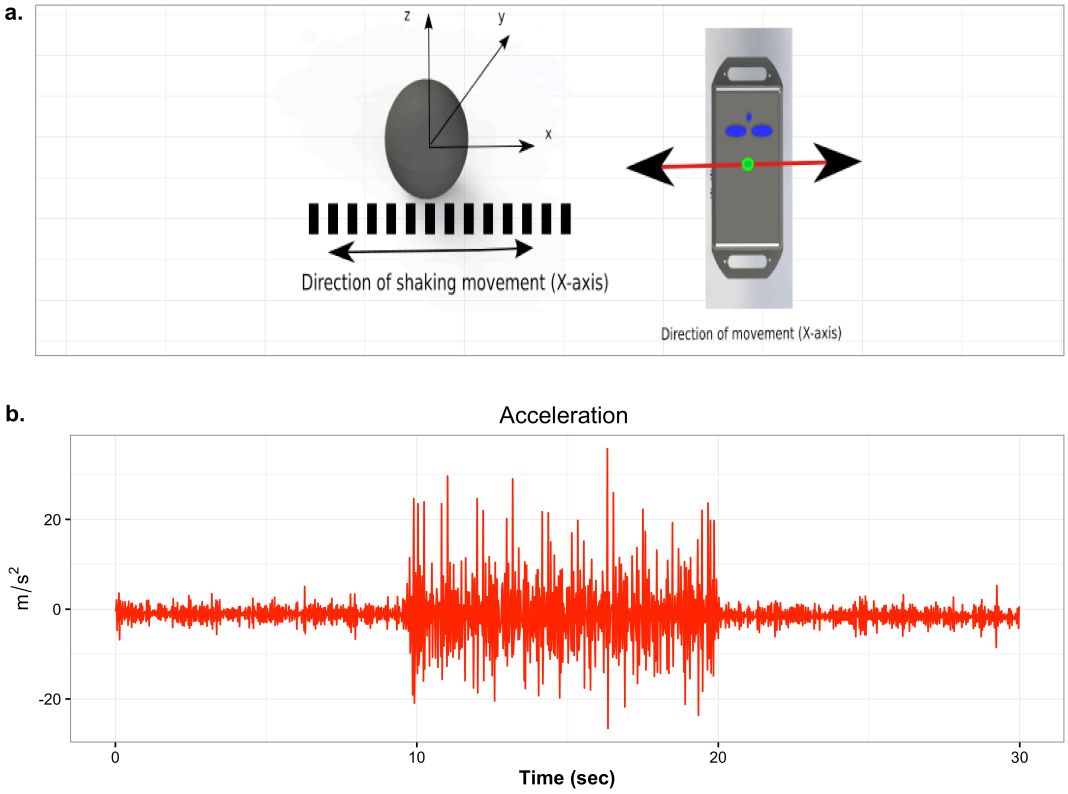

Figure 3.6: **Acceleration from random displacements** a. The orientation of the sensor in response to the shaking table. z is the direction of gravity b. 1D signal along the vibration direction (x). The experiment includes 10 seconds of no-movement, 10 seconds of random oscillation (max displacement 25 mm) and 10 seconds of no-movement. The sampling frequency is 50 Hz.

3.3.2 Data coherence: the importance of case robustness

The robustness of the electronics and the enclosure, attachments and waterproof sealing are critical elements of the design. The effects of failure in part of the assembly are described below. These results show the importance of the rigidity of the inertial frame of the assembly, thus the stable orientation of the sensor inside the enclosure.

For this test, one of the 3D printed spherical cases was deployed. The prototype used here is based on the G-node sensor and not on the latest hi-g TSS-DL-HH-S sensor. Again the experimental set-up consists of a shaking table moving periodically along one axis , however the maximum displacement is set at 70 mm for this demonstration. In addition, this this experiment consists of continuous sequence of periods of low- and high-intensity motion, with no zero-motion periods. Finally, it is important to emphsasize that the G-node is capable of wireless data transmission so the reported frequency (20 Hz) is that which enabled reception of the signals from a mote at a 1.5 m horizontal distance.

The sensor is firmly attached to monitor the acceleration along the dominant axis (parallel to the movement of the table) as shown in the schematic representation of Figure 3.6a (left). The accelerations recorded in this axis must be significantly greater than those due to the rest of the vibrations produced by the whole shaking movement.

During the first experiment (Figure 3.7a) the sensor was enclosed in the case that was designed

following the previously-described procedure. As a result, the sensor was steadily orientated throughout the experiment and was moving as little as possible in relation to the whole case. Figure 3.7a shows the recorded acceleration along the 3 sensor axes during the experiment. The raw signal indicates a dominant periodic impact on the x-axis capable of producing maximum acceleration of 42 m/s^2 which is significantly greater than the accelerations recorded on the other two axes.

In comparison, for the second experiment the sensor was enclosed in a case with the same outer shape but without the internal structure to stabilize the sensor, thus permitting the movement of the sensor within the casing. Figure 3.7b shows the results for the same accelerations, time period and sampling frequency as for Experiment 1. The results show how the movement of the sensor inside the case changes its orientation constantly so that it is difficult to observe the orientation and magnitude of the motion. As a result, the recorded accelerations are inconsistent during the second experiment since: a) the periodic motion of the shaking table is not recorded; and more importantly, b) the relative internal motion of the sensor generates an error as high as 150%, since the maximum acceleration recorded during the previous experiment 42 m/s^2 and during the second experiment the measurements for the x-axis have a maximum of 100 m/s^2.

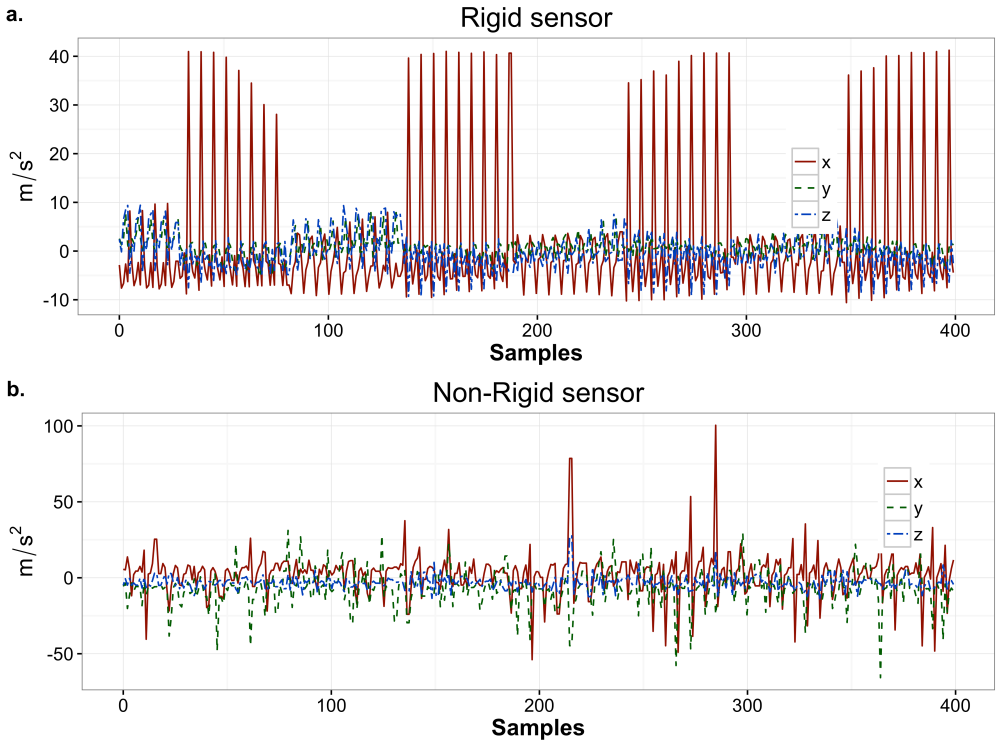

Figure 3.7: **Experimental comparison between steady and unsteady sensor orientations.** a. During Experiment 1 periodic x-axis accelerations reach a maximum of 40 m/s^2 which significantly exceeds maxima on the y- and z-axes (8.5 m/s^2 and 9.6 m/s^2, respectively), confirming the direction and magnitude of the dominant process (periodic movement along the x-axis). b. Experiment 2 was performed without the internal case, hence sensor orientation changed through time. The maximum acceleration for the x-axis is much larger than that produced by the shaking table ($a_{x_{max}}$ = 100 m/s^2). Moreover the periodic movement is not recorded and the comparison with the maxima on the other axes (31.8 m/s^2 and 28 m/s^2 on y and z axes, respectively) is not indicative of the dominant process.

	G-Colta prototype	TSS-DL-HH-S prototypes
Accelerometer range	±16 g	±400 g
Gyroscope	No	±2000°/s
Nominal Frequency	20 Hz (air) , 4 Hz (short range, underwater)	50 Hz (logging)
Radio	Zigbee 2.4G Hz	No
Enclosure material	3D Printed ABS	CAM aluminium
Enclosure shape	Spherical	Spherical and Pebbled

Table 3.1: Summary of the two prototype sensors deployed in laboratory experiments

3.3.3 Deployment Considerations

While it is unlikely that any sensing system will be constructed without taking into account the error produced by not securing the stability of the sensor inside the casing, the second experiment simulates a situation where a casing fails during operation, a prospect that can not be excluded in deployments where accelerations on the order of 100 g are possible.

An operator of this sensor is equally likely to receive both of the above signals during real deployment (Figure 3.7). Especially in a natural setting where the line-of-sight contact with the system is not guaranteed, the only information about the monitored process is that derived from the statistical analysis of these signals. Taking into account that the known magnitude range of instantaneous measured physical properties can be significantly higher that range of the derived measurements, both of these signals could appear to be valid and there is no way to identify the error in the second experiment during the statistical analysis. Consequently, it is important to prioritize stable orientation of the sensor in the case and minimization of internal movement during the design process of such a system.

3.4 Summary

Here a new method for rapid prototyping of sensor enclosures has been demonstrated. Focusing on inertial sensors for monitoring motion, the motivation for the development of this method lies in the potential inconsistency of the sensed data if two critical factors are not incorporated in the casing-design criteria: a) the effect of the physical characteristics of the complete sensor on the movement of the device hence on the representativeness of the derived data; and, b) the stability of the sensor along with the constant orientation in response to the overall frame of the casing.

The design process is versatile and can be adapted to any type of sensor platform and yields casings with pre-determined physical characteristics (such as shape and density). This enables rapid design of casings for specific applications that will enhance the coherence of the data since they will be compatible with the monitored environment and the data-acquisition process.

The results concern the application of this method during the development of a new sensor for monitoring river grain dynamics. Given the rapid improvements in the fast prototyping technologies described (which are both enhancing the quality and decreasing the price of the final case-product), it is possible to apply this method for large scale sensing applications. The same technique can be used as

input to high-standard manufacturing procedures if the 3D printing is not feasible.

Data from two calibration experiments (Figure 3.7, 3.6) suggest a maximum potential error in the order of 150% in terms of magnitude and complete inconsistency in terms of the directional information about the movement of the sensor when the failure of the case to stabilize the sensor platform is simulated. This result can be considered in a context of remote sensing when no other information is available and the statistical analysis gives no indication about the potential error.

For this thesis two types prototypes were used in two different series of lab experiments (Table 3.1).

- A 3D-printed case based on the G-node sensor was used for the experiments described in Chapter 5.
- Two CAM constructed aluminium cases enclosing the TSS-DL-HH-S sensor (one spherical and one elliptical) were used for the experiments reported in Chapter 6.

CHAPTER 4

EULERIAN-LAGRANGIAN MODEL FOR COARSE SEDIMENT TRANSPORT: THEORY

This chapter includes the theory described in the manuscript : Maniatis, G., T. Hoey, R. Hodge, M. Valyrakis and T. Dryrsdale (2016 in preparation for Journal of Geophysical Research: Earth Science): An Eulerian-Lagrangian definition of coarse sediment transport. I. Theory
Material from Sections 4.1.4 and 4.1.6 is included in the manuscript: Maniatis, G., T. Hoey, M. Hassan, J. Sventek, R. Hodge, T. Dyrsdale, and M. Valyrakis (accepted August 2016), Calculation of explicit probability of entrainment based on inertial acceleration measurements, Journal of Hydraulic Engineering

The study of the two-way relationship between the process of sediment transport and the corresponding morphology has a long history (e.g. *Gilbert and Murphy* [1914]). The proposed approaches and mathematical conceptualisations range from purely deterministic [*Gilbert and Murphy*, 1914; *Shields*, 1936] to purely probabilistic [*Einstein H. A.*, 1937].

The absence of an accepted unified approach lies on the fact that sediment transport theory yields poor predictions. Fluvial sediment transport is a multi-variate two-phase flow defined by the synergy of complex subprocesses relevant to: a) hydraulics [*Kline et al.*, 1967; *Nelson et al.*, 1995; *Papanicolaou et al.*, 2002]; b) sediment properties and arrangement [*Ashida and Michiue*, 1971; *Fenton and Abbott*, 1977; *Komar and Li*, 1988; *Kirchner et al.*, 1990; *Buffington et al.*, 1992; *Prancevic and Lamb*, 2015]; and, c) flow history across time scales [*Shvidchenko and Pender*, 2000; *Diplas et al.*, 2008; *Valyrakis et al.*, 2010].

This physical complexity is relevant to an ambiguous definition of the reference frame in which sediment transport is analysed. Given the definition in Chapter 1, an Eulerian frame of reference is fixed in space and all the occurring vectors are defined as properties of time at a given position. For sediment transport, bulk properties such as mean flow velocity, average sediment discharge or average shear stress follow the Eulerian definition.

In contrast to the Eulerian approach, a Lagrangian frame is not fixed in space and the vectors are properties of both space and time. Typically for sediment transport, entities such as particle velocities and step-lengths are in principle Lagrangian. In respect to the above definitions, the literature of fluvial

sediment transport is divided into two groups following the seminal works of *Shields* [1936] and *Einstein H. A.* [1937], respectively.

The vast majority of Eulerian descriptions include deterministic derivations for sediment motion. For example, the assumption of a unique exact threshold bed shear stress that causes the initiation of the initiation of motion of a specific size of sediment is fundamental in the works of *Miller et al.* [1977], *Yalin and Karahan* [1979], *Bridge and Bennett* [1992], *Wilcock* [1993], *Komar* [1996]; and more (see *Bridge* [2003] for further review). However, the extensive critique regarding the uniqueness of such a criterion [*Lavelle and Mofjeld*, 1987; *Buffington and Montgomery*, 1997] lead to a series of stochastic derivations in Eulerian models not only for incipient motions [*Ancey*, 2010; *Furbish et al.*, 2016] but for the whole transport process. Recently the stochasctic framework has been extended with the inclusion of concepts relevant to classical statistical mechanics [*Furbish et al.*, 2012b; *Roseberry et al.*, 2012; *Furbish et al.*, 2012c; *Fathel et al.*, 2015].

A second group of works implements and extends the conceptualisation introduced by HA. Einstein: the hydrodynamic forces are expressed in an Eulerian frame but the sediments are described in a Lagrangian context and a moving reference frame is attached on each moving sediment particle. Although this type of model can be accurately characterised as Eulerian-Lagrangian (according to the more general descriptions of multiphase transport processes [*Zheng et al.*, 2002]), in sediment transport literature the term that characterises the solid phase (sediments) is the predominant (Lagrangian). The extensive testing of Lagrangian models became possible in laboratory experiments only after monitoring technology advanced to a level that permitted the detailed examination of local near bed water turbulence around individual grains [*Papanicolaou et al.*, 1999; *Marion and Tregnaghi*, 2013].

Field experiments with individual sediment tracers are in principle Lagrangian [*Hassan and Ergenzinger*, 2003], however Lagrangian models rapidly developed after the advancement of monitoring equipment including magnetic (e.g. *Schmidt and Ergenzinger* [1992]; *Hassan et al.* [2009]) and RFID tracers (e.g. *Nichols* [2004b]; *Schneider et al.* [2010]; *Liébault et al.* [2012]; *Tsakiris et al.* [2015]). An important contribution to the Lagrangian models was the consistent introduction of Discrete Particle Modelling techniques in sediment transport theory [*McEwan et al.*, 2001, 2004].

Extensive reviews of the contemporary understanding on Einstein's model and specifically on the Lagrangian applications (with emphasis to saltating grains) are included in *Ferreira et al.* [2015] and *Bialik* [2015], respectively. Notably, in contrast to the first group of works, the mathematical derivations for Lagrangian models were always probabilistic, from the initial work of Einstein until today.

Two questions remain open: firstly, are both of these approaches equally effective in all the different types of sediment transport? and secondly, is it possible to compare results between Eulerian-Eulerian and Eulerian-Lagrangian models?

The main argument of this chapter is that, in order to answer both of these questions, it is necessary: a) to re-address the fundamental assumptions behind the reference frame characterisations in sediment transport; b) explain in physical terms the reason behind the above division of the literature; and, c) analyse in detail the capabilities of new technologies for the monitoring of individual sediment particles. My focus is inertial micro-sensors and specifically the physical interpretation of the derived data as outlined in Chapter 3.

To my knowledge a specific reference of the differences between Eulerian and Lagrangian frames in the context of fluvial systems is only found in *Doyle and Ensign* [2009], where sediment monitoring and fish monitoring techniques are presented to demonstrate similarities and differences between the two

frames of reference.

Looking for a physical explanation for the treatment of reference frames in sediment transport, it is important to emphasise that in the field of multi-phase transport systems the reference frames (Eulerian or Lagrangian) are treated separately and formal mutual transformations are used [*Zheng et al.*, 2002]. Incorporation of the research in multi-phase flow systems in sediment transport theory can be mainly found in the most advanced numerical simulations for bed-load transport (e.g. *Wu et al.* [2000]; *Zedler and Street* [2001]; *Arolla and Desjardins* [2015]) and very recently in highly idealised laboratory regimes [*Houssais et al.*, 2015; *Lajeunesse et al.*, 2015].

Finally, strap down IMU sensors have been demonstrated in the context of fluvial sediment transport, as a proof of technical concept, with limitations that restrict their extensive use as was discussed in Chapter 2.

4.1 Development of the Eulerian-Lagrangian model

4.1.1 Rationale: The Stokes number and its interpretation

To understand sediment transport, the fluid phase can be assumed to be continuous as the molecular diameter of water is approximately 0.29 nm. However, the sediment diameter may range from < 60 μm (cohesive sediments) to > 630 mm (large boulders) [*ISO*, 2002] making the assumption of spacial continuity for the solid phase non-general.

As a fluid-solid particles system, sediment transport is a two phase dispersed flow [*Balachandar and Eaton*, 2010]. The origins of this characterisation can be traced back to the original work of Sir G. Stokes [*Stokes*, 1851]. In this context the Stokes number (St, Equation 4.1) of the submerged particles is used to define the interaction between the two phases.

Stokes number is expressed with different derivations depending on the assumptions required for the different applications [*Brennen*, 2005; *Hagiwara*, 2010]. It is important though, to separate the derivation of Stokes number as a dampening parameter in a static fluid [*Joseph et al.*, 2001; *Scheingross et al.*, 2014; *Lamb et al.*, 2015] to the classical derivation for multiphase flows [*Balachandar and Eaton*, 2010] the most fundamental form of which is:

$$St = \frac{\tau_p}{\tau_f} \tag{4.1}$$

where τ_p is the relaxation time of a particle (or particle time scale) and τ_f is a characteristic time of the fluid-flow (or fluid time scale)

For Stokes number $<< 1$ the suspended particles will follow the stream lines of the fluid-flow closely and the obstruction-related component of the fluid turbulence will be minimal. For Stokes number $>> 1$ the obstruction-related turbulence will be high and the particle trajectories will practically become independent of the stream-lines of the fluid-flow [*Tropea et al.*, 2007].

For a particle suspended in a fluid, relaxation time is the time needed to return to a balanced position (equilibrium) after the flow has disturbed its balance. For very low Reynolds numbers (Stokes flow), the ideal Stokes particle time scale is:

$$\tau_{p,Stokes} = \frac{(2\rho_p + \rho_f)d_p^2}{36\mu} \tag{4.2}$$

where ρ_p $[ML^{-3}]$ is the particle density, d_p $[L]$ is the particle diameter and μ $[ML^{-1}T^{-1}]$ is the fluid dynamic viscosity. However, for the larger particle Reynolds numbers (Re_p) relaxation time must be corrected as the flow deviates from the idealised Stokes flow. An overview of the techniques for this correction can be found in [*Beetstra et al.*, 2007].

In fluvial sediment transport the classical definition of Reynolds number for the particle is used, as a function of shear velocity (u^* $[LT^{-1}]$), particle diameter (d_p) and water kinematic viscosity and water density (v) [*Shields*, 1936; *Miller et al.*, 1977; *Buffington and Montgomery*, 1997] as:

$$Re_p = \frac{u^* d_p}{v} \tag{4.3}$$

Equation 4.3 will permit also the direct determination of the denominator in Stokes number, the time scale of the fluid flow (τ_f).

The exact time scale definition for the fluid-flow turbulence (τ_f) is one of the most complex issues in the field of multi-phase flows [*Balachandar*, 2009]. A characteristic time of the fluid-flow is the time needed for the flow to cover a characteristic distance (if the distance is l and velocity of the flow is v_f then the time is l/v_f). Here, the characteristic distance is defined as the particle diameter d_p since the focus is on the flow -particle interaction and the fluid flow velocity is approximated with the depth averaged (bulk) velocity U_b [L.T^{-1}]. Consequently, τ_f is defined as:

$$\tau_f = \frac{d_p}{U_b} \tag{4.4}$$

The above definitions indicate that Stokes number is a measure of the geometry and inertia of the solid (sediment) phase after its interaction with the fluid. Stokes number thus differs from Reynolds number which relates the dynamics of the fluid phase to the geometry of the solid phase

For non-laminar flows, Stokes number must be corrected to account for the effect of non-Stokesian drag force. This problem relates to the scaling of Reynolds number (see Kolmogorov's theory [*Kraichnan*, 1964]).

Here I implement the simplified modification of Stokes number given by *Tsai et al.* [2004] (Equation 4.5) which has been used to calibrate aerosol particle sizers. It is based on the definition of the dimensionless transit velocities for airborne particles based on their inertia [*Wilson and Liu*, 1980]. The experiments show accurate prediction of particle characteristic over a range of Stokes and Reynolds numbers. The modified Stokes number is:

$$Stm = \frac{24St}{Re_p \times C_D} \tag{4.5}$$

where C_D is the drag coefficient.

It is important to emphasise that the inclusion of the particle Reynolds number in the above equation instead of some expression of the flow Reynolds number (eg. the bulk Reynolds number, Re_b) is an idealisation. Specifically it assumes an $\frac{U_b}{u_*} = 1$ and $\frac{d}{d_p} = 1$, ignoring the logarithmic profile of the flow. As a result the following calculation is the first approximation of the modified stokes number and it is unrestricted from the hydrodynamic behaviour. This is the reason why the range of velocities examined below is restricted to the scale of shear velocities (0 to 0.4 m/s). All these assumptions are removed from the generalised modification for Stokes number included in *Maniatis et al.* [2016b].

Equation 4.5 demonstrates the effect of inertia on the conditions during sediment transport. The drag coefficient is also a function of Reynolds number and the latest fitting of the $C_D - Re_p$ relationship for

the full range of Reynolds numbers up 10^6 and for idealised spherical particles can be found in *Morrison* [2013], (Figure 8.13 on page 625).

Figure 4.1 shows the relationship of the Stokes number for a range of particle diameters from 60 μm to 256 mm, and for a shear velocity range (flow increase) from 0 to 0.4 m/s. Even for Reynolds numbers considered in sediment transport ($< 10^5$) the Stokes number increases sharply to values > 1, hence the inertia of the particles will have an important effect on their motion. This result has important implications for the choice of reference frames for the modelling of the sediment transport process (Eulerian or Lagrangian).

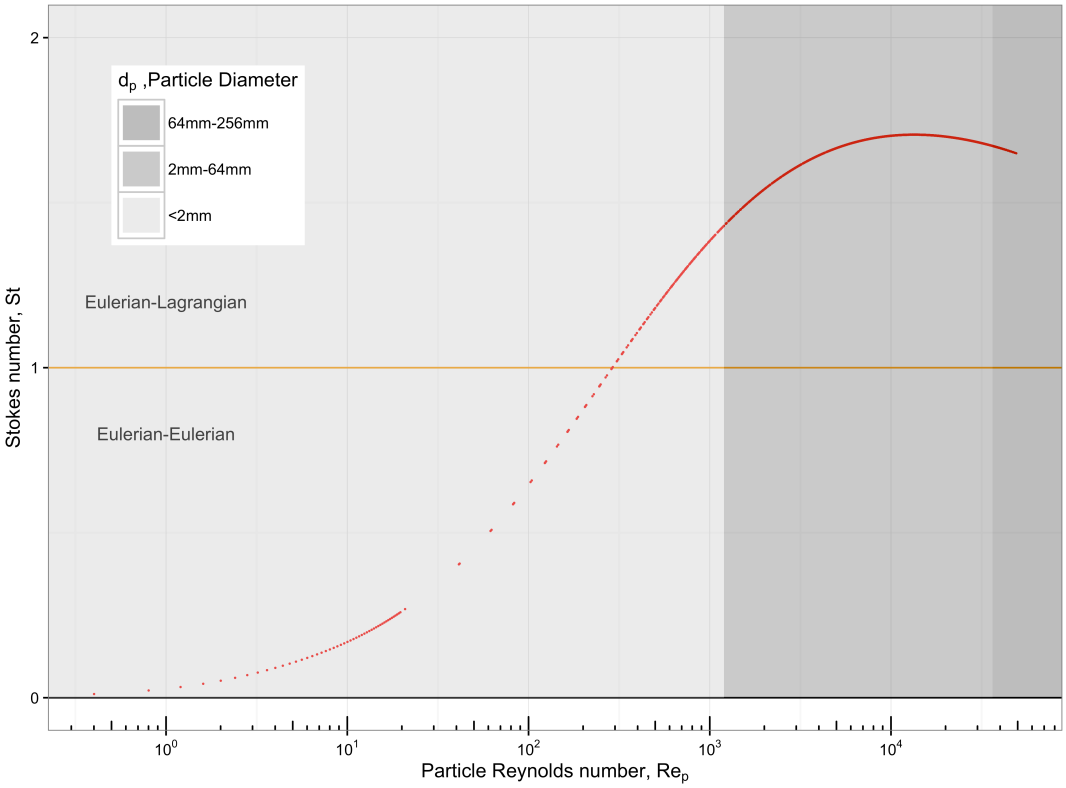

Figure 4.1: **Stokes number approximation.** Calculation of Stokes number as function of particle Reynolds number (Re_p) for a range of particle diameters from 0.004 to 256 mm and a shear velocity range from 0 to 0.4 m/s. As the particle diameter increases (from left to right, shaded areas) both Stokes and Reynolds number increase. This indicates an increase in local flow turbulence as well an increase of the inertia (hence the resistance) of the particle. For particle diameters > 2 mm the Stokes number increases to values that are compatible to an Eulerian-Lagrangian model in contrast to the smaller particles where the Eulerian-Eulerian concept holds consistency. The critical value of $St = 1$ is indicated by the yellow line.

Both of the frames of reference are equally valid for continuous single or multi-phase flows and cross-comparison between the two has led to complex problems in transport processes being solved (e.g. *Gouesbet and Berlemont* [1999]). However, for multi-phase dispersed flows, it is accepted that the Eulerian approach is non-consistent for heavy and/or large particles with Stokes number $St > 1$ since the inertia of the particles exerts greater influence to their motion [*Balachandar and Eaton*, 2010].

Experimental results relevant to sediment transport with low Reynolds numbers and small grains (e.g. *Alfadhli et al.* [2014], $Re_p < 1000$) are in the region where St is close to 1 (Figure 4.1). Hence,

Eulerian-Eulerian parameterisations give accurate predictions when Re_p is small (e.g. *Lajeunesse et al.* [2015]).

In natural streams, Reynolds numbers are much higher than in the laboratory (*Buffington and Montgomery* [1997] show that a particle Reynolds number of $> 10^4$ is more relevant to natural conditions) so St values are significantly greater than 1 (Figure 4.1). With high St values, the inertia of sediment particles is significant and this inertia helps to explain variability in observations of entrainment [*Buffington and Montgomery*, 1997] and transport [*Dietrich and Smith*, 1984; *Ferguson et al.*, 1996; *Wathen et al.*, 1997].

The above calculation is the first step for the inclusion of Stokes number in sediment transport theory. It is necessary to accumulate experimental evidence for the Stokes number of particles under fluvial transport since the correction for non-Stokes flows of Equation 4.5 has been applied for different density ratios compared to a fluvial system ($\rho_{water} >> \rho_{air}$).

For the rest of this thesis, the focus is on the Eulerian - Lagrangian model where the water flow is resolved in a Eulerian reference frame with a static origin and the sediment dynamics are treated in a Lagrangian framework where each moving sediment grain has an attached (inertially fixed) reference frame. Although the Lagrangian model is relevant to a range of sediment classes, with today's monitoring equipment this model can be fully resolved and verified for grain sizes of the order of 100 mm. Nevertheless, it is important to emphasise that the following rigid body derivations are universal (e.g. independent of the grain size).

4.1.2 Rigid Body Theory

4.1.2.1 The Newton-Euler Scheme

Several idealised formulations have been proposed for the initiation of motion of a spherical particle sitting on a bed of spheres (e.g. *White* [1940]; *Wiberg and Smith* [1985]; *Valyrakis et al.* [2011a]). The consideration of the effect of a turning moment (rotation) on initiation of motion was formally introduced recently [*Papanicolaou et al.*, 2002; *Wu and Chou*, 2003] with the expression of the corresponding balance of moments.

The model of *Papanicolaou et al.* [2002] was extended in terms of solving the equation of motion for the different modes of incipient movement [*Valyrakis et al.*, 2010, 2013] and over non-constant flow regimes (impulsive events, *Celik et al.* [2010]; *Diplas et al.* [2008]). However, the basic simplifications in this framework are: a) All the forces act at the centre of mass of the particle; and, b) the tipping point (the point that the balance of torques or moments is resolved) is on the surface of the particle.

In former effort to predict different modes of entrainment, *Wu and Chou* [2003] defined an eccentric point of attack for the fluid forces. However, the torque balance was also resolved on the surface of the particle.

Both of these assumptions are removed by defining a force and torque balance equation for the centre of mass of the target particle. This scheme is found in the literature of rigid body dynamics as system of Newton-Euler Equations [*O'Reilly*, 2008]. For an orthogonal coordinate frame the origin of which coincides with the centre of mass of the free to move pebble (body fixed frame), the Newton-Euler equations considering the hydrodynamic forces system applied on a target particle settling on a bed of spheres are:

$$\sum F = F_D + W + \sum T_L = m \begin{bmatrix} a_x \\ a_y \\ a_z \end{bmatrix} \tag{4.6}$$

$$\sum T = (F_L + \sum T_R) \times R = I_{cm} \begin{bmatrix} \alpha_{rx} \\ \alpha_{ry} \\ \alpha_{rz} \end{bmatrix} \tag{4.7}$$

where F_D is the drag force exerted by the flow on the particle, W is the submerged weight of the particle and $\sum T_L$ is the sum of support forces from the surrounding pebbles, all applied in the centre of the mass of the pebble. For the balance of moments, F_L is the lift force of the flow and $\sum T_R$ is the sum of friction forces, both applied on the surface of the pebble and R is the Radius of the pebble.

In the right hand elements of Equations 4.6 and 4.7, m is the mass of the pebble, I_{cm} is the moment of inertia (uniform for a sphere), a_x, a_y, a_z are linear accelerations on the 3 orthogonal axis of the body-fixed frame of reference and α_{rx}, α_{ry}, α_{rz} are rotational accelerations such that:

$$\begin{bmatrix} a_x \\ a_y \\ a_z \end{bmatrix} = \begin{bmatrix} \frac{du_x}{dt} \\ \frac{du_y}{dt} \\ \frac{du_z}{dt} \end{bmatrix} \tag{4.8}$$

and

$$\begin{bmatrix} \alpha_{rx} \\ \alpha_{ry} \\ \alpha_{rz} \end{bmatrix} = \begin{bmatrix} \frac{d\omega_x}{dt} \\ \frac{d\omega_y}{dt} \\ \frac{d\omega_z}{dt} \end{bmatrix} \tag{4.9}$$

Finally, for a spherical particle (with uniform moments of Inertia (I_{cm}) along all the three axes) the kinetic energy of the particle can be calculated as:

$$K = \frac{1}{2} m V_{norm}^2 + \frac{1}{2} I_{cm} \Omega_{norm}^2 \tag{4.10}$$

where V_{norm} is the norm of linear velocities, Ω_{norm} is the norm of angular velocities, I_{cm} is the uniform moment of inertia for a sphere. For non-spherical particles the total moment of inertia is calculated as the integral of the moments of inertia of the simpler shapes that compose the shape of the particle. The force torque balance system is demonstrated in Figure 4.2. The definition of Equation 4.10 is useful for two reasons:

Firstly it simplifies the incipient motion criteria. The kinetic energy of the pebble is relevant only to the motion of the particle. As a result, a definite and explicit incipient motion criterion, independent of the stochastic nature of the fluid flow, is the $K >= 0$. The duration of the period where $K > 0$ will determine if the pebble is vibrating (close to entrainment) or moving. Moreover, it can be an indication for the mode of motion since if the linear velocity norm is > 0 and the angular velocity norm is 0 then the pebble is sliding. If both of the velocity norms (angular and linear) are > 0 then the pebble is rolling.

The second reason is the relation of this definition with the contemporary IMU sensors. An ideal strapdown Inertial Measurement Unit rigidly placed in the pebble such as its centre of mass coincides with the centre of the mass of the pebble and its orthogonal axis coincident with the body-fixed frame of reference of the pebble (Figure 4.3). It is able to record the $3D$ components of the linear acceleration vector (a_x, a_y, a_z) and the $3D$ components of the angular velocity vector (ω_x, ω_y, ω_z) [*Featherstone*, 2014]. This analysis continues under the assumption that it is possible to derive a set of ideal 3D measurements for body frame accelerations from an accelerometer and body frame angular velocities from a gyroscope.

The above force-torque balance is in principle Lagrangian, not only because it concerns an individual particle but mainly because the case of rotation is also accounted. Consider all the force vectors expressed in a local Eulerian frame (F_L, F_D, W). Since the sensor is rotating with the pebble, the axes of the sensor are not aligned to the axis of the local Eulerian frame, hence the same vectors will be recorded differently in the frame of the sensor compared to their initial form in the Eulerian frame. Consequently, rotation has to be taken into account in order to compare between Lagrangian and Eulerian measurements if the sensor is in a fixed position relative to the particle body frame.

To continue with the theoretical derivations, the hypothesised ideal IMU is rigidly attached to the moving particle such that: a) the centre of the mass of the sensor coincides with the centre of the mass of the particle; and, b) no relative movement occurs between the sensor and the sphere (rigidity is infinite). Finally, the signal from the hypothesised sensor is ideal, hence environmental noise or other signal related errors are ignored for this chapter. Issues arising from the design of the IMU which do not meet all of these assumptions are discussed in Chapters 5 to 7.

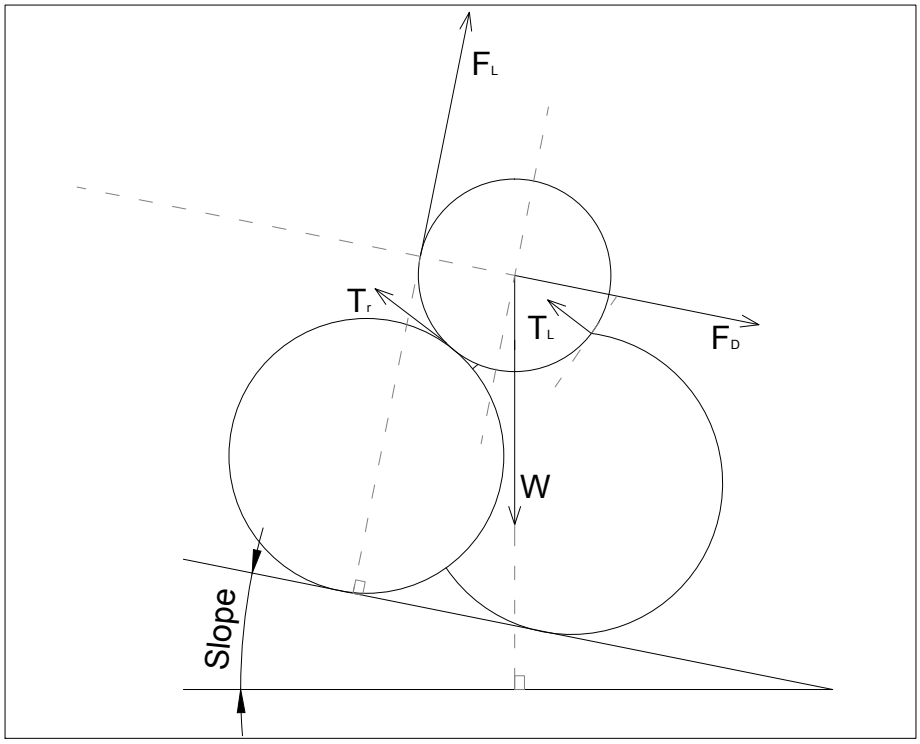

Figure 4.2: **The proposed Force -Torque Balance model (Newton Euler Equations)** for a particle on a river-bed. F_D is the drag force exerted by the flow on the particle, W is the weight of the particle and T_L is a representative support force vector from the surrounding pebbles, all applied in the centre of the mass of the pebble. For the balance of moments, F_L is the lift force of the flow and T_R is a representative friction force vector, both applied on the surface of the pebble and R is the radius of the pebble.

4.1.3 Rotation

There are three different mathematical notations to represent the rotation between two relatively independent frames of reference: the *Cosine matrices*, the *Euler angles* and the *Quaternions*. Here the focus is on attitude representations that resolve in practice the rigid-body dynamics of a pebble under fluvial transport, hence a detailed elaboration on the numerous mathematical derivations is outside the scope of this thesis.

The three methods for rotations do not have the same degree of applicability. The Cosine matrices are used to express the mathematical basis for the problem but they are not possible to be parametrised with inertial measurements directly (based on vector angle measurements). The Euler angles and angle rates are used extensively in engineering applications when the motion of the rigid body is restricted or controlled (not the case of fluvial transport). Further, Euler angles are defined in a standard mathematical framework which makes them intuitively easier to understand. However, only the method of Unit Quaternions can resolve freely the rotational dynamics and this method has to be chosen for the unrestricted motion of a pebble in a river. It is necessary for coherence to briefly introduce the three methods and explain the advantages of the chosen method of unit quaternions.

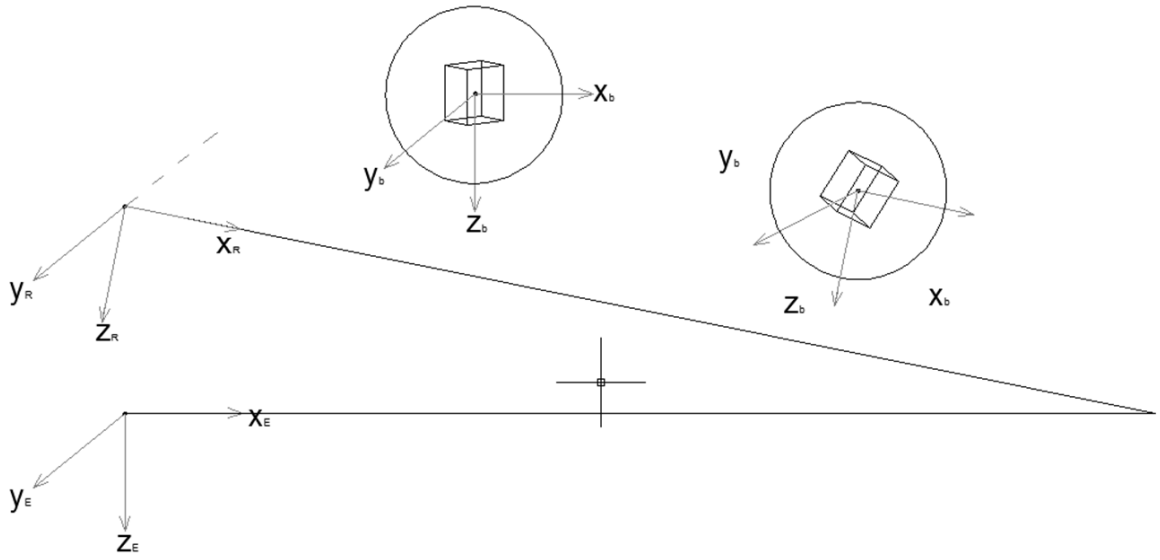

Figure 4.3: **Demonstration of all the the frames of reference** included in a free movement in a river. The body fixed ($_b$) axes are aligned with the Euler frame ($_E$). The River-bed frame ($_R$) can be different from Eulerian which must be taken into account when particle inertial and flow forces are compared.

The literature on rotations and the physically based modelling of inertial tracking is vast and often conflicting. The resources I used for the following summary (apart from the ones provided in text) are:

- the works of *Diebel* [2006], *Shuster and Oh* [1981] and *Shuster* [1993] which are excellent primers on the different representations,
- an applied description of quaternions can be found in *Mukundan* [2002] and a summary on the quaternion algebra in *Zhao and van Wachem* [2013],
- the kinematics described for the tracking of the pebble (Section 4.1.3.5) are based on derivations from the primers in spacecraft dynamics of *Sidi* [1997] and *Phillips et al.* [2000] and on the UAV physical model presented in *Fiorenzani et al.* [2008] ,
- educational material available on-line should not be ignored and the course notes of *Baraff* [1997], and *Großekatthöfer and Yoon* [2012] introduce efficiently most of the following concepts.

4.1.3.1 Cosine Matrices

Cosine matrices represent the transformation from an initial coordinate system (A) to a target coordinate system (B). Let the base vectors of A the base vectors of coordinate system B the transformation matrix from $A \rightarrow B$ is:

$$\mathbf{T_{B \leftarrow A}} = \begin{pmatrix} \cos\sphericalangle(\vec{x_A},\vec{x_B}) & \cos\sphericalangle(\vec{y_A},\vec{x_B}) & \cos\sphericalangle(\vec{z_A},\vec{x_B}) \\ \cos\sphericalangle(\vec{x_A},\vec{y_B}) & \cos\sphericalangle(\vec{y_A},\vec{y_B}) & \cos\sphericalangle(\vec{z_A},\vec{y_B}) \\ \cos\sphericalangle(\vec{x_A},\vec{z_B}) & \cos\sphericalangle(\vec{y_A},\vec{z_B}) & \cos\sphericalangle(\vec{z_A},\vec{z_B}) \end{pmatrix} \tag{4.11}$$

This matrix is always orthogonal and the transpose is equal to the inverse. Also:

$$T^{T}_{B\leftarrow A} = T^{-1}_{B\leftarrow A} = T_{A\leftarrow B} \tag{4.12}$$

which implies that the reverse transformation ($B \rightarrow A$) is expressed by the inverse of the matrix in Eq.4.11

The transformation with rotation of a coordinate frame around the basis vectors at a rotation angle θ is described by the matrices:

$$R^{x}(\theta) = \begin{bmatrix} 1 & 0 & 0 \\ 0 & \cos\theta & \sin\theta \\ 0 & -\sin\theta & \cos\theta \end{bmatrix} \tag{4.13}$$

$$R^{y}(\theta) = \begin{bmatrix} \cos\theta & 0 & -\sin\theta \\ 0 & 1 & 0 \\ \sin\theta & 0 & \cos\theta \end{bmatrix} \tag{4.14}$$

$$R^{z}(\theta) = \begin{bmatrix} \cos\theta & \sin\theta & 0 \\ -\sin\theta & \cos\theta & 0 \\ 0 & 0 & 1 \end{bmatrix} \tag{4.15}$$

where x, y and z are the axes of the coordinate system.

The Euler theorem on rotations proves that every orientation in respect to an inertial frame can be represented by three successive rotations as long as the same axes is not rotated sequentially [*Weisstein*, 2009]. As a result, using the elementary matrices in equations 4.13, 4.14, 4.15 it is possible to reconstruct every attitude by a multiplication of three matrices in a consistent sequence.

4.1.3.2 Euler Angles

A common sequence in aerodynamics is the $Z-Y-X$ rotation (or $3-2-1$), which rotates initially the z-axis of the frame by θz, then the y-axis of the first intermediate frame by θy and then the x-axis of the second intermediate frame by θx (see FigureB.1). The angles θz, θy, θx are called Euler angles when they are applied sequentially and the overall rotation is expressed with the product:

$$Rot(x,y,z) = R(x,\theta_x = \phi) * R(y,\theta_y = \theta) * R(z,\theta_z = \psi) \tag{4.16}$$

Note that rotations are applied in the reverse order.

The corresponding Direction Cosine Matrix is:

$$\begin{bmatrix} \cos\theta\cos\psi & \cos\theta\sin\psi & -\sin\theta \\ \sin\phi\sin\theta\cos\psi - \cos\phi\sin\psi & \sin\phi\sin\theta\sin\psi + \cos\phi\cos\psi & \sin\phi\cos\theta \\ \cos\phi\sin\theta\cos\psi + \sin\phi\sin\psi & \cos\phi\sin\theta\sin\psi - \sin\phi\cos\psi & \cos\phi\cos\theta \end{bmatrix} \tag{4.17}$$

Eq.4.17 rotates from the inertial (Eulerian in our case) to the body fixed frame (Lagrangian).

In the context of sequential rotations the derivatives of the Euler angles can be used $\begin{pmatrix} \dot{\phi} \\ \dot{\theta} \\ \dot{\psi} \end{pmatrix}$ which are usually found in the literature as Euler Rates. It is important to emphasise that Euler rates are not the equivalent of body frame angular velocities, a difference which is analysed further below.

4.1.3.3 Quartenions

Quaternions (or Euler parameters) are mathematical instances discovered by Sir W. Hamilton as an extension of complex numbers [*Hamilton*, 1844]. They consist of a scalar and a vector component and are usually expressed in the form of a 4 x 1 matrix as:

$$q = \begin{bmatrix} s \\ \vec{u} \end{bmatrix} = \begin{bmatrix} s \\ u_x \\ u_y \\ u_z \end{bmatrix} = \begin{bmatrix} q_s \\ q_x \\ q_y \\ q_z \end{bmatrix} \tag{4.18}$$

where s the scalar, v is the vector and q_s, q_x, q_y, q_z are the quaternion components.

The use of quaternions in rotational dynamics is based again on the Eulerian theorem on rotations which also implies that every attitude can be resolved by a rotation over one adequate instantaneous axis [*Palais and Palais*, 2007]. This conclusion connects the derivation of quaternions to the vector of angular body rates (angular velocities): if the rotation is relatively small then the angular velocity of the body can be expressed as a vector and its direction will coincide with the ideal instantaneous axis for Eulerian rotation. In parallel, since quaternions can be normalized (like vectors), it is possible to commute rotations without special attention to the sequence.

As a result, the unit quaternion can be used to represent transformations by rotation. The form of a transformation quaternion from a system A to B is:

$$q = \begin{bmatrix} q_s \\ q_x \\ q_y \\ q_z \end{bmatrix} = \begin{bmatrix} \cos\frac{-\theta}{2} \\ \vec{e} \cdot \sin\frac{-\theta}{2} \end{bmatrix} \tag{4.19}$$

where θ is the rotation angle and $\vec{e}$ is the normalised rotational axis. In the context of sequential rotations the derivative of quaternions is given by the relationship:

$$\dot{q} = \frac{1}{2}\omega q \tag{4.20}$$

where ω is the $3D$ vector of angular velocities.

The integration of Equation 4.20 derives the transition quaternion as function of angular velocities. The direct multiplication method [*Whitmore*, 2000; *Zhao and van Wachem*, 2013] is implemented to integrate Equation 20 as this is consistent with rotations (in contrast to other integration techniques that are based on the addition of quaternions).

The transition unit quaternion is defined as:

$$\widetilde{q} = \begin{bmatrix} \cos\frac{\|\omega\|\delta t}{2}, \sin\frac{\|\omega\|\delta t}{2}\frac{\omega}{\|\omega\|} \end{bmatrix} \tag{4.21}$$

where ω is the instantaneous angular velocity vector in $3D$. Equation 4.21 is the equivalent of Equation 4.19 populated with the components of the angular velocity vector.

Finally, the corresponding Direction Cosine Matrix built with the quaternion components is:

$$T = \begin{bmatrix} q_s^2 + q_x^2 - q_y^2 - q_z^2 & 2(q_x q_y - q_z q_s) & 2(q_x q_z + q_y q_s) \\ 2(q_x q_y + q_z q_s) & q_s^2 - q_x^2 + q_y^2 - q_z^2 & 2(q_y q_z - q_x q_s) \\ 2(q_x q_z - q_y q_s) & 2(q_y q_z + q_x q_s) & q_s^2 - q_x^2 - q_y^2 + q_z^2 \end{bmatrix} \tag{4.22}$$

4.1.3.4 Lagrangian-Eulerian transformation and comparison between Euler and Quaternion DCM

To rotate a vector from an inertial (Eulerian here) to a body fixed frame (Lagrangian) and *vice versa*, a common practice is to use the Direction Cosine Matrix (DCM from this point onwards) of either the Euler angles or the Quaternions. A vector in Eulerian frame $VE = [VE_x, VE_y, VE_z]$ will be transformed to the body frame as:

$$\begin{bmatrix} Vb_z \\ Vb_y \\ Vb_x \end{bmatrix} = DCM * \begin{bmatrix} VE_z \\ VE_y \\ VE_x \end{bmatrix} \tag{4.23}$$

where the Vb_z, Vb_y, Vb_x are the vector's components on the body-fixed Lagrangian frame.

A vector in the Lagrangian frame $V_b = [Vb_z, Vb_y, Vb_x]$ can be transformed to the Eulerian by using the identity of orthogonality (Equation 4.12) of the DCM as:

$$\begin{bmatrix} VE_z \\ VE_y \\ VE_x \end{bmatrix} = DCM^T * \begin{bmatrix} Vb_z \\ Vb_y \\ Vb_x \end{bmatrix} \tag{4.24}$$

where VE_z, VE_y, VE_x are the vector's components in the Eulerian frame.

This comparison between rotation (Euler angles or Quaternions) methods is important. Euler angles are intuitively easier to understand while quaternions are more abstract (their definition is related to a $4D$-space parametrisation). At the same time, Euler angles produce inconsistent results when used for not well defined and slowly rotating systems, mainly because of a discrepancy called Gimbal Lock which concerns the existence of singularities when the second Euler rotation approaches $\pm\frac{\pi}{2}$. Gimbal Lock is extensively analysed in the resources from flight engineering provided above (e.g. *Diebel* [2006]), but in practice it restricts the use of Euler angles to fully controlled systems.

Quaternions do not suffer from Gimbal Lock and are much more efficient computationally, which makes them an ideal choice for the fast changing stochastic environment of fluvial transport. Also, they are defined by a very clear physical quantity: the angular velocity ω, which is included in the force balance model above. A practical comparison between Euler angles and Quaternion representations is given in Appendix B where a vector is rotated using both approaches. This is also the justification for the use of quaternions hereafter, when rotation is considered.

4.1.3.5 IMU measurements and Inertial Tracking

The simplest assembly of a strapdown IMU sensor is a combination of a $3D$ gyroscope and a $3D$ accelerometer. The preceding analysis is relevant to measurements obtained from an ideal gyroscope which will measure the components of the vector of body axis angular velocities ω in $3D$ $[\omega_{bx}(t), \omega_{by}(t), \omega_{bz}(t)]^T$.

Accelerometers measure accelerations acting on the object in which the accelerometer itself is a non-inertial observer; the measurements are commonly referred to as proper accelerations [*Andrejašic*, 2008]. The accelerometer, being located within the mobile particle, also records so-called fictitious forces [*Zylbersztajn*, 1994]. In the case of sediment particles which move only limited distances, only the effect of acceleration due to gravity needs to be considered.

However, the complete derivation for a non-inertial frame in rotation is relevant since all the rotating frames are non-inertial when measurements are derived from inside them and the error in real applications can be important. Especially when the length of the trajectory of non-inertial frame is comparable to the dimensions of the Inertial domain (Coriolis effect) or sensor is displaced in relation to the centre of mass of the sensor assembly (Centripetal acceleration) [*Fiorenzani et al.*, 2008].

In practice, if an accelerometer is placed still on an absolute horizontal plane and its axes are aligned to an inertial frame, it will measure +1 g (9.81 m/s^2) across the direction of gravity (e.g. z-axis of the Eulerian and/or the body frame if the frames are aligned), which is practically the resistance of the plane to the force of gravity. If the sensor is in free-fall then it will measure 0 in all the axes. Finally, if the sensor is in motion due to translational (or external) forces it will measure both the accelerations relative to the inertial frame and the acceleration of gravity.

Consequently, to retrieve the linear translational acceleration, the acceleration which corresponds to the relative movement of the body frame (Lagrangian to the inertial Eulerian frame), from a vector of ideal body axis accelerations $a_b(t) = [a_{bx}(t), a_{by}(t), a_{bz}(t)]^T$ it is necessary to initially transform the vector into Eulerian coordinates and then subtract gravitational acceleration from the Eulerian representation of the vector Equation 4.24:

$$a_E(t) = C(t)a_b(t) - g_E \tag{4.25}$$

Equation 4.25, gives the linear acceleration (a_E) imposed from translational forces in Eulerian coordinates. $C(t)$ is the DCM as described above and g_E the vector of gravity in the Eulerian frame $g_E = [0, 0, 9.81]^T$ m/s^2.

The position tracking of the object in the Eulerian frame it is then done by double integration of a_E:

$$v_E(t) = v_E(0) + \int_0^t a_E(t)\,dt \tag{4.26}$$

$$s_E(t) = s_E(0) + \int_0^t v_E(t)\,dt \tag{4.27}$$

initially to derive velocities and subsequently to derive positions. A conceptual diagram for the calculations of Inertial Navigation is given in Figure 4.4.

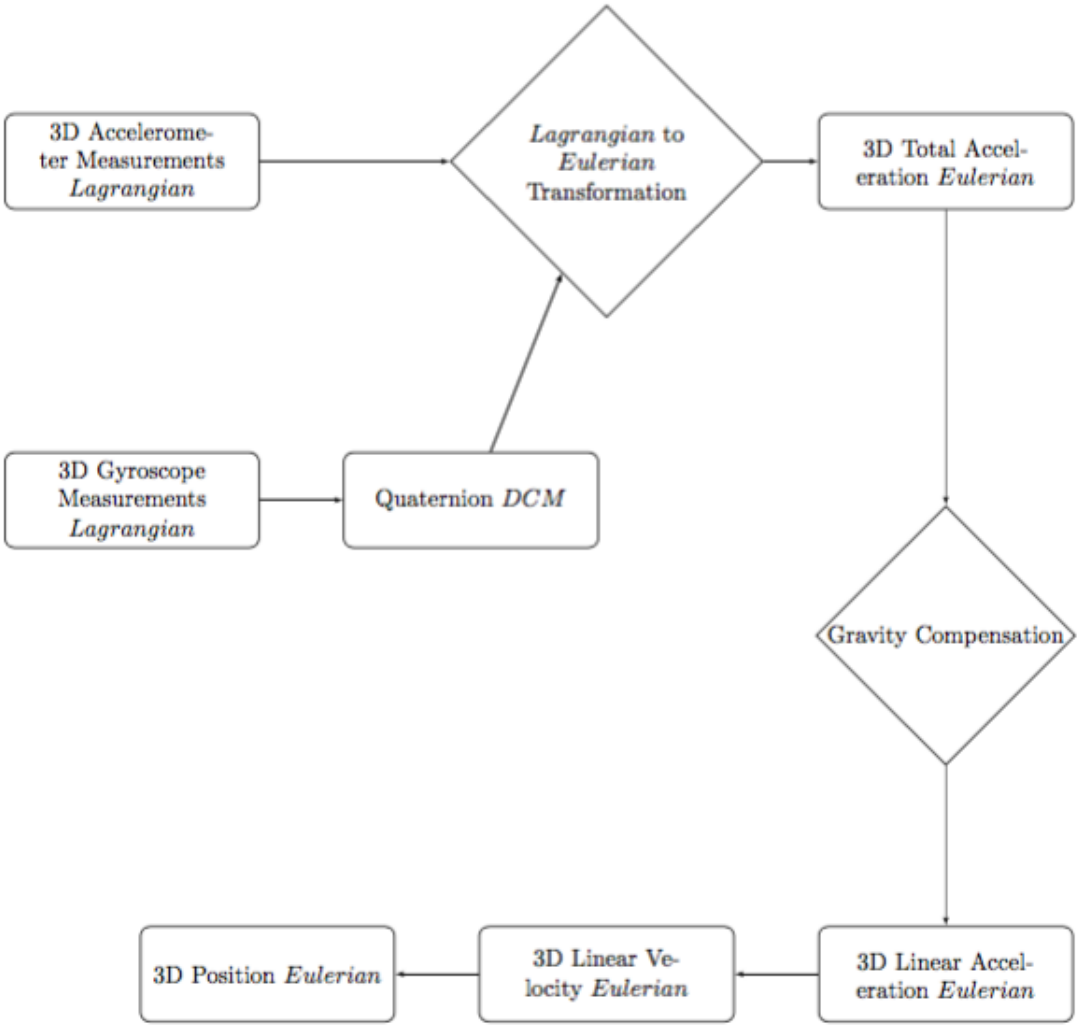

Figure 4.4: **Conceptual Diagram for the Inertial Navigation.** From 3D IMU measurements (Lagrangian Frame) to 3D positions in Eulerian via the Unit Quaternion Transform.

4.1.4 Probabilistic framework: the case of entrainment

The most widely used criterion for incipient motion is Shields' critical shear stress (τ_c). τ_c is the bed shear stress produced by the water flow (if uniform flow is assumed this is approximated as a channel slope-depth product) that is capable of mobilising each specific sediment size class (which, for grain sizes yielding particle Reynolds' Numbers > 70, is correlated with the median diameter of the sediment).

Since Shields' (1936) work, a series of empirical values have been suggested to account for a range of factors including the relative depth of the flow, grain shape and protrusion [*Ashida and Michiue*, 1971; *Fenton and Abbott*, 1977; *Shvidchenko and Pender*, 2000]. In parallel, Shields' criterion has been extensively criticized for its ambiguity and limited applicability [*Church et al.*, 1998; *Buffington and Montgomery*, 1997; *Parker et al.*, 2003; *Bunte et al.*, 2013] and the validity of a single criterion or even the existence of measurable critical threshold conditions have been questioned [*Einstein*, 1950; *Lavelle and Mofjeld*, 1987]. Parallel work has associated the effects of bed micro-topography [*Kirchner et al.*, 1990; *Buffington et al.*, 1992; *Prancevic and Lamb*, 2015], the near bed flow turbulence [*Nelson et al.*, 1995; *Papanicolaou et al.*, 2002] and impulsive [*Diplas et al.*, 2008; *Valyrakis et al.*, 2010] or energetic [*Valyrakis et al.*, 2013] flow events on incipient motion. The combined result of these phenomena cannot be accounted for within a deterministic time-averaged mean stress calculation, although such approaches can still yield useful results.

The core problem with the inclusion of all the above phenomena in any analysis of entrainment is that each of them is difficult to measure or quantify. Advances in monitoring techniques have improved the accuracy of measurements of grain scale near bed forces [*Papanicolaou et al.*, 1999; *Schmeeckle et al.*, 2007] as well as enabling monitoring of impulse events and their energy potential [*Valyrakis et al.*, 2013]. These laboratory measurements reveal great variability of flow dynamics at micro-scale which, combined with the random character of the micro-topography, justifies the treatment of incipient motion as an inherently stochastic processes (comparable to Einstein's description). A summative review of recent studies that define and explore the concept of "pickup probability" or "entrainment probability" as attributed to conditions related to both flow turbulence and sediment arrangement is presented in *Marion and Tregnaghi* [2013].

Marion and Tregnaghi [2013] show how all the stochastic studies of entrainment reutilize and extend the conceptual framework introduced by *Grass* [1970]. Grass suggested calculating the probability of entrainment as a joint probability derived from Probability Density Functions (PDF hereafter) of critical shear stresses (connected to the resistance to entrainment of the sediment grains) and of the distribution of hydrodynamic forces (derived from near bed flow velocities). The probability of entrainment (P_E) is calculated as the exceedance of a random near bed velocity (U_f) represented by a cumulative distribution F_{U_f} having a PDF of f_{U_f}, as:

$$P_E = P(U_f > u_f = u_g) = \int_{u_g}^{\infty} f_{U_f}(u)du = 1 - F_{U_f}(u_g) \tag{4.28}$$

where u_g represents the threshold velocity for grain entrainment. Note that the form of Equation 4.28 is general and also applies to definitions of entrainment in terms of other relevant variables such as shear stress or turbulent kinetic energy.

An aspect of the entrainment problem that has not been extensively investigated is that the existing criteria for sediment entrainment are essentially implicit in the sense that they are based on near particle

flow features (e.g. flow turbulence) rather than characteristics of each individual particle and its local arrangement. This problem has often been identified [*Cao et al.*, 2006], but has not only recently been formally treated by measuring the dynamics that occur in the inertial frame of the particles close to the threshold of entrainment (Chapters 2, 5 and 6).

4.1.5 Definition of explicit probability of entrainment (P_E)

The Newton-Euler system introduced in Equations 4.6 to 4.9 expresses the result of the particle-flow interaction. It is possible to demonstrate this by considering a model were rotation is ignored, but flow turbulence is accounted in detail. For the non-rotational case, after removing the fictitious forces from the accelerometer measurements, we are left with the linear coordinate acceleration. This is the acceleration that mobilises the sensor relative to the bed (or the Eulerian frame of the flow if an explicit description is required). For simplifying the inertial accelerations from the 3D domain it is possible to define:

$$A = \sqrt{a_x^2 + a_y^2 + a_z^2} \quad , \quad CA = A - |\, g \,| \tag{4.29}$$

Where A is the magnitude of total acceleration, a_x, a_y, a_z are the accelerations recorded along the x, y and z axes, respectively, CA is the acceleration norm after gravity compensation and g is the acceleration norm due to gravity (9.81 m.s^{-2} or 1g).

CA hereafter represents the magnitude of the resultant force, the (3D-tensor) force generated on the centre of mass of the particle when the force balance is disturbed.

In the review of *Bialik* [2015], the resultant force on a particle exposed to fluid flow is given by (the Basset force is not included as it is relevant to saltation):

$$\Sigma F = B - G + F_D + F_L + F_M \tag{4.30}$$

Where B and G are Buoyancy and Gravity forces, F_D and F_L are drag and lift generated forces, F_M is the added mass force. The parametrisation of the right hand-side of this equation is based on a number of terms that describe the complex water-particle interaction. These terms include semi-empirical approximations such as the lift, drag and virtual added mass coefficients for the F_D, F_L and F_M, respectively, which is relevant to the approximation used for the estimation of Stokes number in Section 4.1.1 (C_D vs Re_p relationship).

Interestingly, the CA acceleration parameterises directly the left part of Equation 4.30. $\Sigma F = ma$, where m is the mass of the particle and a is the acceleration tensor applied on the centre of mass of the particle. If an ideal accelerometer was placed precisely on the centre of the mass of the exposed particle then the equation $CA = |\, a \,|$ would be consistent since all the forces of are non-fictitious. Unfortunately real accelerometers are not ideal and this is why, in this work, the real acceleration measurements are treated statistically.

Overall, the formalisations presented in this chapter lead to two different explicit definitions: one for the simple non-rotational case and one for the cases the complete Newton Euler model of Section 4.1.2 is used and rotation (angular velocity) is included.

For the non-rotational case, the norm of the total acceleration after gravity compensation can be used from Equation 4.25 as $|\, a_E \,|$. Although $|\, a_E \,|$ is expressed in the Eulerian frame, it represents the dynamics

generated in the body frame as well, since the frames are aligned if no rotation takes place. The above leads to a derivation in the form of:

$$P_E = P(A_f > a_f = a_g) = \int_{a_g}^{\infty} f_{A_f}(a)da = 1 - F_{A_f}(a_g) \tag{4.31}$$

where A_f is a random total inertial acceleration variable for an individual pebble, represented by a cumulative distribution F_{A_f} with a probability density function of f_{A_f}, and a_g is the threshold acceleration for grain entrainment.

Similarly, for the case where rotation is included in the model, the particle energy K of Equation 4.10 can be used towards a derivation in the form of:

$$P_E = P(K_f > k_f = k_g) = \int_{k_g}^{\infty} f_{K_f}(k)dk = 1 - F_{K_f}(k_g) \tag{4.32}$$

where K_f is a random kinetic energy for an individual pebble, represented by a cumulative distribution F_{K_f} with a probability density function of f_{K_f}, and k_g is the threshold kinetic energy for entrainment kg.

Both of the above derivations have the potential to enhance the accurate determination of P_E as it utilises the explicit dynamics of the particles being entrained instead of using implicit flow-related metrics. Also, the statistics of kinetic energy can be used to derive directional information about the motion of individual particles as demonstrated in Chapter 6.

4.1.6 A statistical framework for the evaluation of incipient motion criteria

4.1.6.1 Rationale

The probabilistic derivations for incipient motion differ in terms of the physical definition of the conditional probability that defines the threshold of motion. In the initial framework of *Grass* [1970] the conditional probability is expressed as a function of Shields' shear stress, while in recent derivations the same probability is physically determined by point (e.g. *Papanicolaou et al.* [2002]) or streamwise (e.g. *Bottacin-Busolin et al.* [2008]) flow velocities (Equation 4.28). Furtheremore, here a new physical definition based on the inertial dynamics of the target particle is proposed.

However, one observation is relevant to all the studies, including this one: the definition of a non-abrupt threshold implies that the the measured physical instance (shear stress, flow velocity or inertial dynamics) is defined by two $PDFs$. One of these defines pre-entrainment conditions (mainly representing the resistance to movement of the particle) and one defining the post-entrainment conditions (mainly recording the mobilisation of the particle). This is a representation in an inertial frame of reference of the idea introduced by Grass (1970) in the form of overlapping PDFs, and it implies that the critical point for entrainment lies within the area of overlap of these two distributions.

In a probabilistic context, the degree of overlap between the pre- and post-entrainment $PDFs$ defines the domain of the critical point, hence the exactness of the entrainment criterion. A large overlap of the two distributions suggests a large domain for the threshold, and is thus a less well-defined criterion. A smaller overlap shrinks the domain for the threshold and the derived criterion is better defined. As a result any improvement in the definition of incipient motion thresholds can be quantified by the degree of overlap of the pre- and post-entrainment distributions.

A formal measure for the overlap between two $PDFs$ is the Overlapping Coefficient (OVL) initially proposed by *Weitzman* [1970]. OVL has been used since to quantify the degree of overlap for a range of distributions, from theoretical normal distributions *Inman et al.* [1989] to empirical density functions [*Schmid and Schmidt*, 2006; *Clemons and Bradley*, 2000] which are directly relevant to the analysis presented in this work.

4.1.6.2 A note on the non-parametric estimation of $PDFs$

The KDE is an established technique for the approximation of $PDFs$ of random variables, when no hypothesis can be established for the underlying distribution (non-parametric). Full description of this technique is outside of the scope of this work, however it is necessary to introduce it from the point of application for the coherence of the presented analysis.

The approximations were performed using the default routines implemented in the R-statistical software which are based on the Fast Fourier transform of the kernel estimator introduced by *Rosenblatt* [1956]. The basic algorithm was derived by Silverman [*Silverman*, 1982, 1986] for Gaussian kernels, which is also the type of kernel I choose for KDE in this thesis (the default in R-statistical software).

The KDE, like all smoothing techniques, requires the selection of bandwidth. Numerous automatic bandwidth selectors have been devised (see *Heidenreich et al.* [2013]; *Sheather et al.* [2004]) however they do not all perform equally well [*Park and Turlach*, 1992].

To highlight this effect, I use two bandwidth estimators:

- for display purposes and to derive simple inferences about the data (such as Figure 5.4) the Silverman's rule of thumb is used [*Silverman*, 1986] which tends to over-smooth the data (Figure 4.5).
- for more accurate calculations, such as to calculate the OVL coefficient, the data-based method proposed in *Sheather and Jones* [1991] is used, which for the variability in accelerometer data gives more representative approximations (Figure 4.5).

Both of these methods are options of the default library of the R-statistical software with Silverman's rule of thumb being the default method.

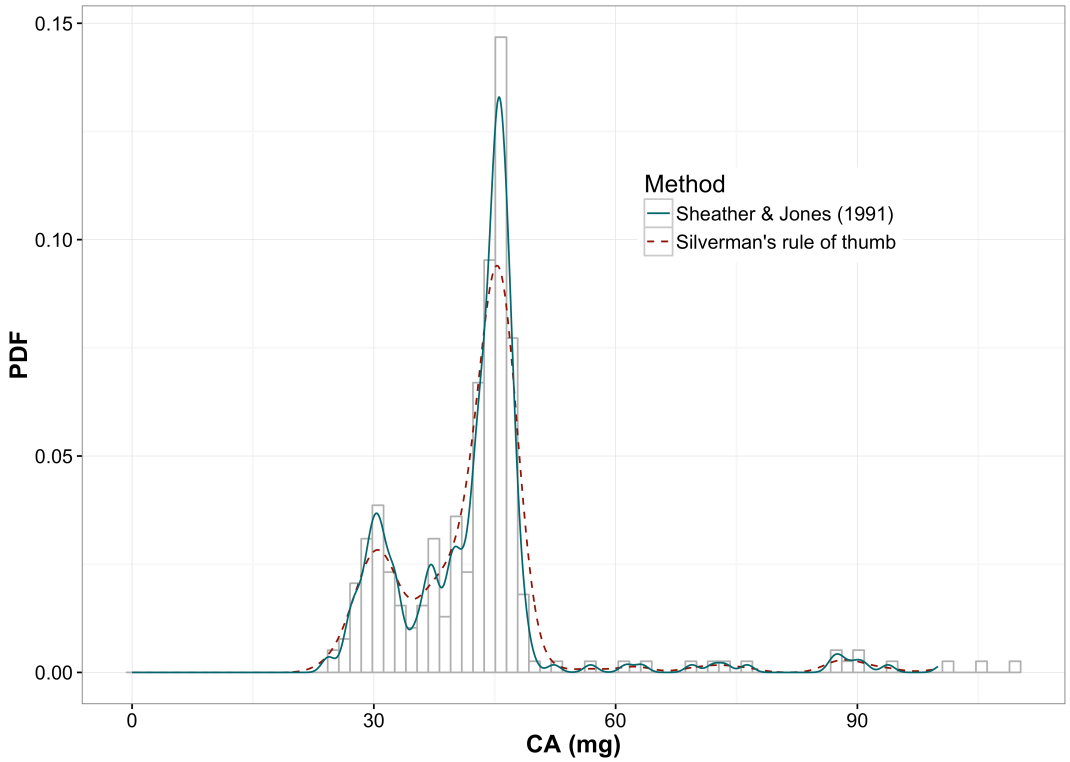

Figure 4.5: **KDE approximation for inertial acceleration.** Figure 4.5 shows two KDE approximations for the absolute accelerations recorded after the entrainment point for $slope = 0.0037$ (histogram, experiments described in Chapter 5). The technique proposed by *Silverman* [1986] is used for display purposes (Figure 5.4) while for the calculation of the Overlapping coefficient (Figure 5.6) the $PDFs$ are approximated using the bandwidth selection method proposed in *Sheather and Jones* [1991].

4.1.6.3 The Overlapping coefficient (OVL)

After the approximation of the $PDFs$ the Overlapping Coefficient is calculated as:

$$OVL = \int_{R_n} min[f_1(x), f_2(x)]dx \tag{4.33}$$

where $f_1(x)$ and $f_2(x)$ are two overlapping PDFs and R_n is the n-dimensional space of real numbers.

The OVL coefficient is always in the range $[0,1]$ and complete overlap between $f_1(x)$ and $f_2(x)$ has $OVL = 1$, while complete distinction gives $OVL = 0$ [*Clemons and Bradley*, 2000]. In the context of evaluating entrainment criteria, an OVL closer to 0 which would suggest smaller overlap between the pre- and post-entrainment $PDFs$

More specifically, if we accept that the threshold of entrainment exists in the region where pre-and post entrainment distributions overlap, then the exactness (and the significance) of the threshold is related to how different the two distributions are. If the distributions were normal and had the same variance the difference of the distributions would be approximated by the separation of the means. The OVL coefficient quantifies this difference for empirically approximated distributions.

A smaller OVL means that the entrainment threshold is better defined. More precisely an $X\%$ reduction of the OVL coefficient represents the maximum % reduction of the variance of the approximated threshold.

4.2 Summary

In this chapter a new Eulerian-Lagrangian model for coarse sediment transport is introduced. The importance of the definition of reference frames in sediment transport is highlighted and explained using an approximation of Stokes number. Stokes number can describe the physical reasons that divide the relative literature in Eulerian and the Lagrangian approaches. The chapter continues with a purely Lagrangian definition of particle dynamics (on their inertial frame) and the transformations from the Lagrangian to the Eulerian domain (and *vice versa*) using the existing theory for rotations. The mathematisation is simplified using the assumption of an ideal IMU, which is the technology used to verify this model in the subsequent chapters. The discussion includes the connection between the deterministic mathematical Eulerian-Lagrangian derivations and the probabilistic framework that is currently used in sediment transport for the case of entrainment. This connection is based on the ability of moving from implicit control variables (water velocity) to explicit particle dynamics (inertial acceleration, kinetic energy) which is a key advantage of the presented conceptualisation. Finally, the OVL coefficient is introduced as a tool to verify the proposed entrainment criteria. This statistical calculation is connected with the model of Grass [*Grass*, 1970], but the physical basis is different as the tested criteria are defined using instances that occur in the inertia frame of the exposed particle.

CHAPTER 5

EULERIAL-LAGRANGIAN MODEL FOR COARSE SEDIMENT TRANSPORT: APPLICATION I. NON-DIRECTIONAL AND NON-ROTATIONAL CASE

Material from this chapter is included in the manuscript: Maniatis, G., T. Hoey, M. Hassan, J. Sventek, R. Hodge, T. Dyrsdale, and M. Valyrakis (accepted August 2016), Calculation of explicit probability of entrainment based on inertial acceleration measurements, Journal of Hydraulic Engineering

The Eulerian-Lagrangian model presented in the previous chapter was simplified under the assumption of deriving 3D-acceleration and 3D-angular velocity measurements from an ideal IMU. Real strap-down IMUs are not ideal and, in practice, the error accumulation for the sensors that are cheap enough to be deployed in large numbers cannot permit their use for 3D tracking of unconstrained motions. A great number of engineers are working on the error identification and modelling from IMUs [*Zekavat and Buehrer*, 2011], since the commercial and surveillance applications of this technology are numerous. The discussion on the magnitude of error in inertial measurements (especially when position is resolved) is initiated here and extended in the following chapter where the complete 3D Eulerian-Lagrangian model (Chapter 4) is experimentally tested. Here the variability of the inertial measurement is treated using a dedicated Kalman filter [*Kalman*, 1960].

It is important to repeat that for no-rotational vibrations (the particle does not generate a trajectory) the Eulerian and the Lagrangian (body frame) domains are aligned. The presented incipient motion experiments of this chapter are relevant to simplified non-rotational motions. In parallel, only the magnitude of inertial acceleration is analysed which leads to a loss of direction in the Eulerian domain. These simplifications were necessary to test the initial prototype sensor (the G-node sensor, Chapter 3) which was equipped with a 3D-accelerometer and no gyroscope.

The focus of this chapter is on the detection of entrainment and the probabilistic parametrisation of absolute gravity compensated inertial accelerations (CA Equation 4.29, Chapter 4) towards an explicit entrainment criterion.

5.1 The Non-Rotational Case

5.1.1 Flume experiments

The deployed prototype consists of a wireless mote platform deployed with a 3-axis accelerometer with a measurement range of ±4 g (G-node) precisely located at the centre of mass of purpose specific sensor assembly. The electronics were enclosed in a spherical enclosure of 111 mm diameter and the overall assembly weighed 1.43 kg, giving a density of 2383 kg/m^3, which is within the range of natural materials. Higher density can be achieved by adding removable weights to voids designed within the case (Chapter 3). The prototype was tested in a series of experiments in the 6 m × 0.6 m [$L \times W$] recirculation flume in the Mountain Channel Hydraulics Experimental Laboratory (MCHEL), University of British Columbia. The scope of the experiments was to make a first evaluation of the 3D inertial acceleration measurements from the prototype sensor under varying flow and slope conditions.

An idealized bed of hemispheres (Figure 5.1) of the same diameter as the the sensor (111 mm) was constructed using 3D-printing. The result was a bed topography with saddle and grain-top positions that approximated the model described in *Kirchner et al.* [1990]. In each experiment, the sensor was placed in a saddle position (position A in Figure 5.1) and the flow initiated from zero with a steadily increasing rate of 0.014 l/s^2 up to a maximum rate of 6.25 l/s which was reached after 446 seconds. Upstream of the bed of hemispheres, large sediment particles generated fully turbulent flows which approximated uniform conditions (equal water depth along the length of the flume) over the full range of discharges used. Flow velocities were monitored using a *Vectrino II* Acoustic Doppler Profiler [*Craig et al.*, 2011] for the discharges where flow depths were sufficient to permit the placement of the probe to be far enough from above the bed to derive measurements. The hydrodynamics for the experiments are summarised in Appendix A. The experiments were designed to observe the following series of processes:

- Entrainment from the saddle position and subsequent deposition in the grain top position (position B in Figure 5.1). As well as providing information on movement from saddle positions, this step removes bias from the placement of the sensor, since the deposition in the second grain top position can be treated as natural with minor random variations in position and pebble orientation.
- A second entrainment of the instrumented particle which transports the sensor out of the monitoring area.

At each of four different flume slopes, 0.026, 0.037, 0.044 and 0.057, nine repeat experiments were undertaken giving 36 experiments in total. The inertial acceleration of the sensor was monitored at a frequency of 4 Hz.

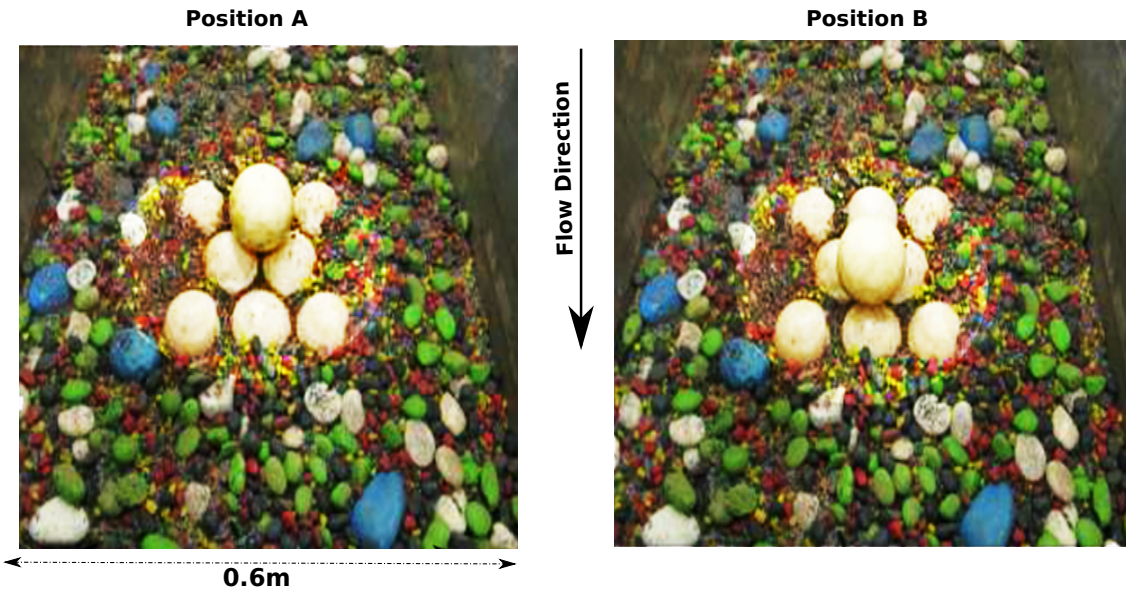

Figure 5.1: **Description of the experimental setting.** The setting represents the theoretical model described in *Kirchner et al.* [1990] with two characteristic entrainment positions (saddle (A) and grain-top (B)). The physical differences of the sensor compared to natural sediment are its shape and its density. A sphere was used to enable robust determination of sensor dynamics in the inertial frame (requiring accurate definition of the center of mass and locations of points of contact) during calibration.

5.1.2 Experimental limitations

The sensor has idealised physical characteristics compared to a natural coarse particle, and was only subjected to shallow flows (up to 0.16 m) and velocities up to 0.37 m/s (Figure 5.2), such that, except at the highest flows at the lowest slope the (0.026), flow depth was less than sensor diameter. When using the data from these experiments the assumptions and the errors inherent to the sensing process need consideration.

The sensor has been developed for natural environments and the testing of relevant signal transmission and wireless communication technologies was crucial for the evaluation for the prototype. Hence, for this prototype, a sampling rate of 4 Hz was used, the maximum sampling rate at which acceleration data could be reliably transmitted over the underwater radio.

The optimal sampling frequency for entrainment of large grains in turbulent flows is less than the frequency for characterising flow turbulence due to the lower sensitivity of particle movement to micro-turbulence. However, the system must record particle dynamics at sampling rates that reflect the physical meaning of the derived inertial measurements. Although previous experiments with artifical pebbles have used very high sampling frequencies for both intertial (e.g. *Šolc et al.* [2012]) and turbulence (e.g. *Valyrakis et al.* [2013] measurements, over-sampling involves redundant data storage and may lead to

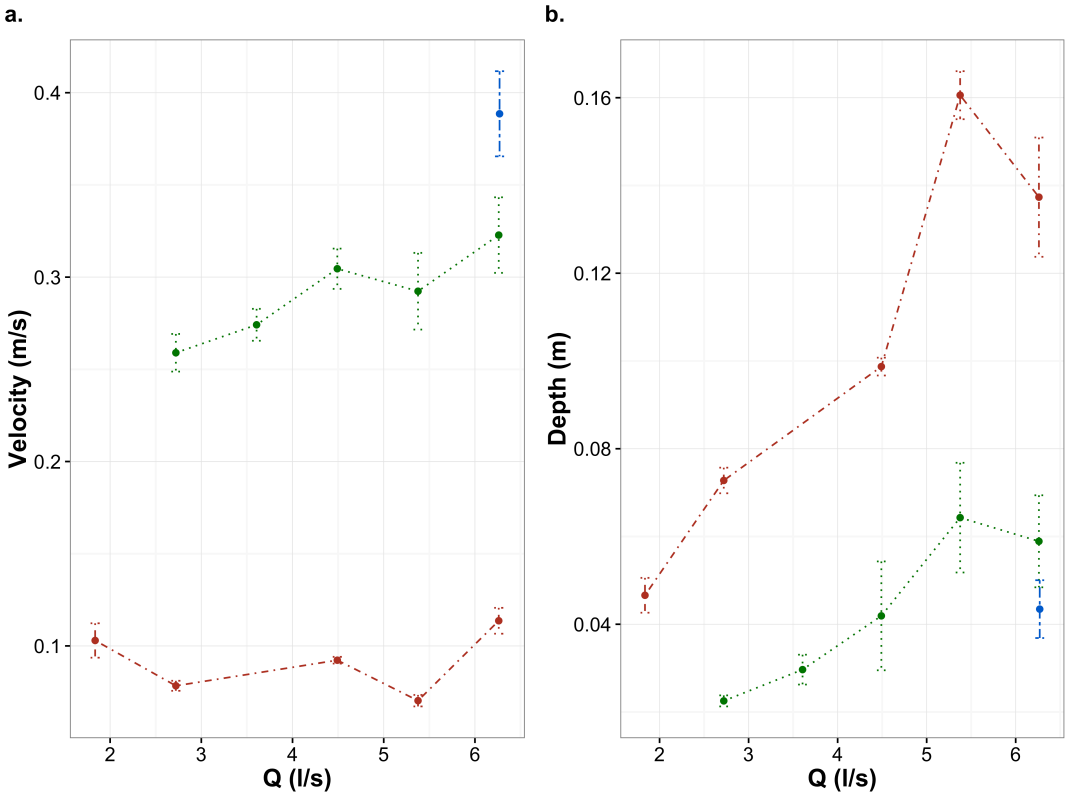

Figure 5.2: **Description of hydraulic conditions.** Near bed flow velocities (a), measured c.0.5 m upstream of the bed of hemispheres. Figure 2b. shows water depths at the measurement points on the bed of hemispheres in the absence of the sensor particle. This was possible for the lower two slopes (0.026 and 0.037) at a range of discharges. At slope = 0.044 velocities could only be measured for the highest discharge (6.25 l/s) and depths were too low at slope = 0.057 for any velocity measurements. In all cases the lower end of the probe was placed at a distance of 15 mm from the bed. The calculated Froude number ($F = u/\sqrt{gd}$) was subcritical, in the range 0.57 to 0.71. The low depth/sediment diameter ratios mean that it was not possible to use a uniform flow approximation of the Shields stress (τ) for cross comparison with the inertial accelerations [*Shields*, 1936]. These low ratios also account for some variability in the responses of depth and velocity to increasing discharge as larger roughness elements were progressively drowned out.

artefacts in the data. The optimal sampling frequency for particle motion can be defined with reference to the velocity of the particle. Assuming maximum displacement velocities of the order of 100 diameters per second, as demonstrated in a experiments for particles of smaller diameter [*Ancey et al.*, 2002], it is possible to suggest a target sampling frequency of about > 50 Hz. This is the rationale behind the use of 50 Hz sampling frequency in the experiments presented in Chapter 6.

To enhance readability the absolute total acceleration (CA) after gravity compensation is redefined as:

$$A = \sqrt{a_x^2 + a_y^2 + a_z^2} \quad , \quad CA = A - |g| \tag{5.1}$$

where A is the magnitude of total acceleration, a_x, a_y, a_z are the accelerations recorded along the x_b, y_b and z_b axes, respectively, CA is the acceleration norm after gravity compensation and g is the

acceleration norm due to gravity (9.81 m/s^2 or 1 g).

An important implication of not measuring angular velocities is the inability to integrate the accelerations in order to derive velocities as it is defined in Chapter 4, which has two aspects. Although the noise threshold was identified during (manufacturer proposed) calibration and subtracted from the measurement, inaccuracies remain and are highly relevant to the sensor's response to gravity (*Woodman* [2007], Chapter 6).

Finally, a combination of restricted sampling frequency and absolute gravity compensation leads to a masking of the pre-entrainment conditions during the statistical treatment of the signal. More specifically, entrainments and pre-entrainment motions occur in the same time-window when the signals from individual experiments are synchronized (Figure 5.3). This is an artefact of the data-processing in order to increase the confidence on the magnitude of the recording dynamics.

5.1.3 Categorisation and summary of Total Acceleration (CA)

5.1.3.1 Pre-entrainment position grouping

The experiments produced two different modes of movement. For the two lowest slopes (0.026 and 0.037) initial entrainment from the saddle position was followed by settling in a grain top position, where the sensor remained until entrained for a second time. On the contrary, for the two higher slopes (0.044 and 0.057), although entrainment from the saddle position was clearly recorded, the sensor did not remain stationary in the grain-top position for sufficient time prior to its second, grain-top, entrainment to allow isolation of pre-entrainment conditions.

For the following analysis entrainments from the saddle position for the low slopes are omitted and data are grouped in two limiting cases:

- high resistance to entrainment (low slope, grain-top position), entrainment from the grain-top position for the lowest two slopes;
- low resistance to entrainment (high slope, saddle position), entrainment from the saddle position for the two higher slopes.

This grouping avoids inconsistent comparisons and allows investigation of a wider range of pre-entrainment dynamics. Note that for the lower slopes, entrainment from the saddle position was identified from the data as an orientation change on the acceleration vector (a_x, a_y, a_z). In the total acceleration signals reported here orientation changes are masked. A representative signal at the entrainment point from an individual experimental run for one slope (0.026) and grain top position is shown in Figure 5.3a. Note that in this individual signal a pre-entrainment wobbling is also recorded c.10 sec before the entrainment event.

5.1.3.2 Derivation of aggregated time series for each slope

The inherit stochasticity of entrainment [*Marion and Tregnaghi*, 2013] can be studied following two strategies. The first is the analysis of individual runs for the identification of entrainment thresholds. The $PDFs$ of the individual thresholds can be used to recover the stochastic behaviour. This process demands a large number of experiments to define robustly the corresponding probability density function (PDF hereafter).

The second strategy (followed in this chapter) is to combine the individual signals over the same time domain and use this time series as an integrated entrainment function. The combined signal can be used to estimate the PDF of entrainment conditions and directly describes the stochastic behaviour. This approach provides a larger data set than would the analysis of individual runs, and enables use of Bayesian statistical methods to address the inherently stochastic entrainment process. In comparison to classical frequentistic methods, Bayesian analysis requires in principle a smaller number of repetitions [*Carlin and Louis*, 1997].

Following the second strategy, the acceleration time series from each individual run were synchronised with the corresponding flow rate curve (Figure 5.3b). Instead of approximating the underlying process for individual runs, the individual acceleration signals for each slope have been aggregated. For a time domain $t_0,..,t_n$ the acceleration signal is defined by a series of $A_0,..,A_n$ absolute acceleration values. If k is the number of experiments for one slope the summed acceleration signal is given by the set:

$$A = \{\{A_1,...,A_k\}_{t_0}, \quad ..., \quad \{A_1,...,A_k\}_{t_n}\} \tag{5.2}$$

The above formulation states the full range of absolute accelerations recorded in each of k repeat experiments ($k = 9$ in this case) for each time point, hence discharge value (Figure 5.3c). The analysis of the aggregated signal has two benefits compared to individual signal analysis:

- given that our analysis is purely statistical all the approximations are performed with a larger input sample of accelerations which increases statistical confidence and thus the significance of the results; and,
- the resulting individual time series for each slope is more representative of a raw signal derived in a natural environment, extending the application range of the presented method.

5.1.4 Analysis of Absolute Acceleration (CA): statistical techniques

5.1.4.1 Dynamic Linear Model Filtering

The aim here is to approximate the underlying dynamical process for each slope by analysing the combined acceleration signal. Space-state estimation techniques for time series analysis are commonly used [*Box et al.*, 2013]. Here *Zhang and Li* [1996] is followed with the use a recursive algorithm for the square root version of the Kalman filter [*Kalman*, 1960]. Appendix E summarises the form of the Kalman filter used by *Zhang and Li* [1996] as well as the "forward" form of an RTS smoother. These algorithms as coded for the R-statistical software by *Petris* [2010].

The summed time series is approximated with a first order polynomial model of the form:

$$\begin{cases} y_t = \theta_t + v_t, \ v_t \sim N(0, V) \\ \theta_t = \theta_{t-1} + \omega_t, \omega_t \sim N(0, \Omega) \end{cases} \tag{5.3}$$

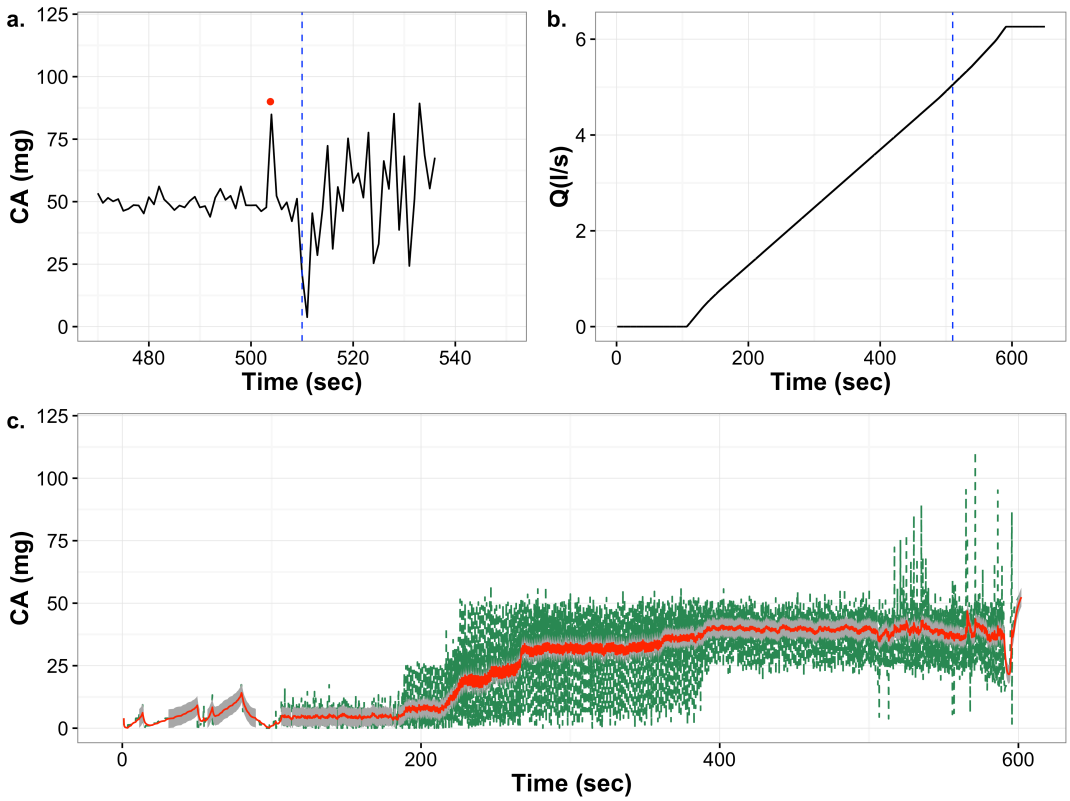

Figure 5.3: **Definition of the underlying entrainment process.** a. shows the total absolute acceleration close to the point of entrainment from one run at slope = 0.026. The sampling frequency is 4 Hz and the point of entrainment (50 mg at $t = 507$ sec, blue-dotted line) is shown as a sudden reduction of the acceleration (dislodging) followed by variable smaller accelerations due to subsequent vibrations. The red dot indicates a distinct pre-entrainment vibration c.10 sec before the entrainment event for this experiment. b. shows the corresponding flow increase (steady increase rate of 0.014 l/s up to a maximum rate of 6.25 l/s for all experiments) and the entrainment point from Figure 3a expressed as discharge (5.17 l/s at $t = 507$ sec, blue line). c. shows the summary signal derived by the process described in Equations 4 and 5 for all nine replicates with $slope = 0.026$. The red line is the underlying process as approximated after the application of the Kalman filter (Eq. 5). The grey band shows the process noise which is modelled as a Gaussian distribution with $\sigma^2 = 0.3$.

where y_t is the vector of observed absolute accelerations after gravity compensation (CA). θ_t is a vector which represents the underlying process (the state) of the system. The observation vector is related to the process vector with the addition of Gaussian noise with variance V ($\sigma^2 = 0.2$). Similarly, the process vector, Ω, is defined as its preceding value with additional covariance ($\sigma^2 = 0.3$). The estimation of these variances is based on the calibration of the sensor under zero (non-gravitational) acceleration conditions. The recursive algorithm of *Zhang and Li* [1996] is then applied to compute the filtering distribution and its variance for each one of the observations. Finally, the variances are used to calculate probability intervals as shown in Figure 5.3c.

5.1.4.2 Logistic Regression Calculation of the Probability of Entrainment

The probability of entrainment is assessed using the derived signals for each individual run, to which a binary categorical variable was attributed with pre-entrainment and post-entrainment states (0 and 1, respectively). This allows the recorded accelerations to be grouped according to grain condition and for calculation of separate probability densities for each condition (Figure 5.4a). Note that, as explained previously, at the lower slopes the measured entrainments are from grain-top positions following initial displacement from saddle positions, whereas at higher slopes entrainment was from the saddle positions (Figure 5.5). The point of entrainment is shown in the derived signals as a sudden drop in the inertial acceleration, followed by high acceleration values due to impacts of the sensor with the flume bed downstream of the monitoring area (Figure 5.3c). In two cases of ambiguity (for slope 0.057) the time of entrainment was verified from video recordings.

To calculate the probability of entrainment a binomial model was fitted using logistic regression [*Hosmer et al.*, 2000] between the binary variable that corresponds to entrainment and the accelerations derived after the space-state filtering of the time-series. As a generalized linear model, logistic regression for binomial data is expressed with the linear predictor function:

$$logit = \left(E\left[\frac{Y_i}{n_i} \mid X_i \right] \right) = logit(p_i) = ln\left(\frac{p_i}{1-p_i} \right) = \beta X_i \tag{5.4}$$

where Y_i is the dependent binary variable with:

$$Y_i \sim B_{in}(n_i, p_i) \quad \text{for} \quad i = 1, ..., n \tag{5.5}$$

X_i being the vector of predictors and β being the vector of regression coefficients *Kay and Little* [1987].

In this case the model was reduced to one predictor variable, equal to the filtered acceleration values. As an optimisation process to estimate the probabilities p_i and the regression coefficients β, Maximum Likelihood Estimation was implemented coded in the R-statistical package for the default function glm [*Faraway*, 2005]. The values fitted by the above process are an explicit calculation of the probability of entrainment as a function of the recorded inertial acceleration. The threshold of entrainment is determined by the acceleration corresponding to 0.5 probability as shown in Figure 5.4b. The determination of the entrainment threshold as a probability of 0.5 is consistent with other applications of probabilistic entrainment criteria that utilize near bed turbulence measurements [*Papanicolaou et al.*, 2002]. The acceleration values corresponding to probabilities < 0.5 represent dynamic conditions that act in favour of the resistance of the particle to entrainment, whereas values corresponding to probabilities ≥ 0.5 represent dynamic conditions where the potential for entrainment is enhanced.

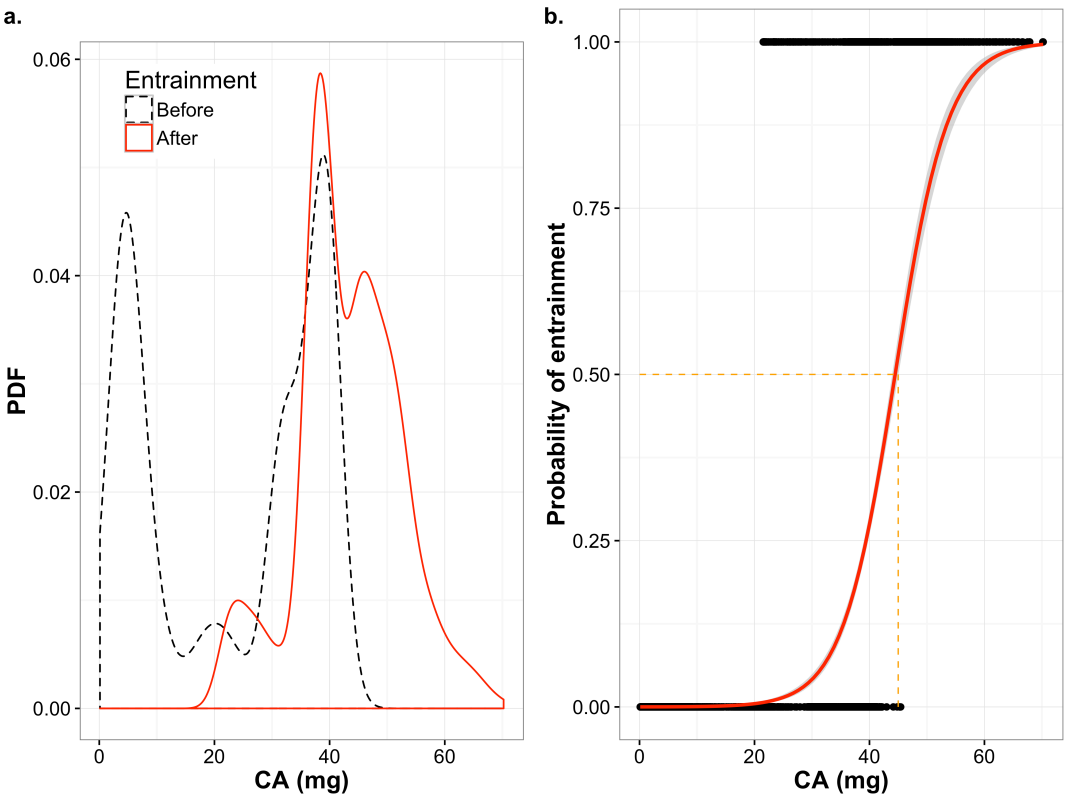

Figure 5.4: **Calculation of the probability of entrainment**. a. shows the classification of acceleration according to the pre- and post-entrainment conditions ($slope = 0.026$). The probability density of the post-entrainment accelerations shows that the grain is subject to greater forces than pre-entrainment which is consistent with the experimental procedure. b. shows the calculation of the probability of entrainment after the application of the logistic regression model (Equations 5 and 6). The orange-dotted line indicates the acceleration threshold of entrainment (44 mg at 0.5 probability). The acceleration value corresponding to 0.5 probability is interpreted as the acceleration where the dynamics start to act in favour of entrainment. The grey band indicates the 95% confidence bands of the logistic regression model.

5.2 Results

5.2.1 Absolute Inertial Accleration (CA) thresholds

The methods described above for the acceleration analysis were applied to data for all the slopes. Figure 5.5 shows the filtered acceleration signals and the fitted probabilities of entrainment: these results are summarised in Table 5.1.

As slope increases the discharge at which entrainment occurs is reduced (Figure 5.6). However, inertial accelerations recorded by the sensor show a more complex pattern (Figure 5.6b). For the lower slopes with final entrainment from grain top positions, there is considerable overlap between accelerations at entrainment with the higher (0.037) slope having the highest accelerations. The steeper slopes, with entrainment from saddle positions, also show considerable overlap but accelerations are significantly lower than for the lower slopes.

As a statistical evaluation for the derived binomial models (Figure 5.5b), the p-values for the signifi-

cance of the coefficients of the independent variable (acceleration, Table5.1) are given. Another relevant metric is the Walden test which is used for the evaluation of single predictor models, but also to evaluate competing models with different numbers of predictors. The p–value of the Walden test for the four fitted probability models was $< 1 \text{ x} 10^{-20}$ which increases our confidence regarding the significance of the derived models [*Montgomery and Runger*, 2010].

Measured inertial accelerations at the point of entrainment were of the order 50 mg (Figures 5.3 and 5.5). The acceleration of mean velocity as a result of the steady increase in discharge through each experiment is four orders of magnitude lower than these inertial accelerations at c.$2x10^{-2}$ mg, justifying the assumption of gradually varied flow that has no direct influence on entrainment forces.

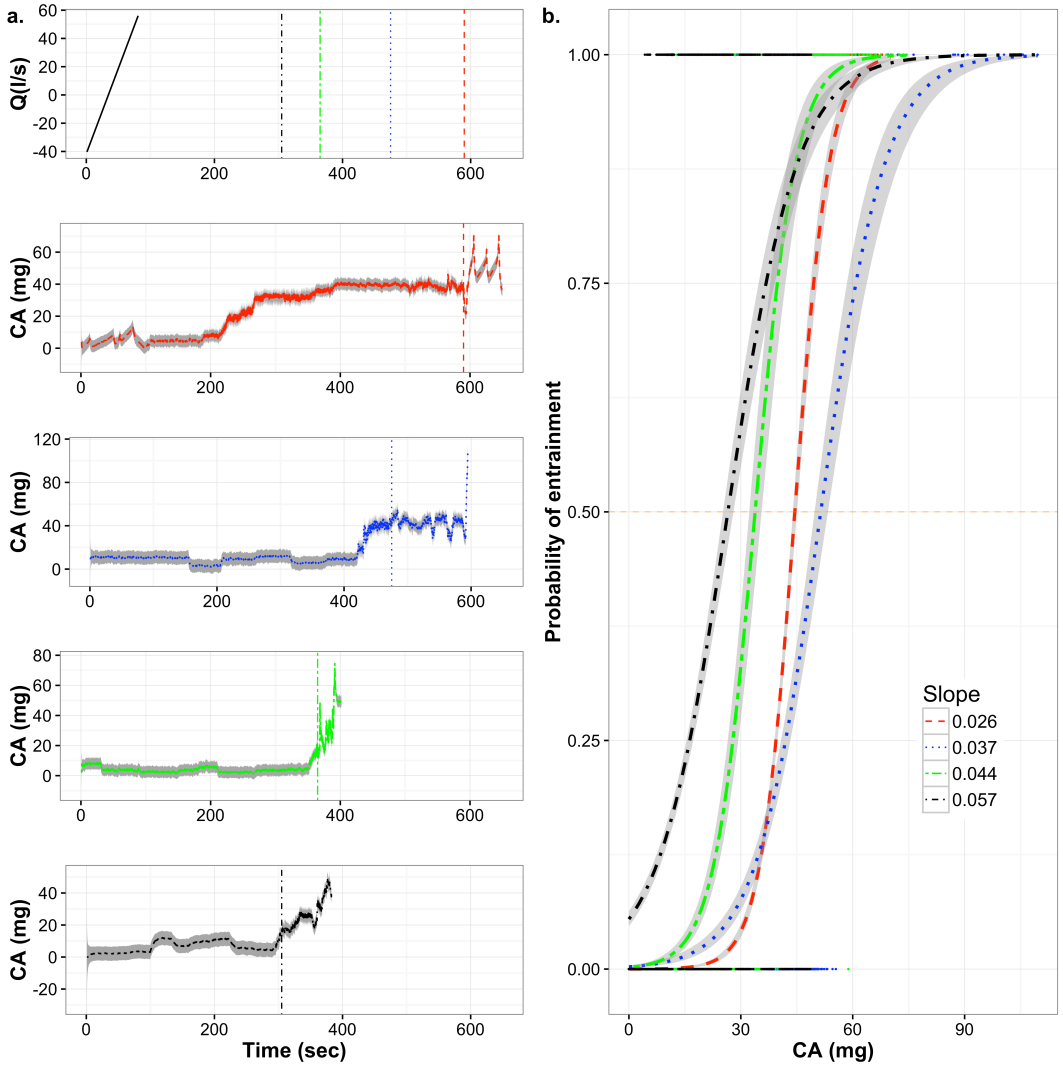

Figure 5.5: **Summary results**. a. total inertial acceleration and the thresholds of entrainment (vertical lines). The same thresholds are synchronised with the corresponding flow increase which is the same for all experiments (top diagram). The numbers out of the axes are bed slopes for each acceleration time-series. b. shows the calculation of the probability of entrainment for all slopes by logistic regression. Grey bands indicate the 95% confidence bands.

Table 5.1: Summary Results (CA and Discharge threshold)

Slope	Threshold acceleration (mg)	Threshold Discharge (l/s)	Type of position pre-entrainment	Significance of logistic regression model for the calculated probability
0.026	44	6.15	Grain–top	$< 2\ \text{x}10^{-16}$
0.037	51	4.3	Grain–top	$< 2\text{x}10^{-16}$
0.044	32	3.21	Saddle	$< 2\ \text{x}10^{-16}$
0.057	25	2.2	Saddle	$< 2\text{x}10^{-16}$

5.2.2 Comparison of Total Inertial Acceleration $PDFs$ with Velocity $PDFs$

Figure 5.6 shows how all the derived signals are synchronised over the same time domain. For the two lower slopes (0.026 and 0.037) the approximated acceleration thresholds (44 and 51 mg, respectively) were projected back to threshold discharges (6.15 and 4.3 l/s, respectively). The latter were used to separate the recorded flow velocities (Figure 5.2) to pre- and post-entrainment distributions the $PDFs$ of which were approximated by KDE and the bandwidth selection technique of *Sheather and Jones* [1991] (Chapter 4). Finally the OVL coefficient was calculated for both the velocity and total acceleration $PDFs$

The results in Figure 5.5 show that for both of the slopes the OVL coefficient for the acceleration $PDFs$ (0.36 for $slope = 0.026$ and 0.21 for $slope = 0.037$) is smaller than the $OVLs$ for the velocity $PDFs$ (0.44 for $slope = 0.026$, and 0.33 for $slope = 0.037$).

5.3 Summary

This chapter presents a new method to approximate the probability of entrainment for individual coarse particles based on inertial acceleration measurements. This became possible after prototyping a purpose specific IMU. The key steps of the method are:

1. Recording of inertial dynamics at an appropriate high frequency (inertial acceleration): in this initial study, data were recorded at 4 Hz for practical reasons and this has been shown to be adequate for laboratory conditions. For laboratory and field deployment, recording frequencies of over 50 Hz are required, although over-sampling should be avoided to ensure both efficiency and reliable interpretation of results.

2. Bayesian filtering of the derived signals (Kalman Filter): nine replicates of each entrainment experiment were conducted. Rather than analyse each separately, combining these into one sychronised data set allows robust interpretation and specification of statistical uncertainty in the results using an appropriate process model (Equation 5.3). This model illustrates both the inter-experiment variability and the trends in the data (Figures 5.3 and 5.5).

3. Categorical characterisation of the filtered signals for pre- and post-entrainment conditions: the individual data sets (e.g. Figure 5.3a) show pre-entrainment vibration increasing through time, entrainment, and post-entrainment oscillations. Categorising these data into pre- and post-entrainment accelerations allows the probability of entrainment to be considered as a function of increasing flow intensity (approximated here by discharge).

4. Logistic approximation of the relationship: After analysing inertial accelerations pre- and post-entrainment, logistic regression provides a way of statistically expressing a gradual increase in the probability of entrainment with increasing accelerations. This also provides confidence intervals (Figures 5.4 and 5.5) which clarify the differences in entrainment processes between different grain positions (saddle vs. grain top) and which also show considerable overlaps between data obtained at different slopes but for the same grain positions. These differences suggest that secondary effects, such as the orientation of initial grain movement, may be significant even for spherical grains.

5. Calculation of the probability of entrainment as a function of inertial acceleration from the conditional threshold probability ($p_i = 0.5$): the notion of entrainment as a gradational increase in probability of movement as flow intensity increases is well-established *Grass* [1970], but has been difficult to quantify for natural conditions. Extension of the proposed approach to natural particle shapes and positions will help to address this data requirement.

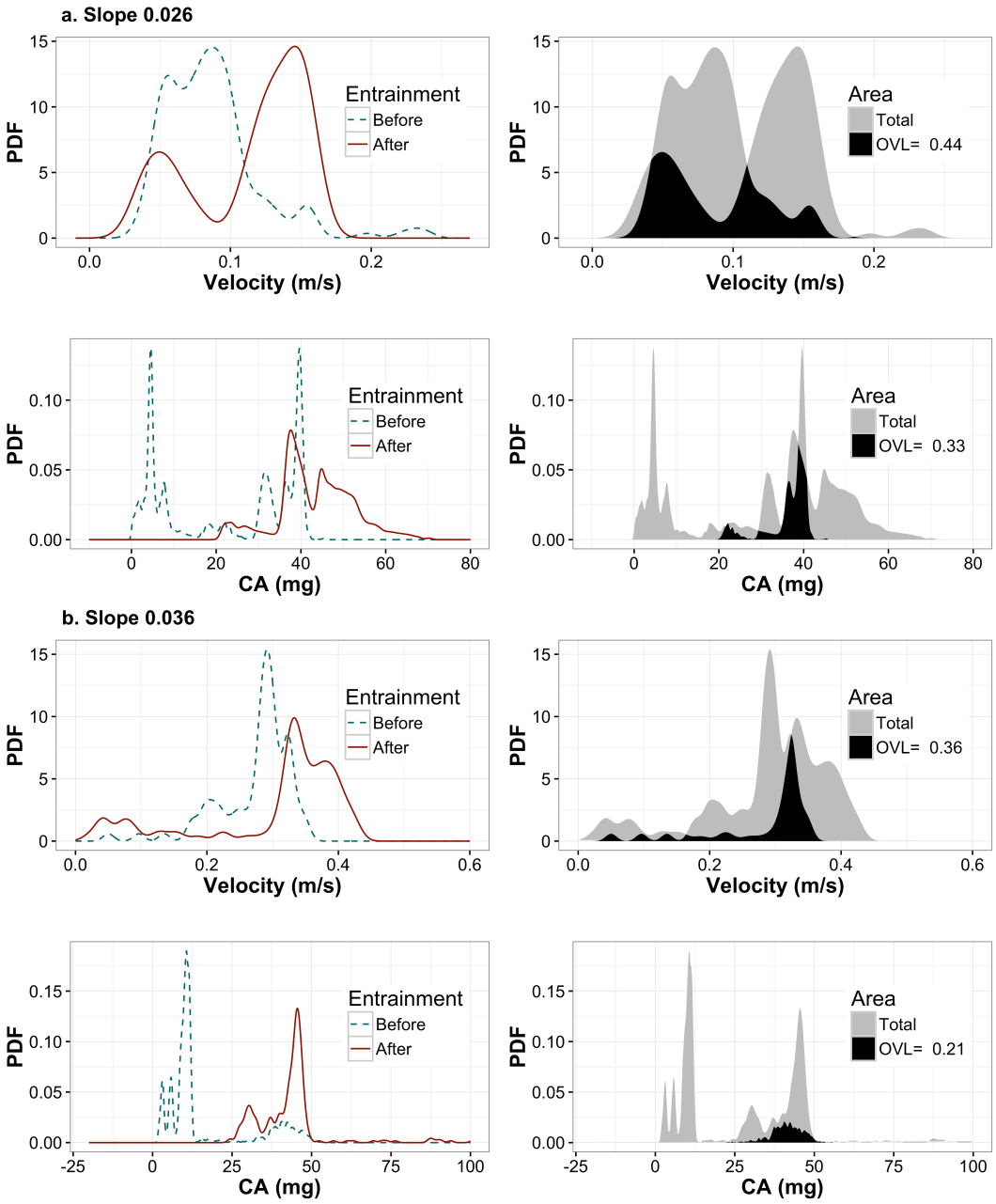

Figure 5.6: **Comparison of velocity and acceleration**. **Figures 5.6a** and **b** show pre- and post-entrainment *PDFs* for two slopes (0.026 and 0.037). Plots on the left side are smoothed PDFs, an the right hand plots show the areas of overlap used to calculate OVL values. The calculation of the OVL coefficient suggests that an incipient motion criterion based on inertial acceleration has the potential two improve prediction as the overlap is reduced at an order of 10% in both cases.

CHAPTER 6

EULERIAN-LAGRANGIAN MODEL FOR COARSE SEDIMENT TRANSPORT: APPLICATION II. 3D- ROTATIONAL CASE

This chapter contains material from the manuscript: Maniatis, G., T. Hoey, R. Hodge, M. Valyrakis and T. Dryrsdale (2016 in preparation for Journal of Geophysical Research: Earth Science): An Eulerian-Lagrangian definition of coarse sediment transport. II. Application

This chapter includes the application of the latest prototype sensors which are based on the Yei-chip (TSS-DL-HH-S sensor, see Chapter 3). The discussion on the error sources for commercially available, low-cost IMUs is extended with the inclusion of 3D-gyroscope measurements. As a result, the computational framework for error compensation and the analysis of the derived measurements are now relevant to the 3D unrestricted rotational motion described by the Eulerian-Lagrangian model of Chapter 4.

The error propagation for the 3D-accelerometer is demonstrated with a calibration experiment on randomly vibrating shaking table. The accelerometer signal is then analysed and corrected using a high-pass filtering integration method. Subsequently, two laboratory experiments are introduced: one relevant to the entrainment of coarse particles, and one to particle-bed impacts. The data-processing sequence is summarised from the individual runs and the gravity compensation (for the 3D case) to the aggregation of the signals, the derivation of statistically representative signals from a series of experiments and the double integration with the high-pass filtering corrections.

For the entrainment experiments, incipient motion is detected using the calculation of the total kinetic energy of the particle inertial frame (Chapter 4, Equation 4.10). This calculation is used to compare the discharge entrainment thresholds between a spherical and a ellipsoid-shaped sensor.

The analysis advances with the calculation of the 3D kinetic energy (in both Lagrangian and Eulerian frames) and the magnitude of 3D instantaneous displacement (Eulerian frame) during entrainment. The calculations are performed again for both the spherical and the ellipsoidal sensors.

The chapter closes with a presentation of the statistics from the particle-bed impact experiments: the kinetic energy exchange between the moving spherical sensor and the bed under flowing water and no

water (air) conditions.

6.1 Error accumulation in non-ideal IMUs

In the technical note of *Woodman* [2007], the non-linearities that occur during the sensing of forces, or rotations, are analysed in a context of control theory. However, the physical models for position and attitude tracking used correspond directly to the framework presented in Chapter 4. A high-level version of the basic model, described in Chapter 4, is presented again here, to enhance readability.

A 3D-strapdown accelerometer (an 3-axis accelerometer rigidly fixed and centred on the centre of a mass of a rigid moving body) will measure the proper acceleration, thus any external force plus the acceleration due to gravity (other fictitious forces are ignored). To decouple the forces, it is necessary to rotate the recorded accelerations to the Eulerian frame and subtract gravity:

$$a_E(t) = C(t)a_b(t) - g_E \tag{6.1}$$

which gives the linear acceleration (a_E) imposed from translational forces in Eulerian coordinates. g_E is the vector of gravity in the Eulerian frame ($g_E = [0,0,9.81]^T$ m/sec^2). $a_b(t) = [a_{bx}(t), a_{by}(t), a_{bz}(t)]^T$ is the vector of body frame accelerations (the 3D accelerometer measurements).

$C(t)$ (Chapter 4 Equation 4.22) is the matrix that performs the transformation from Lagrangian to Eulerian frame (and *vice versa* if transposed). Here, this matrix is treated as a Direction Cosine Matrix (DCM) populated using quaternion components from a quaternion q in the form of:

$$q = \begin{bmatrix} q_s \\ q_x \\ q_y \\ q_z \end{bmatrix} \tag{6.2}$$

The transition unit quaternion at each time-step is defined as:

$$\widetilde{q} = \begin{bmatrix} \cos\dfrac{\|\omega\|\delta t}{2}, \sin\dfrac{\|\omega\|\delta t}{2}\dfrac{\omega}{\|\omega\|} \end{bmatrix} \tag{6.3}$$

where ω is the instantaneous angular velocity vector in $3D$ (the 3D gyroscope measurements). The transition quaterinion has to be multiplied with the quaternion of the previous time-step using quaternion algebra [*Whitmore*, 2000; *Zhao and van Wachem*, 2013] in order to derive a quaternion in the form of Equation 6.2 and populate the rotation matrix $C(t)$ of Equation 6.1.

Finally, to derive velocities and positions a double integration is performed:

$$v_E(t) = v_E(0) + \int_0^t a_E(t)\,dt \tag{6.4}$$

$$s_E(t) = s_E(0) + \int_0^t v_E(t)\,dt \tag{6.5}$$

where $v_E(t)$ and $s_E(t)$ are the velocity and the position in the Eulerian frame, respectively.

In solving equations 6.1 to 6.5, data from the accelerometer and gyroscope are used. During this sequence of calculations, there is accumulation of errors from two sources. Firstly, both the accelerometer and the gyroscope exhibit some type of non-linearity which, no-matter how accurately modelled, will

inherit a random component [*Woodman*, 2007]. Secondly, errors from both sensors (6 inputs in total) are amplified during multiplication (Equations 6.1 to 6.3) and then integration (6.4 to 6.5). As a result, any non-linearities/errors from both of these sensors will be: a) multiplied; and, b) introduced in a double integration series, thus amplified rapidly.

The magnitude of derived positional errors can be assessed from the technical specifications provided with IMU navigation systems (e.g. *Novatel* [2010], *VectorNav* [2016]). The typical error for horizontal position from a high-end IMU of military specifications is calculated at the order of 1.6 km if left un-aided for 1 hour (non corrected by an external system, *VectorNav* [2016]). For the sensors that can, cost-wise, be deployed in large numbers (e.g. tracking many stones in a river), the same error is at an order of 190 km after 1 hour of un-aided position tracking. The latter are classified as industrial IMUs.

The magnitude of this error means that industrial IMUs can be used as orientation sensors (e.g. AHRS algorithms, e.g *Pourtakdoust and Ghanbarpour Asl* [2007]), or as complementary sensors to increase the frequency of position from other systems (GPS-IMU coupling, e.g *Gebre-Egziabher et al.* [1998]). Finally, there are special cases where specific assumptions of the motion of the rigid body can be made, which simplify both the motion and the measurement models (e.g. pedestrian tracking, *Foxlin* [2005]). However, those assumptions are not relevant to the free motion of a stone in a river or any other natural stochastic motion.

Since free non-aided tracking is not possible with the available IMU sensors, the goal here is to present a data analysis that can lead to a robust statistical treatment of the Eulerian-Lagrangian model presented in Chapter 4, and interpret the results in the context of fluvial sediment transport.

The data collected by the sensors can be considered as signals that can be analysed by Fourier analysis [*Grattan-Guinness et al.*, 1972; *Grafakos*, 2004]. The signals can be decomposed into elements due to: (a) constant acceleration due to gravity; (b) varying non-gravitational forces; and, (c) high frequency random noise noise (e.g Direct Current (DC) noise) from the electronic processing of the signal within the IMU circuits. The aim of the analysis is to isolate the non-gravitational forces.

It is possible to argue, by comparing the three sinusoids, that the longer cycle is the gravitational because the magnitude of the source (gravity) is constant. The argument relies on the fact that the non-gravitational forces and the noise (practically random) from the sensor are likely to change much more rapidly than the acceleration of gravity.

Consequently, a high-pass filter (a filter that leaves only the high-frequency component of the signal) will eliminate the gravitational effect and will highlight the accelerations that are connected to velocity changes and displacements for the moving body. High-pass filters have been used to accurately integrate accelerometer measurements [*Geraldo et al.*, 2001; *Ribeiro et al.*, 2003; *Slifka*, 2004; *Arraigada and Partl*, 2006] after calibration. However, high-pass filtering leads to the loss of the local mean of the original signal, so this approach has only been used to detect short term displacements from vibrational (or oscillatory) accelerations.

Despite loss of the local mean, the amplitude and magnitude of the source signal are both represented in the filtered signal. Without the local mean though, the filtered signal does not contain any information regarding the direction of the imposed vector. As a result, it is possible to record the instantaneous magnitude changes on each accelerometer axis but it is not possible to reconstruct the direction of the acceleration vector if the movement is not otherwise constrained.

A further consequence is that, when the second integration is performed to yield positional information, it is possible to calculate instantaneous movements but these displacements cannot reconstruct a full

trajectory since direction of the position vector is unknown. It is important to note that this is the only double integration framework for un-aided accelerometer measurements that yields an accurate order of magnitude for displacements.

Taking into account the above limitations, the scope in this chapter is to define a computational framework for analysing data from low-cost IMU deployed for the monitoring of sediments in fluvial environments. This framework is based on the physical model defined in Chapter 4 and is here statistically treated to account for the realistic capabilities of the non-ideal, commercially available low-cost IMUs.

In this computational framework, Kalman, or in general Bayesian filters, become useful. The state-space model of Equation 5.3 and the recursive algorithm of *Zhang and Li* [1996] remain in the calculations for the 3D unconstrained motion.

Notably, Bayesian filters are extensively used in IMU signal processing for attitude estimation (e.g. *Sabatini* [2006]) and GPS-IMU integration (e.g. *Zhao* [2016]). Here direct Bayesian attitude estimation is not performed (due to the restrictions from the high-pass filtering) and the process presented in Chapter 5 is implemented for each one of the axes of the deployed sensors (3 accelerometer and 3 gyroscope measurements).

In general the data processing includes all the techniques discussed so far:

- For each accelerometer-gyroscope signal gravity compensation is performed using the Eulerian-Lagrangian model of Equations 6.1 to 6.3.
- To extract a statistically representative signal from a series of experiments, the Kalman filter defined by Equation 5.3 is implemented, after aggregating the individual runs.
- To correct the errors from the gravity compensation and their propagation in the double integration process (Equations 6.4 and 6.5) high pass filtering techniques are used.

The result of these calculation procedures is the derivation of 3D acceleration, 3D velocity, and 3D displacment signals which can be used to estimate key components of the Eulerian-Lagrangian model such as kinetic energies and the magnitude of short term displacements. Also, because the orientation of the sensor is known, the same kinetics can be estimated in both the Lagrangian and the Eulerian reference frames.

6.2 Methods

6.2.1 Calibration setting

Before the calibration experiment, the whole IMU was calibrated using the routine proposed by the manufacturer. A calibration of the IMU in the manufacturers casing is necessary for identifying the parameters of the high-pass and Kalman filters as explained in the analysis of the filtering process.

The TSS-DL-HH-S sensor chip was rigidly attached on a horizontal shaking table with the the x-axis of the sensor being parallel to the direction of the table-motion and and the z-axis being parallel to the direction of gravity. The procedure was to record a 30 seconds sequence consisting of 10 seconds of no motion, 10 seconds of random displacements and 10 seconds of no-motion. Sampling was at 50 Hz and the table has a maximum displacement of 0.025 m.

The sensor moved in a straight line with amplitude 50 mm. Figure 6.1 combines an illustration of the experimental setting with the original signal and the result of the double integration before any filtering.

The amplification of error is the result integrating two noise components that are coupled, as can be seen in Figure 6.1b). The components are:

- A static component which is recorded as non-zero acceleration during the no-motion periods. The mean of the x-axis for the non-motion periods is -1.3 ± 3.9 m/s^2
- Non-linearity in the gravity measurements since the mean acceleration during the non-motion periods should be approximately 0 (given that the z-axis had a recorded a mean of 9.2 ± 4.5 m/s^2 through the whole experiment which is close to the acceleration due to gravity = 9.81 m/s^2).

The error of horizontal displacement without any corrections reaches an order of 500 m for the 30 seconds monitoring period. Removing the static components in a form of constant bias reduces the integration error by an order of magnitude (Figure 6.1 b and c, displacement error 80 m). This correction is not sufficient to keep the measurement in scale indicating that the non-linearity of the gravity measurement acts as a non-constant bias (which can also explain the magnitude of the error before any correction is applied).

6.2.2 Zero-reference and FFT - High pass filtering

6.2.2.1 Zero-reference level

The sensor's static noise can be removed in a variety of ways. A simple method [Freescale^{TM} with the reference AN3397, *Seifert and Camacho* [2007]] is to define a minimum absolute acceleration value for all axes, setting values below this threshold to 0. For this application the zero-reference value was set at ± 6 m/s^2 which is the average maximum non-gravitational acceleration recorded on all axes during a 20 minutes non-motion period.

6.2.2.2 FFT - High pass filtering

The next step will be to reduce the non-linearity in the gravity measurement which, for a rotating sensor, is the equivalent of correcting the gravity compensation for a non-ideal IMU (Equation 6.1). The signal is filtered in the frequency domain as this reduces the antialiasing of the signal to a greater degree than other techniques [*Ribeiro et al.*, 2003; *Slifka*, 2004].

The Fourier transform of a signal $g(t)$ is:

$$\mathscr{F}\{g(t)\} = G(f) = \int_{-\infty}^{\infty} g(t) e^{-2\pi i f t} dt \tag{6.6}$$

The inverse Fourier transform, returns the signal from the frequency to the time domain:

$$\mathscr{F}^{-1}\{G(f)\} = \int_{-\infty}^{\infty} G(f) e^{-2\pi i f t} df = g(t) \tag{6.7}$$

In applied signal processing, a version of the Fast Fourier Transform algorithm is used [*Nussbaumer*, 2012] to move from the time domain to frequency and back. Here the FFT algorithm implemented in *scipy.fftpack* python package is used [*Jones et al.*, 2001–].

For high-pass filtering it is necessary to decide the cutoff frequency (which is the lowest frequency that will remain in the spectrum) and then either substitute all the lower frequencies with one selected higher frequency (e.g. *Ribeiro et al.* [2003]) or simply zero the low frequencies and leave the spectrum with only

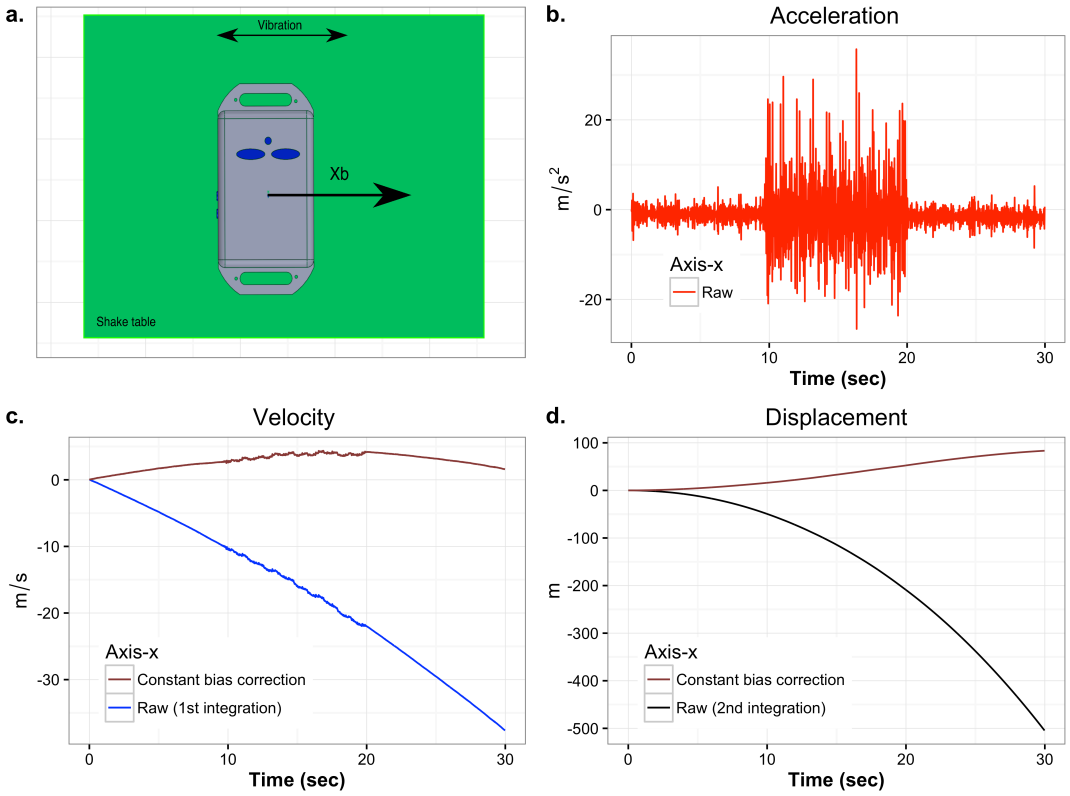

Figure 6.1: **The Calibration process.** a. is a schematic of the experimental setting, the x-axis of the sensor is aligned with the motion direction of the shaking table. The table is horizontal with the gravity parallel to the z-axis of the axis hence no gravity is recorded in the x-axis. b. shows the recorded acceleration on the x-axis. The experiment was a sequence of no-motion, motion, no-motion periods, each period lasting for 10 seconds. The correct measurement for the no-motion periods is 0, so the recorded values are indicative of the static noise of the sensor. c. and d. are the results of integrating the series of b. for velocities and displacements, respectively. The errors accumulate rapidly to the point of recoding an error of 500 m in horizontal displacements if the accelerations are integrated without correction. Removing the static noise as a constant bias in the acceleration measurement (Figures b and c) reduces the error significantly (displacement error 80 m) but not enough to keep the measurements in scale.

the frequencies that are ≥ the cutoff frequency. For simplicity (and because the selection of frequencies is associated with specific assumptions about the motion of the accelerometer) I follow the second technique. Also, since the spectra are symmetric, the focus is on the real part of the transform only.

To proceed to the Digital Double Integration (*DDI*) it is necessary to apply the high pass filter to the acceleration signal initially and then once after each integration step [*Slifka*, 2004]. Overall the DDI series is summarised in FIgure 6.2. The simplified algorithm for FFT-Hi-Pass filtering of a signal s can be summarised as:

```
X=Re(fft(s))
if X < cuttoff
X=0
else
X=X
filtered=iRe(fft(X))
```

To proceed to the DDI (*Digital Double Integration*) it is necessary to apply the high pass filter to the acceleration signal initially and then once after each integration step [*Slifka*, 2004]. Overall the in DDI series is summarised in diagram 6.2.

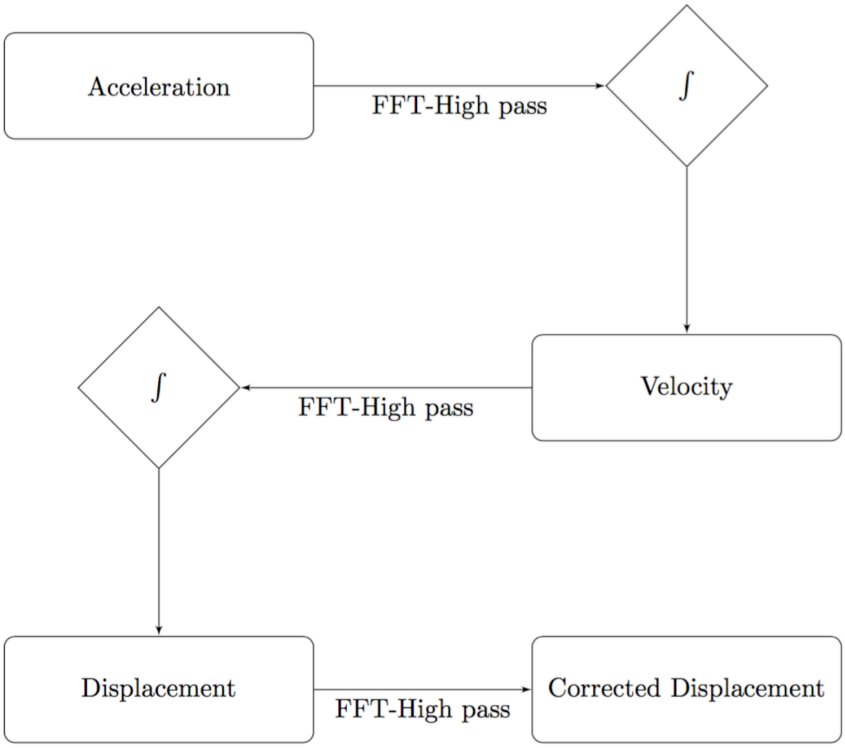

Figure 6.2: Flow diagram of the FFT-DDI method for retrieving displacements from acceleration measurements.

For the x-axis of the sensor, the cutoff frequency that keeps the displacements in scale (maximum displacement= 25 mm) was 2 Hz. The results of the correction for the x-axis are shown in Figure 6.3. The same experiment was performed for the y-axis and the z-axis of the IMU. The cutoff frequencies are different different for each axis (y-axis at 1.7 Hz and z-axis at 2.2 Hz) since the error factors (e.g. misalignments during construction, biases in initial calibration etc.) do not affect the accelerometer uniformly.

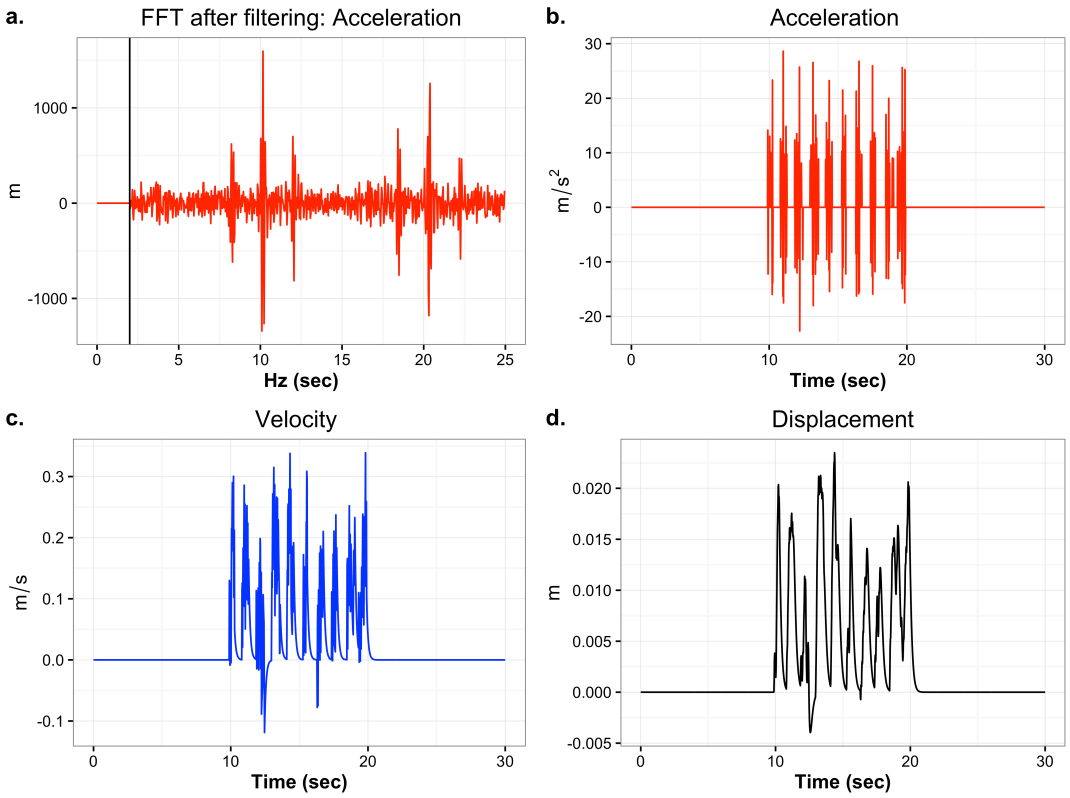

Figure 6.3: **FFT - Hi Pass and Double integration.** a. demonstrates the concept of the FFT-High pass for the acceleration (x-axis). The vertical line shows the cutoff frequency at 2 Hz. b. shows the corrected acceleration on the x-axis. The experimental sequence (no-motion, motion, no-motion) is clear and no static noise is recorded. c. and d. are the results of integrating the series of Figure b. using the high-pass filters for velocities and displacements, respectively. The cutoff frequency of 2 Hz was applied to all the filters to keep the measurements in scale (max displacement = 0.025 m).

6.2.3 Fluvial experiments

6.2.3.1 Sensor Assemblies and Experimental Regime

Two enclosures where constructed using the CAM techniques described in Chapter 3. The first one is a 90 mm diameter sphere, mass 1.019 kg, made of solid aluminium within which the cavity for the sensor was cut around the centre of the mass of the whole assembly. Aluminium was used to approximate the density of sediments (2650 kg/m^3). The second enclosure is an ellipsoid (with axes 100, 70 and 30 mm), weighing 0.942 kg. For the ellipsoid the cavity was designed to ensure that the sensor axes align with the principal axes of the enclosure. The experiments took place at the University of Glasgow in an Armfield flume of 7 m effective length and 0.9 m internal width.

6.2.3.2 Entrainment Experiments

A bed of plastic hemispheres was constructed, following the CAM process presented in Chapter 3. The hemispheres were scaled to the diameter of the spherical sensor ($D = 90$ mm) and the bed was coated with 3 mm sand to increase roughness. All the experiments took place under a constant slope, S, of 0.02. For

the first series of experiments, the spherical particle was placed onto a saddle position (on the centre-line of the flume) in the artificial bed and positioned so that the sensor axes were aligned with the horizontal reference frame (which is the Eulerian fixed frame for all the entrainment experiments). This alignment produced x- and y-axis accelerations with mean 0 ± 6 m/s^2, and z-axis acceleration mean of 9.7 ± 6 m/s^2. $\pm 6 m/s^2$ is the noise threshold established during the calibration process. A steady discharge increase with a rate of 0.028 l/s was imposed until the particle was entrained.

The same experimental protocol was followed for the ellipsoid-shaped enclosure, differing only in the initial alignment of the particle. The initial position of the ellipsoidal sensor was only controlled by aligning the x- and z-axes of the pebble parallel to the flume centre line and orthogonal to the sloping bed, respectively (Figure 6.4a).

Twelve entrainment experiments were performed for each enclosure shape giving a total of 24 entrainment experimental runs. The sensor sampling frequency was 50 Hz. Figure 6.4 describes the experimental setup and one experimental run using the spherical sensor. Gyroscope signals are not post-filtered for individual runs, as the signal is filtered on-board [*YEI*, 2014] resulting in a signal that is much less noisy than that from the accelerometer.

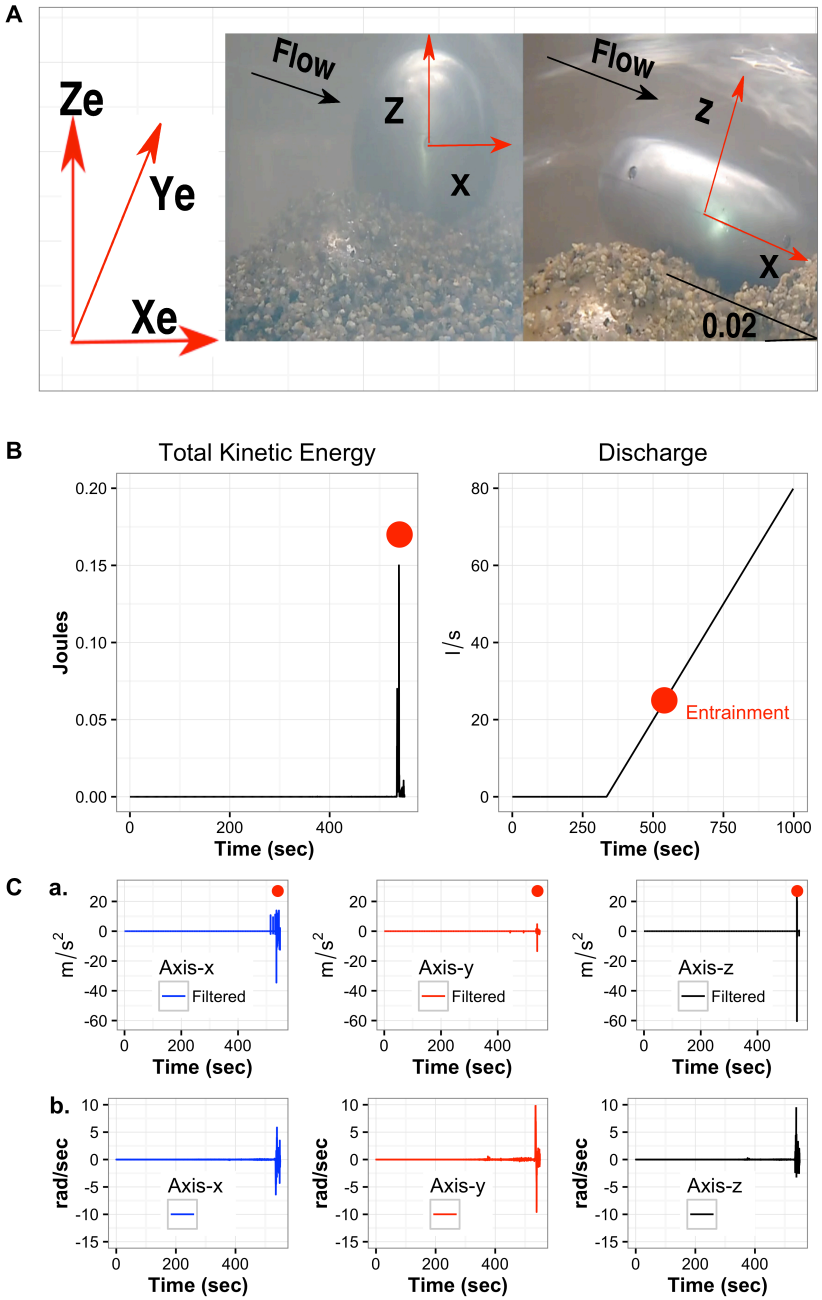

Figure 6.4: **Entrainment Experiments (presentation).** A. Initial alignments for the spherical and the ellipsoid-shaped enclosure. The spherical sensor is aligned to the Eulerian frame (x_e, y_e, z_e) while the ellispoid enclosure is not. B. (left) Total kinetic energy calculation for an entrainment series (sphere, one run). B. (right) Discharge increase during the entrainment experiments. The entrainment point is highlighted with the red dot, relating to the diagrams that present dynamics. C. a. 3D acceleration for one entrainment experiment (sphere). The series have been compensated for gravity and noise (window and FFT-High pass). C. b. 3D angular velocity for one entrainment experiment (sphere). The signal is not post-filtered for the individual runs.

Data processing for particle entrainment: body frame calculations. The analysis of the sensor data collected during entrainment is designed to provide measurements of particle velocity, energy and positional changes during entrainment. For each particle shape, data from all 12 runs was synchronised in terms of discharge, and the combined accelerometer and angular velocity data sets (data from 3 axes for each) sets were statistically analysed.

The analysis follows the process described in Chapter 5. For each axis the signal S is synchronised and aggregated in the form of Equation 5.2 thus:

$$S_t = \{\{S_1,...,S_k\}_{t_0}, \quad ..., \quad \{S_1,...,S_k\}_{t_n}\} \tag{6.8}$$

where k is the number of repetitions of the experiment (12 for the spherical and 12 for the pebble shaped exclosure in this case). The second step is to express the aggregated signal as the DLM of Equation 5.3.

Having generated the DLM, Kalman filtering of the aggregated signal can be performed. The variances V and Ω where set as 0.06 for the accelerometer (absolute maximum value recorded in the no-movement period after gravity and noise compensation). For the gyroscope the same values were set to 0.008. A demonstration of the estimated signal from the x-axis of the spherical sensor from all the 12 repetitions for the spherical sensor is shown in Figure 6.5. To ensure that entrainment is fully represented, signals were truncated 0.5 seconds after the moment of entrainment. Examples of individual entrainment events are shown in Figures 6.4 and 7.1 .

As noted above, after applying the initial high-pass filter the resultant acceleration signal is able to provide acceleration magnitudes but not their directions. On the contrary, angular velocities are applied on the body axis of the sensor consistently and the estimations from the gyroscope axes were used for the derivation of the quaternion calculations with their sign. For the kinetic energy calculations below, the sign is suppressed. After the estimation from the Kalman filter, each acceleration signal is passed to the simplified FFT-DDI algorithm to derive instantaneous linear velocities in the body frame. By combining the linear velocities with the Kalman estimated measurement for the angular velocities, the kinetic energy for each axis of the body frame is calculated as:

$$KE_{bf,axis} = \frac{1}{2} m v_{bf,axis}^2 + \frac{1}{2} I_{bf,axis} \omega_{axis}^2 \tag{6.9}$$

where v_{axis} is the calculated linear velocity for each axis , ω_{axis} is the estimated angular velocity for each axis, m is the mass of the enclosure, and I_{axis} is moment of inertia along each axis. For the spherical sensor the moment of inertia is uniform and:

$$Ix_{sphere} = Iy_{sphere} = Iz_{sphere} = \frac{2}{5} m R^2 = 0.00085 \quad kg \cdot m^2 \tag{6.10}$$

with R being the radius of the sensor = 45 mm.

For the ellipsoidal enclosure the moment of inertia per axis was calculated numerically using Solidworks^{TM} [*Système*, 2016]. The principal components of inertia, for the ellipsoid-shaped sensor are:

$$[Ix_{pebble}, Iy_{pebble}, Iz_{pebble}] = [0.00057, 0.00060, 0.00094] \quad kg \cdot m^2 \tag{6.11}$$

The non-principal components of inertia are sufficiently small that they can be ignored (calculated as approximately 10^{-8} kg m^2). To calculate the total Kinetic energy the components of kinetic energy for each axis were summed:

$$KE_{bf,total} = Kx_{bf} + Ky_{bf} + Kz_{bf} \tag{6.12}$$

The translational kinetic energy in the body frame, the kinetic energy generated from linear velocities only, is also used and is calculated as:

$$KE_{bf,trans} = \frac{1}{2}mv_{bf,x}^2 + \frac{1}{2}mv_{bf,y}^2 + \frac{1}{2}mv_{bf,z}^2 \tag{6.13}$$

These calculations of body frame dynamics require an inverse rotation (from Eulerian to Lagrangian) to that described by Equation 6.1. An algorithmic summary of the body frame calculations is in Appendix C.1.

Data processing for entrainment series: Eulerian frame calculations. After completing the body frame calculations there are two different measurements that are relevant to the Eulerian frame of reference:

- A 3D set of linear velocities in the body frame.
- A quaternion matrix representing the relevant orientation of the sensor axes against the axes of the Eulerian frame (Tbi, AppendixC.1).

It is possible to recover part of the directional information lost during the high-pass filtering by rotating the body frame axes to the Eulerian frame using quaternion matrix. For velocities:

$$\begin{bmatrix} v_{E,z} \\ v_{E,y} \\ v_{E,x} \end{bmatrix} = Tbi^T * \begin{bmatrix} v_{bf,z} \\ v_{bf,y} \\ v_{bf,x} \end{bmatrix} \tag{6.14}$$

where $v_{E,z}, v_{E,y}, v_{E,z}$ are the body frame velocity axes components in the Eulerian coordinates. In practice the rotated FFT-DDI filtered velocity components can only be used to estimate the velocity magnitude components in the Eulerian frame. The translational kinetic energy in the Eulerian frame can be calculated as:

$$KE_{E,trans} = \frac{1}{2}mv_{E,x}^2 + \frac{1}{2}mv_{E,y}^2 + \frac{1}{2}mv_{E,z}^2 \tag{6.15}$$

Finally, the Eulerian linear velocities of Equation 6.14, can be integrated to retrieve instantaneous displacement components in the Eulerian frame. To keep the calculation in scale it is again necessary to apply a high pass filter (Section 6.2.2). The calculated displacements serve as an approximation of the magnitude of the vector components in the Eulerian frame and they do not represent the ground movement of the sensor. The calculations in the Eulerian frame are summarised in Appendix C.2.

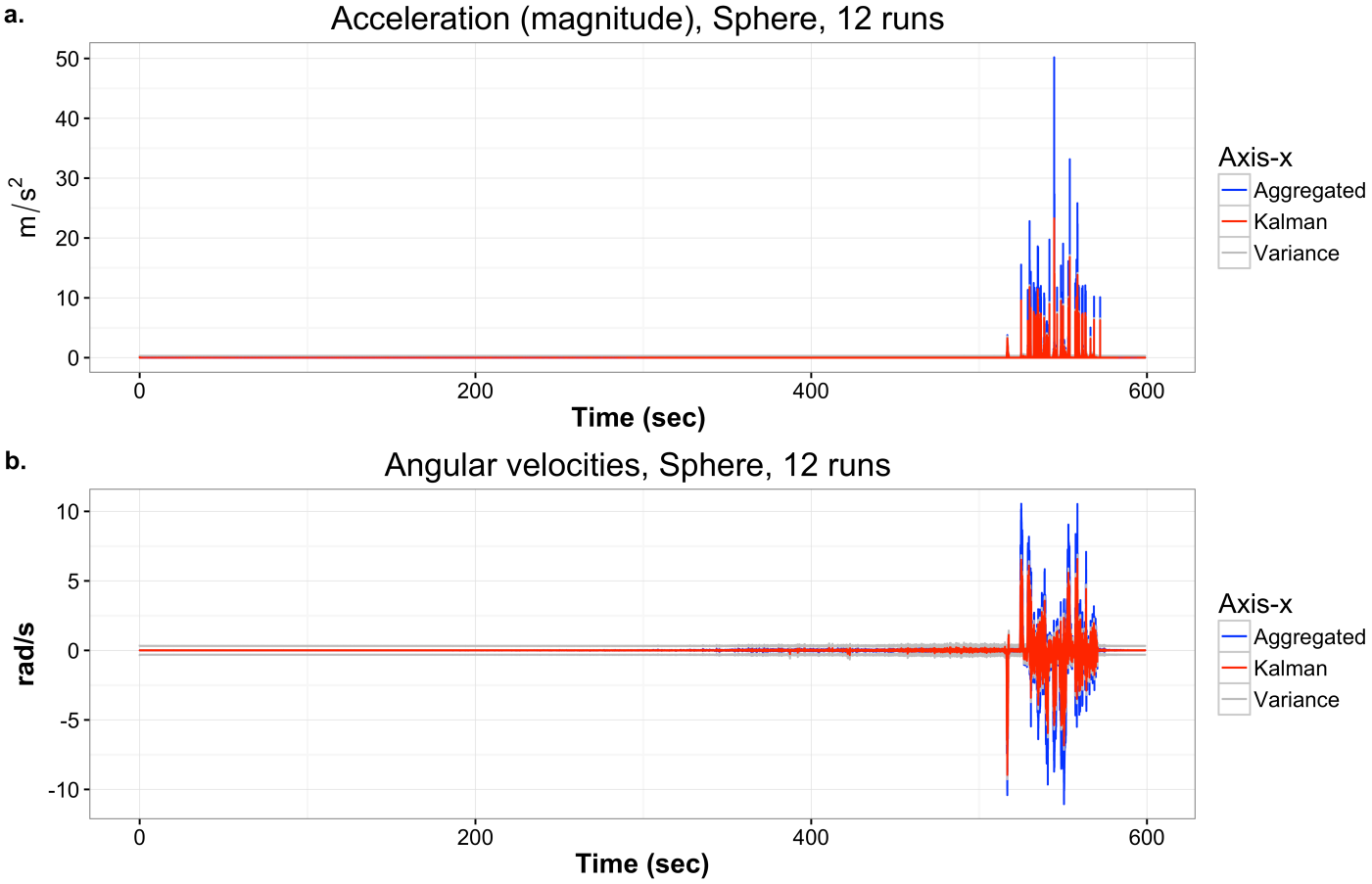

Figure 6.5: **Kalman filtering from aggregated signal.** a. Magnitude of x- axis acceleration values of the body (sensor) frame. The corrected signal (after gravity and noise compensation) from 12 experiments was aggregated and then filtered using a univariate Kalman filter. Observation and process covariances (V and Ω) were set to 0.06). b. Angular velocities for the x-axis of the body frame. The Kalman processing is identical to that for the acceleration data. V and Ω were set to 0.008.

6.2.3.3 Bed impact experiments

To measure impact forces generated by the spherical particle, a 130 mm wide PVC channel was fixed parallel to the bed at a distance above the bed equal to the flow depth at the measured entrainment threshold (0.1 ± 0.05 m). With a flow of 30 l/s, the sphere was released 0.6 m along the channel upstream of the entry point. The hydrodynamics for these conditions are summarised in Appendix A.The initial impact and any immediate consequential motion were recorded by the sensors. The process was repeated 20 times as described and 20 without any water in the flume for comparison. Figure 6.6, demonstrates the experimental set-up and an example of the results.

Data processing for bed impact experiments The forces generated during impact, which consequently affect bed erosion or mobilise other grains, depend on the instantaneous accelerations and angular velocities recorded by the particle. The three components of acceleration, integrated using $dt = 1/50$ s, were used in Equation 6.9 with the angular velocities. The total kinetic energy during impact was calculated from Equation 6.12.

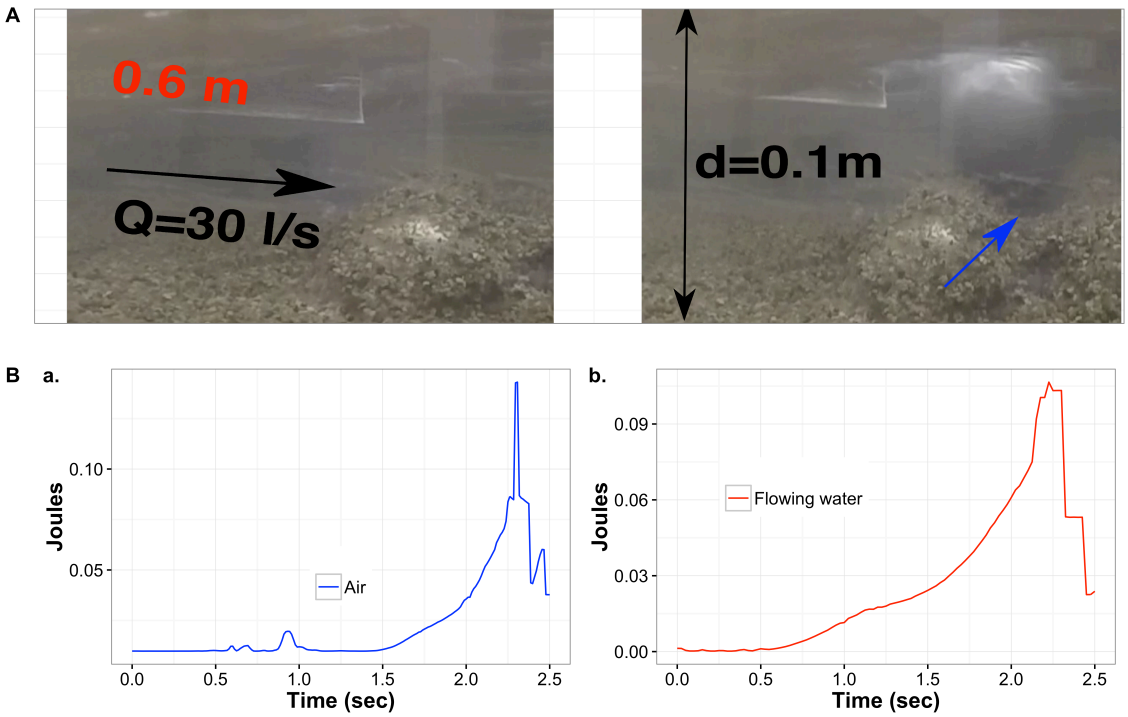

Figure 6.6: **Deposition-impact experiments.** A. Experimental regime for impact experiments. A rolling bar was stabilised in the flume at entrainment threshold depth (0.1 ± 0.05 m), entrainment threshold discharge (30 l/s) and parallel to the bed ($slope = 0.02$). The spherical sensor was let to roll free for 0.6 m along a fixed channel before entering the monitoring areas and impacting on the bed. B. The experiments were conducted with and without flowing water for control. The kinetic energy exchange with the bed is calculated for the instant of the impact (peak in the diagrams).

6.3 Results

Results from both entrainment and impact experiments are presented here. In both cases, the focus is on the short period of time (< 2 s) around the critical event, entrainment or impact. This is the critical time period for observing the forces generated during these events, and consequently the magnitude of displacements reported (Figure 6.9) is small. Analysis of videos of the experiments show that the spherical particle moved 0.16 ± 0.008 m in the first 2 seconds after entrainment, and the ellipsoidal particle moved 0.14 ± 0.03 m in the same time.

6.3.1 Total Kinetic Energy as an Entrainment Criterion

The total kinetic energy of the particle can be used to define an incipient motion criterion (Chapter 4). Figure 6.7, shows the *PDF* of the total kinetic energy calculated after processing the data in the body frame of both the spherical and the ellipsoidal enclosures (Equations 6.9 to 6.12). Only kinetic energy values > 0.003 Joules are shown, removing values recorded until the flow approached the entrainment threshold. This removes the low values associated with the various sources of noise in the data, but the magnitudes of total kinetic energy close to entrainment are such that it can provide an unambiguous entrainment criterion.

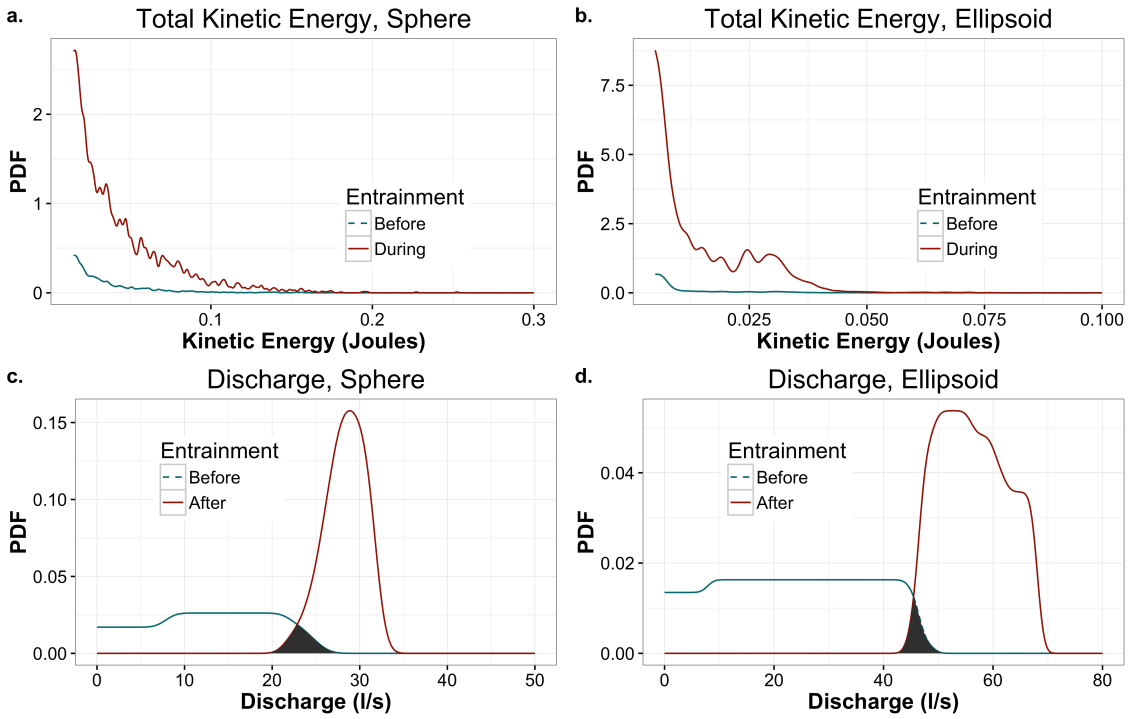

Figure 6.7: **Entrainment Threshold.** a. PDF for the total kinetic energy calculated in the body frame. The spherical and the ellipsoid-shaped sensor exhibit a comparable total kinetic energy energy during entrainment in range from 0 to 0.1 Joules. The kinetic energy before entrainment is negligible, suggesting the use of total kinetic energy as exact entrainment criterion. b. Discharge thresholds for entrainment. The spherical sensor entrained at discharges of 24.8 ± 1.8 l/s. The same threshold for the ellipsoidal sensor was 45.2 ± 2.2 l/s. Thresholds are presented as an overlay of before and after entrainment discharges (shaded area).

6.3.2 3D-energy in Eulerian and Lagrangian frames

The energy component that can be used for cross comparison between the two frames of reference is the translational component of energy ($K_{trans} = \frac{1}{2}mv^2$, where v is the linear velocity). Figure 6.8 shows the comparison between the translational kinetic energy for each axis in the Lagrangian and Eulerian frames. A bias along the z-axis of the particle fixed Lagrangian frame is observed, suggesting a sensitivity in the uplift forces (for the spherical particle the frames are initially aligned). However, during the entrainment the energy in the Eulerian frame is almost uniform and the same dynamics have approximately equal probability of occurring along all the orthogonal axes of the frame.

In contrast with the sphere, the translational kinetic energy distributions for the ellipsoid show a strong bias along the body z-axis direction (normal to the flume bed), suggesting that this shape is more sensitive to the uplift component of the flow forces. The shape of the sensor controls significantly the distribution of enerty in the Eulerian frame, during the instantaneous rotation, where the translational energy is expended mainly along the x-axis of the frame. The comparison between the Lagrangian and the Eulerian distributions suggests a x-z plane rotation during the entrainment for the majority of the experiments. This is confirmed by video analysis since from the 12 repetitions 9 were typical examples of rolling around the y-axis of the pebble.

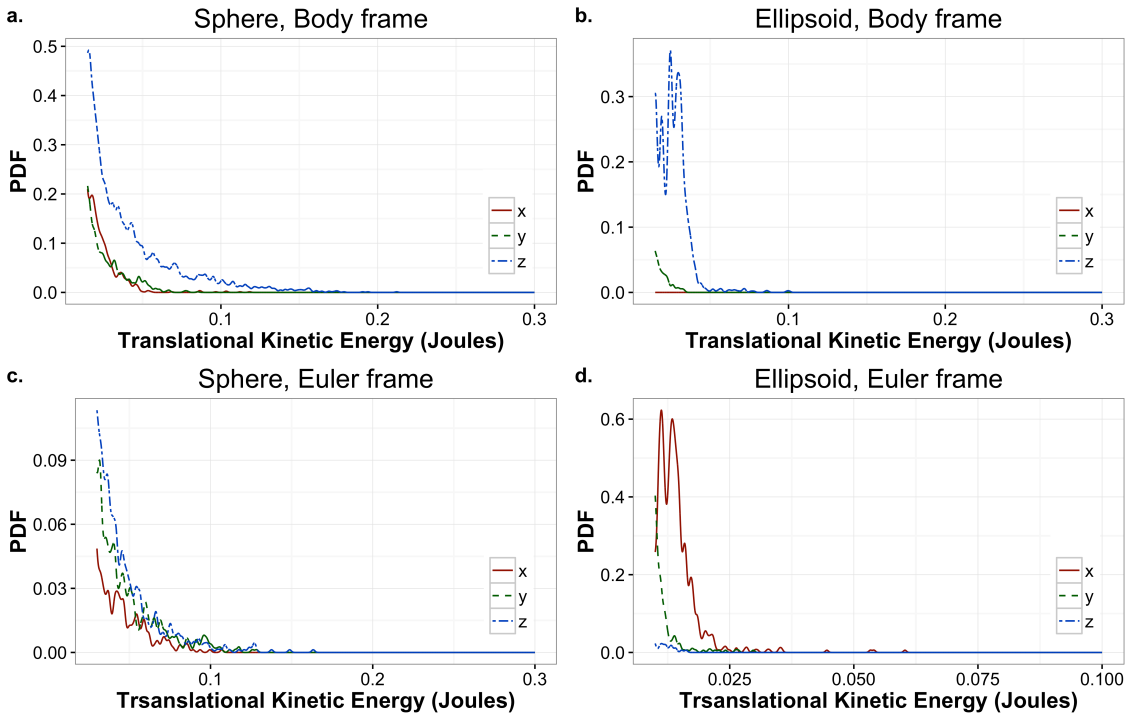

Figure 6.8: **3D Energy distribution.** a.Tranlational Kinetic Energy per axis (x,y,z) in the sensor-Lagrangian frame. b. Translational Kinetic Energy per axis (x,y,z) in the Eulerian frame. For the spherical sensor the uplift component during the entrainment is highlighted (z-axis) in the Lagrangian frame. In the Eulerian frame the spatial distribution of energy for the sphere is statistically uniform. On the contrary, the ellipsoidal sensor shows a strong bias to the uplift force which is transformed into a strong bias along the x-axis of the Eulerian frame.

6.3.3 Magnitude of instantaneous displacements during entrainment (Eulerian frame)

Displacement calculations are meaningful in the Eulerian frame only since the Lagrangian frame is rotating. By calculating the magnitude of instantaneous displacement during entrainment (individual entrainments vary in duration between 1.1 and 3.7 seconds, e.g. Figure 7.1), it is possible to evaluate the control of the characteristics of the particle's inertial frame (shape and distribution of mass in this case) on the process.

Patterns of displacement along the three Eulerian axes (Figure 6.9) show that, for the sphere, the probability of direction of displacement is almost equal between the three axes. This is consistent with the translational kinetic energy results (Figure 6.8). For the ellipsoidal pebble, the direction of movement at entrainment is biased in the x-axis direction, but both y- and z-axis movements were recorded at greater frequencies than the kinetic energy data (Figure 6.8) would suggest.

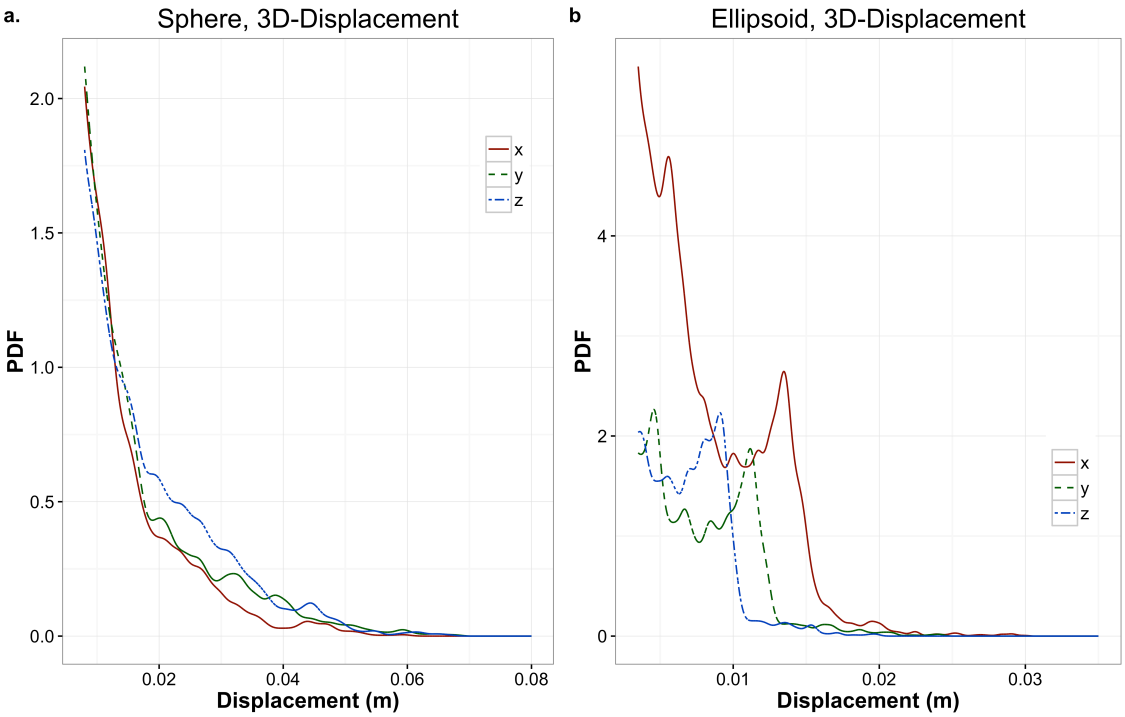

Figure 6.9: **3D-Displacement in the Eulerian frame.** Similarly to the energy calculations, the displacement results suggest that the shape exerts great control in the entrainment process. The PDFs of displacement for the spherical sensor suggest that the during the entrainment the axis-direction of dynamics is equiprobable. On the contrary for the ellipsoid a strong bias along the x-Eulerian direction is observed.

6.3.4 Bed impact experiments

The comparison between the impact through flowing water and through air, suggests that the two cases are statistically indifferent (Wilcoxon test, p-value=0.2). The water slows the particle and causes a reduced median impact energy (0.12 Joules) compared with the fall through air (0.14 Joules). The variability of these energies is much greater for fall through water ($s.d.$ = 0.037 Joules) than air ($s.d.$ = 0.0085 Joules). However, the effect of the water (depth = 0.1 ± 0.05 m) does not suppress the inertial dynamics enough to make the two cases statistically distinguishable. The results suggest that, for the particles that fall to the size class of the spherical sensor, the inertial dynamics are comparable to the hydrodynamic forces. This is especially relevant to circumstances characterised by high D_p/d (D_p is particle diameter, d is point flow depth) ratio (see Discussion, Section 7.1.2).

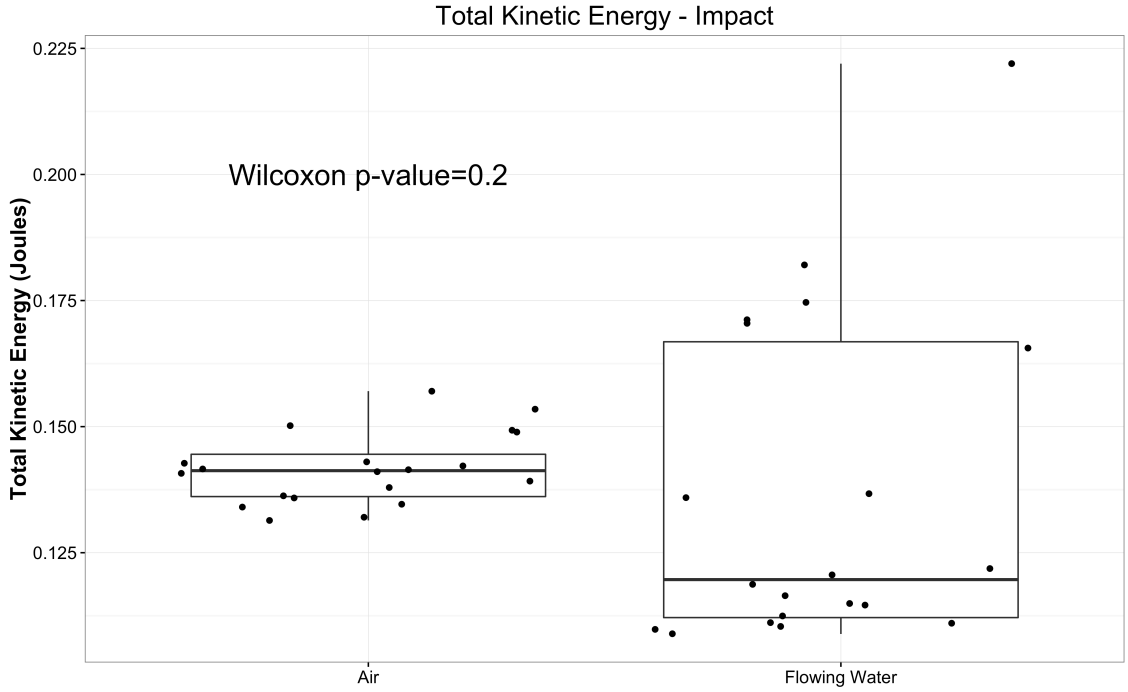

Figure 6.10: **Comparison between the impact through flowing water and through air.** With a flow of 30 l/s, the sphere was released 0.6 m along a fixed, at flow depth (= 0.1 ± 0.05 m), channel parallel to the flume bed upstream of the entry point. Through the flowing water the median energy of the impact is reduced (from 14 to 12 Joules). However the effect of the flowing water is not enough to make the two cases statistically distinguishable (Wilcoxon p-value = 0.2).

6.4 Summary

1. The practical limitations set by the available sensors that are cheap enough to be deployed in large numbers (feasible for sediment transport monitoring) are explained in this chapter. Results from the calibration of a relevant Inertial Measurement Unit analysed for random horizontal oscillations. The high-pass filtering method yields results that can be used in the context of sediment movement [*Ribeiro et al.*, 2003].

2. Two prototype sensors were constructed to evaluate the IMU technology for use in fluvial transport experiments. The first prototype is idealised (spherical) with a diameter of 90 mm which corresponds to coarse sediment classes. The second prototype is an ellipsoid with axes 100, 70 and 30 mm.

3. The two prototypes were tested in a series of entrainment experiments on a fixed idealised bed scaled at the diameter of the spherical sensor 90 mm. The results are used to detect the threshold of entrainment, the spatial distribution of energy and instantaneous displacements during incipient motion. The inertial characteristics of the particle (shape in this case) exert significant control on all the measured instances. The spherical sensor entrained at discharges of 24.8 ± 1.8 l/s. The same threshold for the ellipsoidal sensor was 45.2 ± 2.2 l/s showing higher resistance to the hydrodynamic forces.

4. The spherical sensor was used in a series of bed-impact experiments. The kinetic energy calculations were used to quantify the particle-bed energy exchange under fluvial and non-fluvial conditions. The statistical comparison between the two cases is inconclusive suggesting that the inertial dynamics are comparable with the hydrodynamic forces for the particles fall in the size class of the spherical sensor (90 mm diameter).

CHAPTER 7

DISCUSSION

The primary goal of this work is to evaluate how the technology of IMUs provides new insights into sediment transport mechanics in the theoretical context of Eulerian-Lagrangian frames of reference. In this thesis it is suggested that the Eulerian-Lagrangian model is potentially more relevant and more general than the single frame characterisations (Eulerian or Lagrangian) currently used in sediment transport theory (Chapters 4 and 6). The first contribution of this technology is the inspiration to connect the two frames and the derivation of equations for the cross- translation of dynamics (Lagrangian to Eulerian and *vice versa*).

The IMU sensors that are currently widely available have considerable capabilities for enhancing our understanding of sediment processes, but also possess limitations that need to be understood when interpreting the data.

Due to limitations in sensor accuracy and noise, accurate measurement of Lagrangian particle trajectories is not currently feasible for the time scale of sediment transport (seconds or longer, e.g. Figure 6.1). Thus, accurate positional information over the time of sediment transporting events cannot be obtained from the sensor data. Higher specification sensors, which would also require significant post-processing of data, are currently restricted to military uses (or are very expensive [*VectorNav*, 2016]).

The calibration of the inertial frame dynamics is restricted to the statistical treatment of heavily filtered signals due to rapid error accumulation (FFT-high-pass and Kalman filtering). This type of signal processing can only give the magnitude of local dynamics (after the calibration of the sensor) and for a time period in the order of 10 seconds (Figure 6.3). After this type of data-processing the magnitude of local dynamics recorded by the sensor is in scale with actual values as determined by independent methods: for example, a total kinetic energy in the order of 0.1 Joules for instantaneous inertial accelerations of 10 m/s^2 and displacements of 0.01 m for the first second of incipient motion is consistent with the relevant Newtonian calculations (1 Joule is the energy needed to accelerate a mass of 1 kg at 1 m/s^2 for 1 m).

7.1 The importance of inertia and the effect of the particle inertial frame

The inertia of sediment grains has been shown to be significant both theoretically and experimentally. For grains coarser than 2 mm, Stokes numbers > 1 are calculated, which is an indication of increased particle resistance along with increased flow variability (higher Reynolds number (Chapter 4). Results from the very coarse particles reported in this thesis (Figures 6.7, 6.8, 6.9 and 6.10) provide experimental evidence that particle inertia is a significant element of both grain entrainment and impacts. The inertia of the particles has already been identified as a significant control for sediment entrainment [*Buffington and Montgomery*, 1997]. Although data for translation and deposition of moving grains is not available, I anticipate that the role of inertia in these processes will be significant, as has been postulated by previous researchers (e.g *Dietrich and Smith* [1984]; *Ferguson et al.* [1996]; *Wathen et al.* [1997]).

7.1.1 Entrainment experiments

Overall the total kinetic energy generated during entrainments was statistically comparable for the two enclosures (spherical and ellipsoidal) and the differences can be explained by the difference in the masses of the two enclosures (0.077 kg difference). In parallel, a significantly higher discharge entrainment threshold is observed for the ellipsoid in comparison to the sphere (45.2 ± 2.2 l/s for the ellipsoid, 24.8 ± 1.8 l/s for the sphere). This later result is compatible with previous studies where the saddle entrainment threshold of coarse ellipsoids (parameterised with Shields θ_t) was estimated up to 5 times higher from the saddle-rotation threshold of (equivalent size) coarse spheres [*Komar and Li*, 1986].

The effect of shape on the direction of motion is also consistent with field observations (e.g. *Hassan and Reid* [1990]; *Demir* [2000]). In the entrainment experiments of the spherical sensor both the spatial distribution of kinetic energy and the magnitude of displacement are approximately uniform in the Eulerian frame (Figures 6.8 and 6.9).

In the pebble sensor the dominance of uplift forces in the Lagrangian frame results in a movement predominately along the Eulerian x-direction. Given the need to include the range of sediment sizes, shapes and densities that characterise different environments in sediment transport models [*Houssais and Jerolmack*, 2016], this type of quantification can be used to partly decouple the sediment motion from the stochasticity of flow dynamics.

Historically, the starting point for the analysis of the force-torque balance between the sediment particles and the flow forces has always been the approximation of the point flow turbulence [*Bialik*, 2015; *Cecchetto et al.*, 2016]. The complexity of this force-torque balance leads to highly idealised or semi-empirical results that are difficult to generalise (Section 4.1.5). By measuring the inertia of the sediment particles it is possible to resolve the same force-torque balance using Newton-Euler calculations directly (Section 4.1.2). This analysis results to a statistical treatment of entrainment dynamics that is better constrained compared to flow based parameterisations (Sections 5.2.2, 7.1.3).

7.1.2 Bed impact experiments

The results from the impact experiments also demonstrate the importance of inertia for these sediment classes. There are two characteristics of the experimental procedure that result into conditions that may be encountered in high gradient streams, but which are not universal.

Firstly the particle rolled 0.6 m prior to falling onto the flume bed (Figure 6.6), which can potentially lead to a momentum accumulation higher than a typical natural sediment translation. However, it is clear in the comparison between the experiments with and without water that damping occurs in the fluvial process indicating the effect of the flowing water on the motion of the particle (Section 6.3.4). In addition, the momentum accumulation is identical for both of the experiments until the point of contact with the flow as the sensor was released from the same point.

Secondly, the depth of the flow during the impact which was comparable to the sensors diameter (0.1 m). This condition makes the experiment highly relevant to mountain streams where there is a high probability of entrainment occurring under supercritical flow (high pebble diameters vs shallow steep flows, e.g. *Smart* [1984]).

The effect of inertia is highlighted by the fact that the two cases (impact through flowing water and through air) are not statistically distinguishable. Part of this statistical non-difference is due to the increased variability in the presence of water (Figure 6.10) and part of it by the momentum accumulation which for a particle of this size is found comparable to the effect of water forces.

The Eulerian-Lagrangian model presented here accounts for particle inertia explicitly. The assumption of a fixed mobile inertial frame (Lagrangian) gives the opportunity to translate the dynamics (from Lagrangian to Eulerian and *vice versa*) but can also be used to test the assumption of spatial continuity for sediments. For sediments assumed continuous, the integration of (consistently translated) Lagrangian dynamics will be close to the analysis in the Eulerian domain.

Coarse sediments are often organised in patches (thus not in a spatial continuum, *Hodge et al.* [2016]). The integration of Lagrangian dynamics will be different from the Eulerian definition, and the increased particle inertia will deviate the Lagrangian trajectories from any predictions based on Eulerian dynamics.

7.1.3 Inertial parametrisation for incipient motion

The data from Figure 6.7 suggest that the total kinetic energy has the potential to provide an unambiguous definition of entrainment events, even after the original signals have been filtered to remove noise and subjected to the Kalman filter. The Kalman filter models a representative behaviour from the repetition of each of the two sets of entrainment experiments (spherical and ellipsoidal particles). The resulting time series does not represent the extreme events, because the Kalman filter is mainly affected the majority of entrainments which occurred at comparable dynamics. This stochastic representation helps us understand if the data processing is in scale (by increasing our statistical sample), and it can be a useful framework for generalisations in the future after experimenting in different conditions (Sections 5.1.3, 6.2.3.2).

Individual runs can also give significant information about the physics of entrainment. For example, different patterns of the kinetic energy during the entrainment event were observed which relate directly to the approximations of the particle energy during incipient motion presented in *Valyrakis et al.* [2013]. Figure 7.1 shows examples of short term high-energy entrainments, in contrast to longer low-energy events. A crucial difference with the results in *Valyrakis et al.* [2013] is the duration of entrainment events which here scales in seconds instead of milliseconds. This difference is attributed to the responsiveness of the constructed enclosures and our effort to approximate the natural sediment density (in *Valyrakis et al.* [2013] a 12.7 mm diameter, teflon (density = 2200 kg/m^3) sphere is used as the target particle). This comparison is one more indication for the control exerted on the process of entrainment by the inertia of the particles (especially the coarser).

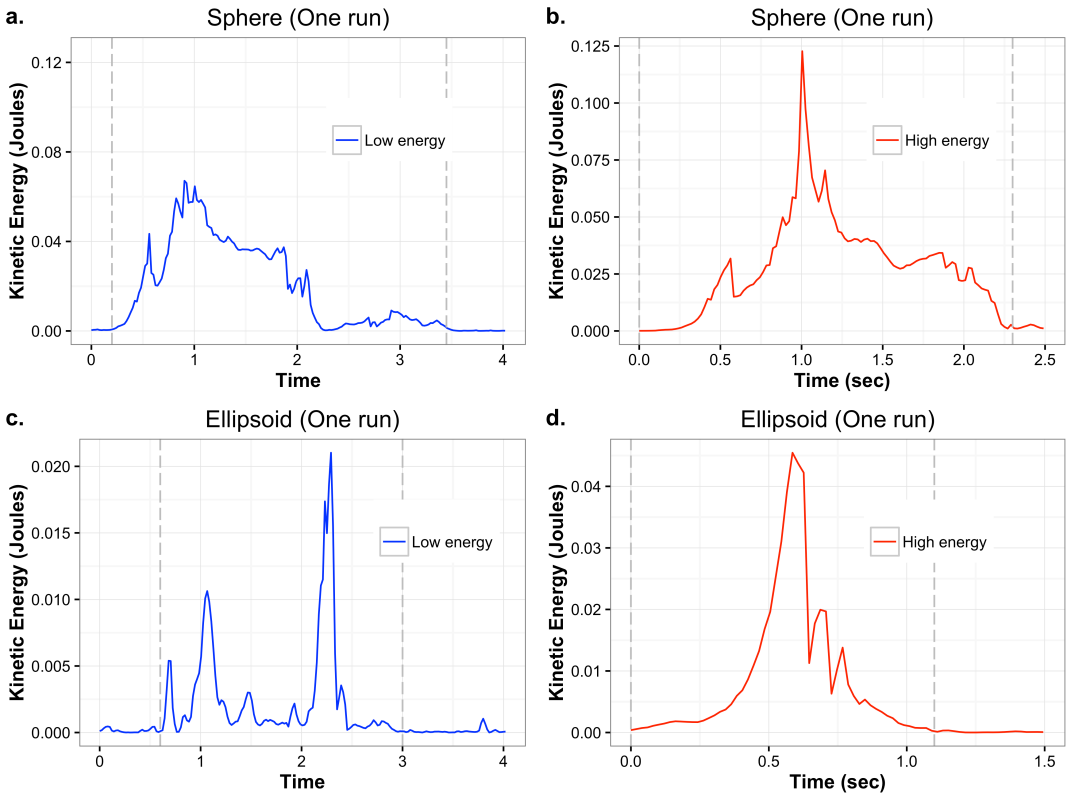

Figure 7.1: **Examples of total kinetic energy during typical entrainment events.** The distinction between low-energy long entrainments and high-energy short entrainments was initially highlighted by *Valyrakis et al.* [2013]. The differences here are the addition of an angular component to the calculation of kinetic energy and the response time of the particle which here scales in seconds (in contrast to micro-seconds).

In Chapter 4 two probabilistic explicit entrainment criteria are introduced (Equations 4.31 and 4.32). The more general (Equation 4.32) has the form:

$$P_E = P(K_f > k_f = k_g) = \int_{k_g}^{\infty} f_{K_f}(k)dk = 1 - F_{K_f}(k_g) \tag{7.1}$$

where K_f is the kinetic energy for an individual pebble, represented by a cumulative distribution F_{K_f} with a probability density function of f_{K_f}, and k_g is the threshold kinetic energy for entrainment. k_g can also be calculated depending on the definition of entrainment. Defining entrainment as having occurred when the particle moves one diameter (more relevant to geomorphological descriptions) will lead to an approximation of the threshold as the kinetic energy needed to accelerate the mass of the given pebble one pebble diameter. The hydrodynamics that will generate this energy can be constrained but not deterministically predicted (this is the stochastic component of the transport). However, the threshold can be based exclusively on the inertial characteristics of the particle. More detailed hydraulic representations of entrainment can also be calibrated following the same concept. This observation explains why the inertial measurement are the first step towards decoupling the hydrodynamic forces from the resulting sediment movement. The importance of this decoupling is highlighted thought this thesis (Sections 5.2.2, 7.1.3, 7.1.1)

The comparison of the simplified inertial acceleration-based threshold with a flow velocity based prediction (OVL coefficient, Chapter 4), suggests that the overlap of pre- and post-entrainment distribution is reduced by c.10%. Moreover, the reduction is greater for the higher slope where the variability of the hydrodynamics is greater as demonstrated from the $PDFs$ of Figure 5.6. As a result, even with the simplified non-rotational framework it is possible to hypothesise that, for medium-large grain scales, the inertia of the particles exerts a more significant control on their motion than flow generated forces [*Bathurst*, 1985].

Further study of the proposed criteria under varied conditions is required and is likely to reveal a range of types of behaviour dependent on the same issues which lead to variability in the definition of Shields' criterion [*Buffington and Montgomery*, 1997]. However, the range of behaviour may be better constrained as actual forces are directly measured rather than being inferentially related to measurable parameters such as grain shape and protrusion. The approach therefore has the potential to lead to a general inertial force-based (and particle kinetic energy) equivalent of Shields' diagram which will not be restricted by the assumption of uniform flow (or any other flow characterisation) and will have broad applicability.

7.2 Implications for sediment transport theory

One of the advantages of the two frame characterisation (Eulerian-Lagrangian) is that grain rotations are resolved in a relatively simple mathematical framework. In the conditions examined, the rotational energy was significantly lower from the energy expended to translate the particle. This is explained by the magnitude of the moment of inertia (order of $I_{cm} = 0.001$) of the constructed enclosures.

In Chapters 4 and 6 is demonstrated how the rotational kinetic energy is included in the Eulerian-Lagrangian model and how it participates to the calculation of the total kinetic energy (Equation 4.10) of the particle under transport. This contribution cannot be neglected before experimental evidence over a range of dynamic conditions shows that it is negligible.

Consequently, there are two reasons why particle rotation needs to be accounted for: a) it is required to produce acceptable positional accuracy estimates from acceleration and angular velocity measurements; and, b) rotation can in principle contribute a significant proportion of the total energy of a mobile particle.

This Newton-Euler scheme (Equations 4.6 to 4.10) contributes to better understanding of the flow-energy distribution around a particle during transport, the important of which has been highlighted in recent years, mainly from rom consideration of impulse events [*Diplas et al.*, 2008; *Valyrakis et al.*, 2011a, 2013]. There is no physical reason that restricts the use the of the mathematical framework presented (Chapters 4, 5 and 6) in the context of impulsive flow events. On the contrary, the unconstrained Eulerian-Lagrangian model can lead to the identification of the flow-particle energy exchange, again because we explicitly account for the effective energy of the flow, the energy that is transformed into particle kinetic energy.

Only recently has the monitoring equipment been miniaturised sufficiently to address a large range of scales and this is the reason why the inclusion of more complicated physics in the framework of sediment transport becomes necessary. For example, a derivation such as the Lagrangian (L) of a multi-body system of particles can be simplified in a form:

$$L = \frac{1}{2}\sum(mv^2) + \frac{1}{2}\sum(I_{cm}\omega^2) \tag{7.2}$$

expressing the total kinetic energy of the multi-body system. This formulation is relevant to the Lagrangian frame of individual particles but this upscaled form can be used in the context of many particle random-walk simulations, Monte-Carlo and Markov-Chain randomisations [*Tsai and Lai*, 2014], neuro-fuzzy [*Valyrakis et al.*, 2011b] and Bayesian models [*Schmelter et al.*, 2011]. When parametrised statistically, these approaches rely on robust calculation of probabilities, such as the probability of entrainment (Section 7.1.3), since they can be utilized either as real transition probabilities for the state-space derivations or as training functions and priors for the inference systems. For the first time it is possible to perform a calibration for these simulations based on directly relevant measurements. The incorporation of the quaternion algebra can also improve these conceptual studies as it has been shown from the corresponding fields of transport processes [*Höfler and Schwarzer*, 2000].

7.3 Implications for the use of IMU sensors for monitoring sediment transport

In geomorphology, accelerometers have not been generally deployed as dynamic sensors but mainly as part of stop-motion and tilt sensing units (e.g. *Olinde and Johnson* [2015]; *Frank et al.* [2015]). This is not surprising since these sensors are usually developed for well constrained and much less dynamic environments than the natural and experimental regimes of fluvial transport.

The rate of technical development, and associated cost reductions, is fast and today compact strapdown IMUs that can measure accelerations of $> \pm 200$ g are readily available. Important improvements have also taken place in terms of the signal processing, the on-board computing and the compensation of errors related to the construction of the sensor (e.g. gyroscope drifts). The upgrade of the sensor devices will not lead to enhanced scientific understanding without improved conceptual frameworks and data analytical techniques.

Any sensor used for sediment transport measurements has to address a number of physical requirements [*Maniatis et al.*, 2013]. The localisation model in Section 4.1.3.5 assumes an ideal sensor. Given the rigid-body kinematics for the sensor, the two most important physical characteristics for the derivation of coherent inertial data are: the mass distribution of the sensor assembly, and the coincidence of the centre of masses of the IMU-sensor and the whole sensor assembly (Chapters 4 and 6).

For artificial particles, ensuring even mass distribution and correct positioning of the IMU can be achieved in the design process. When inserting sensors into natural particles, uniform density of the particle is assumed and the IMU positioning can be determined from 3D CAD modelling (Section 3.1).

In terms of analysing the rotational data (Section 6.1), it is demonstrated that the quaternions are the best choice. Quaternion based descriptions are not based on assumptions for the rotational dynamics of the moving frame (such as Euler angle descriptions) and can be parametrised directly using IMU data. Also in the high-energy environments, discrepancies such as the Gimbal Lock will make the use of Euler angles (in the classical definition) inconsistent as demonstrated numerically in the Appendix B.

Finally, specific considerations during sensor deployment have to be considered. For example, during field deployment, the initial orientation of the IMU relative to what it is defined as the local Euler frame is crucial. If the sensor is not robustly aligned with the frame of reference of the localisation (the Eulerian in the mathematical derivations of this work) then the error propagate and be amplified in the in the trajectory estimation, consequent on the double integrations (Equations 6.4 and 6.5). A direct way to resolve this problem is to always define the Eulerian frame as one where the gravity vector is parallel the

its Z_E axes (Chapter 6), and align the IMU such so it measures +1 g (or −1 g) on its Z_b axis and 0 g on both the X_b and Z_b axes. Then the Eulerian frame is the one which coincides with this initial body frame orientation ($X_E = X_b$ and $Y_E = Y_b$ for this aligned sensor position) and all the subsequence Lagrangian measurements can be resolved relative to this.

For an experimental deployment the initial alignment is important, however, the adaption of the sensor to the resolution needed for a fluvial experiment is equally important. An IMU sensor is valid for the monitoring of the particle-flow interaction but the adaptation of the IMU-sampling frequencies to the frequencies related to the water flow turbulence (PIV measurements) is not yet easily addressed. For smaller particles, sensors without the capabilities of the IMUs had to be adapted to frequencies of the order of 500 Hz to record the flow-particle interaction coherently [*Valyrakis et al.*, 2011a, 2013]. However, the adequacy of the sampling frequency is highly depended on the inertia of the particle that is monitored and remains an open research question. For the artificial particles utilised the experimental evaluation presented in the adjoint application paper, a sampling frequency of 50 Hz resolved the dynamics robustly for the calculation of statistics relevant to incipient motion.

7.4 Future developments

7.4.1 Sensor development - telemetry

Since the technical and theoretical developments introduced in this thesis have been tested exclusively in laboratory conditions, the natural next step is the evaluation of the latest prototypes in the field. The IMU based description of sediment movement so far is more relevant to coarse sediments, because of the size of available sensors. As a result, mountain streams or coarse beaches a better candidate for this initial field evaluation.

Having explored the limits of the available off-the-shelf IMU sensors, I come to the conclusion that purpose specific electronic sensing components are necessary. There are additional errors that they are not relevant to to measurement of short-term incipient motion events, but which can significantly affect accuracy during longer mobile periods (e.g. long period gyroscopic drifts). The other requirements discussed in this thesis such as range, rigidity and the very important initial calibration (which for an end-user is a black box) can also be addressed accurately and specifically for the the expected range of sediment motions during design and manufacturing phases.

Even with the best custom IMU the requirement of high-frequency positional data cannot be satisfied if it is kept at a feasible price. This can be resolved by coupling the IMU technology with an external telemetry technique which will constrain the position of the sensor. Having accurate positional information at a lower frequency and collecting high-frequency IMU data for the intermediate positions can lead to accurate definition of particle trajectories.

Traditional radio based telemetry has proven to be very difficult to apply for long periods (Chapter 2). Other localisation techniques can provide sufficient spatial accuracy and temporal resolution for long-distance transport (GPS) but there are technical considerations for the the scale of sediment transport events (meters to hundreds of meters). Appendix F includes a simulation which demonstrates the limitations of the available telemetric sensors when the specific case of fluvial micro-localization is considered.

For the above reasons, alternative telemetry techniques which are based on magnetic induction are

more suitable for fluvial environments [*Sear et al.*, 2002; *Markham et al.*, 2012]. The system of *Markham et al.* [2012] has been extensively tested for the tracking of underground animals and I have tested the technique in the flume laboratory for the case of sediment movement. It will demand a modification of the purpose specific IMU prototype, in order to accommodate magnetic coils/receivers.

7.4.2 Sediment transport theory

The development of new sensing technology coupled with new mathematical formulations of sediment transport theories, will allow new research questions to be investigated. The diffusion of sediment particles during transport [*Nikora et al.*, 2002; *Ganti et al.*, 2010] is a fundamental problem towards the increase of our prediction power over bed-load transport.

Many researchers worked on the challenge of a physically based model for anomalous diffusion. An approach to the diffusion problem that offers promise is the ensembles approach of *Furbish et al.* [2012a] which has been extended by [*Fathel et al.*, 2015, 2016]. From the point of single particle dynamics (semi-Lagrangian in the context of this thesis since the rotation is not calculated) there are important theoretical advancements from the extension by [*Bialik et al.*, 2012, 2015] of the conceptualisation suggested by *Nikora et al.* [2002]. There are two reasons that make the generalisation of such a model difficult. Firstly, the experimental verification of such models is restricted to small particles ($d_{50} = 5$ mm). Secondly, we have new theories which demonstrate, experimentally and theoretically, that a significant part of bed-load transport is controlled the micro-turbulence of the flowing water (Impulse theory, *Diplas et al.* [2008] and subsequent papers).

The technology and the theory presented in this thesis have the potential to isolate the particle motion metrics from the sediment-water interaction. Today we cannot exclude the possibility that much of the diffusive behaviour we model and observe is hydrodynamic. Pure Lagrangian measurment of particle accelerations, velocities and positions will reduce this uncertainty and will test the diffusion regimes from the other end of the sediment sizes (coarse).

CHAPTER 8

CONCLUSIONS

This chapter includes a list with the main conclusions of this thesis. The list follows the structure of the thesis from the literature review and the construction of the prototype sensors to the development of the corresponding theory, the experimental deployments and the outcomes that are relevant to the study of sediment transport.

- Considering the problem of monitoring individual grain dynamics in fluvial processes, there are three critical conclusions regarding the sensing techniques applied in both field and laboratory deployments. The first concerns the lack of dynamical information at a frequency that can address the diffusive time scales of sediment transport (especially from field deployments). Despite the advancement of tracking sensors (eg. PIT tags), it is only possible to derive individual grain positions before and after an event but not during the transport. The second is that the high-frequency measurement of inertial accelerations in laboratory settings cannot be translated to high-frequency positional information directly (Chapter 5). Finally, the critical restriction for deploying off-the-shelf IMU sensors into the field is the accelerometer measurement range (in a natural setting it is necessary to capture an order of magnitude of ± 100 g). Only recently accelerometers of $> \pm 200$ g measurement range became commercially available.
- For the construction of inertial sensors for monitoring sediment motion, it is critical to consider separately the casing-design criteria in parallel to the sensing requirements. The physical characteristics of the sensor's enclosure affects directly the movement of the device and derived data. In addition, the stability of the sensor in response to the overall frame of the casing is critical for both the quality of the derived data (chapter 3) and the theoretical analysis in the context of coarse sediment motion (chapter 4).
- The thesis demonstrates the devision of sediment transport literature into Lagrangian and Eulerian models, for the both the monitoring and the analysis of sediment motion (chapters 2 and 4). The analysis of flow hydrodynamics is predominately Eulerian. One relevant conclusion is that metrics implemented in the general field of two phase transport processes (such as the Stokes number) can be used to investigate the physical reasons behind the division of the literature. In parallel, it is

possible to define a complete Eulerian-Lagrangian model for coarse sediment transport starting from the purely Lagrangian definition of particle dynamics (on their inertial frame) and defining the transformations from the Lagrangian to the Eulerian domain where flow is analysed (and vice versa) . The optimum mathematisation for the rotational transformations includes the definition of unit quaternions (chapter 4, appendix B). The whole model is simplified by the assumption of an ideal IMU rigidly attached on the centre of mass of the Lagrangian particle sampling accelerations and angular velocities. Two probabilistic entrainment criteria are defined using the framework of inertial dynamics: one based on inertial accelerations and one based on the total kinetic energy of the particle under entrainment.

- The Eulerian-Lagrangian model is initially evaluated experimentally for the non-rotational case (Chapter 5). Absolute inertial accelerations were recorded at a 4 Hz frequency from a spherical instrumented particle (111 mm diameter and 2383 kg/m^3 density) in a series of entrainment threshold experiments on a fixed idealised bed. Three statistical techniques were used to analyse the acceleration signal: Kalman Filtering, Logistic Regression and the OVL coefficient (Chapters 4 and 5). All three techniques are evaluated in the context of identifying the threshold of entrainment for the instrumented particle and it is shown that the inertial acceleration threshold performs significantly better than water flow velocity based entrainment thresholds (10% reduction of the OVL coefficient). For the instrumented particle, the grain-top inertial acceleration entrainment threshold was approximated at 44 and 51 mg for slopes 0.026 and 0.037 respectively. The saddle inertial acceleration entrainment threshold was at 32 and 25 mg for slopes 0.044 and 0.057 respectively.

- For the evaluation of the complete Eulerian-Lagrangian model two prototype sensors are presented. The first prototype is idealised (spherical) with a diameter of 90 mm and the second is an ellipsoid with axes 100, 70 and 30 mm. The two prototypes are instrumented with a complete IMU, capable of sampling 3D inertial accelerations and 3D angular velocities at 50 Hz. The calibration process indicates the need to extend the signal analysis with the inclusion of noise threshold and high-pass filtering techniques (Chapter 6). After the analysis, the results can be used in the context of sediment movement but they do not contain positional information [*Ribeiro et al.*, 2003]. Both sensors were tested in a series of entrainment experiments similar to the evaluation of the 111 mm prototype but for one slope only (0.02). The spherical sensor entrained at discharges of 24.8 ± 1.8 l/s while the same threshold for the ellipsoidal sensor was 45.2 ± 2.2 l/s, indicating higher resistance to the hydrodynamic forces and highlighting the control of the inertial characteristics of the particle (shape in this case) on the resulting motion. Overall, the total kinetic energy generated during entrainments was statistically comparable for the two enclosures (spherical and ellipsoidal) at a scale of 0.1 Joules. The kinetic energy threshold differences are attributed to mass difference (0.077 kg) between the two enclosures (Chapters 6 and 7).

- Kinetic energy calculations were used to quantify the particle-bed energy exchange under fluvial and non-fluvial conditions. The 90 mm spherical sensor was rolled into flowing water at discharge slightly higher than the threshold of entrainment (30 l/s) initially and subsequently directly onto the bed (no flow). The inconclusive comparison between the two cases suggests that the inertial dynamics are comparable with the hydrodynamic forces for the coarser particles.

- The Eulerian-Lagrangian model presented in this thesis accounts for particle inertia explicitly. With a fixed mobile inertial frame (Lagrangian) it is possible to translate the dynamics (from

Lagrangian to Eulerian and vice versa) but also test the assumption of spatial continuity for sediments. The analysis of dynamics of continuous sediments will be similar in the integrated Lagrangian and the Eulerian domains. Inertial dynamics also enhance the definition of entrainment as the exact threshold can be defined based on the inertial characteristics of each particle. While the hydrodynamics that will produce this threshold cannot be deterministically predicted, the inertial analysis suggests that they can be constrained, especially for the entrainment of coarser particles (Sections 5.2.2, 7.1.3, 7.1.1)

- Finally it is suggested that a purpose specific IMU sensor is necessary in order to address all the requirements for the monitoring of individual sediment particles in natural settings. The coupling of IMU technology with advanced telemetric techniques will resolve the problem of acquiring high frequency positional information and enhance our understanding regarding the nature of the diffusive behaviour observed in fluvial sediment transport.

APPENDIX A

EXPERIMENTAL PARAMETERS

Table A.1: Key parameters for the four measured experimental settings

Experiment	ρ_p/ρ_f	P (m)	d_p (m)	P/d_p	S_b	B (m)	Flow increase (l/s^2)		Q (l/s)	d (m)	A (m^2)	U_b (m/s)	R_b	F	B/d	u_* (m/s)	τ_*	R_*	R_p
UBC 1	2.383	0.065	0.11	0.59	0.026	0.6	0.014	Min	1.836	0.026	0.0156	0.055	3060	0.044	3.736	0.081	0.004	2117	8957
								Max	6.261	0.160	0.0963	0.075	10435	0.077	8.333	0.202	0.027	32495	22261
UBC 2	2.383	0.065	0.11	0.59	0.033	0.6	0.014	Min	2.721	0.022	0.0132	0.139	4535	0.175	9.331	0.089	0.005	1965	9829
								Max	6.261	0.064	0.0385	0.202	10435	0.375	20.230	0.152	0.015	9822	16804
UBC 3	2.383	0.065	0.11	0.59	0.044	0.6	0.014		6.25	0.04	0.02	0.239	10416	0.367	13.809	0.136	0.012	5950	15064
Glasgow	2.7	0.045	0.09	0.5	0.02	0.9	0.028		30	0.1	0.09	0.3	33333	0.336	9	0.140	0.013	14007	12606

In Table A.1 the experimental parameters for four experimental settings are presented. The first three (UBC 1 to 3) are estimated parameters for the experiments presented in Chapter 5. For the two lower slopes (0.02 and 0.033) it was possible to estimate the parameters for the whole duration of flow increase and the full range is reported (Min-Max). For the higher slopes (0.044 and 0.057), the parameters are estimated at discharge and depth of 6.25 l/s and 0.04 m respectively and for the the 0.044 slope only.

For the experimental setting of Chapter 6 (Glasgow experiment) the estimated parameters are for the threshold discharge for entrainment of the spherical particle (30 l/s), estimated using a flow rate increase of 0.028 l/s^2 . This is also the flow rate used for the impact experiments of Section 6.2.3.3.

The parameters are estimated as follows: ρ_p/ρ_f is the ratio of an experimental particle density to fluid density (ρ_f = 1000 kg/m^3); P/D is the ratio of the particle protrusion P (measured from the top of the surrounding fixed hemispheres to the top of the experimental particle). d_p is the particle diameter (all the estimations are performed for the spherical particles); S_b is bed slope; d is the flow depth (measured from the bottom of the bed to the water surface. $Ub = Q/A$ is the bulk mean velocity (Q is the flow rate and A is the cross sectional area of the flow); $R_b = (U_b d)/\nu$ is the bulk Reynolds number (where ν is the fluid kinematic viscosity); $F = U_b/(gd)^{0.5}$ is the Froude number; B/d is the aspect ratio (B is the flume width); u_* is the shear velocity, estimated as $u_* = (\tau_b/\rho_f)^{0.5} = (gdS_b)^{0.5}$; τ_b is bed shear stress; and $R_* = (u_* d)/\nu$ is the friction Reynolds number. Shields number was calculated as $\tau_* = (\rho_f gHS)/[(\rho_p - \rho_f)gd_p]$. Finally the particle Reynolds number is estimated as $R_p = d_p u_*/\nu$

APPENDIX

B

EULER ANGLES VS QUARTENIONS

In principle the calculations of the DCM from the Euler angles and the DCM from the quaternions are equivalent, in the sense that they both represent the attitude of the moving Lagrangian frame in relation to the fixed Eulerian frame. However, the equivalence of these calculations is compromised by practical issues which are summarised here as they are not widely considered in the literature.

Two observations are important:

Firstly, Euler angles are expressed as a set of three sequential rotations in contrast to quaternions which explicitly describe a single rotation around one axis. When a DCM is calculated from the Euler angles will always represent the rotation in terms of magnitude but not in terms of sequence since many sequences of the same Euler angles can result to the same DCM [*Slabaugh*, 1999].

Secondly, the Euler angle rates (the rate of change of rotation angles) do not generally represent angular velocities. Equivalence is often used to linearise the DCM from a triplet of Euler angles but for the general case the body angular rates for a triplet of Euler rates are given by the matrix:

$$\begin{matrix}\Omega_1^b \\ \Omega_2^b \\ \Omega_3^b\end{matrix} = \begin{bmatrix} 1 & 0 & -\sin\theta \\ 0 & \cos\phi & \cos\theta\sin\phi \\ 0 & -\sin\phi & \cos\theta\cos\phi \end{bmatrix} \begin{matrix}\dot{\phi} \\ \dot{\theta} \\ \dot{\psi}\end{matrix} \tag{B.1}$$

for a ZYX Euler Rotation Sequence: $\Omega_1^b = \omega_x$, $\Omega_2^b = \omega_y$, $\Omega_3^b = \omega_z$ and $\begin{pmatrix}\dot{\phi} \\ \dot{\theta} \\ \dot{\psi}\end{pmatrix}$ are the Euler rates.

An graphical representation of the difference between Euler and body axes rotations is shown in Figure B.1

Combining the two observations it becomes apparent that although the DCM calculated from Euler angles (Equation 4.17) corresponds to more than one Euler sequence, the transformation of angular velocities is explicit for each Euler series. Given that the quaternion is directly related to the vector of instantaneous angular velocities (ω in Equation 4.21), the DCM from quaternions (Equation 4.22) does not correspond to the DCM from Euler angles (Equation 4.17) generally.

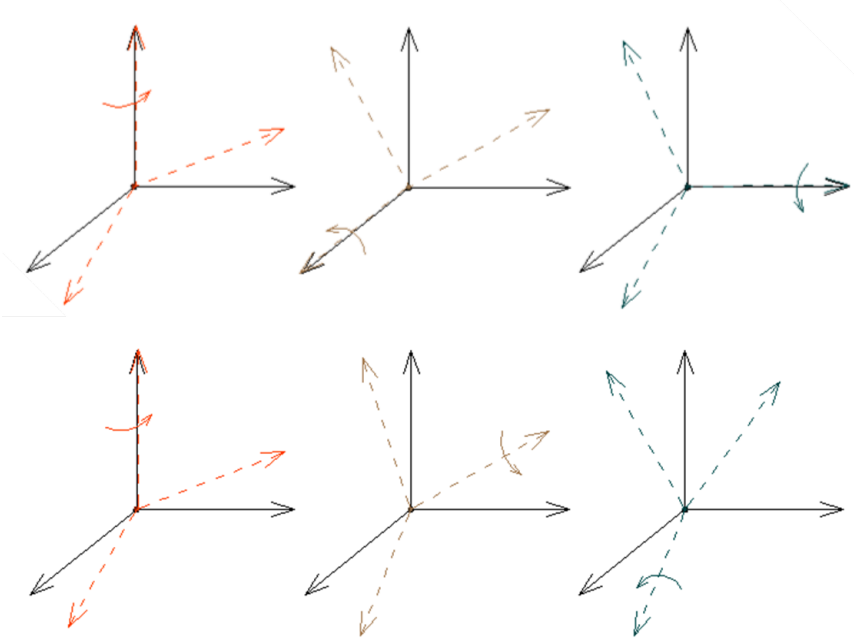

Figure B.1: **Examples of independent (up) and dependent sequential (down) rotations.** While the first series can be directly transformed to angular velocities and quaternions the second (which corresponds to the classical definition of Euler angles) cannot. An implication of this is the ambiguity in the definition of the Direction Cosine Matrix that corresponds to the dependent transformations, since different sequences can result to the same final transformation matrix. In parallel, while there is a direct physical measurement for body angular velocities (gyroscope measurements), Euler angles rates cannot be measured directly.

It is not possible to compare the two rotation representations after we have defined the DCM. However, it is possible to transform the quaternions to Euler angles using the following equations (B.2):

$$\begin{aligned} \phi &= atan2(-2q_xq_y + 2q_sq_z, q_x^2 + q_s^2 - q_z^2 - q_y^2) \\ \theta &= asin(2q_xq_z + 2q_sq_y) \\ \psi &= atan2(-2q_yq_z + 2q_sq_z), q_z^2 - q_y^2 - q_x^2 + q_s^2) \end{aligned} \tag{B.2}$$

where q_s, q_x, q_y, q_z are the quaternion components and ϕ,θ,ψ are the Euler angles for a $Z-Y-X$ rotation sequence.

To demonstrate the advantage of quaternions we rotate randomly the static vector of gravity. In an orthogonal Cartesian frame where the z axis is coincident with the centre of the Earth, gravity is measured as $[G_x, G_y, G_z] = [0, 0, 9.81]$ m/sec^2. If we assume a rigid body rotating freely and randomly in this frame we can do the rotation calculations as presented in Section 4.1.3. Avoiding further mathematisation, the series of the calculations is the following:

- Randomisation of the body frame angular velocities of the rigid body $\omega_x, \omega_y, \omega_z$ in a $[-2\pi, 2\pi]$ range. A time step of 100 Hz is used.
- Calculation of the unit quaternion and the quaternion derivative using multiplication (Equations 19-21) and using the random angular velocities.

- Transform the quaternions in each time step after the multiplication [*Whitmore*, 2000; *Zhao and van Wachem*, 2013].
- Calculate the DCM for quaternions (Equation 22) and the DCM for Euler angles (Equation 17).
- Rotate the vector of gravity in the body frame of the rigid body using both of the DCMs using Equation 23.

The vector expressed in the body fixed Lagrangian frame is shown in Figure B.2. The results are different and Gimbal lock (an inconsistent axis change when the second rotation approaches $\pm\pi/2$) occurs after the 450^{th} iteration which corresponds to $8sec$ in simulation time.

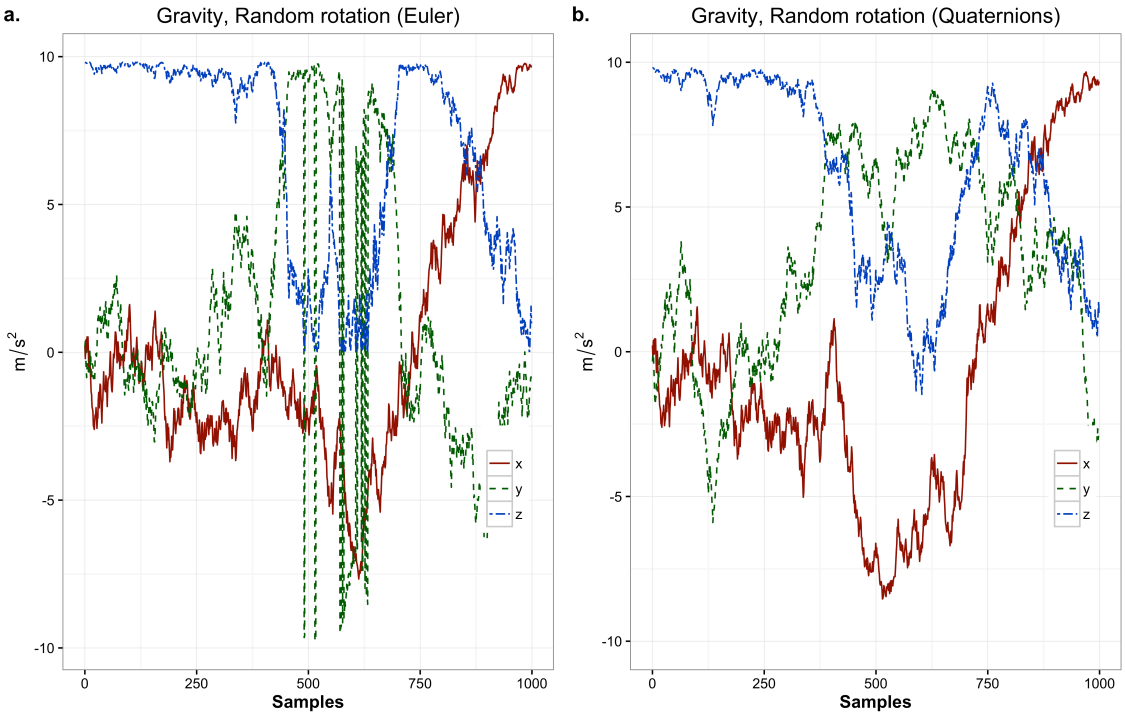

Figure B.2: **Random rotation of the static vector of Gravity.** $[g_x, g_y, g_z] = [0, 0, 9.81]$ m/sec^2 in the Eulerian frame of reference as expressed in the body frame of randomly rotating rigid body ($dt = 1/100$ sec). a. demonstrates the rotation calculations with the usage of Euler angles. Gimbal lock occurs after the 400 iterations. b. shows the same rotation series calculated via quaternions. No Gimbal lock occurs and the result is easily to interpret as it is based on the use of the measured body frame angular velocities.

APPENDIX C

SUMMARY OF REFERENCE FRAME CALCULATIONS

C.1 Summary for Body Frame Calculations

1. Derivation of 3D-Body Frame accelerations and 3D- Body Frame angular velocities (x-y-z, individual experiments).
2. Calculation of the rotation Matrix using the angular velocities and the quaternion formulations. For the conventions we are following the quaternion Matrix is given by:

$$Tbi = \begin{bmatrix} q_s^2 + q_x^2 - q_y^2 - q_z^2 & 2(q_x q_y - q_z q_s) & 2(q_x q_z + q_y q_s) \\ 2(q_x q_y + q_z q_s) & q_s^2 - q_x^2 + q_y^2 - q_z^2 & 2(q_y q_z - q_x q_s) \\ 2(q_x q_z - q_y q_s) & 2(q_y q_z + q_x q_s) & q_s^2 - q_x^2 - q_y^2 + q_z^2 \end{bmatrix} \tag{C.1}$$

3. Rotation of Gravity in the body frame (bf hereafter). In the Eulerian frame $Gravity = [0, 0, 9.81 m/s^2]$).

$$Gravity_{(bf)} = Tbi * Gravity \tag{C.2}$$

4. Calculation of linear body frame accelerations for each axis (x-y-z, individual experiments).

$$Acceleration_{(bf,linear)} = Accelerometer - Gravity_{(bf)} \tag{C.3}$$

5. Window and FFT-High-pass filter for linear accelerations (x-y-z, individual experiments, Section 6.2.2).
6. Aggregation and Kalman filtering for linear body frame accelerations and angular velocities per axis using the equations Eq 6.8 and 5.3. The result is a statistically representative set of 3D linear accelerations and 3D angular velocities from all the individual experiments (12 for the sphere and 12 for the pebble shaped sensor).
7. Calculation of linear velocities with integration of the estimated linear acceleration signal.
8. FFT-High-pass filter of linear velocities (Section 6.2.2).
9. Calculation of Kinetic Energy per axis (Equation 6.9).

C.2 Summary for Euler Frame Calculations

1. Derivation of 3D linear body frame velocities and Quaternion rotation matrix (Appendix C.1).
2. Rotation of linear velocities in the Eulerian frame using Equation 6.14.
3. Calculation of Translational Kinetic Energy (Equation 6.15).
4. Integration of the linear velocities to derive instantaneous displacements int eh Eulerian frame.
5. FFT-High pass filter of instantaneous displacements.

APPENDIX D

SUMMARY QUATERNION ALGEBRA

The quaternions can be written in the form

$$a = a_1 + a_2 i + a_3 j + a_4 k \tag{D.1}$$

The quaternion conjugate is given by

$$\bar{a} = a_1 - a_2 i - a_3 j - a_4 k \tag{D.2}$$

The sum of two quaternions is then

$$a + b = (a_1 + b_1) + (a_2 + b_2)i + (a_3 + b_3)j + (a_4 + b_4)k \tag{D.3}$$

and the product of two quaternions is

$$\begin{aligned} ab = {} & (a_1 b_1 - a_2 b_2 - a_3 b_3 - a_4 b_4) + (a_1 b_2 + a_2 b_1 + a_3 b_4 - a_4 b_3)i \\ & + (a_1 b_3 - a_2 b_4 + a_3 b_1 + a_4 b_2)j + (a_1 b_4 + a_2 b_3 - a_3 b_2 + a_4 b_1)k \end{aligned} \tag{D.4}$$

The quaternion norm is therefore defined by

$$n(a) = \sqrt{\bar{a}a} = \sqrt{a_2^2 + a_1^2 + a_3^2 + a_4^2} \tag{D.5}$$

In this notation, the quaternions are closely related to four-vectors.
Quaternions can be interpreted as a scalar plus a vector by writing

$$a = a_1 + a_2 i + a_3 j + a_4 k = (a_1, a) \tag{D.6}$$

where $a = [a_2 a_3 a_4]$. In this notation, quaternion multiplication has the form

$$q_1 q_2 = (s_1, v_1).(s_2, v_2) = (s_1 s_2 - v_1 . v_2, s_1 v_2 + s_2 v_1 + v_1 x v_2) \tag{D.7}$$

Division is uniquely defined and the inverse (reciprocal) of a quaternion is given by

$$a^{-1} = \frac{\bar{a}}{[n(a)^2]} \tag{D.8}$$

and the norm is multiplicative

$$n(ab) = n(a)n(b) \tag{D.9}$$

A rotation about the unit vector $\hat{n}$ by an angle θ can be computed using the quaternion

$$q = (s, v) = (\cos(\frac{1}{2}\theta), \hat{n}\sin(\frac{1}{2}\theta)) \tag{D.10}$$

The components of this quaternion are called Euler parameters. After rotation, a point $p = (0, p)$ is then given by

$$p' = qpq^{-1} = qp\bar{q} \tag{D.11}$$

since $n(q) = 1$.

A concatenation of two rotations, first q_1 and then q_2, can be computed using the identity

$$q_2(q_1 p\bar{q_1})\bar{q_2} = (q_2 q_1)p(\bar{q_1}\bar{q_2}) = (q_2 q_1)p\overline{q_2 q_1} \tag{D.12}$$

APPENDIX E

KALMAN FILTER EQUATIONS AND R-T-S SMOOTHER

Consider the following discrete-time linear system described by:

$$\begin{cases} x_{k+1} = \Phi_k x_k + w_k \\ y_k = H_k x_k + v_k \end{cases} \tag{E.1}$$

where $k = 0,1,...,N, X_k \in R^n$ is the state vector, $Y_k \in R^m$ is the measurement vector, $W_k \in R^n$ and $V_k \in R^m$ are process and measurement noises, respectively. The sequencesW_k and V_k are assumed to be zero mean Gaussian white noise sequences as: $E[w_k] = 0, E[v_k] = 0, E[w_k w_j^T] = Q_k \delta_{kj}, E[v_k v_j^T] = R_k \delta_{kj}$

The initial state x_0 is assumed to be a Gaussian random variable with mean μ_0 and covariance P_0. It is assumed that the process and measurement noise sequences and the initial state random vector are mutually uncorrelated.

Given the model E.1, the Kalman filter formulation in covariance/information mode, used in the forward pass of the smoother, is then described by

Prediction:

$$\hat{x}_{k+1|k} = \Phi_k \hat{x}_{k|k} \tag{E.2}$$

$$P_{k+1|k} = \Phi_k P_{k|k} \Phi_k^T + Q_k \tag{E.3}$$

Update:

$$\hat{x}_{k+1|k+1} = \hat{x}_{k+1|k} + K_{k+1}(Y_{k+1} - H_{k+1}\hat{x}_{k|k} \tag{E.4}$$

$$P^{-1}_{k+1|k+1} = P^{-1}_{k+1|k} + H^T_{k+1} R^{-1}_{k+1} H_{k+1} \tag{E.5}$$

$$K_{k+1} = P_{k+1|k+1} + H_{k+1}^T R_{k+1}^{-1} \tag{E.6}$$

Then the R-T-S smoothing algorithm is described by

$$\hat{x}_{k|N} = \hat{x}_{k|k} + G_k(\hat{x}_{k+1|N} - \hat{x}_{k+1|k}) \tag{E.7}$$

$$P_{k|N} = P_{k|k} + G_k(P_{k+1|N} - P_{k+1|k})G_k^T \tag{E.8}$$

$$G_k = P_{k|k}\Phi_k^T P_{k+1|k}^{-1} \tag{E.9}$$

and the recursion is a backward sweep from $k = N$ down to $k = 0$.
The computationally intensive parts of the smother are:

- the smoother gain, given by Equation E.7 (matrix inversion).
- the smoother covariance recursion, Equation E.6, difference of positive semi-definite matrices that is subject to numerical instability.

Zhang and Li [1996] reduce complexity with an algorithm based on the SVD form of the smoother (Singular Value Decomposition)

APPENDIX

GISRUK Paper

Constraints on accurate positioning of mobile environmental sensors

G. Maniatis[1,2], T.B. Hoey[1], J. Sventek[2], R. Hodge[3]

[1]School of Geographical and Earth Sciences, University of Glasgow; [2]School of Computing Science, University of Glasgow; [3]Department of Geography, Durham University
Telephone: +44 141 330 2000
Email of corresponding author: g.maniatis.1@research.gla.ac.uk

1. Introduction

The availability of GNSS positioning techniques with global coverage offers considerable potential for localization in GIS. The widespread use of GPS provides users with high precision and relatively high accuracy in real time within a global reference frame. To realise the potential of automated, wireless environmental monitoring systems in inaccessible dynamic environments, location often needs to be known with high accuracy and at high frequencies. For example, the movements of a landslide or a river pebble are rapid but episodic and tracking the periods of motion requires positioning at high frequencies. While this may appear a problem that can be resolved readily by deployment of a dense in situ network of transmitters, so enabling position to be determined by triangulation with in-built redundancy where more than three transmitters are used, the speed of movement and consequent need for very high precision, mean that limits on the precision of time information provides a significant constraint. Here we investigate the origins of this problem and evaluate potential solutions in the context of a mobile sensor designed to track particle movement in natural systems.

While the problem addressed is generic, our specific application here concerns sediment transport in river or coastal environments. Sediment transfer over distances of 10 to 1000 m is considered, representing a range of settings (from small streams to the most active parts of large rivers or gravel beaches).

The global reference frame of GNSS poses two limitations for the applied technology: a) the locality problem - fixing the position of a sensor provides a challenge of finding the optimal resolution of the positioning grid to provide desired spatial accuracy; and, b) the mobility problem - as the sensor moves, tracking its position is subject to a number of movement-related constraints (such as the minimum detectable movement, the speed of the movement, and whether movement is continuous or episodic) and is a function both of spatial accuracy and of temporal accuracy and precision.

The locality problem can be approached using network-based solutions: building a local sub-grid in each sector of the global grid with optimal spatial configuration increases spatial resolution and maximises accuracy in particular deployments. The mobility problem is less readily resolved and the only viable solutions are currently restricted to special cases of the full range of the possible movement-tracking cases. The most difficult of these cases demand

high-frequency positioning in locations that cannot be connected directly to the global grid due to technological or physical limitations. For example, underwater tracking where there is a need to track complex movements (whether of mammals, underwater robots or UAVs in oceans, or sediment grain movement in shallow fresh-waters) in a medium where the most readily applied technology can only be made operational, if at all, after extensive modifications.

Tracking of sensors that are, at least temporarily, submerged, is our focus here. The demand for oceanic tracking triggered the development of acoustic (Sonar) and optical wavelength (IR) based techniques as an alternative to radio frequency (RF) based approaches, since the latter are difficult to apply underwater at commonly used frequencies. Underwater RF localization has been explored theoretically and experimentally for both marine and fresh waters and is physically possible at low frequencies (from the VLF band of 3-30kHz for sub-sea applications to the VHF band of 30-300 MHz for river systems) which are incompatible with the operational range of contemporary GPS (1176-15575 MHz, UHF band) [Che et al 2010].

Aside from the problem of RF propagation in water, the key constraint affecting the use of GPS in our application is its precision. GPS is a radio signal localization technique, specifically Time of Arrival or Time Difference of Arrival. GPS operates by monitoring the delay of a radio signal in a triangulation scheme due to distance differences between the nodes of this scheme. Since radio waves propagate at the speed of light ($3 \times 10^8 m.s^{-1}$), the delay between Earth and a typical GPS satellite is c. 100 milliseconds. For the scale of this application (meters to kilometres) the required delay is of the order of nanoseconds, a temporal resolution/precision achieved by processors with clocks above 1GHz. The energy demands of these processors currently make them inefficient for mobile applications, where less powerful but more efficient processing units are typically deployed with clocks up to 16 MHz (thus capable of processing at a temporal resolution of order 10 μs).

Two approaches can be taken to resolve these issues: a) firstly, alternative signal-based localization techniques can be developed. The power signal changes as a known function of distance and time and this can be measured using a Radio Signal Strength Indication, RSSI, value. Although theoretically feasible, this approach is at an early stage of development and a number of technological challenges remain, mainly related to signal inconsistency caused by environmental variability (signal attenuation, fading, refraction) and to the non-standardization of the on-board radio boards (each radio chip deploys different circuitry and is calibrated under different conditions) [Chen et al. 2010]. b) secondly, localization can be considered as an inertial navigation problem; i.e. consider a system with known initial position, movement away from which is resolved through continuous monitoring of accelerations and orientation changes (often referred in the literature as dead-reckoning localization) . The basic challenge these techniques face is error accumulation, mainly due to low precision time references (which need to be both real-time and external to the system) since all subsequent positions are determined in reference to an initial position. Delays that are insignificant for static or slowly changing systems (such as the very small time difference between a sensor making a measurement and these data being stored in a digital memory) accumulate quickly for large monitoring times [Bao et al. 2014].

2. Conceptual Description of the proposed system

To address the level of position resolution needed to resolve the movement of individual sediment grains and record the scheme of forces that define this movement, we propose a micro-location system that combines radio signal-based localization with INS-dead-reckoning localization techniques.

Specifically, we assess the feasibility of a system in which a mobile sensor logs acceleration and orientation data while simultaneously transmitting a radio signal to a local network. The design criteria of such a system can be divided into two categories: the criteria related to physical sensing and the criteria relevant to the accurate positioning of the sensor.

2.1 Physical Sensing-Sensor design criteria.

These criteria are the accuracy and the resonance of the dynamic data that will be sensed and logged by the mobile sensor-transmitter. These criteria are strongly related to the understanding of the sediment transport processes in our application and frame all the specific characteristics of the sensor (computational, electrical and physical).

The scheme of forces in which the sensor must survive and operate is defined by local accelerations in a range from 0 to ±100 g. This range is reported in the relevant literature [Vatne et al. 2008] as an ambiguous measurement which currently includes both translational accelerations related to sediment movement during gradual discharge fluctuations and also rapid shocks applied on individual grains during rapid flow changes and (most probably) grain-grain interactions.

The magnitude of these forces defines the specifications for the mobile sensor (from the capabilities of the on-board processor and the memory capacity of the logging system to the robustness of the sensor-enclosure [Maniatis et al. 2013]). The required measuring range for the acceleration-impact sensor (magnitude of an order of 100g and sampling frequency of c. 100Hz) is itself a technological challenge in a context of long-term mobile real-time sensing [Frank 2003].

2.2 Localization-tracking related criteria.

The criteria of this type correspond to the accuracy and the representativeness of the positional information extracted from the system defining the specifications of both the mobile transmitter and the network used for localization.

This aspect of the system is designed in respect to the mode of movement that needs to be resolved (individual grain movements with a stochastic character) and the high force-impact underwater environment. At a sensor –transmitter level we propose the INS- dead-reckoning approach, using gyroscopes and magnetometers to define orientation changes during the movement. The final multi-sensor will simultaneously log accelerations (three accelerometers), changes of angular velocity (gyroscope) and the direction of a constant reference point (the centre of the earth using the magnetometer). This information allows the resolution of the 6 degrees of freedom of the sensor-movement according to the INS methodology. The logged data can be acquired post-event (through a USB interface for example) but can also be sent wirelessly to the local network through a radio transmitter in real-time.

At a local network level, we propose a system of antennas-receivers in order to apply radio-signal based localization techniques and reduce the error accumulated in the logged data. The basic constraints for the radio signal transmission are: a) the fact that the transmitter will be (at least temporarily) submerged; and, b) it must take place at a frequency adequate to permit real time correction of position through the definition of multiple reference points. This frequency is defined by the range of the possible displacements of the mobile-transmitter and can vary from very low values (≤1 Hz for zero, or very slow, displacements) to frequencies that challenge the limits of radio-based localization and correspond to rapid displacements at the high end of the occurring forces (close to the 100Hz sampling frequency considered for the accurate sensing of large impacts).

3. Initial Assessment of positional accuracy.

The scale of the monitoring system does not permit the direct use of GPS. As a result we consider the localization principal applied in the GPS for the local network we design. This multilateration technique uses the Time of Arrival (ToA) of the transmitted radio signal to the different receivers or the Time Difference of Arrival (TDoA) between two (or more) receivers to calculate the distances between the transmitter and the receivers which are typically located at pre-defined reference points. Distances are calculated using the propagation velocity of the signal and a linear propagation model (propagation velocity= speed of light= distance*time of signal propagation). A minimum of three linearly independent distances are needed to locate the transmitter (with 3 Cartesian coordinates) in the reference frame defined by the receivers (trilateration) [Munoz et al. 2009].

The core of this approach is the assumption that the time differences (occurring at a scale of nanosecond for distances of meters to km) can be detected by the receivers. For our specific application we face a technical limit since the relative instrumentation and controlling software applications are typically capable of synchronization at an order of micro-second [Verdone et al 2010]. To demonstrate this limit we set up a simulation of localization using a random walk in three stages:

Stage 1: At first we model a 2-D unbiased scaled random walk where the four receivers are located at distances appropriate to our application (100 m). The transmitter is capable of performing of 1 meter step per iteration. Each iteration corresponds to a time difference of one second thus the sensors moves with a constant velocity of $1 m.s^{-1}$ towards four predefined directions (North -South along the y axes and East-West along the x-axes) one of which is chosen randomly for every individual step. Our interest is to record the time of arrival of a signal with a propagation velocity of $3 \times 10^8 m.s^{-1}$ received by four receivers located at predefined locations which form an area of 100x100 m^2 (L x W) [Figure 1.1]. The localization error records the absolute difference of the location of the transmitter as recorded by the random walk algorithm and the location detected by the multilateration algorithm [Figure 1.2].

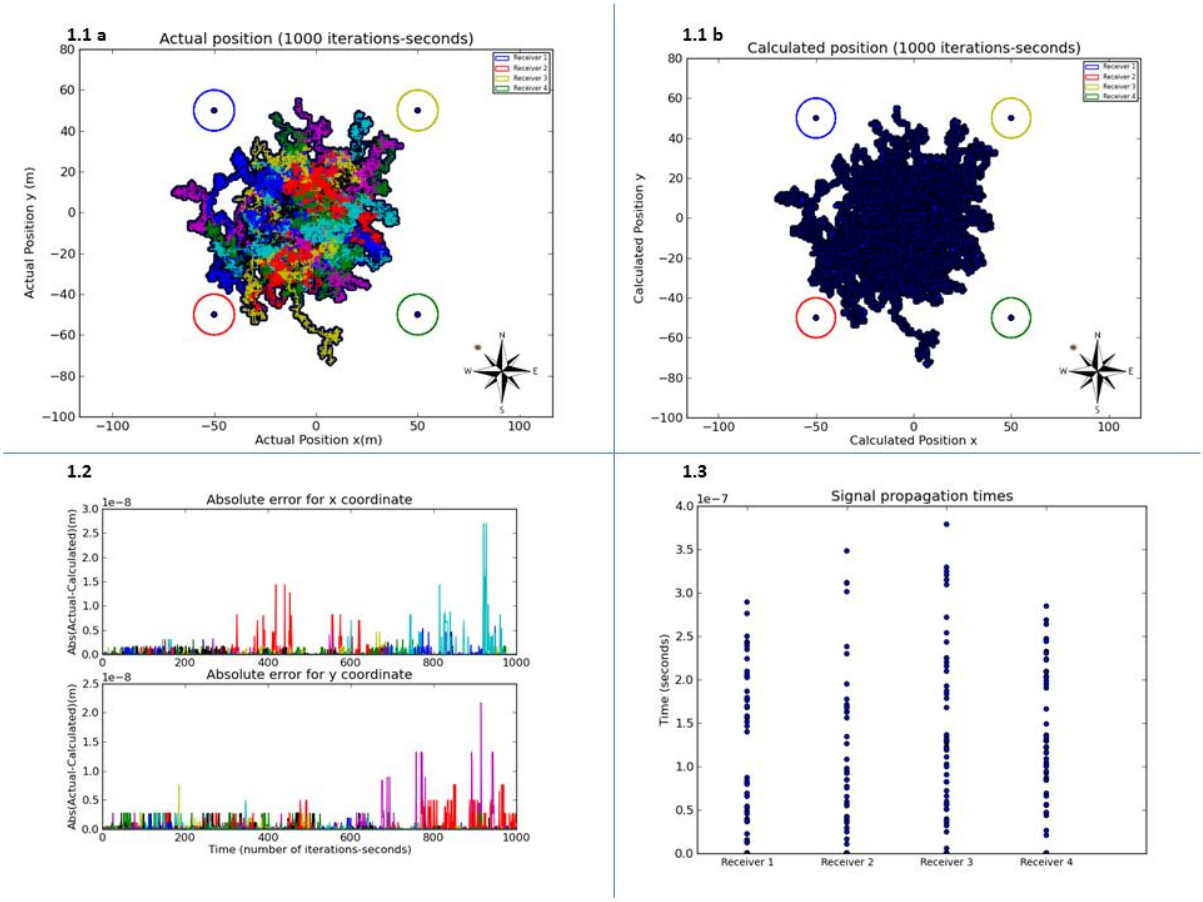

Figure 1. : Simulation of 60 unbiased random walks and positioning using multilateration method (radio-localization principal). The simulation is scaled: 1 unit corresponds to 1 meter (m) and each iteration represents a time difference of 1 second. The moving objects represent sensor-transmitters moving in a coverage area defined by a grid of four receivers located at a predefined positions (Figure1.1a). The transmitter is capable of moving towards four predefined directions (N, S, W, E), one of which is chosen randomly for every iteration. The sensor moves 1 unit-meter every iteration-second (representing a velocity of 1 $m.s^{-1)}$. Figure 1.1b shows the calculated positions after the application of the multilateration algorithm**. Figure 1.2**.Absolute positional error. The localization error is calculated as the absolute difference between the position recorded from the random walk algorithm (actual position in Figure 1.1 a.) and the position detected from the mulilateration algorithm. Fig 1.2 b. **Figure 1.3** Signal propagation times transmitted from the moving sensor as recorded by the 4 receivers. The signal propagation velocity is $3x10^8$ $m.s^{-1}$.

Stage 2: The second stage models a more realistic scenario where we bias the 2D random walk to mimic the movement in a river flowing along the x-direction (from West to East). We specifically restrict the movement between two horizontal limits in the y-direction (North and South simulating the banks of a river), we minimize the probability of moving towards the -x direction (West-upstream) and we assign a double distance movement (2 meters per step) when moving towards the +x direction (East -downstream direction /direction of flow). The location of the receivers is set to represent the reception from river banks producing an area relevant to the simulation of stage 1 (length of area is 100m). The signal propagation model and the velocity of the transmitter (distance per iteration step) are identical to the previous stage. The mode of the movement of the transmitter affects the accuracy of the detected position [Figure 2]. The high step velocity ($1m.s^{-1}$) leads the sensors to move outside the area defined by the positions of the receivers.

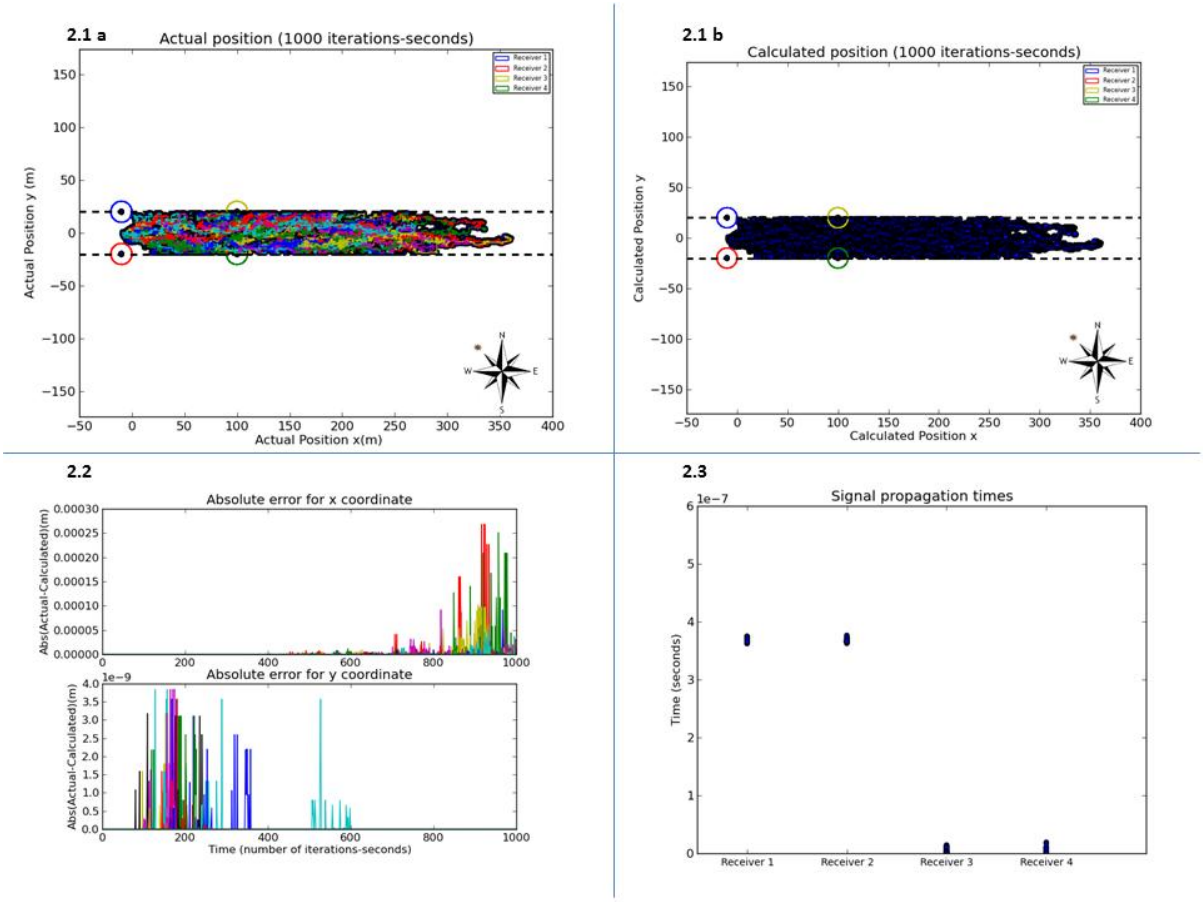

Figure 2. Simulation of 60 biased random walks and positioning using multilateration method (radio-localization principal). The simulation is scaled similarly to Figure1. The mode of movement is different since the random walk is restricted along the y direction (North-South) between two linear limits which represent the river banks (at ±20m). In parallel the walk is biased along the x direction with zero probability for moving West (-x, representing upstream) and a double distance step of 2 unit-meters when moving East (+x, downstream) in order to mimic the movement in a river flowing from West to East. The minimum velocity is 1 unit-meter per iteration-second for the unbiased directions (1 $m.s^{-1}$). Figure 2.1 b shows the calculated positions after the application of the multilateration algorithm. **Figure 2.2**.Absolute positional error. The localization error is calculated similarly to Figure 1. We observe an increase of the error along the unrestricted direction (West-East, x direction) while the error is practically zero for the y coordinate suggesting a decrease in accuracy as the transmitter moves away from the area defined by the position of the receivers. **Figure 2.3** Signal propagation times transmitted from the moving sensor, recorded from the four receivers. Propagation velocity is $3x10^8$ $m.s^{-1}$.

Stage 3: Finally we extend the simulation in stage two by defining a more realistic velocity for the transmitter (0.4 $m.s^{-1}$) and by modifying the radio propagation model so it corresponds to underwater radio-transmission. Freshwater is typically modelled as a low loss medium, and the propagation velocity of the signal is calculated according to the following equation [Equation 1].

$$\upsilon = c/\sqrt{(\mu_r \varepsilon_r)} \qquad (1)$$

Where μ_r and ε_r are the relative permeability and relative permittivity of freshwater. The calculated propagation velocity of the radio signal in freshwater is approximately 3.3 x 10^7 ms^{-1}. For this demonstration we did not consider other parameters that significantly affect signal propagation (such as the water –air interface or the noise added by flow fluctuations). However none of these parameters changes the scale of propagation velocity [Sadiku 2007]. Our focus at this stage is to assess the effect of the delay of the radio signal from the water

interference to the timestamps recorded by the receivers [Figure 3].

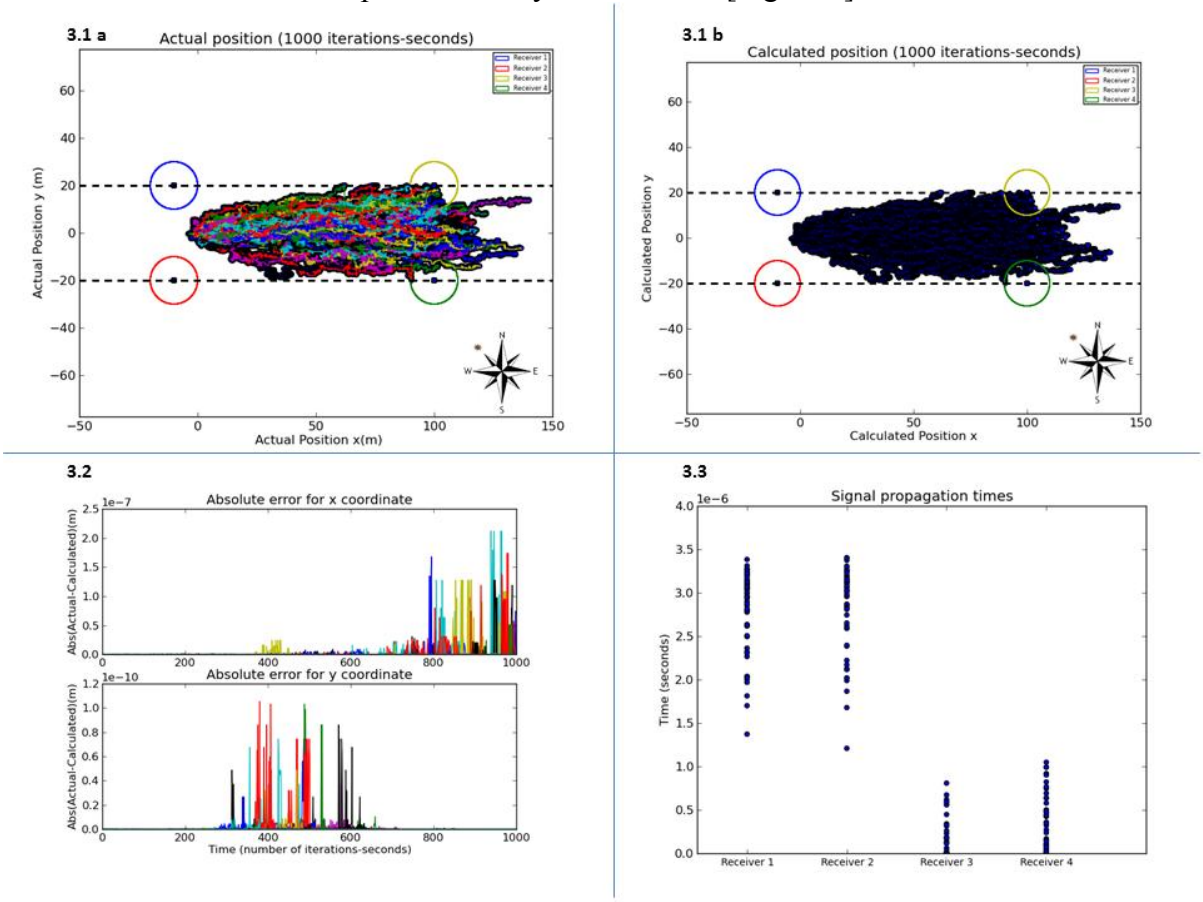

Figure 3. Simulation of 60 biased random walks and positioning using multilateration method (radio-localization principal). The scale and the mode of movement are identical to Figure2. The minimum velocity is set at a more representative 0.4 unit-meter per iteration-second for the unbiased directions (0.4 $m.s^{-1}$). Figure 3.1 b shows the calculated positions after the application of the multilateration algorithm. **Figure 3.2.** Absolute positional error. The localization error is calculated similarly to Figures 1 and 2. We observe a behaviour similar to the simulation of Figure 2. However the differences are at a scale of 10^{-7} to 10^{-10} unit- meters since the maximum distances are significantly smaller (<150meter-units compared to the 350 meter-units max distance of the previous simulation). **Figure 3.3** Signal propagation times transmitted from the moving sensor, recorded from the 4 receivers. Propagation velocity is set to the value for radio wave propagation in freshwater (3.3×10^7 ms^{-1}). The delay of the signal leads to record propagation times at the order of micro-seconds (Receivers 1 and 2). However a significant number of times still occur at an order 10^{-7} seconds or less (Receivers 3 and 4).

4. Alternative localization techniques.

Two results from the above simulation challenge the feasibility of the GPS technique for this application. Firstly, the time differences for the received signal occur constantly at a scale of equal or smaller to micro-second even for the underwater case where the signal is delayed (Figure 3.3). Secondly we observe an effect of the mode of the movement on the accuracy of the calculated position. For the unbiased random walk the errors along the y and the x direction are comparable and do not reveal an obvious structure that would imply error accumulation. On the contrary, for the biased –restricted walk (simulations 2 and 3) we observe an increasing error along the unrestricted direction (x coordinate) which can be interpreted as a loss of accuracy when the transmitter moves close or over the limits of the coverage area defined by the receivers.

The above considerations lead us to assess alternative radio-based localization techniques. These techniques are based on the measurement of the strength of the received signal with specific metrics (such as the Radio Signal Strength Indicator) in an attempt to replace the propagation velocity-distance model used in the GPS framework with a radio signal strength-distance model. The calibration of this model is an open research challenge and previous applications are typically restricted to indoor short –range environments [Park et al. 2014]. However the method has increased in performance the recent years and it has the potential for long-range application since the latest studies suggest a stabilization of the metrics (decrease of variability) at distances greater than 10 meters which can permit the robust modelling at those scales [Asadpour et al. 2013]. Other experimental radio -localization techniques suggest different types of modulation, or different time synchronization metrics (relevant to Doppler shifts that can occur at the specific RF band) but are not currently applicable for freshwater environments [Hattab et al 2013].

5. Conclusion and Future Work

Here we present an a example case that can challenge the reliability of the positional data stored in a GIS. Despite the special characteristics of the environment we are interested into, similar constrains are relevant to all the mobile applications of similar scale and implement real-time radio-based positioning (GPS measurements). The error existing in the data from this type of localization needs to be carefully considered since it stays inherited to all the possible complex transformations performed during the data analysis-manipulation process of high-level geo-location applications.

For the specific application we work on three separate research challenges.
At first, the success of our approach is dependent on the robustness of the calibration of the radio signal – distance relationship which remains an open research topic [Chakraborty et al. 2009]. We work on providing a robust signal strength-signal model for underwater radio transmission while assessing possible alternative techniques.

Secondly, to maximise the use of information gathered from mobile environmental sensors and combine this with positional data it is necessary to provide a common mathematical framework where both of these measurements can be synchronized and interpreted. Optimising the positioning system in terms of accuracy and computational efficiency depends on *a priori* understanding of the mathematical framework to be used to analyse the data. There is a need to formally combine very different mathematical approaches to extract information and perform useful predictions about localization even at an experimental stage. In the combined and scalable system that we introduce, the deterministic description of Euler transformations for rigid body movement in 3D-space [Akeila et al. 2010] is combined with the position estimate from purely stochastic techniques, such as Kalman filtering and other Monte-Carlo related descriptions [Zanella et al. 2012]. This framework will also permit the nesting of the local wireless network within a global coordinate system and will have general applicability.

Finally we try to enhance the understanding of the physically sensed data and use them in the contemporary fluvial morphodynamics and sediment transport processes context. Our interest is, through a sequence of fluvial experiments and mathematical simulations, to provide robust calibration data and test the hypotheses used in the predictive and description models and are relevant to the local dynamics at grain scale [Hodge et al 2011].

6. Acknowledgements

Georgios Maniatis is funded by a Kelvin Smith Scholarship, provided by the University of Glasgow.

7. References

AKEILA, E., SALCIC, Z., SWAIN, A.: "Smart pebble for monitoring riverbed sediment transport". *Sensors Journal, IEEE*, 2010, 10.11: 1705-1717.

ASADPOUR M., GIUSTINIANO D. and HUMMEL K A.: "From ground to aerial communication: dissecting WLAN 802.11 n for the drones". In: *Proceedings of the 8th ACM international workshop on Wireless network testbeds, experimental evaluation & characterization*. ACM, 2013. p. 25-32.

BAO H, Wong W-C: "A Novel Map-Based Dead-Reckoning Algorithm for Indoor Localization". Journal of Sensor and Actuator Networks. 2014; 3(1):44-63.

CHAKRABORTY U., TAPAS T., and CHATTERJEE R. P.: "Exploiting the loss-frequency relationship using RF communication in underwater communication networks." Computers and Devices for Communication, 2009. CODEC 2009. 4th International Conference on. IEEE, 2009.

CHE X, WELLS I., DICKERS G., KEAR P., and GONG X.: "Re-evaluation of RF electromagnetic communication in underwater sensor networks ". IEEE Communications Magazine, vol. 48, no. 12, pp. 143–151, 2010.

CHEN, Y., TERZIS, A: "On the mechanisms and effects of calibrating RSSI measurements for 802.15. 4 radios. In: Wireless Sensor Networks. Springer Berlin Heidelberg, 2010. p. 256-271.

FRANK F., and WALKER J., eds. "Fundamentals of noise and vibration". CRC Press, 2003.

HATTAB G., EL-TARHUNI M, AL-ALI M,, JOUDEH T., and QADDOUMI N.: "An Underwater Wireless Sensor Network with Realistic Radio Frequency Path Loss Model." International Journal of Distributed Sensor Networks, vol. 2013, Article ID 508708, 9 pages, 2013.

HODGE, R.A., HOEY, T.B., SKLAR L. S: "Bed load transport in bedrock rivers: The role of sediment cover in grain entrainment, translation, and deposition". *Journal of Geophysical Research: Earth Surface (2003–2012)*, 2011, 116.F4.

MANIATIS G., HOEY T., and SVENTEK J.: " Sensor Enclosures: Example Application and Implications for Data Coherence". *Journal of Sensor and Actuator Networks*, 2013, 2.4: 761-779.

MUNOZ D. et al.: "Position location techniques and applications". Academic Press, 2009.

PARK, G. JEON, M. and OH, C.: "Indoor Wireless Localization Using Kalman Filtering in Fingerprinting-based Location Estimation System". International Journal of Software Engineering and Its Applications Vol.8, No.1 (2014), pp.235-246.

SADIKU M.: "Elements of Electromagnetics ", Oxford University Press, New York, NY, USA, 2007.

VATNE, G., TAKØY N. Ø., SKÅRHOLEN, T., BEYLICH, A. A., and BERTHLING, I.: "Bed load transport in a steep snowmelt-dominated mountain stream as inferred from impact sensors". Norsk Geografisk Tidsskrift-Norwegian Journal of Geography, 62(2), 66-74.2008.

VERDONE, Roberto, et al.: "Wireless sensor and actuator networks: technologies, analysis and design". Academic Press, 2010.

ZANELLA F., CENEDESE A..: "Multi-agent tracking in wireless sensor networks: implementation". In: *Proceedings WSEAS-ITCN12*, 2012.

APPENDIX G

JSAN Paper

J. Sens. Actuator Netw. **2013**, *2*, 761-779; doi:10.3390/jsan2040761

OPEN ACCESS

Journal of Sensor and Actuator Networks

ISSN 2224-2708

www.mdpi.com/journal/jsan

Article

A New Method for Rapid Prototyping of Purpose-Specific Sensor Enclosures: Example Application and Implications for Data Coherence

Georgios Maniatis [1,2,*], Trevor Hoey [2] and Joseph Sventek [1]

[1] School of Computing Science, University of Glasgow, Sir Alwyn Williams Building, Lilybank Gardens, Glasgow G12 8QQ, Scotland, UK; E-Mail: Joseph.Sventek@glasgow.ac.uk

[2] School of Geographical and Earth Sciences, University of Glasgow, East Quadrangle, University Avenue, Glasgow G12 8QQ, Scotland, UK; E-Mail: Trevor.Hoey@glasgow.ac.uk

* Author to whom correspondence should be addressed; E-Mail: g.maniatis.1@research.gla.ac.uk; Tel.: +44-0-1413-302-000.

Received: 15 October 2013; in revised form: 2 December 2013 / Accepted: 2 December 2013 / Published: 11 December 2013

Abstract: Sensors deployed in natural environments, such as rivers, beaches and glaciers, experience large forces and damaging environmental conditions. Sensors need to be robust, securely operate for extended time periods and be readily relocated and serviced. The sensors must be housed in materials that mimic natural conditions of size, density, shape and roughness. We have developed an encasement system for sensors required to measure large forces experienced by mobile river sediment grains. Sensors are housed within two discrete cases that are rigidly conjoined. The inner case exactly fits the sensor, radio components and power source. This case can be mounted within outer cases of any larger size and can be precisely moulded to match the shapes of natural sediment. Total grain mass can be controlled by packing the outer case with dense material. Case design uses Solid-Works™ software, and shape-matching involved 3D laser scanning of natural pebbles. The cases were printed using a HP Designjet™ 3D printer that generates high precision parts that lock rigidly in place. The casings are watertight and robust. Laboratory testing produces accurate results over a wider range of accelerations than previously reported.

Keywords: environmental sensors; wireless sensors; robust enclosures; rapid prototyping

---

1. Introduction

Many contemporary sensing applications entail the remote, continuous, unattended and *in-situ* monitoring of natural processes. Such applications are possible, due to recent developments in the fields of Micro-Electro-Mechanical Systems and Wireless Sensor Networks and can pose technologically challenging demands, which were not *a priori* incorporated in the design/optimization criteria for either of these two fields [1–3].

For environmental deployment, the production of flexible, robust sensor housings is an essential pre-requisite. Casings affect the overall usefulness of any monitoring system, since they define the limits of *in-situ* monitoring without the risk of damage, as well as other practical aspects, such as the ease of recovery or repair. These aspects become even more important in harsh and very variable natural environments, such as the ocean [4], volcanoes [5], glaciers [6] and rivers (on Earth and other planets [7]), where complex processes take place, the understanding of which is based on the quality of the sensed data.

In parallel with practical considerations, it is crucial to understand how the sensor itself affects the process of data-acquisition, hence the quality of the derived data and the general theoretical context in which such data are analysed. The effects of the physical properties (e.g., shape, weight, density) of the sensor are especially important in the case of inertial sensors that are deployed for monitoring movement (such as accelerometers and gyroscopes), because the sensors inevitably become part of the process.

We are particularly interested in sensors that measure aspects of grain movement in rivers. The work reported here is based upon our experience in constructing wireless sensor systems to perform such measurements. Later phases of the work will address sensor design, power and radio communication aspects. Here, we particularly focus on a repeatable process for generating robust sensor casings that guarantee the physical and electrical integrity of the sensor and enable highly accurate calibration of the sensor *in-situ*.

1.1. Problem Statement: Motivation

Earth-surface processes often involve the movement of material at scales ranging from single grains to mass movements affecting entire hillslopes [8]. To assess material transport rates, morphological changes and environmental hazards, a common monitoring strategy is to tag and track a number of individual grains. This approach generates understanding of the displacement of sediment during events, but is often restricted to before- and after-event comparisons. Many methods have been devised to tag tracer grains, ranging from simple visual identification (painting) to very complex and technologically challenging techniques, such as the deployment of magnetic and radio frequency tags [9–11].

Advances in sediment transport theory have been delayed by the absence of suitable technology to test theoretical predictions [12]. The lack of continuous data with accurate positional and timing references precludes reliable mathematical and statistical descriptions of the system, so restricting the use of these predictions [13].

1.2. Casing Design Criteria Related to the Natural System

The shape of natural sediment grains exerts a strong influence over their movement [14–17]. Theoretical analyses, however, have assumed idealised spherical grains (e.g., Wiberg and Smith [18], *etc.*); this simplification makes the solution of the force-balance equations feasible, and the consequent results have been found to have widespread applicability (e.g., Hodge *et al.* [19]). We begin with a spherical case, the performance of which can be precisely evaluated against theory and then generalise to the full range of natural shapes.

As well as grain shape, the density of the sensor must replicate that of natural material. The deployment of sensors, such as accelerometers, is useful only if the sensor behaves as a rigid body of uniform density (something that can be assumed for individual natural grains). The overall density and distribution of mass within the sensor must match those of natural materials without affecting the operation of the device.

The material properties of the case (such as the roughness of the surface or the plasticity) also affect the quality of the data. Experience from previous field studies shows that the design criteria include several environmental factors, such as chemical weathering of the case or its trapping by trees or debris, that affect greatly the long-term deployment of the sensor. These factors cannot be addressed if the system optimization is based exclusively on electronics-computing-related optimization criteria.

1.3. Scope and Structure of the Paper

Here, we present the first results from the development of a new mobile sensor, designed for acquiring data representative of the instantaneous forces experienced by individual pebbles in a river or a similar natural environment. We present a general framework that can potentially address one of the key challenges, the construction of adequate sensor casings. We discuss how the combination of available 3D modelling tools and fast prototyping technology (3D printing) speeds up the development process and has the potential to enhance the coherence of the sensed data.

Section 2 provides an overview of previous work, addressing the core limitations that restrict the deployment of this type of sensor and reviews common approaches to sensor housing in underwater environments. In Section 3, we describe the prototyping method and how it enhances the securing of the sensor and the representativeness of the derived data. In Section 4, we describe initial test results from a prototype sensor and housing and assess these results in the context of potential field deployment of the system. In Section 5, we summarize the key points.

2. Previous Relevant Work

2.1. Sediment Transport Sensing

A number of projects have developed 'smart' loggers, instrumented with suitable sensors that are able to store data, which, in principle, can be used to resolve the actual paths taken by individual grains through post-event analysis [20–22]. This approach initially faced many technical challenges in acquiring, storing and transmitting the data [20,21]. Recent advances in the field of

Micro-Electro-Mechanical Systems have enhanced data acquisition and storage [23,24]. However, none of these projects has reached the stage of large-scale field deployment nor has published data that can be interpreted in a theoretical framework of natural sediment movement. The basic limitations are:

- **Mismatch between the measurement range of the deployed sensors and the magnitude of the physical processes.** Instantaneous point forces in natural systems are of greater magnitude than the measurement range of the sensors, and time-averaging leads to underestimates of peak forces. For example, static sensors used to measure river sediment movement record either the number of impacts or the maximum acceleration produced by impacting particles during a predetermined sampling interval [25,26]. These measurements are known to underestimate the impact forces on individual grains; however, they do suggest a range of forces the sensor has to operate reliably. Instantaneous vibrations of an order of 100 g [26] have been recorded, an order of magnitude higher than the measurement range of the inertial accelerometers deployed in the majority of previous applications. An exception was the Smart-Cobble [21], where the accelerometer alone was capable of capturing peak accelerations of 5,000 g, and the whole sensor had a measuring range of +/−480 g for an non-amplified signal (reducing to an operational range of +/−48 g after analogue amplification). This initial deployment of heavy-duty, high-range accelerometers was not continued in subsequent studies [23,24].

- **The development of robust and representative sensor casings/enclosures.** Deployment in natural environments requires durable, long-lasting and waterproof sensor housings. The sensor and housing together require physical characteristics (size, shape, weight, density, roughness) that ensure the representativeness of the data.

- **The lack of real-time reference.** A key limitation is that post-event analysis can be done robustly only in very controlled and well-defined time-space domains (which can be reproduced only in a laboratory setting), making difficult the connection with the real, highly variable conditions in a river system. Aberyawardana *et al.* [23] were able to extract very precise information about the entrainment conditions of a sensor, after a very detailed sensor-calibration process, but the post-event analysis of the data does not permit the accurate resolution of the path followed by their ”smart” pebble.

As a result of these issues, sediment movement is currently monitored using techniques that provide information on sediment movement over long time periods. The most advanced techniques involve attaching magnetic or Radio Frequency Identification-tags to natural or artificial pebbles, to identify the initial position of the tracers before a flood, and, then, either try to identify the rest of the positions of the tracers after the flood using hand-held detectors [27] or combine this technique with the tracking of the position of the tracers as they pass a known downstream position during the transport event, when the process is underway at the time of detection (e.g., [28,29]).

2.2. Underwater Sensor Housings

The majority of the existing underwater-sensing equipment concerns oceanographic applications[30], where there is a general requirement for robustness and long-lasting water-proof performance under very

high pressures and harsh conditions. Environmental applications deployed static sensing units until very recently [1], and underwater sensor mobility is investigated either in the context of robotics and vehicle navigation [31] or for depth adjustments towards the optimization of underwater acoustic networking techniques [32]. In rivers, the common sensing equipment used is also static (pressure sensors, chemical sensors, *etc*.), and except for not requiring durability under high pressures, the casing requirements are similar to oceanographic applications [33]. Consequently, the common sensor housing practice is the mounting of the sensors on a steady frame, which is protected by a durable cover made of PVC or metal.

Although the enclosures have never been addressed as a separate research challenge for underwater sensing systems [34], research has been performed for increasing the lifetime of the case against specific erosion processes, such as bio-fouling [35]. However, the contemporary casing design criteria do not restrict or specifically define properties, such as the size, the shape or the density of the enclosures, as long as durability is secured.

3. Experimental Section

3.1. Case Design Procedure

Initially, it is critical to ensure that the sensor will not be excessively stressed and will remain dry during operation. The second critical requirement is to keep the sensor immobile and permanently oriented in relation to the final frame of the case. Achieving this integrity would be difficult if the whole design matched a natural shape. Hence, we use a two-part design: (1) an internal case for the sensor that has an internal structure to fit the sensor, holding it in place and keeping it operational; and (2) an outer case that fits rigidly around the first and that defines the overall shape of the sensor.

3.2. Design and Construction of the Internal Case

This phase begins with a 3D representation (a 3D model) of the actual sensor platform around which the inner casing is to be constructed. Figure 1 shows the 3D models of two commercial platforms that were tested for this application: the AdvanticSys CM4000 mote platform [36], with the C01000 sensor platform [37] attached, and the G-node mote platform with the G-Colta sensor board attached, both produced by SOWNET Technologies [38] . The G-Colta sensor board is equipped with the ADXL-345 3-axial accelerometer with a maximum measurement range of +/−16 g produced by Analog Devices [39].

The software used to produce the designs was Solid-Works™ provided by Dassault Systèmes [40]. Although the sensor platforms can have relatively complicated 3D structures, it is possible to input the geometrical metrics at a 1:1 scale without significant error. However, a 3D scanner can be used in order to input an initial point-cloud sketch, which can then be manipulated through the software and corrected using manual measurements. The design can then be input into a 3D printer, producing a plastic 3D copy of the sensor's structure (this step is not essential and is used here for demonstration purposes). Figure 1 shows the digital and the actual copies for the two sensor platforms.

Figure 1. 3D models of tested sensors: (**A**) Digital design (left) and 3D printing, right of the CM4000 sensor mote with the compatible attached sensor board (right). The 3D design of the sensor is the base for the design of the case, making the fit exact; (**B**) Design and 3D printing of the G-node with the compatible G-Colta sensor board.

Given the 3D model of the sensor platform as a base, it is possible to modify regular 3D shapes to incorporate the structure of the mote with great accuracy. The tools provided by the software enable the production of regular shapes (like ellipses and cubes), so they have an inertial form shaped as the exact negative of the sensor platform's 3D structure, while keeping the overall shape unaffected. This exact fit of a void within the regular shape to the sensor platform guarantees that the sensor platform will be immobile within the inner casing and consistently oriented relative to the outer casing. This enables the platform to be calibrated appropriately. Examples of the designs and the constructed internal enclosures are shown in Figure 2 for the two sensor platforms.

3.3. Outer Case

The initial stage in the process of development of this type of purpose-specific sensor is the testing of commercial, off-the-shelf platforms to assess the level of customization needed to fulfil the requirements of the application. The casing developed for this calibration/evaluation procedure must be idealized and regular in order to permit comparisons. As a result, the methodology was initially developed for

idealized enclosures of regular shape and subsequently extended for the construction of cases with more realistic and natural shapes.

Figure 2. The development of internal case: (**A**) The sensor is accommodated rigidly by the internal structure of the case, matching the structure of the sensor, shown here for the CM4000 sensor-mote; (**B,C**) The final 3D printed case fits the sensor accurately, keeping the overall assembly compact and minimizing the movement of the sensor (examples for CM4000 (B) and G-node (C)); (**D**) Modifications can be made to accommodate special features, such as the modified antenna of the G-node, which can be secured within the spiral sculptured into the external surface of the case constructed for the G-node (D).

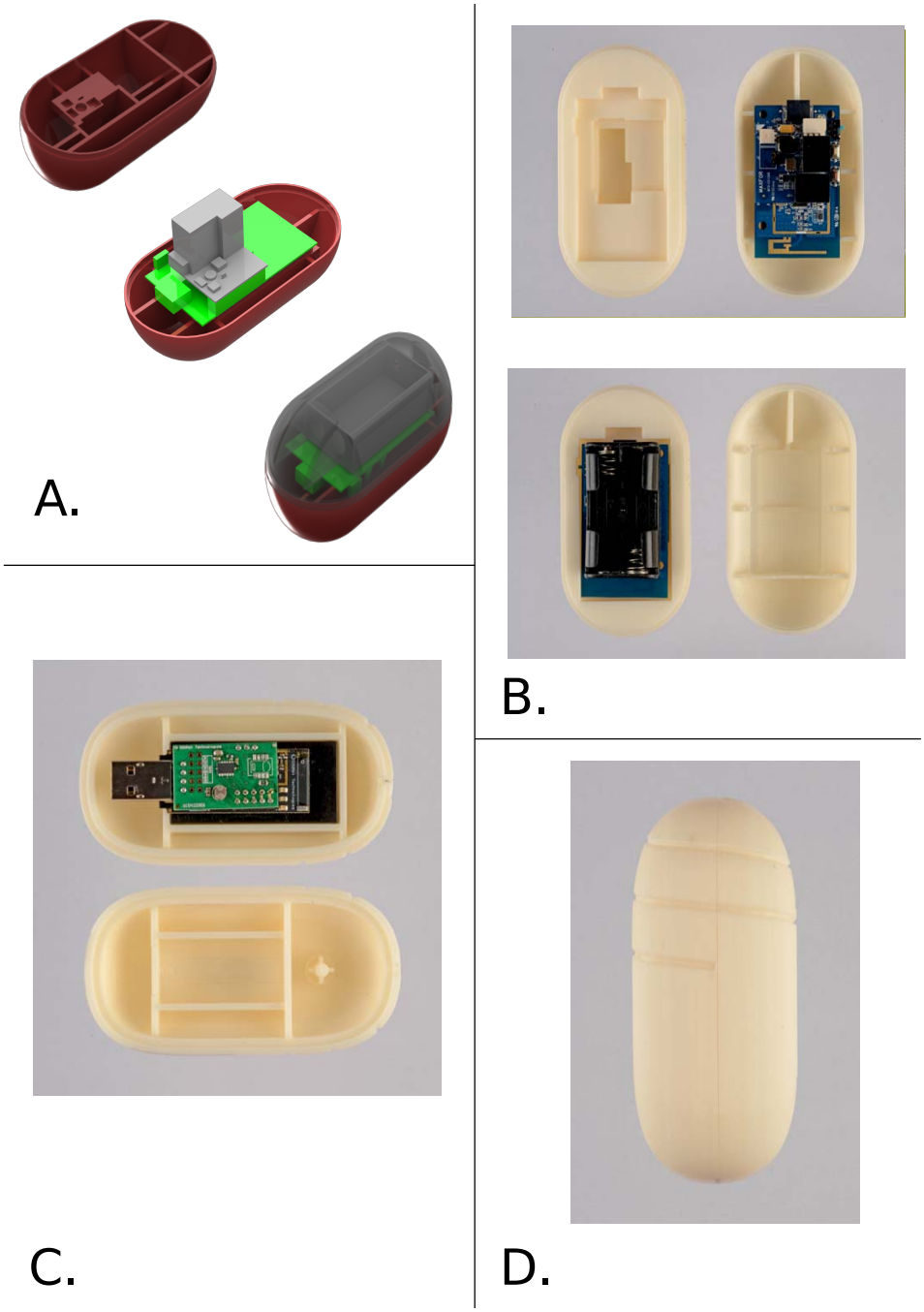

3.3.1. Cases of Regular Shape

We use the inner case as a base around which to construct an outer case that has a desirable shape. As previously, the software tools enable the enclosure of the inner case with high precision.

The outer case must also have the internal support required to ensure overall durability (to ensure that the plastic will not crack under sudden stress) and can be used to enhance the water-proofing of the entire system. Durability is achieved by designing strong internal support structures and waterproofing by sculpturing structures, like O-rings, which can be filled with insulating materials (e.g., silicon or rubber). In parallel, the internal structure can be used to control the density of the whole assembly. To achieve this, we constructed the outer case with support structures and void spaces that can be filled with materials of known density that enable control over total mass and density (Figure 3A).

A challenge is to enable easy access to the sensor when required without risking the case coming open during operation. This requirement is fulfilled by building locking structures into the joints that keep the case firm and rigid when it is closed but enable it to be opened by moving it in a specific way (Figure 3C).

3.3.2. Cases of Non-Regular Shape

Our ultimate goal is the construction of an outer case to simulate the movement of natural pebbles of variable shapes (hence, the sensor data is as representative as possible). Here, the major concern is to copy effectively the shape of a natural pebble and use it as prototype for the overall case.

For this purpose, the internal case is placed in a modified outer enclosure to generate a more natural shape. There is no single representative shape for any rock type or sedimentary environment [41], but modern scanning technology allows the replication of any shape.

We model two very different natural stones to illustrate the procedure. The first is a compact blade-shaped stone with medium sphericity (Pebble A in Figure 4), and the second is a compact platy stone with low sphericity (Pebble B in Figure 4) [41]. 3D models of these two cases where generated by a 3D laser scanner (Roland^{TM} 600 DS [42]).

Simpler shapes, such as Pebble A, could be represented using simpler input methods, such as those used for the prototypes of the sensors, but this approach is inadequate for capturing the complexity of the pebbles, such as Pebble B. The design for the second case is exclusively based on the 3D scan, as this is the most accurate and fastest procedure.

A basic advantage of this design process is that it is possible to integrate almost directly the internal structure designed for the spherical case (which secures the durability and control of the density), by following simple scaling and integration tools provided by the software.

The above method is very versatile in terms of scaling, since it is possible to construct cases that are based on stones much larger or much smaller than the actual sensor. Accurate scaling can enhance the representativeness of the derived data, because when a representative pebble shape is determined for a specific site, it can be scaled to fit the sensor, no matter how diverse is the sample of stones upon which this decision was based,given that the procedure for deciding the representative shape of the grains for a specific site involves sampling and performing a number of statistical calculations that result in a number of characteristic shapes for the site. For example, in Figure 4, the 3D representation of Pebble A printed

at 1:1 scale for demonstration (Figure 4B) and the constructed case based on this pebble (Figure 4B,C) were designed using the same input. Figure 4 also shows a scaled representation for Pebble B.

Figure 3. Spherical outer case: (**A**) Designs for the internal structure of the outer case. The case can be designed to enhance durability (support structures), water-proof performance (O-rings) and density control (voids); (**B**) Incorporation of the internal case for the G-node (design and photograph); (**C**) Demonstration of the locking system to make the overall assembly rigid, but not impossible to open.

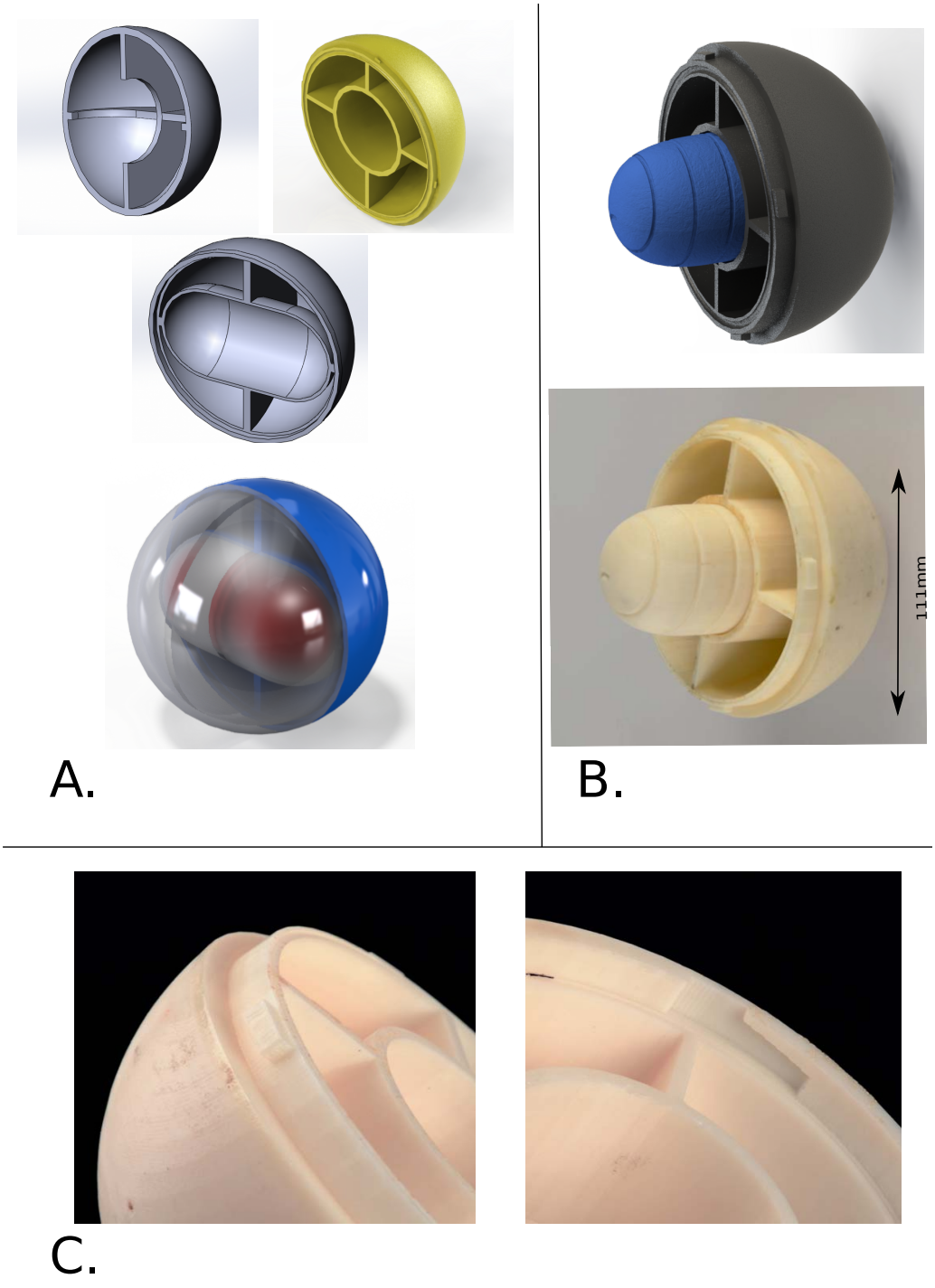

Figure 4. Scaled copies of natural stones and representative example case: (**A**) 3D designs of natural stones after processing the data from the 3D scanner. Note the differences in angularity and sphericity (Pebble A is blade-shaped with medium sphericity; Pebble B is compact and platy with low sphericity); (**B**) Scaled 3D printings of Pebble A (**left**) and Pebble B (**right**); (**C**) Outer case based on Pebble A. The internal structure incorporates the internal case for the G-node. This outer case has a simple internal structure, but more complicated internal designs, such as used for the spherical cases, can be incorporated (Figure 3).

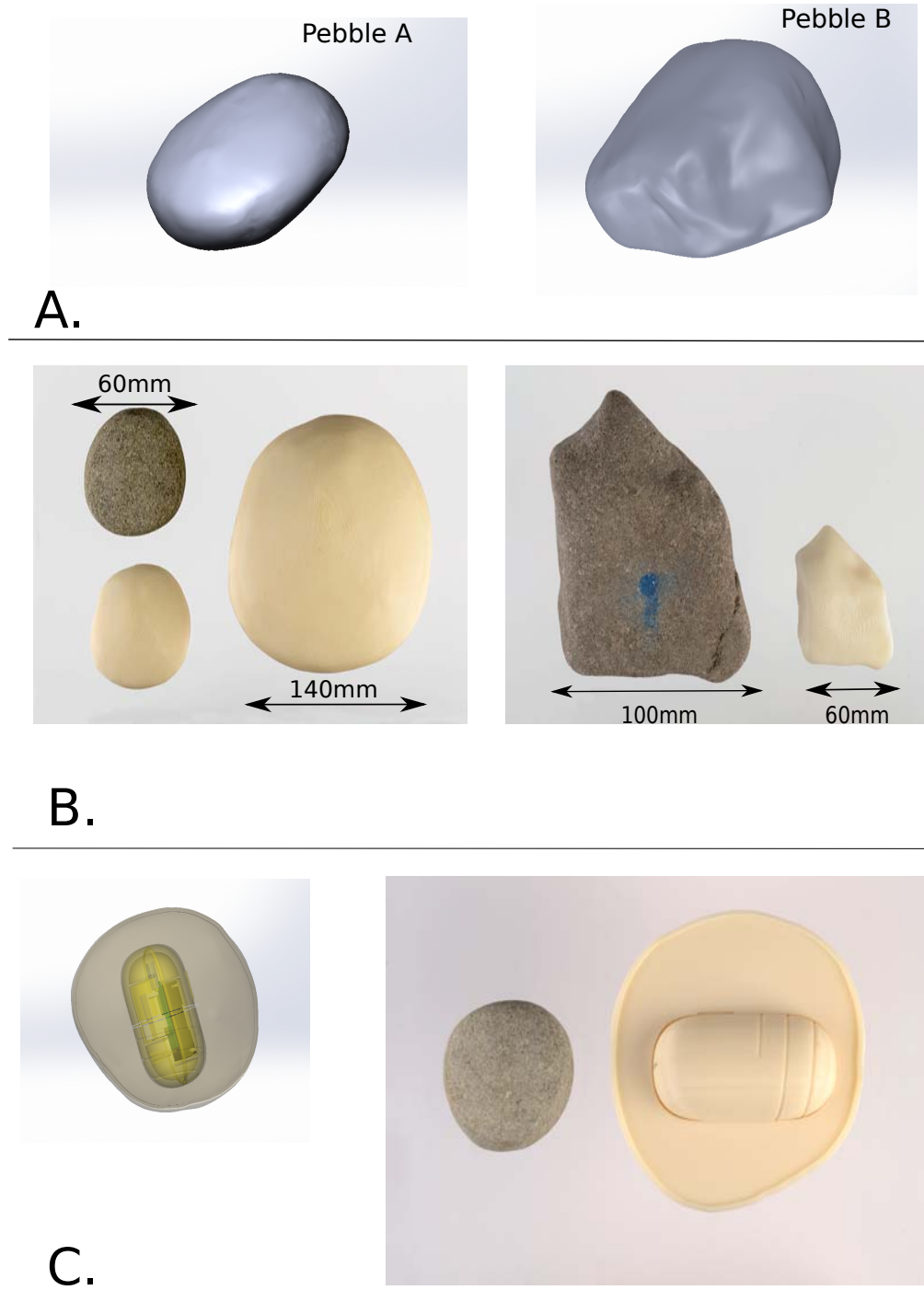

4. Results and Discussion

4.1. Timing of Development: Technical Considerations

We printed with an HP Designjet™ 3D printer [43] using standard, compatible with the printer, PVC plastic. The quality of the printer is crucial for the time of development (3D printing proved to be the most time-consuming part of the whole procedure), as well as for the quality of the final product. This becomes more apparent during the latter stages of the development, where the actual enclosures are produced. As an indication, the printing time for the replicates of the sensors (Figure 1) (a length of 64 mm for the CM4000, for example) is close to four hours, while the 3D printing of the outer enclosures varies from eight to 20 h, depending upon the thickness, the internal supports and the complexity of the shapes being reproduced.

The time required to produce the 3D designs is highly variable and depends on the experience of the modeller and familiarity with the software. However, a modeller relatively familiar with the principals of Digital Design and commonly used 3D Modelling /Computer Aided Design software can be expected to create a first prototype for a given sensor in less than a week, especially if the outer case is based on a natural pebble or an enclosure that can be scanned with the 3D scanner.

It is important that fast prototyping and 3D printing is possible for other materials besides the ABS plastic that is used for this application [44]. Moreover, the same design process can be followed to create casts for the creation of cases constructed with different materials (e.g., carbon fibre or metals) that can address the requirements for several applications. The inputs and the initial designs in this case would be manipulated following exactly the same procedure. The only differences would be at the final stage, where the designs used as input from the 3D printer must be modified to represent the exact negatives of the desired enclosure (a process very similar to the one followed in order to enclose accurately the sensors in the internal case).

4.2. Data Coherence: Initial Laboratory Tests

The complete testing of the data generated by sensors constructed as described above is ongoing. Here, we demonstrate how selected design features of the case affect the calibration process of the sensor and can potentially enhance the field deployment of such a system.

Firstly, the ability of the casing to rigidly fix the sensor in position is critical. Figure 5 shows the difference between accelerations measured with the same sensor (the G-node) using two different enclosures. The experimental set-up consists of a shaking table moving periodically along one axis and capable of producing a variable acceleration with a known maximum of 4 g. The sensor is firmly attached to monitor the acceleration along the dominant axis (parallel to the movement of the table), as shown in the schematic representation of Figure 5A. The accelerations recorded in this axis must be significantly greater than those due to the rest of the vibrations produced by the whole shaking movement.

Figure 5. Experimental comparison between steady and unsteady sensor orientations. (**A**) Schematic resolution of the 3D orientation of the sensor in relation to the periodic movement of the shaking table. The table creates a range of accelerations up to 4 g. Left: the axes of acceleration in relation to the outer casing. Right: axis of shaking (x-axis) relative to the internal case; (**B**) Comparison of the raw three-axis acceleration for the two experiments (sampling rate 20 Hz. During Experiment 1, periodic x-axis accelerations reach a maximum of 4.2 g, which significantly exceeds the maxima on the y- and z-axes (0.85 g and 0.96 g, respectively), confirming the direction and magnitude of the dominant process (periodic movement along the x-axis). Experiment 2 was performed without the internal case; hence, sensor orientation changed through time. The maximum acceleration for the x-axis is much larger than that produced by the shaking table ($x_{max} = 10$ g). Moreover, the periodic movement is not recorded, and the comparison with the maxima on the other axes (3.18 g and 2.8 g on the y- and z-axes, respectively) is not indicative of the dominant process.

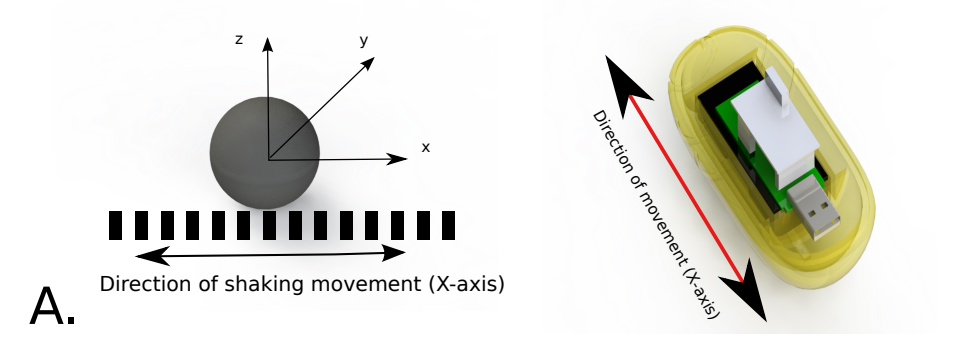

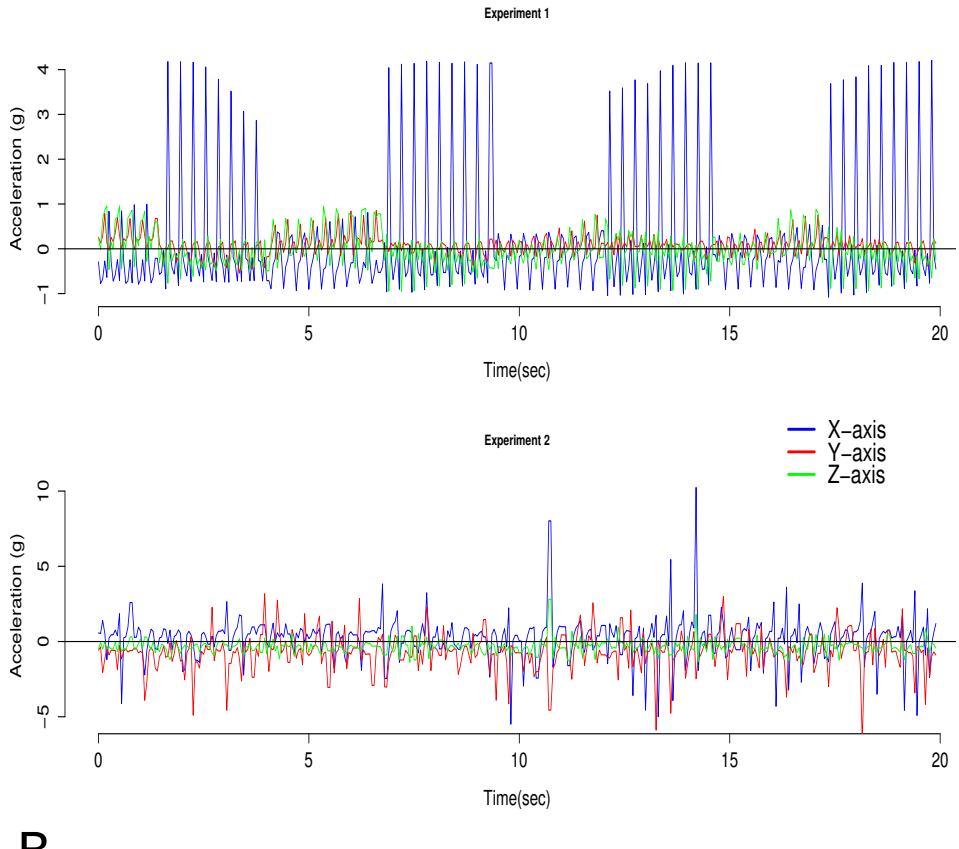

During the first experiment (Figure 5B), the sensor was enclosed in the case that was designed following the previously-described procedure. As a result, the sensor was steadily orientated throughout the experiment and was moving as little as possible in relation to the whole case. Figure 5B shows the recorded acceleration along the three axes during a time period of 20 s at a sampling rate of 20 Hz. The raw signal indicates a dominant periodic impact on the x-axis capable of producing maximum acceleration of 4.2 g, which is significantly greater than the accelerations recorded on the other two axes.

In comparison, for the second experiment, the sensor was enclosed in a case with the same outer shape, but without the internal structure to stabilize the sensor, thus permitting the movement of the sensor within the casing. Figure 5B shows the results for the same accelerations, time period and sampling frequency as for Experiment 1. The results show how the movement of the sensor inside the case changes its orientation constantly, so that it is difficult to observe the orientation and magnitude of the motion. As a result, the recorded accelerations are inconsistent during the second experiment since: (a) the periodic motion of the shaking table is not recorded; and, more importantly; (b) the relative internal motion of the sensor generates an error as high as 150%, since the maximum acceleration produced from the shaking table is 4 g and, during the second experiment, the measurements for the x-axis have a maximum of 10 g.

4.3. Statistical Analysis

Moving a step further, we demonstrate how misleading the statistical analysis of data from a non-rigid sensor can be. Common practice for time series analysis involves the comparison of the distribution of each measurement and the application of linear filters (smoothing) in order to identify any trends or patterns that drive the monitored process. Figure 6 shows a statistical comparison between the acceleration signals derived during the two experiments.

4.3.1. Comparison Based on Variability

The first comparison concerns the kernel density of the signals for the three axes (x, y, z). For the first experiment (Figure 6A), the results reveal similar probability distributions for the accelerations on the y- and z-axes. The mean acceleration is very close to 0 g (0.078 g for the y-axis and -0.02 g for the z-axis), the standard deviation is of the same order (0.21 g and 0.4 g for y and z, respectively), as well as the range ($[-0.544,0.856]$ g for the y-axis and $[-0.952,0.960]$ g for the z-axis).

Interestingly, the probability distribution for acceleration on the x-axis is considerably different. The statistics of this signal reveal a different behaviour (the mean is equal to 0.074 g, with a standard deviation of 1.28 g, and the range is $[-1.080,4.208]$ g). More importantly, the kernel density increases near the value of 4 g, indicating the significance of the maximum values. This peak can be interpreted as an indication of the periodic character of the effect. Overall, these results are representative for the magnitude and the direction of the dominant process, which is movement along the x-axis.

In comparison, the results from the second experiment are not representative. The results reveal similar probability distributions for the accelerations along the y- and x-axes. The mean acceleration is -0.7 g (standard deviation of 1.23 g) for the y-axis and 0.2 g (standard deviation of 1.47 g) for the x-axis, which makes the observation of the dominant process difficult. Moreover, the data give no indication of the periodic movement.

Figure 6. Statistical comparison of acceleration signals: (**A**) Kernel densities for acceleration signal (three-axes). Experiment 1 data shows the magnitude of x-axis acceleration as an increase in probability density near 4 g. The unstable signal from Experiment 2 does not give any indication about the dominant process, since the distributions of the three axis signals are statistically similar; (**B**) Moving Average Smoothing are the caps necessary of x-axis acceleration signals. Linear filters ($a = 7$ and $a = 17$) retain the periodic pattern during Experiment 1 with an approximate period of 5 s, while for Experiment 2, there is no indication of this behaviour.

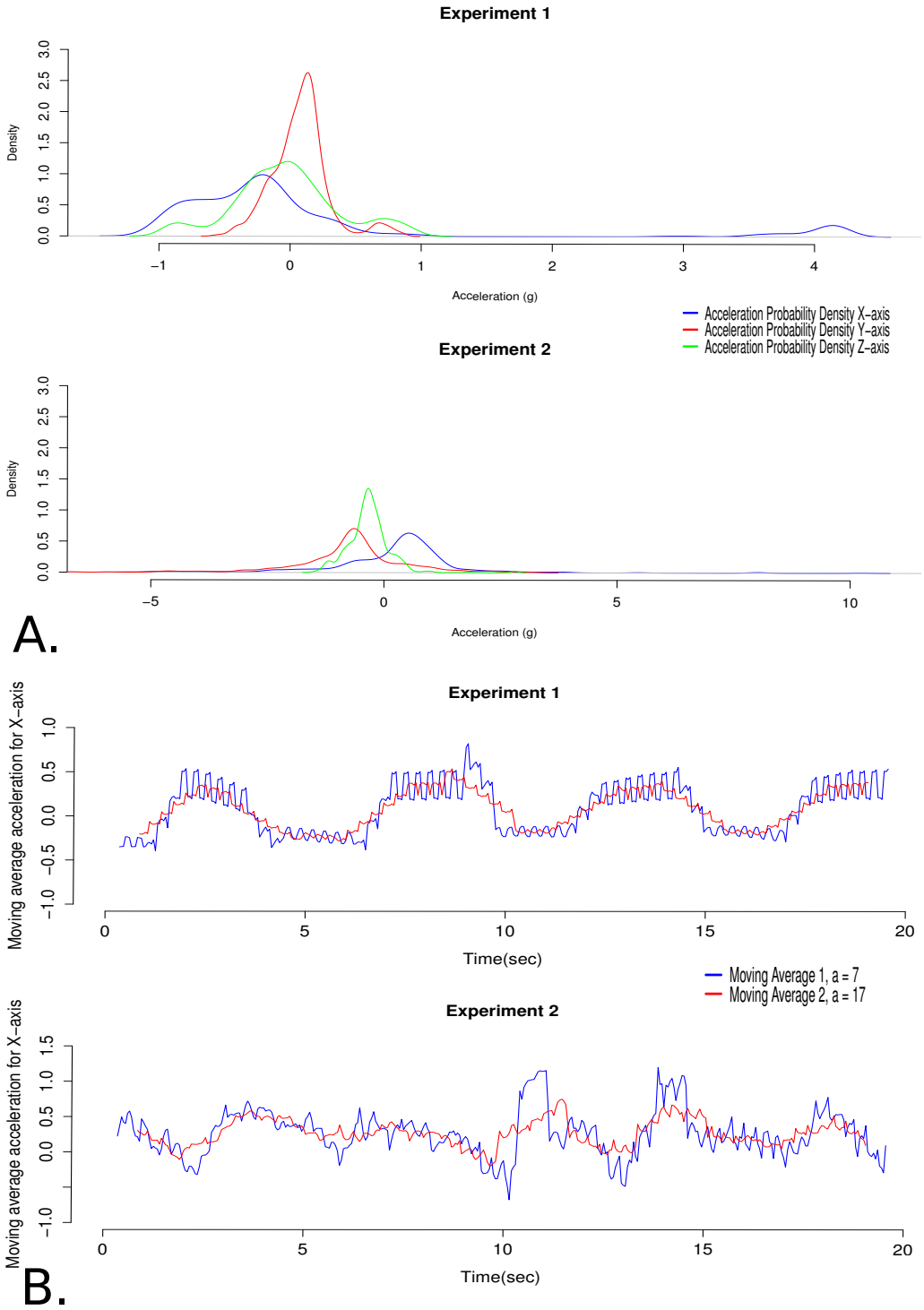

4.3.2. Comparison Based on Linear Filtering (Smoothing)

Following the common practice, we applied two moving average filters to the time series of the acceleration signal on the x-axis (where the dominant movement takes place). The averaging factor for the first filter is $a = 7$ and for the second $a = 17$. The results for the first experiment (Figure 6B) reveal the seasonal periodic pattern in the time series suggesting an approximate period of 5 s (which is in agreement with the period measured after the analysis of the video recordings of the experiment). On the contrary, the results from the second experiment do not reveal this type of pattern, which is inconsistent, given the movement of the sensor.

4.3.3. Deployment Considerations

While it is unlikely that any sensing system will be constructed without taking into account the error produced by not securing the stability of the sensor inside the casing, our second experiment simulates effectively a situation where a casing fails during operation, a prospect that cannot be excluded in deployments where accelerations on the order of 100 g are possible.

An operator of this sensor is equally likely to receive both of the above signals during real deployment (Figure 5). Especially in a natural setting where the line-of-sight contact with the system is not guaranteed, the only information about the monitored process is that derived from the statistical analysis of these signals. Taking into account that the known magnitude range of instantaneous measured physical properties can be significantly higher than the range of the derived measurements, both of these signals could appear to be valid and there is no way to identify the error in the second experiment during the statistical analysis. Consequently, it is important to prioritize stable orientation of the sensor in the case and minimization of internal movement during the design process of such a system.

5. Conclusions

Here, we demonstrate a new method for rapid prototyping of sensor enclosures. Focusing on inertial sensors for monitoring motion, the motivation for the development of this method lies in the potential inconsistency of the sensed data if two critical factors are not incorporated in the casing-design criteria: (a) the effect of the physical characteristics of the complete sensor on the movement of the device, hence on the representativeness of the derived data; and (b) the stability of the sensor along with the constant orientation in response to the overall frame of the casing.

We have described a versatile design process that can be adapted to any type of sensor platform and yields casings with pre-determined physical characteristics (such as shape and density). This enables the rapid design of casings for specific applications that will enhance the coherence of the data, since they will be compatible with the monitored environment and the data-acquisition process.

The results concern the application of this method during the development of a new sensor for monitoring river grain dynamics. Given the rapid improvements in the fast prototyping technologies described (which are both enhancing the quality and decreasing the price of the final case product), it is possible to apply this method for large-scale sensing applications.

Finally, we present results from two calibration experiments using an acceleration-impact sensor. The statistical analysis of the results suggests a potential error on the order of 150% in terms of magnitude and complete inconsistency in terms of the directional information about the movement of the sensor when the failure of the case to stabilize the sensor platform is simulated. This result can be considered in the context of remote sensing when no other information is available and the statistical analysis gives no indication about the potential error.

Acknowledgments

The authors thank Ewan Russell for his help during the production of the designs and 3D printed prototypes and cases.

Georgios Maniatis is a PhD student funded by a University of Glasgow Kelvin-Smith Scholarship.

Conflicts of Interest

The authors declare no conflict of interest.

References

1. Hart, J.K.; Martinez, K. Environmental sensor networks: A revolution in the earth system science? *Earth Sci. Rev.* **2006**, *78*, 177–191.
2. Corke, B.P.; Wark, T.; Jurdak, R.; Hu, W.; Valencia, P.; Moore, D. Environmental wireless sensor networks. *Proc. IEEE* **2010**, *98*, 1903–1917.
3. Oliveira, L.M.; Rodrigues, J.J. Wireless sensor networks: A survey on environmental monitoring. *J. Commun.* **2011**, *6*, 143–151.
4. Benelli, G.; Pozzebon, A.; Bertoni, D.; Sarti, G. An RFID-based toolbox for the study of under- and outside-water movement of pebbles on coarse-grained beaches. *IEEE J. Sel. Topics Appl. Earth Observ. Remote Sens.* **2012**, *5*, 1474–1482.
5. Werner-Allen, G.; Lorincz, K.; Welsh, M.; Johnson, J.; Lees, J. Deploying a wireless sensor network on an active volcano. *IEEE Inter. Comput. Sens. Netw. Appl.* **2006**, *10*, 18–25.
6. Martinez, K.; Hart, J.K.; Ong, R. Deploying A Wireless Sensor Network in Iceland. In *GeoSensor Networks*; Springer: Berlin, Germany, 2009; pp. 131–137.
7. Pedersen, L.; Bualat, M.; Kunz, C.; Lee, S.; Sargent, R.; Washington, R.; Wright, A. Instrument Deployment for Mars Rovers. In Proceedings of the 2003 IEEE International Conference on Robotics and Automation (ICRA 2003), 14–19 September 2003, Taipei, Taiwan; pp. 2535–2542.
8. Whipple, K.X.; Tucker, G.E. Implications of sediment-flux-dependent river incision models for landscape evolution. *J. Geophys. Res.* **2002**, *107(B2)*, ETG 3-1–ETG 3-20.
9. Hassan, M.A.; Ergenzinger, P. Use of Tracers in Fluvial Geomorphology. In *Tools in Fluvial Geomorphology*; John Wiley & Sons, Ltd: Hoboken, NJ, USA, 2005; pp. 397–423.
10. Habersack, H.M. Use of radio-tracking techniques in bed load transport investigations. In Proceedings of Erosion and Sediment Transport Measurement in Rivers: Technological and Methodological Advances: Workshop, Oslo, Norway, 19–21 June 2002; pp. 172–180

11. Allan, J.C.; Hart, R.; Tranquili, J.V. The use of Passive Integrated Transponder (PIT) tags to trace cobble transport in a mixed sand-and-gravel beach on the high-energy Oregon coast, USA. *Mar. Geol.* **2006**, *232*, 63–86.
12. Furbish, D.J.; Ball, A.E.; Schmeeckle, M.W. A probabilistic description of the bed load sediment flux: 4. Fickian diffusion at low transport rates. *J. Geophys. Res.* **2012**, *117*, F03034.
13. McEwan, I.; Habersack, H.; Heald, J. Discrete Particle Modelling and Active Tracers: New Techniques for Studying Sediment Transport as a Lagrangian Phenomenon. In *Gravel-Bed Rivers V*; New Zealand Hydrological Society: Wellington, New Zealand, 2001; pp. 339–360.
14. Demir, T. The Influence of Particle Shape on Bedload Transport in Coarse-Bed River Channels. Ph.D. Thesis, Durham University, Durham, UK, 2000.
15. Ergenzinger, P.; Jupner, R. Using COSSY (CObble Satellite SYstem) for measuring the effects of lift and drag forces. In *Erosion and Sediment Transport Monitoring Programmes in River Basins*; IAHS Press: Oxford, UK, 1992; pp. 41–50.
16. Krumbein, W.C. Measurement and geological significance of shape and roundness of sedimentary particles. *J. Sediment. Res.* **1941**, *11*, 64–72.
17. Carling, P.; Kelsey, A.; Glaister, M. Effect of Bed Roughness, Particle Shape and Orientation on Initial Motion Criteria. In *Dynamics of Gravel Bed Rivers*; John Wiley and Sons: Chichester, UK, 1992; pp. 24–39.
18. Wiberg, P.L.; Smith, J.D. Model for calculating bed load transport of sediment. *J. Hydraul. Eng.* **1989**, *115*, 101–123.
19. Hodge, R.A.; Hoey, T.B.; Sklar, L.S. Bed load transport in bedrock rivers: The role of sediment cover in grain entrainment, translation, and deposition. *J. Geophys. Res.* **2011**, *116*, 1–19.
20. Sear, D.; Lee, M.; Collins, M.; Carling, P. The Intelligent Pebble: A New Technology for Tracking Particle Movements in Fluvial and Littoral Environments. In Proceedings of Erosion and Sediment Transport Measurement: Technological and Methodological Advances Workshop, Oslo, Norway, 19–21 June 2002; pp. 19–21.
21. Spazzapan, M.; Petrovčič, J.; Mikoš, M. New tracer for monitoring dynamics of sediment transport in turbulent flows. *Acta Hydrotech.* **2004**, *22*, 135–148.
22. Abeywardana, D.K.; Hu, A.P.; Kularatna, N. Design Enhancements of the Smart Sediment Particle for Riverbed Transport Monitoring. In Proceedings of 4th IEEE Conference on Industrial Electronics and Applications, Xi'an, China, 25–28 May 2009; pp. 336–341.
23. Abeywardana, D.K.; Hu, A.P.; Kularatna, N. IPT Charged Wireless Sensor Module for River Sedimentation Detection. In Proceedings of 2012 IEEE Sensors Applications Symposium (SAS 2012), Deauville, France, 11–13 September 2012; pp. 1–5.
24. Frank, D.P.; Foster, D.L.; Kao, P.C.Y.M. *In-Situ* Measurements within Mobile Bed Layers with Electronic Pebbles. In Proceedings of American Geophysical Union Conference, San Francisco, CA, USA, 9–15 December 2012; p. 3.
25. Rickenmann, D.; McArdell, B. Continuous measurement of sediment transport in the Erlenbach stream using piezoelectric bedload impact sensors. *Earth Surf. Process. Landf.* **2007**, *32*, 1362–1378.

26. Vatne, G.; Naas, O.T.; Skãrholen, T.; Beylich, A.A.; Berthling, I. Bed load transport in a steep snowmelt-dominated mountain stream as inferred from impact sensors. *Nor. Geogr. Tidsskr. Nor. J. Geogr.* **2008**, *62*, 66–74.
27. Nichols, M. A radio frequency identification system for monitoring coarse sediment particle displacement. *Appl. Eng. Agric.* **2004**, *20*, 783–787.
28. Bradley, D.N.; Tucker, G.E. Measuring gravel transport and dispersion in a mountain river using passive radio tracers. *Earth Surf. Process, Landf.* **2012**, *37*, 1034–1045.
29. Liedermann, M.; Tritthart, M.; Habersack, H. Particle path characteristics at the large gravel-bed river Danube: Results from a tracer study and numerical modelling. *Earth Surf. Process. Landf.* **2012**, *38*, 512–522.
30. Heidemann, J.; Stojanovic, M.; Zorzi, M. Underwater sensor networks: Applications, advances and challenges. *Philos. Trans. R. Soc. A Math. Phys. Eng. Sci.* **2012**, *370*, 158–175.
31. Fiorelli, E.; Leonard, N.; Bhatta, P.; Paley, D.; Bachmayer, R.; Fratantoni, D. Multi-AUV control and adaptive sampling in monterey bay. *IEEE J. Ocean. Eng.* **2006**, *31*, 935–948.
32. Detweiler, C.; Doniec, M.; Vasilescu, I.; Basha, E.; Rus, D. Autonomous Depth Adjustment for Underwater Sensor Networks. In Proceedings of the Fifth ACM International Workshop on UnderWater Networks, New York, NY, USA, 30 September–1 October 2010; pp. 12:1–12:4.
33. Hanrahan, G.; Patil, D.G.; Wang, J. Electrochemical sensors for environmental monitoring: Design, development and applications. *J. Environ. Monitor.* **2004**, *6*, 657–664.
34. Akyildiz, I.F.; Vuran, M.C. Wireless Underwater Sensor Networks. In *Wireless Sensor Networks*; John Wiley & Sons: Hoboken, NJ, USA, 2010; pp. 399–442.
35. Delauney, L.; Compere, C.; Lehaitre, M. Biofouling protection for marine environmental sensors. *Ocean. Sci.* **2010**, *6*, 503–511.
36. AdvanticSys, CM4000 Mote Webpage. Avaiable online: http://www.advanticsys.com/shop /mtmcm4000msp-p-8.html (accessed on 28 November 2013).
37. AdvanticSys, CO1000 Sensor-Board Webpage. Avaiable online: http://www.advanticsys.com /shop/mtsco1000-p-17.html (accessed on 28 November 2013).
38. SOWNET Technologies, G-Node Mote Webpage. Avaiable online: http://www.sownet.nl /index.php/products/gnode (accessed on 28 November 2013).
39. Analogue Devices, ADXL-345 Digital Accelerometer Webpage and Datasheet. Avaiable online: http://www.analog.com/en/mems-sensors/mems-inertial-sensors/adxl345/products/product.html (accessed on 28 November 2013).
40. Dassault Systèmes, SolidWorks Software Webpage. Avaiable online: http://www.solidworks.com (accessed on 28 November 2013).
41. Benn, D.I.; Ballantyne, C.K. The description and representation of particle shape. *Earth Surf. Process. Landf.* **1993**, *18*, 665–672.
42. Roland 3D-Scanners Webpage. Avaiable online: http://www.rolanddga.com/products/scanners /lpx600/ (accessed on 28 November 2013).
43. Hp Designjet 3D Printer Webpage. Avaiable online: http://www.hp3dprinting.co.uk /hp-designjet-color-3d-printer.html (accessed on 28 November 2013).

44. Lipson, H.; Kurman, M. *Fabricated: The New World of 3D Printing*; John Wiley & Sons: Hoboken, NJ, USA, 2013.

BIBLIOGRAPHY

AdvanticSys (2013a), *CO4000 sensor-board webpage*, http://www.advanticsys.com/shop/mtmcm4000msp-p-8.html, Accessed 28 November 2013.

AdvanticSys (2013b), *CM1000 mote webpage*, http://www.advanticsys.com/shop/mtsco1000-p-17.html, Accessed 28 November 2013.

Akeila, E., Z. Salcic, and A. Swain (2008), Implementation, calibration and testing of GFINS models based on six-accelerometer cube, in *TENCON 2008-2008 IEEE Region 10 Conference*, pp. 1–6, IEEE.

Akeila, E., Z. Salcic, and A. Swain (2010), Smart pebble for monitoring riverbed sediment transport, *Sensors Journal, IEEE*, *10*(11), 1705–1717.

Akyildiz, I. F., and M. C. Vuran (2010), *Wireless Underwater Sensor Networks*, pp. 399–442, John Wiley & Sons, Ltd, doi:10.1002/9780470515181.ch16.

Alfadhli, I., S.-Q. Yang, et al. (2014), Influence of vertical motion on initiation of sediment movement, *Journal of Water Resource and Protection*, *6*(18), 1666.

Allan, J. C., and R. Hart (2007), Profile dynamics and particle tracer mobility of a cobble berm constructed on the oregon coast, in *Proceedings of the Sixth International Symposium on Coastal Engineering and Science of Coastal Sediment Processes, New Orleans, USA*, pp. 1–14.

Allan, J. C., R. Hart, and J. V. Tranquili (2006), The use of Passive Integrated Transponder (PIT) tags to trace cobble transport in a mixed sand-and-gravel beach on the high-energy oregon coast, usa, *Marine Geology*, *232*(1), 63–86.

Allan, J. D. (2004), Landscapes and riverscapes: the influence of land use on stream ecosystems, *Annual Review of Ecology, Evolution, and Systematics*, pp. 257–284.

Analogue Devices (2013), *ADXL-345 digital accelerometer*, http://www.analog.com/en/mems-sensors/mems-inertial-sensors/adxl345/products/product.html, Accessed 28 November 2013.

Ancey, C. (2010), Stochastic modeling in sediment dynamics: Exner equation for planar bed incipient bed load transport conditions, *Journal of Geophysical Research: Earth Surface (2003–2012)*, *115*(F2).

Ancey, C., F. Bigillon, P. Frey, J. Lanier, and R. Ducret (2002), Saltating motion of a bead in a rapid water stream, *Physical review E*, *66*(3), 036,306.

Anderson, R. S. (1990), Aeolian ripples as examples of self-organization in geomorphological systems, *Earth-Science Reviews*, *29*(1), 77–96.

Andrejašic, M. (2008), *MEMS accelerometers*, University of Ljubljana. Faculty for Mathematics and Physics, Department of Physics, Seminar, http://mafija.fmf.unilj.si/seminar/files/2007_2008/MEMS_accelerometerskoncna.pdf/.

Arolla, S. K., and O. Desjardins (2015), Transport modeling of sedimenting particles in a turbulent pipe flow using Euler–Lagrange large eddy simulation, *International Journal of Multiphase Flow*, *75*, 1–11.

Arraigada, M., and M. Partl (2006), Calculation of displacements of measured accelerations, analysis of two accelerometers and application in road engineering, in *Proceedings of the 6th Swiss Transport Research Conference, Ascona, Switzerland*, vol. 1517.

Ashida, K., and M. Michiue (1971), An investigation of river bed degradation downstream of a dam, in *in Proceedings of 14th Int. Association of Hydraulic Research Congress*, vol. 3, pp. 247–255, Wallingford, U.K.

Bailard, J. A. (1981), An energetics total load sediment transport model for a plane sloping beach, *Journal of Geophysical Research: Oceans*, *86*(C11), 10,938–10,954.

Balachandar, S. (2009), A scaling analysis for point–particle approaches to turbulent multiphase flows, *International Journal of Multiphase Flow*, *35*(9), 801–810.

Balachandar, S., and J. K. Eaton (2010), Turbulent dispersed multiphase flow, *Annual Review of Fluid Mechanics*, *42*, 111–133.

Baraff, D. (1997), *An introduction to physically based modeling: rigid body simulation with unconstrained rigid body dynamics*, SIGGRAPH Course Notes.

Barrière, J., A. Krein, A. Oth, and R. Schenkluhn (2015), An advanced signal processing technique for deriving grain size information of bedload transport from impact plate vibration measurements, *Earth Surface Processes and Landforms*, *40*(7), 913–924.

Bathurst, J. C. (1985), Flow resistance estimation in mountain rivers, *Journal of Hydraulic Engineering*, *111*(4), 625–643.

Beetstra, R., M. Van der Hoef, and J. Kuipers (2007), Drag force of intermediate Reynolds number flow past mono-and bidisperse arrays of spheres, *AIChE Journal*, *53*(2), 489–501.

Benelli, G., A. Pozzebon, D. Bertoni, and G. Sarti (2012), An rfid-based toolbox for the study of under-and outside-water movement of pebbles on coarse-grained beaches, *IEEE Journal of Selected Topics in Applied Earth Observations and Remote Sensing*, *5*(5), 1474–1482.

Benn, D. I., and C. K. Ballantyne (1993), The description and representation of particle shape, *Earth Surface Processes and Landforms*, *18*(7), 665–672.

Bialik, R., V. Nikora, and P. Rowiński (2012), 3d lagrangian modelling of saltating particles diffusion in turbulent water flow, *Acta Geophysica*, *60*(6), 1639–1660.

Bialik, R. J. (2015), Lagrangian modelling of saltating sediment transport: a review, in *Rivers–Physical, Fluvial and Environmental Processes*, pp. 427–441, Springer.

Bialik, R. J., V. I. Nikora, M. Karpiński, and P. M. Rowiński (2015), Diffusion of bedload particles in open-channel flows: distribution of travel times and second-order statistics of particle trajectories, *Environmental Fluid Mechanics*, *15*(6), 1281–1292.

Bottacin-Busolin, A., S. J. Tait, A. Marion, A. Chegini, and M. Tregnaghi (2008), Probabilistic description of grain resistance from simultaneous flow field and grain motion measurements, *Water resources research*, *44*(9).

Box, G. E., G. M. Jenkins, and G. C. Reinsel (2013), *Time Series Analysis: Forecasting and Control*, John Wiley & Sons.

Bradley, N. D., and G. E. Tucker (2012), Measuring gravel transport and dispersion in a mountain river using passive radio tracers, *Earth Surface Processes and Landforms*, *37*(March), 1034–1045, doi:10.1002/esp.3223.

Brennen, C. E. (2005), *Fundamentals of Multiphase Flow*, Cambridge University Press.

Bridge, J. (2003), *Rivers and Floodplains, pp 491*, Blackwell Publishing, Malden, Mass.

Bridge, J. S., and S. J. Bennett (1992), A model for the entrainment and transport of sediment grains of mixed sizes, shapes, and densities, *Water Resources Research*, *28*(2), 337–363.

Buffington, J. M., and D. R. Montgomery (1997), A systematic analysis of eight decades of incipient motion studies, with special reference to gravel-bedded rivers, *Water Resources Research*, *33*(8), 1993–2029.

Buffington, J. M., W. E. Dietrich, and J. W. Kirchner (1992), Friction angle measurements on a naturally formed gravel streambed: implications for critical boundary shear stress, *Water Resources Research*, *28*(2), 411–425.

Bunte, K., J. P. Potyondy, and S. R. Abt (2003), Development of an improved bedload trap for sampling gravel and cobble bedload in coarse mountain streams, in *Sediment Monitoring Symposium, Flagstaff AZ*.

Bunte, K., S. R. Abt, J. P. Potyondy, and S. E. Ryan (2004), Measurement of coarse gravel and cobble transport using portable bedload traps, *Journal of Hydraulic Engineering*, *130*(9), 879–893.

Bunte, K., S. R. Abt, K. W. Swingle, D. A. Cenderelli, and J. M. Schneider (2013), Critical Shields values in coarse-bedded steep streams, *Water Resources Research*, *49*(11), 7427–7447.

Busskamp, R., and B. Hasholt (1996), Coarse bed load transport in a glacial valley, Sermilik, South East Greenland, *Zeitschrift fur Geomorphologie*, *40*(3), 349–358.

Cao, Z., G. Pender, and J. Meng (2006), Explicit formulation of the Shields diagram for incipient motion of sediment, *Journal of Hydraulic Engineering*, *132*(10), 1097–1099.

Carlin, B. P., and T. A. Louis (1997), Bayes and empirical Bayes methods for data analysis, *Statistics and Computing*, *7*(2), 153–154.

Carling, P. (1987), Bed stability in gravel streams, with reference to stream regulation and ecology, *River Channels: Environment and Process. Blackwell Scientific Publications, Oxford, UK*, pp. 321–347.

Carling, P., A. Kelsey, and M. Glaister (1992), Effect of bed roughness, particle shape and orientation on initial motion criteria, *Dynamics of gravel-bed rivers*, pp. 24–39.

Cecchetto, M., M. Tregnaghi, A. Bottacin-Busolin, S. Tait, and A. Marion (2016), Statistical description on the role of turbulence and grain interference on particle entrainment from gravel beds, *Journal of Hydraulic Engineering*, p. 06016021.

Celik, A. O., P. Diplas, C. L. Dancey, and M. Valyrakis (2010), Impulse and particle dislodgement under turbulent flow conditions, *Physics of Fluids (1994-present)*, *22*(4), 046,601.

Chacho, E., R. Burrows, and W. Emmett (1989), Detection of coarse sediment movement using radio transmitters, in *International Association for Hydraulic Research XXIII Congress August 21-25, 1989, Ottawa, Canada. 1989. p B 367-B 373, 3 fig, 1 tab, 7 ref.*

Chatanantavet, P. (2007), *Physically-based models of bedrock incision processes in mountain streams*, PhD Thesis, ProQuest.

Cheetham, G. (1979), Flow competence in relation to stream channel form and braiding, *Geological Society of America Bulletin*, *90*(9), 877–886.

Church, M., M. A. Hassan, and J. F. Wolcott (1998), Stabilizing self-organized structures in gravel-bed stream channels: Field and experimental observations, *Water Resources Research*, *34*(11), 3169–3179.

Clemons, T. E., and E. L. Bradley (2000), A nonparametric measure of the overlapping coefficient, *Computational Statistics & Data Analysis*, *34*(1), 51–61.

Corke, P., T. Wark, R. Jurdak, W. Hu, P. Valencia, and D. Moore (2010), Environmental wireless sensor networks, *Proceedings of the IEEE*, *98*(11), 1903–1917.

Craig, R. G., C. Loadman, B. Clement, P. J. Rusello, and E. Siegel (2011), Characterization and testing of a new bistatic profiling acoustic doppler velocimeter: The vectrino-ii, in *Current, Waves and Turbulence Measurements (CWTM), 2011 IEEE/OES 10th*, pp. 246–252, IEEE.

Delauney, L., C. Compere, and M. Lehaitre (2010), Biofouling protection for marine environmental sensors, *Ocean Science*, *6*(2), 503–511.

Demir, T. (2000), The influence of particle shape on bedload transport in coarse-bed river channels, Ph.D. thesis, Durham University.

Detweiler, C., M. Doniec, I. Vasilescu, E. Basha, and D. Rus (2010), Autonomous depth adjustment for underwater sensor networks, in *Proceedings of the Fifth ACM International Workshop on UnderWater Networks*, WUWNet '10, pp. 12:1–12:4, ACM, New York, NY, USA, doi:10.1145/1868812.1868824.

Diebel, J. (2006), Representing attitude: Euler angles, unit quaternions, and rotation vectors, *Matrix*, *58*, 15–16.

Dietrich, W. E., and J. D. Smith (1984), Bed load transport in a river meander, *Water Resources Research*, *20*(10), 1355–1380.

Diplas, P., C. L. Dancey, A. O. Celik, M. Valyrakis, K. Greer, and T. Akar (2008), The role of impulse on the initiation of particle movement under turbulent flow conditions, *Science*, *322*(5902), 717–720.

Doyle, M. W., and S. H. Ensign (2009), Alternative reference frames in river system science, *BioScience*, *59*(6), 499–510.

Einstein, H. A. (1950), *The bed-load function for sediment transportation in open channel flows*, 1026, US Department of Agriculture.

Einstein H. A. (1937), Bedload Transport as a Probability Problem, Mitteilung der Versuchsanstalt für Wasserbau an der EidgenÃssischen Technischen Hochschule, p. 110.

Ergenzinger, P., and J. Conrady (1982), A new tracer technique for measuring bedload in natural channels, *Catena*, *9*(1-2), 77–80.

Ergenzinger, P., and C. De Jong (2003), Perspectives on bed load measurement, *IAHS Publication*, pp. 113–125.

Ergenzinger, P., and R. Jupner (1992), Using COSSY (CObble Satellite SYstem) for measuring the effects of lift and drag forces, *Erosion and Sediment Transport Monitoring Programmes in river Basins*, *IAHS Publi*(210), 41–50.

Ergenzinger, P., K. Schmidt, and R. Busskamp (1989), The Pebble Transmitter System (PETS)-1st results of a technique for studying coarse material erosion, transport and deposition, *Zeitschrift fur Geomorphologie*, *33*(4), 503–508.

Ergenzinger, P., K. Schmidt, and R. Busskamp (1991), Neue analysen zum transport von grobgerschiebe:messung lagragesher parameter mit der radiotracertechnik(petsy), *Deutche Gewaesserkundliche Mittellungen*, *35*, 57–63.

Faraway, J. J. (2005), *Extending the linear model with R: generalized linear, mixed effects and nonparametric regression models*, CRC press.

Fathel, S., D. Furbish, and M. Schmeeckle (2016), Parsing anomalous versus normal diffusive behavior of bed load sediment particles, *Earth Surface Processes and Landforms*.

Fathel, S. L., D. J. Furbish, and M. W. Schmeeckle (2015), Experimental evidence of statistical ensemble behavior in bed load sediment transport, *Journal of Geophysical Research: Earth Surface*, *120*(11), 2298–2317.

Featherstone, R. (2014), *Rigid body Dynamics Algorithms*, Springer.

Fenton, J., and J. Abbott (1977), Initial movement of grains on a stream bed: the effect of relative protrusion, in *Proceedings of the Royal Society of London A: Mathematical, Physical and Engineering Sciences*, vol. 352, pp. 523–537, The Royal Society.

Ferguson, R., T. Hoey, S. Wathen, and A. Werritty (1996), Field evidence for rapid downstream fining of river gravels through selective transport, *Geology*, *24*(2), 179–182.

Ferguson, R. I., D. J. Bloomer, T. B. Hoey, and A. Werritty (2002), Mobility of river tracer pebbles over different timescales, *Water Resources Research*, *38*(5).

Ferreira, R. M., M. A. Hassan, and C. Ferrer-Boix (2015), Principles of bedload transport of non-cohesive sediment in open-channels, in *Rivers–Physical, Fluvial and Environmental Processes*, pp. 323–372, Springer.

Fiorelli, E., N. Leonard, P. Bhatta, D. Paley, R. Bachmayer, and D. Fratantoni (2006), Multi-AUV control and adaptive sampling in monterey bay, *Oceanic Engineering, IEEE Journal of*, *31*(4), 935–948, doi: 10.1109/JOE.2006.880429.

Fiorenzani, T., C. Manes, G. Oriolo, and P. Peliti (2008), Comparative study of unscented Kalman filter and extended Kalman filter for position/attitude estimation in unmanned aerial vehicles, *Inst. for Systems Analysis and Computer Science (IASI-CNR), Rome, Italy, Rept*, pp. 08–08.

Foxlin, E. (2005), Pedestrian tracking with shoe-mounted inertial sensors, *Computer Graphics and Applications, IEEE*, *25*(6), 38–46.

Frank, D., D. Foster, I. M. Sou, J. Calantoni, and P. Chou (2015), Lagrangian measurements of incipient motion in oscillatory flows, *Journal of Geophysical Research: Oceans*, *120*(1), 244–256.

Frank, D. P. (2014), Incipient motion within the wave bottom boundary layer, Ph.D. thesis, University of New Hampshire.

Froehlich, W. (1982), The mechanism of fluvial transport and waste supply into the stream channel in a mountainous flysch catchment, *Prace Geogr. IGiPZ PAN*, *143*, 1–144.

Furbish, D. J., A. E. Ball, and M. W. Schmeeckle (2012a), A probabilistic description of the bed load sediment flux: 4. Fickian diffusion at low transport rates, *Journal of Geophysical Research*, *117*(F3), F03,034, doi:10.1029/2012JF002356.

Furbish, D. J., P. K. Haff, J. C. Roseberry, and M. W. Schmeeckle (2012b), A probabilistic description of the bed load sediment flux: 1. theory, *Journal of Geophysical Research: Earth Surface (2003–2012)*, *117*(F3).

Furbish, D. J., J. C. Roseberry, and M. W. Schmeeckle (2012c), A probabilistic description of the bed load sediment flux: 3. the particle velocity distribution and the diffusive flux, *Journal of Geophysical Research: Earth Surface (2003–2012)*, *117*(F3).

Furbish, D. J., S. L. Fathel, and M. W. Schmeeckle (2016), Particle motions and bed load theory: The entrainment forms of the flux and the Exner equation, *Gravel-bed Rivers: Processes and Disasters*.

Ganti, V., M. M. Meerschaert, E. Foufoula-Georgiou, E. Viparelli, and G. Parker (2010), Normal and anomalous diffusion of gravel tracer particles in rivers, *Journal of Geophysical Research: Earth Surface*, *115*(F2).

Gebre-Egziabher, D., R. C. Hayward, and J. D. Powell (1998), A low-cost GPS/inertial attitude heading reference system (ahrs) for general aviation applications, in *Position Location and Navigation Symposium, IEEE 1998*, pp. 518–525, IEEE.

Geraldo, J., T. Ribeiro, J. T. P. de Castro, and J. L. de France Freire (2001), New improvements in the digital double integration filtering method to measure displacements using accelerometers, in *Proceedings of SPIE, the International Society for Optical Engineering*, vol. 4359, pp. 538–542, Society of Photo-Optical Instrumentation Engineers.

Gilbert, G. K., and E. C. Murphy (1914), *The transportation of debris by running water*, 86, US Government Printing Office.

Gomez, B. (1994), Effects of particle shape and mobility on stable armor development, *Water Resources Research*, *30*(7), 2229–2239.

Gouesbet, G., and A. Berlemont (1999), Eulerian and Lagrangian approaches for predicting the behaviour of discrete particles in turbulent flows, *Progress in Energy and Combustion Science*, *25*(2), 133–159.

Grafakos, L. (2004), *Classical and Modern Fourier Analysis*, Prentice Hall.

Grass, A. J. (1970), Initial instability of fine bed sand, *Journal of the Hydraulics Division*, *96*(3), 619–632.

Grattan-Guinness, I., J. B. J. Fourier, and J. R. Ravetz (1972), *Joseph Fourier, 1768-1830*.

Gronz, O., et al. (2016), Smartstones: A small 9-axis sensor implanted in stones to track their movements, *Catena*, *142*, 245–251.

Großekatthöfer, K., and Z. Yoon (2012), *Introduction into quaternions for spacecraft attitude representation*, TU Berlin.

Habersack, H. (1998), Field measurements with the radio telemetry system at the Angerbach and Wien river, *Internal report at the U. fuer Bodenkultur Vienna*.

Habersack, H. (2001), Radio-tracking gravel particles in a large braided river in New Zealand: a field test of the stochastic theory of bed load transport proposed by einstein, *Hydrological Processes*, *15*(3), 377–391.

Habersack, H., H. Nachtneb El, and J. Laronne (2001), The continuous measurement of bedload discharge in a large alpine gravel bed river, *Journal of Hydraulic Research*, *39*(2), 125–133.

Habersack, H., H. Seitz, and M. Liedermann (2010), Integrated automatic bedload transport monitoring, *US Geological Survey Scientific Investigations Report*, *5091*, 218–235.

Habersack, H. M. (2003), Use of radio-tracking techniques in bed load transport investigations, *IAHS Publication*, pp. 172–180.

Hagiwara, Y. (2010), Local Stokes number for particles in turbulent flows, in *Proceedings of 7th Int. Conference on Multiphase Flow*, pp. 1–5.

Hamilton, W. R. (1844), Lxxviii. On quaternions; or on a new system of imaginaries in algebra: to the editors of the Philosophical Magazine and Journal.

Hanrahan, G., D. G. Patil, and J. Wang (2004), Electrochemical sensors for environmental monitoring: design, development and applications, *Journal of Environmental Monitoring*, *6*(8), 657–664.

Hart, J. K., and K. Martinez (2006), Environmental Sensor Networks: A revolution in the Earth system science?, *Earth-Science Reviews*, *78*(3-4), 177–191, doi:10.1016/j.earscirev.2006.05.001.

Hassan, M. A., and P. Ergenzinger (2003), Use of tracers in fluvial geomorphology, *Tools in fluvial geomorphology (ed. Kondolf, G Mathias and Piégay, Hervé)*, pp. 397–423.

Hassan, M. A., and I. Reid (1990), The influence of microform bed roughness elements on flow and sediment transport in gravel bed rivers, *Earth Surface Processes and Landforms*, *15*(8), 739–750.

Hassan, M. A., and A. G. Roy (2016), Coarse particle tracing in fluvial geomorphology, *Tools in Fluvial Geomorphology*, pp. 306–323.

Hassan, M. A., M. Church, and A. P. Schick (1991), Distance of movement of coarse particles in gravel bed streams, *Water Resources Research*, *27*(4), 503–511.

Hassan, M. A., M. Church, and P. J. Ashworth (1992), Virtual rate and mean distance of travel of individual clasts in gravel-bed channels, *Earth Surface Processes and Landforms*, *17*(6), 617–627.

Hassan, M. A., M. Church, J. Rempel, and R. J. Enkin (2009), Promise, performance and current limitations of a magnetic bedload movement detector, *Earth Surface Processes and Landforms*, *34*(7), 1022–1032.

Heidemann, J., M. Stojanovic, and M. Zorzi (2012), Underwater sensor networks: applications, advances and challenges, *Philosophical Transactions of the Royal Society A: Mathematical, Physical and Engineering Sciences*, *370*(1958), 158–175.

Heidenreich, N.-B., A. Schindler, and S. Sperlich (2013), Bandwidth selection for kernel density estimation: a review of fully automatic selectors, *AStA Advances in Statistical Analysis*, *97*(4), 403–433.

Heyman, J., and C. Ancey (2014), Tracking bed load particles in a steep flume: Methods and results, in *Proceedings of River Flow 2014, Seventh International Conference on Fluvial Hydraulics*.

Hodge, R., T. Hoey, G. Maniatis, and E. Leprêtre (2016), Formation and erosion of sediment cover in an experimental bedrock-alluvial channel, *Earth Surface Processes and Landforms (in press)*.

Hodge, R. A., T. B. Hoey, and L. S. Sklar (2011a), Bed load transport in bedrock rivers: The role of sediment cover in grain entrainment, translation, and deposition, *Journal of Geophysical Research: Earth Surface*, *116*(F4).

Hodge, R. A., T. B. Hoey, and L. S. Sklar (2011b), Bed load transport in bedrock rivers: the role of sediment cover in grain entrainment, translation, and deposition, *Journal of Geophysical Research*, *116*(F4), 1–19, doi:10.1029/2011JF002032.

Höfler, K., and S. Schwarzer (2000), Navier-Stokes simulation with constraint forces: Finite-difference method for particle-laden flows and complex geometries, *Physical Review E*, *61*(6), 7146.

Hosmer, D. W., S. Lemeshow, and R. X. Sturdivant (2000), *Introduction to the Logistic Regression Model*, Wiley Online Library.

Houssais, M., and D. J. Jerolmack (2016), Toward a unifying constitutive relation for sediment transport across environments, *Geomorphology*.

Houssais, M., C. P. Ortiz, D. J. Durian, and D. J. Jerolmack (2015), Onset of sediment transport is a continuous transition driven by fluid shear and granular creep, *Nature Communications*, *6*.

Hovius, N., C. P. Stark, and P. A. Allen (1997), Sediment flux from a mountain belt derived by landslide mapping, *Geology*, *25*(3), 231–234.

Hp (2013), *Hp Designjet 3D printer webpage*, http://www.hp3dprinting.co.uk/hp-designjet-color-3d-printer.html.

Inman, H. F., J. Bradley, and L. Edwin (1989), The overlapping coefficient as a measure of agreement between probability distributions and point estimation of the overlap of two normal densities, *Communications in Statistics-Theory and Methods*, *18*(10), 3851–3874.

ISO, E. (2002), 14688-1: 2002: Geotechnical investigation and testing–identification and classification of soil–part 1: identification and description, *British Standards Institution*.

Jones, E., T. Oliphant, P. Peterson, et al. (2001–), *SciPy: Open source scientific tools for Python*, http://www.scipy.org/.

Joseph, G., R. Zenit, M. Hunt, and A. Rosenwinkel (2001), Particle–wall collisions in a viscous fluid, *Journal of Fluid Mechanics*, *433*, 329–346.

Kalman, R. E. (1960), A new approach to linear filtering and prediction problems, *Journal of Fluids Engineering*, *82*(1), 35–45.

Kay, R., and S. Little (1987), Transformations of the explanatory variables in the logistic regression model for binary data, *Biometrika*, *74*(3), 495–501.

Kirchner, J. W., W. E. Dietrich, F. Iseya, and H. Ikeda (1990), The variability of critical shear stress, friction angle, and grain protrusion in water-worked sediments, *Sedimentology*, *37*(4), 647–672, doi: 10.1111/j.1365-3091.1990.tb00627.x.

Kline, S., W. Reynolds, F. Schraub, and P. Runstadler (1967), The structure of turbulent boundary layers, *Journal of Fluid Mechanics*, *30*(04), 741–773, doi:10.1017/S0022112067001740.

Komar, P. D. (1996), Entrainment of sediments from deposits of mixed grain sizes and densities, *Advances in Fluvial Dynamics and Stratigraphy*, pp. 127–181.

Komar, P. D., and Z. Li (1986), Pivoting analyses of the selective entrainment of sediments by shape and size with application to gravel threshold, *Sedimentology*, *33*(3), 425–436.

Komar, P. D., and Z. Li (1988), Applications of grain-pivoting and sliding analyses to selective entrapment of gravel and to flow-competence evaluations, *Sedimentology*, *35*(4), 681–695.

Kraichnan, R. H. (1964), Kolmogorov's hypotheses and Eulerian turbulence theory, *Physics of Fluids (1958-1988)*, *7*(11), 1723–1734.

Krein, A., R. Schenkluhn, A. Kurtenbach, R. Bierl, and J. Barrière (2016), Listen to the sound of moving sediment in a small gravel-bed river, *International Journal of Sediment Research*.

Krumbein, W. C. (1941), Measurement and geological significance of shape and roundness of sedimentary particles, *Journal of Sedimentary Research*, *11*(2), 64–72.

Kularatna, N., J. McDowall, B. Melville, D. Kularatna-Abeywardana, A. P. Hu, and A. Dwivedi (2010), Low-cost autonomous 3-d monitoring systems for hydraulic engineering environments and applications with limited accuracy requirements, *IEEE Sensors Journal*, *10*(2), 331–339.

Lajeunesse, E., O. Devauchelle, F. Lachaussée, and P. Claudin (2015), Bedload transport in laboratory rivers: the erosion-deposition model, *Gravel-bed Rivers: Processes and Disasters. John Wiley and Sons. (in press)*.

Lamarre, H., and A. G. Roy (2008), The role of morphology on the displacement of particles in a step–pool river system, *Geomorphology*, *99*(1), 270–279.

Lamarre, H., B. MacVicar, and A. G. Roy (2005), Using passive integrated transponder (pit) tags to investigate sediment transport in gravel-bed rivers, *Journal of Sedimentary Research*, *75*(4), 736–741.

Lamb, M. P., N. J. Finnegan, J. S. Scheingross, and L. S. Sklar (2015), New insights into the mechanics of fluvial bedrock erosion through flume experiments and theory, *Geomorphology*, *244*, 33–55.

Lavelle, J. W., and H. O. Mofjeld (1987), Do critical stresses for incipient motion and erosion really exist?, *Journal of Hydraulic Engineering*, *113*(3), 370–385.

Lenzi, M. A. (2004), Displacement and transport of marked pebbles, cobbles and boulders during floods in a steep mountain stream, *Hydrological Processes*, *18*(10), 1899–1914.

Liébault, F., H. Bellot, M. Chapuis, S. Klotz, and M. Deschâtres (2012), Bedload tracing in a high-sediment-load mountain stream, *Earth Surface Processes and Landforms*, *37*(4), 385–399.

Liedermann, M., M. Gerstl, M. Trithart, and H. Habersack (2010), Monitoring artificial tracer stones at the danube east of vienna, in *EGU General Assembly Conference Abstracts*, vol. 12, p. 12457.

Liedermann, M., M. Tritthart, and H. Habersack (2013), Particle path characteristics at the large gravel-bed river danube: results from a tracer study and numerical modelling, *Earth Surface Processes and Landforms*, *38*(5), 512–522.

Lipson, H., and M. Kurman (2013), *Fabricated: The New World of 3D Printing*, John Wiley & Sons.

Maniatis, G., T. Hoey, and J. Sventek (2013), Sensor enclosures: example application and implications for data coherence, *Journal of Sensor and Actuator Networks*, *2*(4), 761.

Maniatis, G., T. Hoey, M. Hassan, J. Sventek, R. Hodge, T. Dyrsdale, and M. Valyrakis (2016a), Calculation of explicit probability of entrainment based on inertial acceleration measurments, *Journal of Hydraulic Engineering, Accepted August 2016*.

Maniatis, G., T. Hoey, R. Hodge, M. Valyrakis, and T. Dyrsdale (2016b), Eulerian-lagrangian description of fluvial sediment transport: I. theory, *Submitted in Journal of Geophysical Research: Earth Science*.

Marion, A., and M. Tregnaghi (2013), A new theoretical framework to model incipient motion of sediment grains and implications for the use of modern experimental techniques, in *Experimental and Computational Solutions of Hydraulic Problems*, pp. 85–100, Springer.

Markham, A., N. Trigoni, D. W. Macdonald, and S. A. Ellwood (2012), Underground localization in 3-d using magneto-inductive tracking, *IEEE Sensors Journal*, *12*(6), 1809–1816.

Martinez, K., J. K. Hart, and R. Ong (2009), Deploying a wireless sensor network in iceland, in *GeoSensor Networks*, pp. 131–137, Springer.

May, C., and B. Pryor (2014), Initial motion and bedload transport distance determined by particle tracking in a large regulated river, *River Research and Applications*, *30*(4), 508–520.

McEwan, I., H. Habersack, and J. Heald (2001), Discrete particle modelling and active tracers: new techniques for studying sediment transport as a lagrangian phenomenon, *Gravel bed rivers V (ed. MP Mosley)*, pp. 339–360.

McEwan, I., M. Sørensen, J. Heald, S. Tait, G. Cunningham, D. Goring, and B. Willetts (2004), Probabilistic modeling of bed-load composition, *Journal of Hydraulic Engineering*, *130*(2), 129–139.

McNamara, J., J. Oatley, D. Kane, and L. Hinzman (2008), Case study of a large summer flood on the north slope of alaska: bedload transport, *Hydrology Research*, *39*(4), 299–308.

McNamara, J. P., and C. Borden (2004), Observations on the movement of coarse gravel using implanted motion-sensing radio transmitters, *Hydrological Processes*, *18*(10), 1871–1884.

Miller, M., I. McCave, P. Komar, et al. (1977), Threshold of sediment motion under unidirectional currents, *Sedimentology*, *24*(4), 507–527.

Montgomery, D. C., and G. C. Runger (2010), *Applied Statistics and Probability for Engineers*, John Wiley & Sons.

Morrison, F. A. (2013), *An Introduction to Fluid Mechanics*, Cambridge University Press.

Mukundan, R. (2002), Quaternions: From classical mechanics to computer graphics, and beyond, in *Proceedings of the 7th Asian Technology conference in Mathematics*, pp. 97–105.

Nelson, J. M., R. L. Shreve, S. R. McLean, and T. G. Drake (1995), Role of near-bed turbulence structure in bed load transport and bed form mechanics, *Water Resources Research*, *31*(8), 2071–2086, doi: 10.1029/95WR00976.

Nichols, M. (2004a), A radio frequency identification system for monitoring coarse sediment particle displacement, *Applied Engineering in Agriculture*, *20*(6), 783.

Nichols, M. (2004b), A radio frequency identification system for monitoring coarse sediment particle displacement, *Applied Engineering in Agriculture*, *20*(6), 783–787.

Nikora, V., H. Habersack, T. Huber, and I. McEwan (2002), On bed particle diffusion in gravel bed flows under weak bed load transport, *Water Resources Research*, *38*(6), 17–1–17–9.

Niño, Y., and M. García (1998), Experiments on saltation of sand in water, *Journal of Hydraulic Engineering*, *124*(10), 1014–1025.

Novatel (2010), *IMU Errors and Their Effects*, www.novatel.com/assets/Documents/Bulletins/APN064.pdf, Accessed 2016-05-09.

Nussbaumer, H. J. (2012), *Fast Fourier Transform and Convolution Algorithms*, vol. 2, Springer Science & Business Media.

Olinde, L., and J. P. Johnson (2015), Using RFID and accelerometer-embedded tracers to measure probabilities of bed load transport, step lengths, and rest times in a mountain stream, *Water Resources Research*, *51*(9), 7572–7589.

Oliveira, L. M., and J. J. Rodrigues (2011), Wireless sensor networks: a survey on environmental monitoring, *Journal of Communications*, *6*(2), 143–151.

O'Reilly, O. M. (2008), Intermediate dynamics for engineers: a unified treatment of Newton-Euler and Lagrangian mechanics, *AMC*, *10*, 12.

Palais, B., and R. Palais (2007), Euler' s fixed point theorem: the axis of a rotation, *Journal of Fixed Point Theory and Applications*, *2*(2), 215–220.

Papanicolaou, A., P. Diplas, N. Evaggelopoulos, and S. Fotopoulos (2002), Stochastic incipient motion criterion for spheres under various bed packing conditions, *Journal of Hydraulic Engineering*, *128*(4), 369–380.

Papanicolaou, A. N., P. Diplas, M. Balakrishnan, and C. L. Dancey (1999), Computer vision technique for tracking bed load movement, *Journal of Computing in civil engineering*, *13*(2), 71–79.

Park, B., and B. Turlach (1992), *Practical performance of several data driven bandwidth selectors*, Thechnical Report, Université catholique de Louvain, Center for Operations Research and Econometrics (CORE).

Park, C., and P. H. Chou (2006), Eco: Ultra-wearable and expandable wireless sensor platform, in *International Workshop on Wearable and Implantable Body Sensor Networks (BSN'06)*, pp. 4–pp, IEEE.

Parker, G., G. Seminara, and L. Solari (2003), Bed load at low Shields stress on arbitrarily sloping beds: Alternative entrainment formulation, *Water Resources Research*, *39*(7).

Pedersen, L., M. Bualat, C. Kunz, S. Lee, R. Sargent, R. Washington, and A. Wright (2003), Instrument deployment for Mars rovers, in *Proceedings of the 2003 IEEE International Conference on Robotics and Automation, ICRA 2003, September 14-19, 2003, Taipei, Taiwan*, vol. 2, pp. 2535–2542, IEEE.

Petris, G. (2010), An R package for dynamic linear models, *Journal of Statistical Software*, *36*(12), 1–16.

Phillips, C. B., R. L. Martin, and D. J. Jerolmack (2013), Impulse framework for unsteady flows reveals superdiffusive bed load transport, *Geophysical Research Letters*, *40*(7), 1328–1333.

Phillips, W., C. Hailey, and G. Gebert (2000), A review of attitude kinematics for aircraft flight simulation, in *AIAA 2000-4302 Modeling and Simulation Technologies Conference*, pp. 1–20.

Pourtakdoust, S., and H. Ghanbarpour Asl (2007), An adaptive unscented Kalman filter for quaternion-based orientation estimation in low-cost AHRS, *Aircraft Engineering and Aerospace Technology*, *79*(5), 485–493.

Prancevic, J. P., and M. P. Lamb (2015), Particle friction angles in steep mountain channels, *Journal of Geophysical Research: Earth Surface*, *120*(2), 242–259.

Reid, I. (2009), River landforms and sediments: evidence of climatic change, in *Geomorphology of Desert Environments*, pp. 695–721, Springer.

Reid, S. C., S. N. Lane, J. M. Berney, and J. Holden (2007), The timing and magnitude of coarse sediment transport events within an upland, temperate gravel-bed river, *Geomorphology*, *83*(1), 152–182.

Ribeiro, J. G., J. T. De Castro, and J. L. Freire (2003), Using the FFT-DDI method to measure displacements with piezoelectric, resistive and ICP accelerometers, in *Conference and Exposition on Structural Dynamics*.

Richardson, K., I. Benson, P. Carling, J. Bogen, T. Fergus, D. Walling, et al. (2003), An instrument to record sediment movement in bedrock channels., in *Erosion and sediment transport measurement in rivers: technological and methodological advances: Workshop, Oslo, Norway, 19-21 June, 2002.*, pp. 228–235, IAHS Press.

Rickenmann, D., and B. W. McArdell (2007), Continuous measurement of sediment transport in the erlenbach stream using piezoelectric bedload impact sensors, *Earth Surface Processes and Landforms*, *32*(9), 1362–1378.

Rickenmann, D., J. M. Turowski, B. Fritschi, A. Klaiber, and A. Ludwig (2012), Bedload transport measurements at the erlenbach stream with geophones and automated basket samplers, *Earth Surface Processes and Landforms*, *37*(9), 1000–1011.

Roland (2013), *Roland 3D-scanners webpage*, `http://www.rolanddga.com/products/scanners/lpx600/`.

Roseberry, J. C., M. W. Schmeeckle, and D. J. Furbish (2012), A probabilistic description of the bed load sediment flux: 2. particle activity and motions, *Journal of Geophysical Research: Earth Surface (2003–2012)*, *117*(F3).

Rosenblatt, M. (1956), Remarks on some nonparametric estimates of a density function, *The Annals of Mathematical Statistics*, *27*(3), 832–837.

Sabatini, A. M. (2006), Quaternion-based extended Kalman filter for determining orientation by inertial and magnetic sensing, *Biomedical Engineering, IEEE Transactions*, *53*(7), 1346–1356.

Scheingross, J. S., F. Brun, D. Y. Lo, K. Omerdin, and M. P. Lamb (2014), Experimental evidence for fluvial bedrock incision by suspended and bedload sediment, *Geology*, *42*(6), 523–526.

Schmeeckle, M. W., J. M. Nelson, and R. L. Shreve (2007), Forces on stationary particles in near-bed turbulent flows, *Journal of Geophysical Research: Earth Surface (2003–2012)*, *112*(F2), doi:10.1029/2006JF000536.

Schmelter, M., M. Hooten, and D. Stevens (2011), Bayesian sediment transport model for unisize bed load, *Water Resources Research*, *47*(11).

Schmid, F., and A. Schmidt (2006), Nonparametric estimation of the coefficient of overlapping: theory and empirical application, *Computational statistics & data analysis*, *50*(6), 1583–1596.

Schmidt, K.-H., and P. Ergenzinger (1992), Bedload entrainment, travel lengths, step lengths, rest periods Äîstudied with passive (iron, magnetic) and active (radio) tracer techniques, *Earth Surface Processes and Landforms*, *17*(2), 147–165.

Schneider, J., R. Hegglin, S. Meier, J. Turowski, M. Nitsche, and D. Rickenmann (2010), Studying sediment transport in mountain rivers by mobile and stationary rfid antennas, in *River flow*, vol. 2010, pp. 1723–1730, Bundesanstalt für Wasserbau: Karlsruhe, Germany.

Sear, D., M. Lee, M. Collins, and P. Carling (2002), The intelligent pebble: A new technology for tracking particle movements in fluvial and littoral environments., in *Erosion and Sediment Transport Measurement: Technological and Methodological Advances Workshop*, pp. 19–21.

Seifert, K., and O. Camacho (2007), *Implementing Positioning Algorithms Using Accelerometers*, https://www.nxp.com/files/sensors/doc/app-note/AN3397.pdf.

Sheather, S. J., and M. C. Jones (1991), A reliable data-based bandwidth selection method for kernel density estimation, *Journal of the Royal Statistical Society. Series B (Methodological)*, pp. 683–690.

Sheather, S. J., et al. (2004), Density estimation, *Statistical Science*, *19*(4), 588–597.

Shields, A. (1936), Application of similarity principles and turbulence research to bed-load movement, *Technical Report, Soil Conservation Service*.

Shuster, M. D. (1993), A survey of attitude representations, *Navigation*, *8*(9), 439–517.

Shuster, M. D., and S. Oh (1981), Three-axis attitude determination from vector observations, *Journal of Guidance, Control, and Dynamics*, *4*(1), 70–77.

Shvidchenko, A. B., and G. Pender (2000), Flume study of the effect of relative depth on the incipient motion of coarse uniform sediments, *Water Resources Research*, *36*(2), 619–628.

Sidi, M. J. (1997), *Spacecraft Dynamics and Control: a practical engineering approach*, vol. 7, Cambridge university press.

Silverman, B. (1982), Algorithm as 176: Kernel density estimation using the fast fourier transform, *Journal of the Royal Statistical Society. Series C (Applied Statistics)*, *31*(1), 93–99.

Silverman, B. W. (1986), *Density estimation for statistics and data analysis*, vol. 26, CRC press.

Slabaugh, G. G. (1999), Computing euler angles from a rotation matrix, *Retrieved on August*, *6*(2000), 39–63.

Slifka, L. D. (2004), An accelerometer based approach to measuring displacement of a vehicle body, Master Thesis, University of Michigan–Dearborn.

Smart, G. M. (1984), Sediment transport formula for steep channels, *Journal of Hydraulic Engineering*, *110*(3), 267–276.

Šolc, T., A. Stefanovska, T. Hoey, and M. Mikoš (2012), Application of an instrumented tracer in an abrasion mill for rock abrasion studies, *Strojniški vestnik-Journal of Mechanical Engineering*, *58*(4), 263–270.

Sownet Technologies (2013), *G-node mote webpage*, http://www.sownet.nl/index.php/products/gnode, Accessed 28 November 2013.

Stokes, G. G. (1851), *On the Effect of the Internal Friction of Fluids on the Motion of Pendulums*, vol. 9, Pitt Press.

Système, D. (2016), *Dassault Systèmes, SolidWorks Software webpage*, http://www.solidworks.com.

Syvitski, J. P., M. D. Morehead, D. B. Bahr, and T. Mulder (2000), Estimating fluvial sediment transport: the rating parameters, *Water Resources Research*, *36*(9), 2747–2760.

T.I (2001), *TEXAS Instruments Low-RFID kit 2000*.

Tropea, C., A. L. Yarin, and J. F. Foss (2007), *Springer Handbook of Experimental Fluid Mechanics*, vol. 1, Springer Science & Business Media.

Tsai, C.-J., S.-C. Chen, C.-H. Huang, and D.-R. Chen (2004), A universal calibration curve for the tsi aerodynamic particle sizer, *Aerosol Science and Technology*, *38*(5), 467–474.

Tsai, C. W., and K.-C. Lai (2014), Three-state continuous-time markov chain model for mixed-size sediment particle transport, *Journal of Hydraulic Engineering*, *140*(9).

Tsakiris, A. G., A. N. Papanicolaou, and T. J. Lauth (2014), Signature of bedload particle transport mode in the acoustic signal of a geophone, *Journal of Hydraulic Research*, *52*(2), 185–204.

Tsakiris, A. G., A. Papanicolaou, I. Moustakidis, and B. K. Abban (2015), Identification of the burial depth of radio frequency identification transponders in riverine applications, *Journal of Hydraulic Engineering*, *141*(6), 04015,007.

Tunnicliffe, J., A. S. Gottesfeld, and M. Mohamed (2000), High resolution measurement of bedload transport, *Hydrological Processes*, *14*(15), 2631–2643.

Valyrakis, M., P. Diplas, C. L. Dancey, K. Greer, and A. O. Celik (2010), Role of instantaneous force magnitude and duration on particle entrainment, *Journal of Geophysical Research: Earth Surface (2003–2012)*, *115*(F2).

Valyrakis, M., P. Diplas, and C. L. Dancey (2011a), Entrainment of coarse grains in turbulent flows: An extreme value theory approach, *Water Resources Research*, *47*(9).

Valyrakis, M., P. Diplas, and C. L. Dancey (2011b), Prediction of coarse particle movement with adaptive neuro-fuzzy inference systems, *Hydrological Processes*, *25*(22), 3513–3524.

Valyrakis, M., P. Diplas, and C. L. Dancey (2013), Entrainment of coarse particles in turbulent flows: An energy approach, *Journal of Geophysical Research: Earth Surface*, *118*(1), 42–53.

Vatne, G., O. y. Takøy Naas, T. Skãrholen, A. a. Beylich, and I. Berthling (2008), Bed load transport in a steep snowmelt-dominated mountain stream as inferred from impact sensors, *Norsk Geografisk Tidsskrift - Norwegian Journal of Geography*, *62*(2), 66–74, doi:10.1080/00291950802094817.

VectorNav (2016), *Inertial Measurement Units and Inertial Navigation*, VecotrNav webpage: www.vectornav.com/support/library/imu-and-ins, Accessed 2016-05-09.

Warburton, J., and T. Demir (2000), Influence of bed material shape on sediment transport in gravel-bed rivers: a field experiment, *Tracers in Geomorphology: Chichester, UK, John Wiley & Sons*, pp. 401–410.

Wathen, S. J., T. B. Hoey, and A. Werritty (1997), Quantitative determination of the activity of within-reach sediment storage in a small gravel-bed river using transit time and response time, *Geomorphology*, *20*(1), 113–134.

Weisstein, E. W. (2009), *Euler angles*, Wolfram Research, Inc.

Weitzman, M. S. (1970), *Measures of overlap of income distributions of white and Negro families in the United States*, vol. 22, US Bureau of the Census.

Werner-Allen, G., K. Lorincz, M. Welsh, J. Johnson, and J. Lees (2006), Deploying a Wireless Sensor Network on an Active Volcano, *IEEE Internet Computing Sensor-Network Applications*, (April), 18–25.

Whipple, K. X., and G. E. Tucker (2002), Implications of sediment-flux-dependent river incision models for landscape evolution, *Journal of Geophysical Research: Solid Earth*, *107*(B2).

White, C. (1940), The equilibrium of grains on the bed of a stream, *Proceedings of the Royal Society of London. Series A, Mathematical and Physical Sciences*, pp. 322–338.

Whitmore, S. A. (2000), Closed-form integrator for the quaternion (Euler angle) kinematics equations, US Patent 6,061,611.

Wiberg, P. L., and D. J. Smith (1989), Model for calculating bed load transport of sediment, *Journal of Hydraulic Engineering*, *115*(1), 101–123.

Wiberg, P. L., and J. Smith (1985), A theoretical model for saltating grains in water, *Journal of Geophysical Research: Oceans*, *90*(C4), 7341–7354.

Wilcock, P. R. (1993), Critical shear stress of natural sediments, *Journal of Hydraulic Engineering*, *119*(4), 491–505.

Wilcock, P. R. (1997), Entrainment, displacement and transport of tracer gravels, *Earth Surface Processes and Landforms*, *22*(12), 1125–1138.

Wilson, J. C., and B. Y. Liu (1980), Aerodynamic particle size measurement by laser-doppler velocimetry, *Journal of Aerosol Science*, *11*(2), 139–150.

Woodman, O. J. (2007), An introduction to inertial navigation, *University of Cambridge, Computer Laboratory, Technical Report. UCAMCL-TR-696*, *14*, 15.

Wu, F.-C., and Y.-J. Chou (2003), Rolling and lifting probabilities for sediment entrainment, *Journal of Hydraulic Engineering*, *129*(2), 110–119.

Wu, W., W. Rodi, and T. Wenka (2000), 3D numerical modeling of flow and sediment transport in open channels, *Journal of Hydraulic Engineering*, *126*(1), 4–15.

Yalin, M. S., and E. Karahan (1979), Inception of sediment transport, *Journal of the Hydraulics Division*, *105*(11), 1433–1443.

YEI, T. (2014), *3-Space Sensor, User's Manual*, YEI Trechnology.

Yost Labs (2016), *YEI 3-Space Sensor Watertight USB/RS232* , https://www.yostlabs.com/productdisplay/3-space-watertight-usbrs232, Accessed 5 of July 2016.

Zedler, E. A., and R. L. Street (2001), Large-eddy simulation of sediment transport: currents over ripples, *Journal of Hydraulic Engineering*, *127*(6), 444–452.

Zekavat, R., and R. M. Buehrer (2011), *Handbook of Position Location: Theory, Practice and Advances*, vol. 27, John Wiley & Sons.

Zhang, Y., and X. Li (1996), Fixed-interval smoothing algorithm based on singular value decomposition, in *Control Applications, 1996., Proceedings of the 1996 IEEE International Conference on*, pp. 916–921, IEEE.

Zhao, F., and B. van Wachem (2013), A novel quaternion integration approach for describing the behaviour of non-spherical particles, *Acta Mechanica*, *224*(12), 3091–3109.

Zhao, Y. (2016), Performance evaluation of cubature Kalman filter in a GPS/IMU tightly-coupled navigation system, *Signal Processing*, *119*, 67–79.

Zheng, C., G. D. Bennett, et al. (2002), *Applied Contaminant Transport Modeling*, vol. 2, Wiley-Interscience New York.

Zylbersztajn, A. (1994), Newton's absolute space, Mach's principle and the possible reality of fictitious forces, *European Journal of Physics*, *15*(1), 1.